Charles University

Faculty of Science

Developmental and Cell Biology

Mgr. Alena Koukalová

Lipid Membranes at the Nanoscale: Single-Molecule Fluorescence Approach

Studium lipidových membrán v nanorozlišení pomocí fluorescenční detekce jednotlivých molekul

Ph.D. Thesis

Supervisor: prof. RNDr. Jan Černý, Ph.D.

Supervisor-consultant: RNDr. Radek Šachl, Ph.D.

Prague, 2018

Declaration:

I hereby declare that my thesis is a presentation of my original research work. Wherever contribution of others is involved, every effort is made to indicate this clearly, with reference the literature. This thesis contains no material that has been submitted previously, in whole or in part, for the award of any other academic degree or diploma.

Prohlášení:

Prohlašuji, že jsem závěrečnou práci zpracovala samostatně, a že jsem uvedla všechny použité informační zdroje a literaturu. Tato práce ani její podstatná část nebyla předložena k získání jiného nebo stejného akademického titulu.

V Praze, 10. 9. 2018

Podpis (Signature)

Acknowledgements

Abstract

The complexity of cell membranes is far from being only a simple assembly of lipids and proteins separating cells from the surrounding environment. Each of the thousands of different membrane components performs its specific role in cellular functions, since a multitude of biological processes is mediated by membranes. The understanding of the molecular basis of these processes is one of the important aims of current biological research. Our research employing single-molecule fluorescence methods (e.g. FCS, FCCS, FLIM-FRET) has made a contribution to the knowledge of membrane lateral organization or mechanism of membrane fusion. Furthermore, we revealed the mechanism of membrane activity of a small natural compound. As native cell membranes are very complex structures, we performed the experiments on simplified model lipid membranes that allow studying lipid-lipid or lipid-protein interactions at the molecular level in a controlled way.

The first part of this thesis deals with the mode of action of a membrane active secondary metabolite didehydroroflamycoin (DDHR). We demonstrated that DDHR is a pore-forming agent and that this activity is influenced by the presence of cholesterol. Direct visualization of intrinsic fluorescence of DDHR revealed its preferential partitioning into membrane areas with higher lipid order.

The second part concentrates on the membrane lateral heterogeneity close to the phase separation boundary. Membrane heterogeneity plays an important role in multiple cellular processes, but its nature is controversial. Although conventional fluorescence microscopy techniques do not allow direct visualization of these sub-microscopic structures, we were able to detect them by various single-molecule approaches. We identified approximately 9 nm sized fluid nanodomains in GUVs composed of ternary DOPC/Chol/SM and even in binary DOPC/SM lipid compositions. Furthermore, we showed that also ganglioside GM1 clusters into nanoscale domains and that its availability for binding by cholera toxin B subunit is influenced by GM1 density as well as by the presence of cholesterol.

The third part is focused on investigation of complementary coiled-coil forming lipopeptides CP_nK_4 and CP_nE_4 that serve as a model system for membrane fusion. Single-molecule fluorescence techniques were employed to study their roles in the initial steps of the fusion process mediated by these lipopeptides. Our research revealed the asymmetrical nature of this fusion system. We proposed a model where the peptide moiety of the lipopeptide CP_nE_4 acts as a "handle" for positively charged peptide moiety of CP_nK_4 resulting in liposome docking, while the peptide K_4 interacts with the membrane causing local deformations, which enhances the fusion process.

Abstrakt

Komplexita buněčných membrán zdaleka není jen pouhé náhodné uskupení lipidů a proteinů, které odděluje buňku od okolního prostředí. Každá z tisíců různých složek membrán vykonává své specifické funkce důležité pro funkci celé buňky, neboť mnoho biologických procesů se odehrává právě na membránách. Pochopení těchto procesů na molekulové úrovni je cílem současného biologického výzkumu. Náš výzkum využívající detekci jednotlivých fluorescenčních molekul (např. FCS, FCCS, FLIM-FRET) přispěl k poznání laterální organizace membrán nebo mechanismu membránové fúze. Dále jsme odhalili mechanismus účinku membránově aktivního sekundárního metabolitu. Vzhledem k tomu, že je membránový systém živých buněk příliš složitý, byly naše experiment prováděny na modelových lipidových membránách, které umožňují studium lipid-lipidových a lipid-proteinových interakcí na molekulové úrovni kontrolovaným způsobem.

První část této práce se zabývá studiem mechanismu působení sekundárního metabolitu didehydroroflamycoinu (DDHR) v membránách. Zjistili jsme, že DDHR je molekula tvořící póry v membránách a že je tato schopnost ovlivněna přítomností cholesterolu. Přímá vizualizace vlastní fluorescence DDHR ukázala jeho preferenční lokalizaci do oblastí membrán s vyšší uspořádaností lipidů.

Druhá část práce je věnována studiu laterální heterogenity membrán v blízkosti fázového přechodu lipidů. Heterogenita membrán hraje významnou úlohu v mnoha buněčných procesech, její charakter však není dosud znám. Přestože konvenční fluorescenční mikroskopie neumožňuje přímou vizualizaci submikroskopických struktur, jejich existenci jsme zaznamenali pomocí různých technik založených na detekci jedné molekuly. Díky tomuto přístupu jsme identifikovali 9 nm velké fluidní nanodomény v GUV membránách o složení DOPC/Chol/SM a DOPC/SM. Dále jsme ukázali, že gangliosidy GM1 agregují a vytváří nanometrové domény a že je jejich přístupnost pro navázání ligandu B-podjednotky cholera toxinu ovlivněna denzitou GM1 molekul i přítomností cholesterolu.

Třetí část této práce je zaměřena na studium komplementárních lipopeptidů CP_nK_4 a CP_nE_4, které mezi sebou vytváří tzv. "coiled-coil" vazbu a které slouží jako modelový systém pro fúzi membrán. Pokročilé fluorescenční metody nám umožnily studovat počáteční fáze membránové fúze zprostředkované těmito lipopeptidy. Ukázali jsme, že peptidová část lipopeptidu CP_nE_4 pouze přitáhne kladně nabitou peptidovou část lipopeptidu CP_nK_4 k membráně, což vede k přiblížení liposomů. Peptid K_4 interaguje s membránou a způsobuje její deformace, což následně přispívá k membránové fúzi.

Table of Contents

Introduction

Life is a unique condition clearly distinct from inorganic matter. All living organisms manifest fundamental common properties such as metabolism, ability to reproduce, maintenance of their homeostasis or ability to adapt to the surrounding environment. Cell is considered as the smallest fundamental unit of life. It can exist on its own or in a community forming a multicellular organism, where it cooperatively interacts with other cells in a concert. A living cell is minimally composed of plasma membrane, cytoplasm and a nucleic acid. Plasma membrane, as an indispensable cellular component, separates the interior of a cell from the outside environment, so that maintaining the internal conditions necessary for basic cellular functions is possible. The interior of eukaryotic cells is further separated by additional membranes enclosing their organelles. Membranes are not only passive cell or organelle envelopes, but they also actively participate in cellular communication, adhesion or transport of molecules, provide a support for a variety of proteins and even protect cells against pathogens. Without membranes, life as we know it would not exist.

Based on the fact that membranes fulfil very important cellular functions and are indispensable for life itself, it is important to study their overall biophysical properties. The knowledge of the membrane characteristics would reveal to us hidden processes of life, and therefore we could better understand the cellular physiology in detail. By studying membranes we not only get insight into the processes in the membranes themselves, but we also gain a lot of information about membrane-interacting proteins that are other key elements for life. However, cellular membranes are very difficult to study directly because of their complexity and it is rather problematic to control all relevant parameters during experiments. Thus, model membrane systems provide convenient tools for examining membrane properties or molecules that interact with the membranes in a controlled way.

In order to study the structure and dynamics of the biological membranes, numerous techniques have been employed, for instance, magnetic nuclear resonance (NMR), atomic-force microscopy (AFM) or fluorescence microscopy together with a variety of biochemical methods. Fluorescence techniques have an eminent place in the field of membrane research due to high sensitivity, low invasiveness and a potential to be used in living organisms. Recent rapid progress in the fluorescence instrumentation has enabled us to study the detailed picture of membranes even at the molecular level.

This thesis presents results on research concerning the membranes and their interactions with other elements on artificial model membranes employing fluorescence as a tool to monitor processes on a single-molecule level.

The first part of this thesis is aimed on studying mechanism of action of a novel secondary metabolite didehydroroflamycoin produced by soil bacteria *Streptomyces durmitorensis*. We focused on membrane interactions and pore-forming activity of this compound.

The second part deals with sub-resolution model membrane heterogeneity that is expected to be analogous to the plasma membrane organization. Employing single-molecule fluorescence techniques combined with a computational approach, we aimed to uncover the nature of these membrane sub-microscopic heterogeneities. In the study investigating the role of ganglioside GM1 in the membranes, we examined not only the character of nanodomains formed by GM1, but also the relation between binding activity of GM1 and its ligand CTxB.

In the third part, we investigated the membrane interactions of fusogenic coiled-coil forming lipopeptides and their roles in the initial steps of membrane fusion.

Since the research topics are diverse, this thesis comprises of a general introductory part that is followed by three main parts. Each part involves a broader introduction related to the topic of a particular publication that is followed by summary of the main results discussed in the context of other relevant works. The conclusions are summarized at the end of this thesis.

Biological membranes

Biological membranes are thin and selectively permeable layers of amphipathic molecules surrounding cells, as well as their intracellular organelles, and separate them from the outside environment. Plasma membrane encircles the whole cell and it is usually the only membrane structure in prokaryotes (with exception of Gram-negative bacteria containing two membrane envelopes) and enveloped viruses. In eukaryotic cells, additional membranes compartmentalize the intracellular space defining the cellular organelles such as mitochondria or chloroplasts, endoplasmic reticulum or Golgi apparatus etc., which maintain specific cellular environment for various chemical reactions. The cellular membranes are not only passive separators of the organelles, but they also actively participate in communication of cells or cellular organelles with outside environment comprising exchange of metabolites, transport of ions or other molecules or they provide platforms for energy production and signal transduction. Membranes consist of a mixture of lipids, carbohydrates and proteins that are orchestrated to various functions.

Lipids

Biological membranes are complex and dynamic assemblies of lipids and proteins. The membrane structure is created by a double sheet of lipid molecules (with exception of some archaea where the lipid bilayer can be replaced by a monolayer) composed of a polar headgroup and usually two hydrocarbon chains that are responsible for hydrophobic effect maintaining a membrane bilayer as a stable structure. The hydrophilic headgroups interact with water molecules as well as with polar parts of neighbouring molecules, which forms an energetically stable system. Thanks to these properties, lipids spontaneously self-associate in aqueous solutions into micelles, liposomes or even sheets in order to minimize contact of the nonpolar fatty acyl chains with water.

Eukaryotic cells are composed of thousands of different lipid species resulting in a high complexity in composition and function. Differences of particular membrane lipids in their polar headgroups are crucial for maintaining various cellular functions, such as endo/exocytosis, cell signaling etc. In addition, the length and saturation of hydrophobic chains together with their number (e.g. single fatty acyl chain in lysobisphosphatidic acid) play very important role in rigidity of membranes, influence the transition temperature of lipids from the solid to liquid phase and are crucial for the compartmentalization of membranes into domains.

Originally, membranes were considered as a simple platform for proteins [1]. Nevertheless, during the past decades, the importance of particular lipid species has been revealed and their roles in the cellular processes have been more

appreciated [2]. Lipid composition dictates many membrane properties, such as fluidity, order, thickness or elasticity. It was shown, for instance, that membranes contain distinct regions with specific lipid composition or different thickness, which points out to diverse function of these domains.

Lipid species can be divided into three main structural lipid classes that compose the majority of biological membranes: glycerophospholipids, sphingolipids and sterols (Fig. 1).

Glycerophospholipids are major membrane constituents responsible for maintaining the membrane as a functional bilayer. They are derivatives of glycerol with two (or possibly one) hydrocarbon tails of variable length attached to the glycerol molecule substituting –OH groups. The third hydroxyl group is linked to one phosphate that can bear hydrophilic headgroup e.g. choline (phosphatidylcholine - PC), ethanolamine (phosphatidylethanolamine – PE), inositol (phosphatidylinositol – PI) or serine (phosphatidylserine – PS), each having its specific properties and charge.

Sphingolipids are a group of lipids containing a backbone of a long-chain (sphingoid) base. The simplest sphingolipid in structure is ceramide, more complex sphingolipids possess additional groups, such as phosphate or sugar group attached to the sphingoid base. In most mammalian tissues, the most abundant sphingolipid is sphingomyelin containing 18-carbon sphingoid base, two hydroxyl groups, an amine group and a long hydrophobic chain. Sphingolipids are predominantly located in the plasma membrane where they play various biological roles. For instance, thanks to their predominantly saturated and trans-unsaturated acyl chains, they rigidify the membrane, self-aggregate into micro- and nanodomains or influence functions of numerous membrane proteins.

Sterols are a group of small planar molecules with a great impact on membrane fluidity and lateral membrane organization. The most important sterol in mammalian cells is cholesterol that is an essential and the most abundant component of their membranes as well as a precursor for steroid hormones or vitamins. In contrast, yeast membranes contain predominantly ergosterol as a main membrane sterol component.

A specific group of lipids are glycolipids, where monosaccharide or oligosaccharide is attached to the lipid moiety. The lipid backbone most often comprises glycerol or sphingosine and the hydrophobic tail. Glycolipids are generally found on the extracellular leaflet of eukaryotic cellular membranes and inside vesicles of endo-lysosomal system. They participate in a wide range of cellular phenomena, for instance, they facilitate cell-cell interactions via recognition of carbohydrate binding proteins (lectins) or form a highly hydrated protective glycocalyx. A group of glycosphingolipids – gangliosides – bear a

headgroup composed of one or more sialic acids attached to a sugar part of glycosphinglipid. These lipids are also known as receptors for viral particles or toxins, such as Cholera toxin or Shiga toxin [3] [4].

Variability of lipids is considered to be crucial for membrane robustness and stability; for example, in case when osmolality fluctuates from physiological levels [5]. The composition of different kinds of lipids strongly varies with function of the membrane and the type of cell.
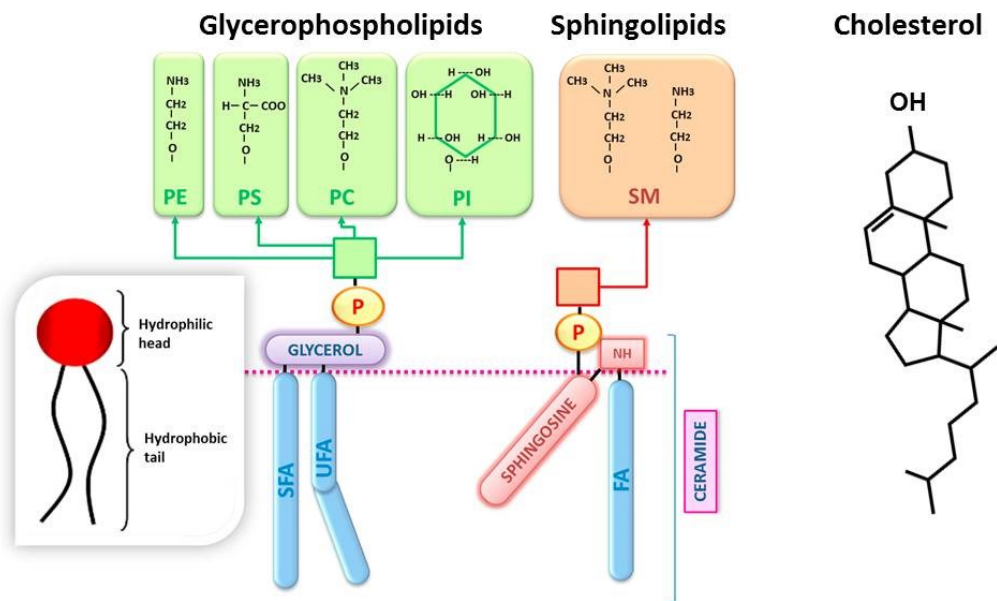
Figure 1. Chemical structures of membrane lipids (adapted from [6]**).**
The diagram shows the schematic structures of phospatidylethanolamine (PE), phosphatidylserine (PS), phosphatidylcholine (PC), phosphatidylinositol (PI), sphingomyelin (SM) and cholesterol. The hydrophilic headgroups of phospho- or sphingolipids are attached to sphingosine or fatty acids (FA) that can be either saturated (SFA), or unsaturated (UFA).

Membrane proteins

Besides lipid molecules, the membrane is composed of many different proteins involved in a variety of cellular processes. The lipid bilayer provides dock for their correct localization [7] and is crucial for their proper function. Membrane lipid to protein mass ratio considerably varies depending on the type of cellular membrane or a type of the cell. For example, the myelin sheath wrapped around axons of nerve cells contains nearly 80 % of lipids; in comparison with other membranes, the protein content is low. On the other hand, the inner mitochondrial membranes accommodate about 80 % of proteins and only 20 % of lipids.

However, in most cell types, proteins represent approximately a half of the total membrane mass [8].

Membrane proteins can pass the whole length of the bilayer (integral proteins) or attach to the membrane surface by a lipid anchor, through charges of the anionic headgroup of phospholipids or via binding to the integral proteins (peripheral proteins). A few proteins (e.g. caveolins) represent a group of membrane proteins that penetrate only one membrane leaflet.

Membrane proteins perform various functions, such as signaling, ion transport, uptake of nutrients, energy transduction etc. In eukaryotic cells, membranes are also associated with the cytoskeletal network, which plays a key role in determining cell shape and a tissue integrity. This structure called actomyosin cortex is a specialized layer of proteins on the inner membrane leaflet forming protrusions like filopodia or lamelliopodia, polymerizing against a membrane on the leading edge of a cell elicit amoeboid migration. Another type of cytoskeletal network – microtubules – form highly stable membrane protrusions (cilia, flagelae) that are responsible for cellular movement or signal transduction.

Transmembrane parts of proteins are buried in the membrane core and directly interact with lipids. Naturally, lipid composition affects the protein activity through lipid-protein interactions [2], surface charge, fluidity or hydrophobic mismatch [9]. For example, specific lipid-protein interactions play an important role in sorting proteins from endoplasmic reticulum to the cell surface [10] or in holding protein oligomers together [11].

Membrane characteristics

The physical state of membranes can be characterized by a range of properties. Among the most important ones are fluidity or lateral inhomogeneity. Cellular membranes, in contrast to artificial membranes, have also asymmetric distribution of lipids between membrane leaflets.

MEMBRANE FLUIDITY

A cellular membrane model of Singer and Nicolson [1] emphasized fluidity as one of the most important membrane features. This property enables the majority of membrane components to diffuse freely within the lipid bilayer, rotate or easily adopt their optimal conformation as well as to maintain the membrane integrity. Membrane fluidity allows proteins to cluster, enables lipids to form specific regions – domains, or is fundamental for various chemical reactions and cellular processes. Membrane fluidity is related to lipid packing and can be modified by saturation of lipid acyl-chains or temperature [12]. Lipids with long and saturated hydrophobic chains tend to be packed more tightly, due to more van der Waals interactions that can be arranged between the acyl chains. On the other hand, lipids with shorter and/or unsaturated hydrophobic chains form less packed and more fluid membranes. Membrane fluidity is highly influenced by the presence of cholesterol. Thanks to its shape, cholesterol is attracted close to the lipid acyl chains, where it either rigidifies the membranes formed by unsaturated lipids by its accommodation between unsaturated hydrocarbon chains, or it makes more fluid the saturated membranes by separating lipid acyl chains. Without cholesterol, the cellular membranes would be too fluid and permeable. It has been proposed that packing of cholesterol and sphingolipids contributes to higher plasma membrane rigidity and consequently to higher resistance to stress [13].

DIFFERENCES IN LIPID COMPOSITION BETWEEN ORGANELLES

Cellular organelles are surrounded by membranes with different lipid compositions, which is crucial for their correct function. For instance, endoplasmic reticulum maintains very low level of sphingolipids and cholesterol. In contrast, plasma membrane contains high amounts of these lipids presumably for its higher stability that protects cellular integrity. On the other side, cardiolipin is an anionic lipid found almost exclusively in the inner membrane of mitochondria that plays a crucial role in mitochondrial physiology. Similarly, lysobisphosphatidic acid (LBPA) is enormously enriched in the inner membranes of lysosomes or multivesicular late endosomes, where it forms specialized membrane domains [14]. LBPA often represents about 15 % of all phospholipids in these organelles. In contrast, this lysophospholipid is almost absent in mitochondria, plasma membrane or endoplasmic reticulum.

PLASMA MEMBRANE ASYMMETRY

Cells maintain lipid asymmetry not only between cellular organelles, but also between the membrane leaflets. The exoplasmic leaflet is enriched in sphingomyelin and glycolipids, while phosphatidylserine, phosphatidylinositol and phosphatidylethanolamine are predominantly located in the cytosolic leaflet. Such lipid asymmetry plays a critical role in many biological and cellular processes and contributes to the membrane diversity and complexity. For instance, sugar moieties of glycolipids are always oriented to the extracellular space, where they form, together with sugar moieties of glycosylated proteins, so called glycocalyx that is involved in cellular adhesion and protects the cells against chemicals. Membrane asymmetry is also preserved for maintaining negative charge in the inner leaflet, which is vital for many intracellular processes.

Lipid asymmetry is actively maintained by various transport proteins called flippases, and floppases. In opposite, scramblases can randomize the membrane asymmetry, for instance during apoptosis, when phosphatidylserine needs to be externalized as an "eat me" signal for phagocytic cells [15]. Spontaneous translocation of lipids between the leaflets is rare and extremely slow [16].

LATERAL HETEROGENEITY OF MEMBRANES

About three decades ago, membrane lateral heterogeneity has been proposed to play an essential role in the correct function of cellular processes [17]. As already mentioned, biological membranes are composed of diverse lipids and proteins that can be spatially organized into distinct heterogeneous regions named also as domains. Their formation is related to the tendency of lipids to be surrounded by other lipids with similar chain length and saturation, which protects the hydrophobic core of the bilayer from the water molecules. Not only lipids self-assembly, but also lipid-protein or protein-protein interactions have been proven to participate in membrane inhomogeneity that is responsible for domain formation. It is important to mention that cholesterol plays a crucial role in domain formation. Lateral membrane heterogeneity is described in detail elsewhere in this thesis.

Membrane heterogeneity and the role of cholesterol

Cholesterol is a key molecule essential for cellular viability, since it plays an important role in maintaining membrane integrity of animal cells, signaling [18] and the regulation of intracellular vesicular trafficking [19]. Living cells either biosynthesize the cholesterol, or import it via endocytic way from outside usually in the form of lipoprotein particles.

Cholesterol content in membranes of higher eukaryotes varies between 20 and 50 mol%, depending on the cellular organelle or cell type. Thus, it is evident that cholesterol is a very important membrane molecule. As already mentioned, cholesterol fulfills many functions. It is crucial not only for metabolism of hormones and vitamins, but also for membrane mechanical resistance, as well as for regulation of membrane phase behaviour. Cholesterol in membranes

considerably reduces transmembrane passive diffusion of water or other small molecules [20] and is very important factor for regulation of liquid ordered and liquid disordered phase ratio. The presence of cholesterol in fluid membranes composed of unsaturated lipids increases the acyl chain order, reduces area per lipid and decreases the mobility. On the other hand, the opposite effect was observed for membranes composed of saturated phospholipids, where the presence of cholesterol increases the membrane fluidity [21]. In addition, cholesterol plays a key role in formation of lateral membrane heterogeneities and domains. However, the detailed mechanism that drives the domain formation in membranes is not well understood.

Besides cholesterol, the presence of other membrane sterols, such as ergosterols or sitosterols in fungi or in plants, respectively, indicates that eukaryotic membranes evolutionary adopted sterols as important players in membrane integrity and function. However, some organisms (e.g. ciliated protozoans or diverse low-oxygen-adopted eukaryotes) produce, instead of sterols, the cyclic triterpenoid lipid tetrahymanol. Moreover, a number of anaerobic protists utilize neither sterols nor tetrahymanol in their membranes [22]. On the other hand, the usage of sterols is not restricted to the eukaryotic domain as a few bacterial species also synthetize sterols [23], although their main membrane fluidity regulatory molecules are hopanoids.

Membrane organization models

Biological membranes represent a complex system of various lipids and proteins with thousands of "players" that perform a wide range of physiological processes and influence the membrane characteristics. Before direct visualization of membranes by electron microscopy in 1950s, there were considerable speculations about their real structure. Similarly, the lateral organization of the membranes remains a controversial issue.
Below are summarized the most notable membrane organization models.

MODELS OF PLASMA MEMBRANE STRUCTURE
The very first concept of membrane organization was proposed by Gorter and Grendel in 1925 [24] (Fig. 2A). They investigated the surface area of lipids isolated from red blood cells employing Langmuir monolayer and postulated that the membranes are organized as either a lipid bilayer or a bimolecular leaflet, as the surface area of the monolayers was about two times larger than the surface area of the cells.
Ten years later, in 1935, Davson and Danielli came up with a model that included also proteins (Fig. 2B). According to this model, phospholipid bilayers are sandwiched between two layers of globular proteins that are not allowed to penetrate into the lipid bilayer [25].

In 1966, Benson and Green demonstrated that the inner mitochondrial membrane can be separated into segments containing both lipids and proteins and subsequently reconstituted into fully active membranes [26]. Thus, they proposed that membrane lipids function as a solvent for embedded globular proteins.

Current view on the organization of the biological membranes is based on the fluid mosaic model proposed in 1972 by Singer and Nicolson [1] (Fig 2C). They imaged the membrane as a fluid flat-shape lipid bilayer with either embedded proteins that traverse the bilayer, or peripheral proteins associating with the membrane via electrostatic or hydrogen-bond interactions. Proteins and lipids can, according to this model, move freely within the bilayer allowing them to form lipid or protein assemblies. This model represents an important step in the current view of membrane organization and provides a backdrop for all subsequent models.
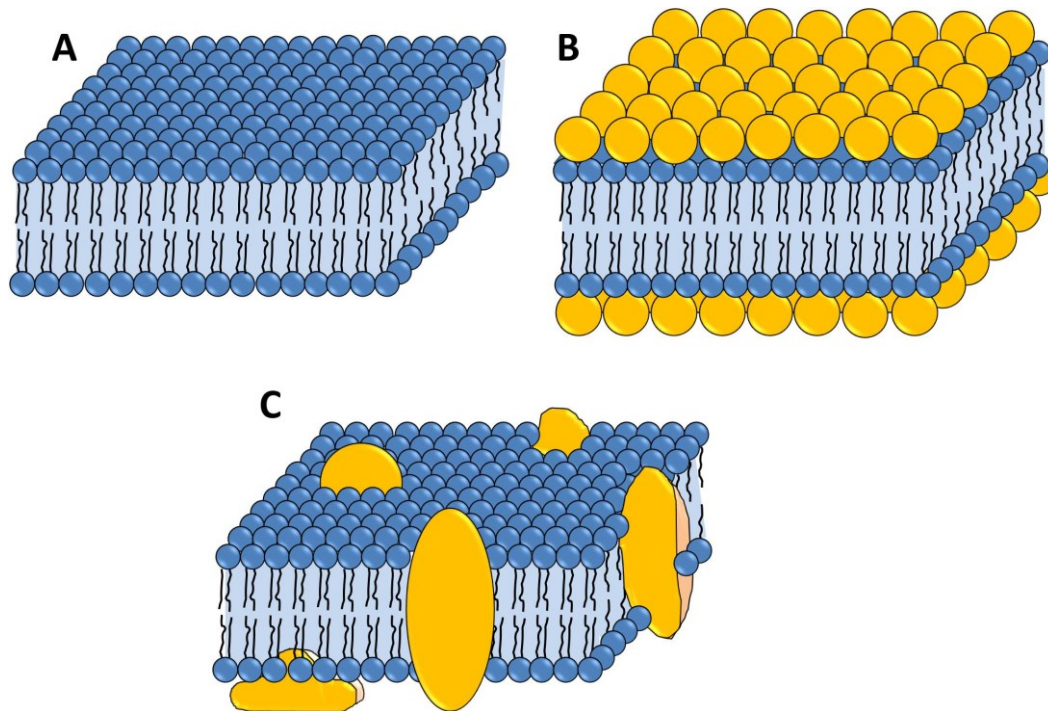
Figure 2. Models of plasma membrane structure.
A) Bimolecular lipid leaflet proposed by Gorter and Grendel (1925). This model assumes that there is a bi-layer with the hydrophilic headgroups facing the aqueous environment and hydrophobic tails facing inward the membrane. **B) Davson-Danielli model (1935).** A phospholipid bilayer is sandwiched between two layers of globular proteins. **C) The fluid mosaic model of Singer and Nicholson (1972).** According to this model, phospholipid molecules are organized as a discontinuous and fluid bilayer embedding membrane proteins.

MODELS OF LATERAL ORGANIZATION OF THE PLASMA MEMBRANE

Cell membranes are composed of a wide range of different lipids and membrane proteins that interact with each other causing lateral segregation. Despite recent advances in lipid and protein analysis, the function of lipid diversity and their aggregation in membranes remain enigmatic. The existence of lateral heterogeneity in membranes has been observed by various biochemical and biophysical techniques. To better illustrate their nature, scientists have come up with several models that help them to plan experiments and subsequently interpret their results. Note that the models below do not exclude each other so that it is possible to regard them as coexisting principles.

Domain formation in planar membranes was first suggested by Jain and White [27]. They proposed so called "*plate model*", where more ordered and less ordered regions coexist in biological membranes as a result of specific intermolecular interactions.

Picket-fence model proposes that the plasma membrane is segregated into distinct compartments by cortical actin filaments that are associated with the inner leaflet of the membrane and anchored by transmembrane protein "pickets" [28] (Fig. 3A). This model suggests free lipid and protein diffusion within sections surrounded by sub-membrane actin barriers. The size of these compartments was estimated to be about a few hundred nanometers, though there is high diversity between various cell types [29].

Mattress model is based on the assumption that lipids surround the hydrophobic parts of transmembrane proteins not randomly, but they match the length of their transmembrane domains [30] (Fig. 3B). It can result in local membrane thickening or thinning in case the length of protein transmembrane domain does not match the thickness of the lipid bilayer. It has also been shown that this aspect is crucial for protein sorting within the cell [31] [32].

Lipid raft model is probably the most discussed model for membrane organization. This model assumes that two distinct lipid phases, fluid and less ordered together with rigid and highly packed lipid ordered phase, coexist in the plasma membrane (Fig. 3C).

Existence of lipid rafts as a functional plasma membrane heterogeneity was first proposed by Simons and van Meer in 1988 [33]. Using Madin-Darby canine kidney epithelial cells, they observed that sorting of glycosphingolipids occurs in the Golgi network and that these lipids are preferentially sorted to the apical membrane domain of these cells. To explain this phenomenon, they came up with a hypothesis that clusters of glycosphingolipids formed in the outer leaflet of trans-Golgi membrane represent sorting centers for proteins determined for delivery to the particular plasma membrane domain (apical or basolateral).

Since then, numerous studies on the membrane heterogeneities (= "lipid rafts") have been designed. The existence of rigid lipid rafts was proposed based on the finding that certain plasma membrane components are insoluble by mild non-ionic detergents (e.g. Triton X-100, NP-40 or Brij-series). Biochemical analysis of these detergent-resistant membranes (DRMs) revealed their enrichment in cholesterol and sphingolipids [34]. Further studies highlighted the importance of DRMs in the cellular functions. It was proposed that these domains influence the protein activity and allow the proteins to be laterally sorted, which could serve as another regulatory mechanism for their function [35] [36].

Similar domains rich in cholesterol and sphingomyelin (SM) have also been detected in phase separated artificial lipid bilayers where L_o (liquid ordered) phase, a raft-like phase, and L_d (liquid disordered) phase, non-raft phase, coexisted together. L_d phase is characterized by high lipid mobility, whereas L_o phase displays a high degree of order and reduced lipid diffusion due to packing of saturated acyl chains of sphingolipids and the intercalated cholesterol [34]. As a result, it was suggested that the L_o phase structures in both cellular and artificial membranes are of the same nature. Thus, the L_o phase observed in artificial membranes became a well-accepted model for lipid rafts in cells.

However, it has become clear that the "lipid rafts" are heterogeneous not only in lipid and protein composition, but also in their temporal stability. Moreover, their biological relevance was unclear due to the lack of their direct observation *in vivo* and vague definition of the "raft" concept. To address this uncertainty, the definition of lipid rafts was formulated at the 2006 Keystone Symposium of Lipid Rafts and Cell Function: "Lipid rafts are small (10 - 200 nm), heterogeneous, highly dynamic, sterol- and sphingolipid-enriched domains that compartmentalize cellular processes. Small rafts can sometimes be stabilized to form larger platforms through protein-protein and protein-lipid interactions" [37].

Nevertheless, the existence of "lipid rafts" in living cells is a hot issue in modern biology and biophysics for a while. Despite many published results suggesting the existence of rigid domains, there is no direct observation of "rafts" *in vivo*. However, although the existence of raft-like structures in cellular membranes has been strongly supported by influential researchers, it has not been fully accepted due to a lack of enough artifact-prone evidences and experiment ambiguities. Therefore, the membrane domain structure, dynamics and the exact biological function still remain a matter of debate.

It should be mentioned that besides eukaryotic cells, there is plenty of evidence of raft-like structures in prokaryotes or yeast. In yeast cells, the protein complexes in their membranes resembling "rafts" were named as eisosomes [38]. In prokaryotes, it was originally believed that no domains exist in their membranes due to the lack of sterols. Nevertheless, it has been recently shown that the presence of hopanoids – structural analogues of sterols – is sufficient for formation of hopanoid-enriched domains [39]. In addition, although the raft

theory is usually discussed in context with cellular plasma membranes, there are studies reporting about the "rafts" in endosomes, too [40].

In summary, there is no universal and satisfactory model that would describe all aspects of the membrane properties and organization. Therefore, the understanding of membrane organization still remains an open question. More biophysical and biochemical studies are needed to figure out this issue. Likewise, the development or employment of novel biophysical techniques is of high importance.
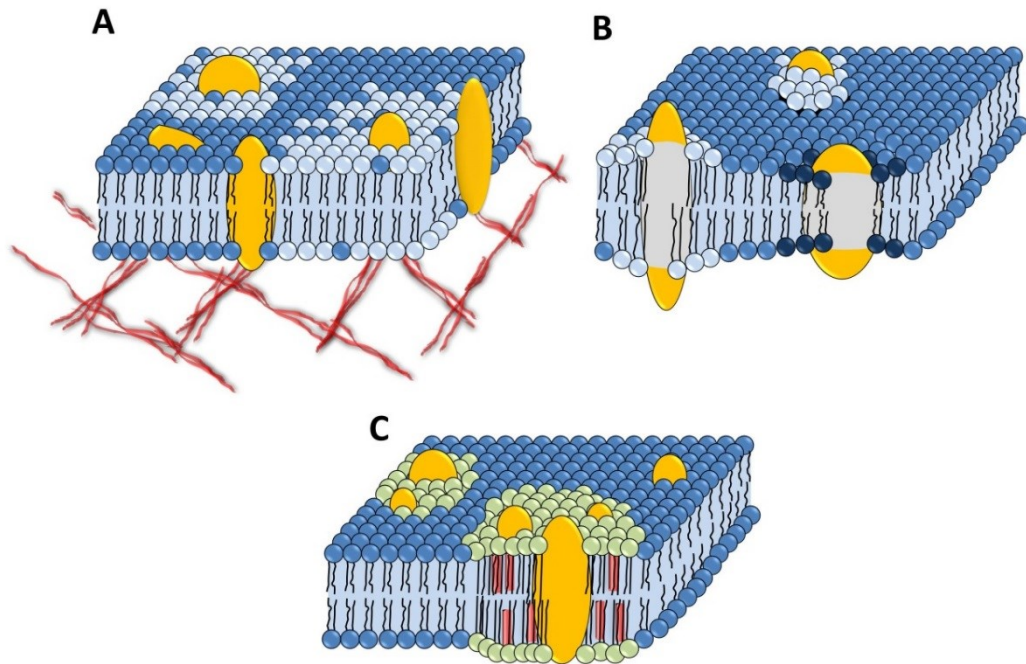
Figure 3. Models of lateral organization of the plasma membrane.
A) Picket-fence model. Cortical actin network underlying the membrane divides the lipid bilayer into small compartments via membrane-associated "picket" proteins. **B) Mattress model.** Lipids with variable hydrophobic chain length preferentially reside in the annulus of protein transmembrane domains in order to match their length, which results in membrane areas with variable thickness. **C) Lipid raft model.** Domains enriched in sphingolipids and cholesterol are in L_o phase and float freely in the sea of less packed fluid lipids.

Model membranes

The physiological cell membrane is a very complex and highly diverse system with thousands of "participants" that is not easy to isolate and maintain in its native physiological condition. Therefore, there is a significant interest in generating simplified artificial model membranes with reduced lipid composition allowing controlled experimentation. Model membranes are useful reductionist tools to study physicochemical properties of proteins, lipids or fluorescent probes in lipid bilayers by various biophysical techniques in a controlled way. Thanks to relative simplicity of these membranes and easy handling, we can get insight into the membrane characteristics, without being affected by surrounding complex environment. There are various types of such membrane assemblies from tiny free-floating micelles, bicelles and nanodiscs to large fully free-standing giant unilamellar vesicles (Fig. 4), each of which has its advantages and disadvantages with regards to stability, ease of preparation or the ability to mimic properties of real cellular membranes. The choice of a convenient model system depends on specific requirements.
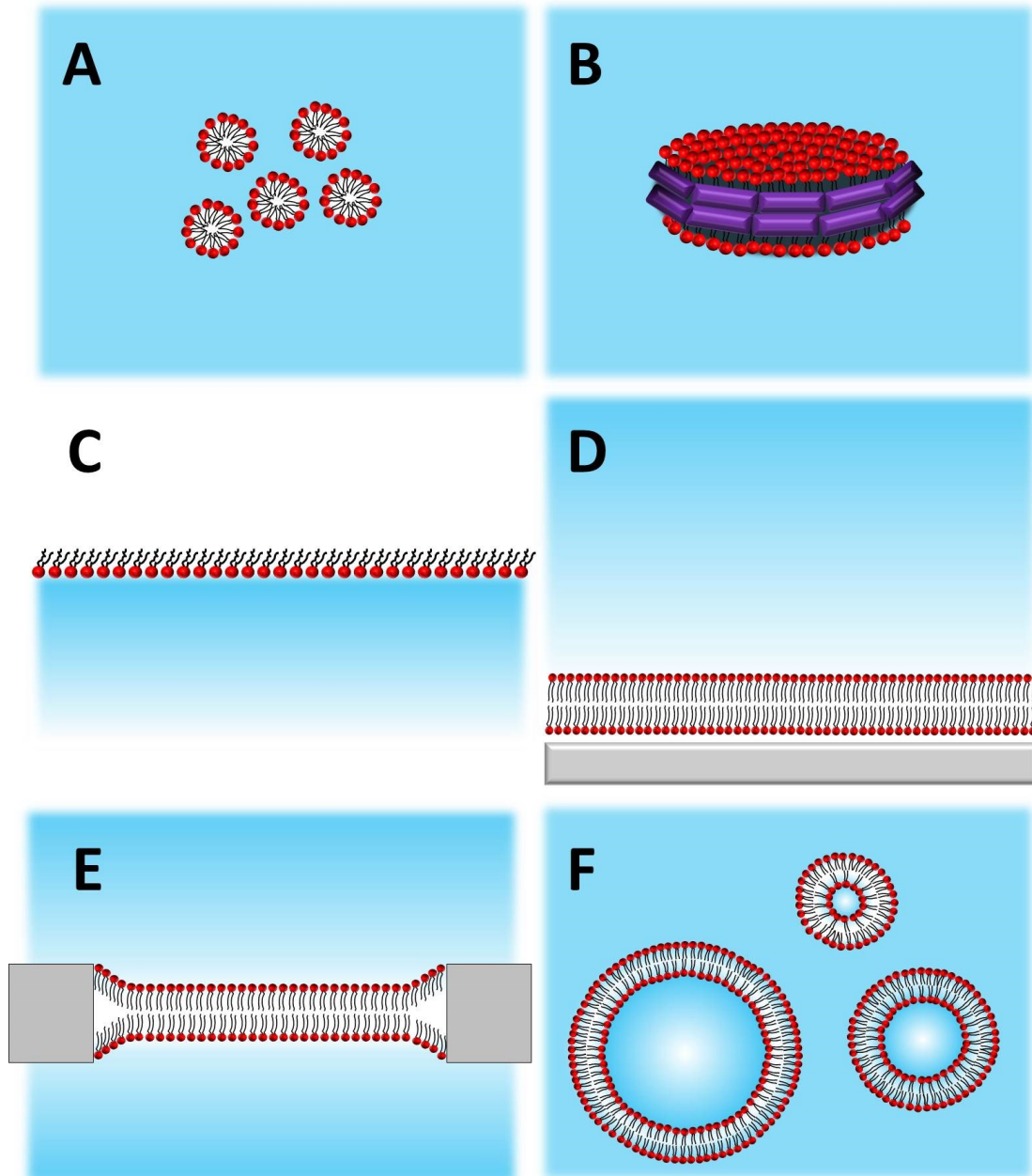
Figure 4. Schematic pictures of model membrane systems.
A) micelles, **B)** nanodiscs, **C)** lipid monolayers, **D)** supported phospholipid bilayers, **E)** black lipid membranes, **F)** free standing membranes including small unilamellar vesicles, large unilamellar vesicles and giant unilamellar vesicles

The simplest membrane models *micelles* and *nanodiscs* [41] (Fig. 4A, 4B) are used mainly for membrane-protein interaction studies [42] or in experiments where larger lipid assemblies could be a problem.

Lipid monolayers (Fig. 4C) are lipid films formed on the air-water interface that offer an appropriate model to study lipid-lipid or lipid-protein interactions since this system enables to control many molecular parameters in one, such as surface pressure or molecular packing [43]. However, lipid monolayers are not suitable

for studying transmembrane proteins as the monolayers consist of only one lipid layer.

Supported phospholipid bilayers (SPBs) (Fig. 4D) are lipid bilayers standing on a solid support, for instance, on glass or silicone. They provide a useful model for their simplicity in preparation, stability and an easy implementation in high-resolution imaging techniques such as atomic force microscopy. Although the solid support decreases membrane fluidity in comparison to free standing membranes [44], the dynamics of such membranes is comparable to some extent with plasma membrane of living cells, where the dynamics of lipids is hindered by cytoskeleton.

Another suitable research system are *black lipid membranes* (BLMs) (Fig. 4E), prepared as a bilayer sheet in an aperture, used mainly for characterization of electrical properties of the membrane or for ion channel studies. Modification of this technique, *patch clamp*, can separate the real plasma membrane into small patches containing limited number of lipids and proteins.

Recently, a new membrane model system combining the advantages of supported lipid bilayers and black lipid membranes called *pore-spanning membranes* has been developed [45] [46]. This membrane model can be prepared using porous alumina or silicone with wide range of nano- or micrometer pore sizes. In contrast to BLMs lacking long-term stability and SPBs impacted by direct contact of the membrane with the solid support, pore-spanning membranes are accessible from both sides and long-term stable.

Important free-standing model membranes are vesicles (Fig. 4F) - spherically shaped bilayers that can be prepared in a variety of sizes.

Small unilamellar vesicles (SUVs) and *large unilamellar vesicles* (LUVs) represent the smallest group of free standing model membrane systems with sizes below the resolution of classical optical microscopes. Typical diameters of SUVs are in the range of 15 - 50 nm, LUVs exhibit a diameter from 25 nm to a few microns. These vesicles are submicrometer particles that provide model systems for studies of the membrane interactions with proteins, peptides or other biomacromolecules [47].

The most popular free standing membrane models are *giant unilamellar vesicles* (GUVs) with sizes varying between 5 - 100 μm. GUVs have been proposed as models mimicking the living cells thanks to their size, observability by optical microscopy and unilamellarity. They provide an excellent research system because of their stability, easy handling and a possibility to prepare with coexisting microscopically observable L_o and L_d phase (Fig. 5). The drawback of this model is that particular vesicles may differ in lipid composition and size [48]. Another disadvantage is that the lipid asymmetry is not maintained. Nevertheless, recent studies reported a method to obtain also asymmetric GUVs [49].

In addition, there is another promising model membrane system that has been recently developed and characterized. The so-called *giant plasma membrane vesicles* (GPMVs) could be isolated directly from cells, therefore they preserve to some extent the structure and composition of their original membranes including membrane proteins as well as transmembrane asymmetry [50] but not actin-based cortical cytoskeleton. However, these membranes are prepared by chemical vesiculation procedure that may introduce several artifacts in the experimental results.
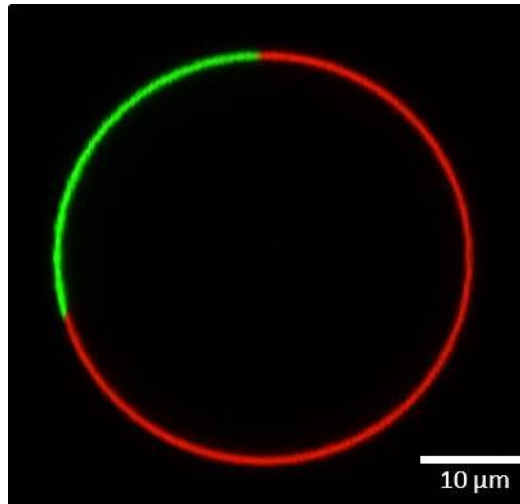
Figure 5. Fluorescent microscopy image of L_o/L_d phase separated giant unilamellar vesicle made of DOPC/SM/Chol 2:1:1.
DiD (1 mol%) was used as a marker for the L_d phase (red) and BODIPY-FL-GM1 (0.5 mol%) as a marker of the L_o phase (green).

Fluorescence techniques

Fluorescence techniques are very useful for biological or biophysical research thanks to their high sensitivity, non-invasiveness and selectivity. Variety of different fluorescence methods allows us to study problems starting at the level on the whole tissue and finishing up at the single-molecule level. For that reason, fluorescence is an excellent tool to study various biological problems including membrane properties, such as its dynamics, hydration, lipid phase separation or lipid/protein clustering.

Theory of fluorescence

Fluorescence is a phenomenon, in which particles absorb light of a particular wavelength and subsequently emit photons of longer wavelength due to loss of energy. Basic principle of fluorescence can be explained by Jablonski diagram (Fig. 6).

At the beginning, the molecule is in its ground state S_0. Absorption of photon(s) with appropriate energy generates an excited state called first (S_1) or second (S_2) excited electronic singlet state, which is followed by molecular relaxation and transformation to the lowest vibrational state of S_1. This process is called internal transformation. After reaching the lowest level S_1, the molecule returns to the ground state, which is either irradiative and not accompanied by photon emission, or radiative via the emission of a photon. The whole process is very fast occurring generally at the nanosecond time scale. There are also other ways of reaching S_0 state, such as energy transfer, which will be discussed later.

Another type of light emitting transition is phosphorescence. In contrast to fluorescence that stops emitting photons right after switching off the excitation light, phosphorescence persists up to a few hours. After excitation, phosphorescent molecules undergo the same transitions as their fluorescent partners, but only until S_1 state is reached. Then, if the triplet state T_1, which lies energetically between the state S_0 and S_1, is more favorable, so-called intersystem crossing occurs. In contrast to internal transformation, intersystem crossing is associated with the change of electron spin. While electrons undergo transition between the lowest T_1 state and S_0 state, the emission of photons is rather weak and slow, because the spin of electron has to be reversed again.
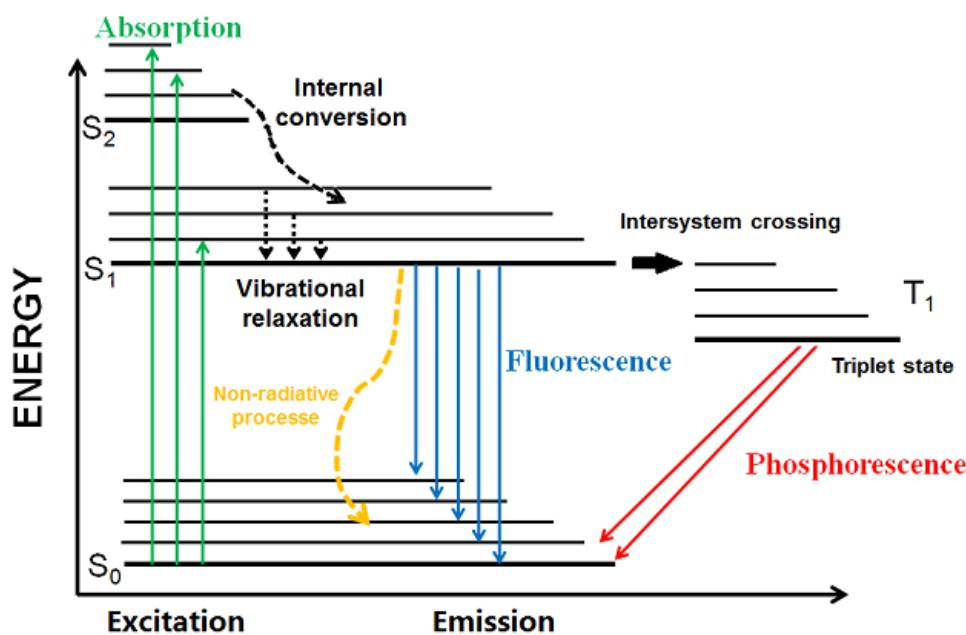
Figure 6. Jablonski diagram depicting the energy states of a molecule during photon absorption and fluorescence or phosphorescence emission [51]**.**

Fluorescent dyes

Fluorescent dyes are the molecules that are able to absorb excitation energy and emit it as fluorescence. This characteristic is usually enabled by the system of conjugated double bonds.

Many fluorophores are naturally-occurring, for instance, chlorophyll, NADH or flavins, including aminoacids with aromatic ring (i.e. tyrosine, tryptophan and phenylalanine). However, most cellular molecules are non-fluorescent. For their visualization it is necessary to label them with suitable fluorophores, either with organic compounds or fluorescent proteins. Organic fluorescent dyes are widely used in various microscopic techniques. There is a wide range of synthetic fluorophores such as Atto or Alexa dyes, comprising plenty of variants that differ in fluorescence spectra. DiD, DiO or perylenes are widely used as membrane markers. There is also a variety of fluorescent lipid analogues, for instance NBD-cholesterol or BODIPY-ceramide (Fig. 7). Fluorescent proteins, such as GFP, YFP or mCherry, are also suitable fluorophores for microscopy studies, although their photophysical properties are less favorable in comparison to organic dyes.

Besides these, there are also a number of naturally fluorescent small molecules (often secondary metabolites) directly interacting with the membranes. For example, filipin is an established tool to study cellular physiology in the context of free (i.e., non-esterified) cholesterol concentration and localization [52] [53].

Membrane fluorescence probes need to be at least partly hydrophobic to incorporate efficiently into the lipid bilayer. However, synthetic fluorescent dyes Atto or Alexa are water soluble. Thus, it is necessary to conjugate them with

either a lipid that naturally bear a hydrophobic part, or with another hydrophobic structure, for instance hydrophobic peptides. There are two approaches, how to prepare fluorescently labeled lipids. The first one uses attachment of a fluorophore to the lipid headgroup usually via the reaction of amine group in phosphatidylethanolamine with a maleimide reactive group attached to a dye. Another possibility is to covalently modify lipid acyl chains. The latter approach is less favorable, because lipid chains tend to loop back closer to the water environment due to hydrophilicity of attached fluorescent dyes [54].

On the contrary, fluorescent proteins are suitable fluorophores used to label cellular biomacromolecules but too bulky to serve as appropriate fluorophores for labeling lipids, as they are usually about 30 times larger than a phospholipid molecule. They might highly influence the properties of lipids and result in experimental artifacts. Another drawback of fluorescent proteins is their lower quantum yield compared to synthetic dyes.

Frequently used fluorescent dyes DiD, DiI or DiO resemble the structure of lipids, so they readily incorporate into the membranes.

Another group of fluorophores (e.g. filipin or perylenes) are of amphipathic or hydrophobic nature, therefore, they directly interact with the membranes by themselves. Thanks to their internal fluorescence, there is no need to label them with any additional fluorophore.

Fluorescent dyes are used not only for labeling and visualizing distinct molecules, such as proteins or lipids, but they can also serve as probes monitoring their surroundings (polarity, viscosity, pH etc.), as they change their spectral characteristics in different environments. A typical and widely used probe of this type is Laurdan, whose emission spectrum is shifted in response to solvent polarity and viscosity. Thanks to this feature, we can monitor water content within a lipid bilayer as well as its mobility.

Despite wide variety of available fluorophores, a study of membrane heterogeneities by fluorescence methods is still challenging due to lack of enough suitable fluorophores partitioning into L_o phase. Surprisingly, fluorescent analogues of raft lipids (e.g. BODIPY-ceramide or NBD-cholesterol) show low partitioning into L_o phase [55]. Therefore, fluorescently labeled proteins known to interact with membrane rafts (e.g. GFP-GPI or labelled cholera toxin B subunit) need to be used instead with need of extremely careful data interpretation to avoid experimental artifacts.

Alexa Fluor 546   Atto 655   Perylene

BODIPY-ceramide   NBD-cholesterol   DiD
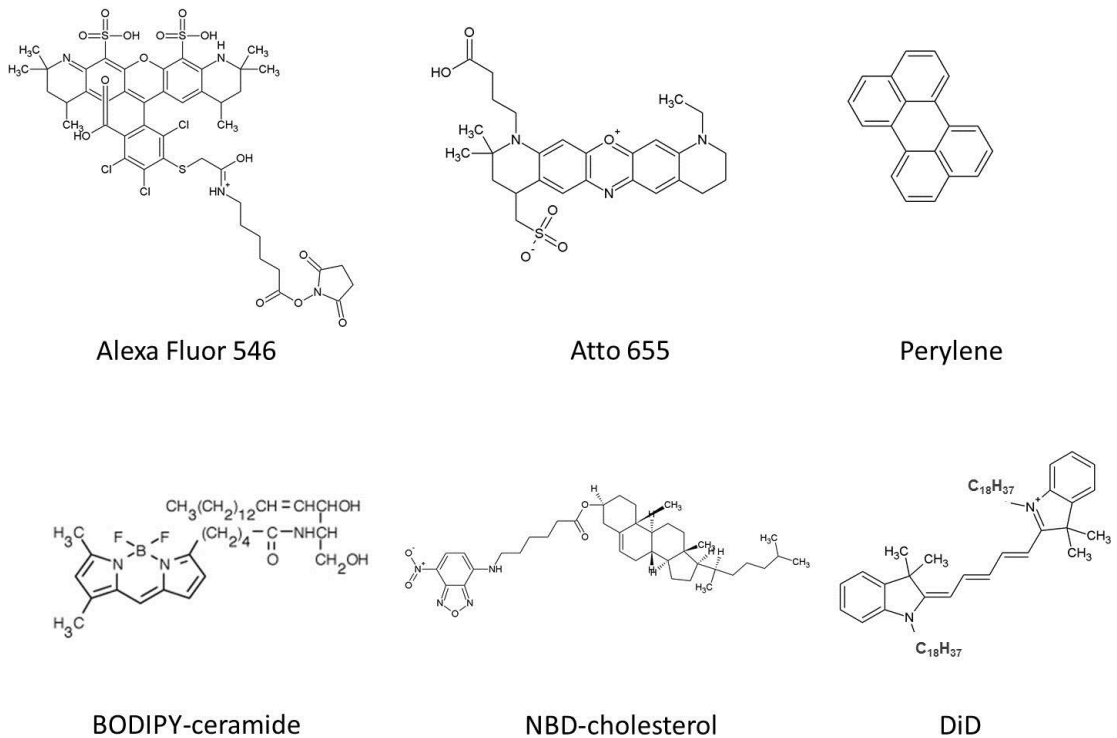
Figure 7. Chemical structures of representative fluorescent dyes and lipid analogues used in membrane visualization.

Introduction to fluorescence methods

Fluorescence methods are useful biophysical tools to examine and analyze protein-protein, protein-nucleic acid, protein-lipid, or lipid-lipid interactions. Single-molecule fluorescence methods can probe these processes even at the nanoscale level. Below are briefly described fluorescent methods that are relevant to this work.

Confocal microscopy

Laser scanning confocal microscopy is a widely used microscopy technique in biological sciences. The motivation to develop this kind of microscope was to improve image contrast.

The original concept of confocal microscopy was introduced in 1950s by an American scientist Marvin Minsky, but the first real confocal microscope using a Nipkow-disk system was built by Mojmír Petráň from the Faculty of Medicine in Pilsen (Czechoslovakia) [56].

The advantage of confocal over wide-field microscopy is considerable. Light from a light source of a conventional wide-field fluorescence microscope illuminates

the whole sample and excites all parts of the specimen at the same time. Resulting fluorescence light coming from focused but also from out-of-focus parts of the specimen generates a blurred background and decreases resolution.

On the contrary, confocal microscope illuminates the sample by a laser beam point by point and a pinhole arranged in front of a detector eliminates out-of-focus fluorescent light. Therefore, only fluorescence coming from the focal plane is detected, which improves resolution and the overall image quality. As a consequence, confocal microscopy allows non-invasive optical sectioning of the specimen with an improved resolution.

The principle and a simplified scheme of a confocal microscope is shown in Figure 8.
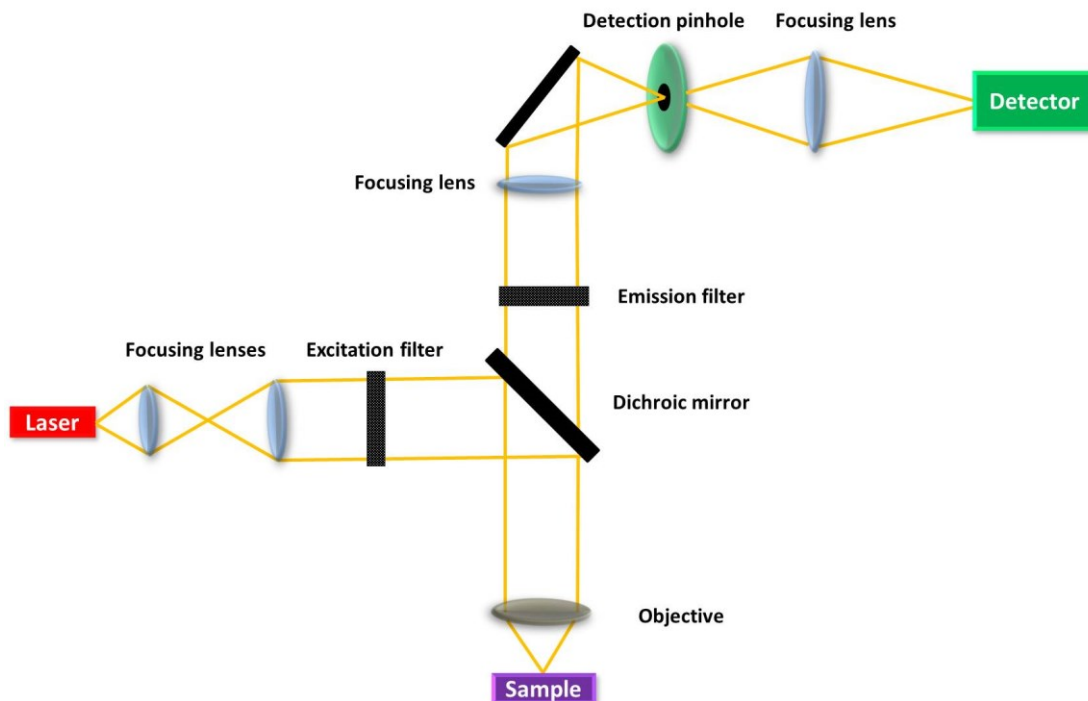
Figure 8. Schematic illustration of a confocal microscopy principle.
A laser beam is reflected by a dichroic mirror into an objective that focuses the beam into a sample. Red shifted fluorescence signal is reflected back and collected and collimated by the same objective. Then it transmits through the dichroic mirror and, after being separated from the excitation light by an emission filter, is focused through a pinhole onto a detector. Only light from the focus plane can pass through the pinhole. Thus, out-of-focus light does not blur the resulting image.

Multiphoton microscopy has been developed as an alternative to common confocal microscopy. The principle of this technique arises from simultaneous excitation of a fluorophore by two photons. The absorbed photons have a wavelength about twice that of the fluorophore absorption peak. Due to the fact that the laser is focused at the same volume in the specimen, there is almost zero light absorption in out-of-focus specimen area. It results in a "natural" confocality without a need of additional pinhole in a microscope setup. Another benefit is the deep penetration of excited light into a specimen. In addition, two-photon excitation minimizes photodamage and photobleaching of sensitive fluorophores.

Fluorescence correlation spectroscopy (FCS)

Fluorescence correlation spectroscopy (FCS) represents a sensitive and elegant method to detect highly mobile single molecules.
It was first introduced in 1974 by Elson&Magde [57] as a single molecule detection technique to study the abundance, mobility and interactions of fluorescence-labeled molecules.

This method is based on analysis of the fluorescence intensity fluctuations coming from the focal volume of a confocal microscope. A fluorescent molecule diffuses across the focal volume, where it is excited, and the burst of the emitted light is detected by sensitive detectors. The fluorescence signal coming from repeatedly excited and emitted molecules diffusing through the detection volume is statistically analyzed and the fluctuations in time are described by normalized autocorrelation function G(τ):

$$G(\tau) = \frac{\langle I(t)I(t+\tau)\rangle}{\langle I(t)\rangle^2} \tag{1}$$

where I(t) means fluorescence intensity in time t and τ represents so-called lag time. The angle brackets indicate time averaging.

By fitting G(τ) to a model, diffusion time τ_D that provides information about how long a fluorophore dwells in the focal volume and the average number of fluorophores in the focal volume (PN) can be determined. Two-dimensional model is employed in case of analyzing fluorophores in planar lipid bilayers [57]:

$$G(\tau) = 1 + \frac{1}{PN} \frac{1}{1+\left(\frac{\tau}{\tau_D}\right)} \tag{2}$$

Diffusion coefficient D that is more relevant parameter to describe lateral diffusion can be calculated directly from τ_D:

$$D = \frac{\omega_0{}^2}{4\tau_D}$$

(3)

where ω_0 means the radius of the detection volume. Figure 9 shows a principle of this method.

The results provide information about mobility and concentration of the fluorescent molecules. Single-molecule sensitivity makes FCS popular in many fields of research. The most common application is measuring the molecular diffusion and concentration of the analyzed particles that can refer, for instance, about the condition or alteration of lipid bilayers. Besides, measurements of kinetic rate constants of chemical reactions or other quantities accompanied with intensity fluctuations in the observed volume are possible as well. However, the principle of FCS requires using very low concentrations (nanomolar or picomolar) of fluorescent molecules, because the highest signal to noise ratio is reached in case of presence on average one fluorescent molecule in the detection volume.
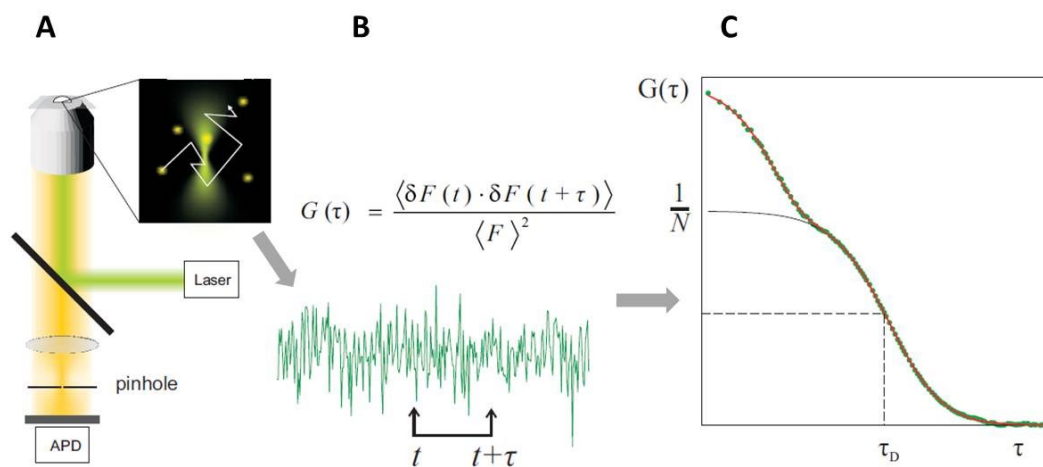
Figure 9. Principle of FCS measurements (adapted from [58]**).**
A) A laser beam excites fluorescent particles diffusing in the detection volume.
B) Emission of the fluorophores causes fluorescence intensity fluctuations that are recorded by a detector. **C)** Fluctuations in fluorescence intensity are correlated resulting in an autocorrelation curve. The diffusion time τ_D is calculated at the half maximum of the autocorrelation function.

To date, scientists modulate the classical FCS method in order to solve complexity of problems. We can name z-scan FCS or fluorescence cross-correlation spectroscopy that are described below. Another variant of FCS employed in this thesis is fluorescence antibunching. This method allows us to determine the number of emitters in a cluster [59].

Fluorescence cross-correlation spectroscopy (FCCS)

Fluorescence cross-correlation spectroscopy (FCCS) is a method, which is usually used to detect molecular interactions of two diffusing molecules labeled with spectrally distinct fluorophores. The emitted light of both fluorescent species diffusing through the focal volume is recorded by two independent detectors and the intensity fluctuations are cross-correlated. The cross-correlation function is described as:

$$G_{AB}(\tau) = \frac{\langle I_A(t).\ I_B\,(t+\tau)\rangle}{\langle I_A(t)\rangle\langle I_B(t)\rangle} \tag{4}$$

where I_A and I_B correspond to the fluorescence intensity of fluorescent molecules detected in a channel A (I_A) or a channel B (I_B). When the labelled molecules move independently, the cross-correlation amplitude G_{AB} equals zero. On the other hand, G_{AB} higher than zero points out to a particular or complete interaction and co-diffusion of both fluorophores. Therefore, this technique allows us to clearly distinguish between bound and unbound/free molecules.

Z-scan fluorescence correlation spectroscopy (z-scan FCS)

Z-scan FCS is a modification of a classical FCS technique that has been developed mainly for measurements of fluorescent molecule diffusion in planar lipid bilayers [60]. This method relies on acquiring of a set of individual point-FCS measurements along the z-axis in defined intervals. Each point is correlated and the resulting diffusion time (τ_D) and the particle number (*PN*) values are plotted in dependence on their position in the detection volume and fitted with a parabolic dependence. The results directly provide radius of the detection volume ω_0 and the diffusion coefficient *D* in the membrane. In contrast to classical FCS, z-scan FCS does not require calibration of the detection volume diameter, as its radius can be calculated directly from fitting the measured data. Another advantage of z-scan FCS is that we can easily determine diffusion coefficient *D* as well as *PN* corresponding to the position of the lipid bilayer accurately in the focal plane. A schematic principle of z-scan FCS is imaged in the Figure 10.
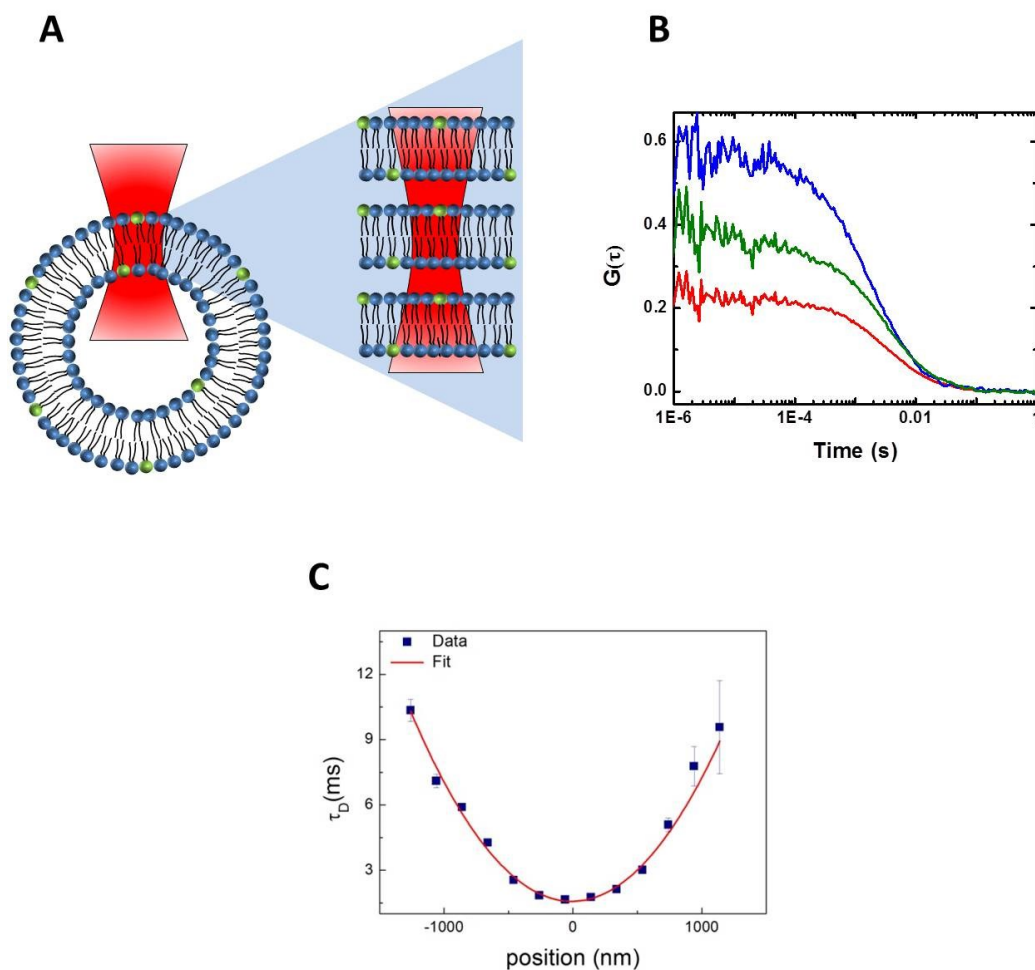
Figure 10. Principle of z-scan FCS.
A) Lipid bilayers are scanned along the z-axis of the confocal volume, **B)** Autocorrelation functions are analyzed for each recorded position, **C)** τ_D (or possibly *PN*) is plotted against the z-position and fitted with a parabolic curve

Time resolved fluorescence spectroscopy

Time-resolved fluorescence spectroscopy is based on the time-correlated single photon counting (TCSPC) method that provides detailed information about the molecular environment, dynamics and interactions of the system. This technique relies on the short pulses of excitation light that must be substantially shorter than the lifetime of an excited fluorophore. The first emitted photon arrived after the excitation pulse is detected by a sensitive photomultiplier and the time between the pulse and the arrival of the photon is calculated. A volume of a particular memory channel that corresponds to the time between the excitation pulse and the detection of a photon is increased by one. After collection of a sufficient amount of photons, an exponential decay curve characteristic for a particular fluorescence sample is obtained and provides a basis for calculation of the fluorophore lifetime (Fig. 11).
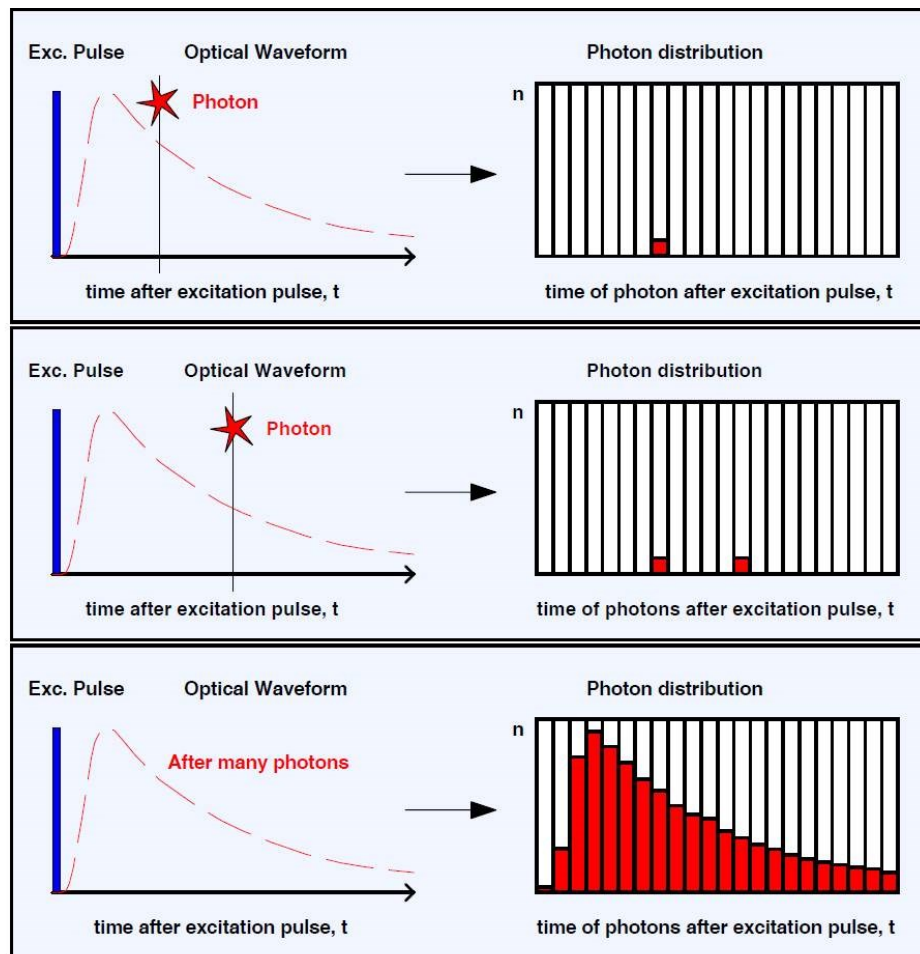
Figure 11. Principle of time-resolved fluorescence spectroscopy [61]**.**
The time between sample excitation by a short laser pulse and the arrival of the emitted photon is measured. Distribution of the photons builds up a lifetime decay.

By this method, we are able to monitor molecular interactions in the picosecond/nanosecond time scale, which can be used for studying molecular dynamics and structure. In addition, this technique can be combined with FCS allowing us to discriminate two fluorophores with overlapping emission spectra that simultaneously differ in their lifetimes.

Fluorescence-lifetime imaging microscopy (FLIM)

Fluorescence-lifetime imaging microscopy is a technique that can measure the fluorescence lifetime of fluorescent probes in each individual pixel of an acquired image. Apart from detecting the arrival time of photons after the excitation pulse, we also obtain additional information about the spatial distribution of a particular fluorophore. It is necessary to collect a sufficient amount of photons for each pixel to picture the whole lifetime image. This technique is especially useful to monitor changes of environment within the entire cell, as the lifetime of some fluorophores

are affected by the conditions such as viscosity, polarity, pH or temperature. The other advantage is that thanks to measuring fluorescence lifetimes in each pixel, we can distinguish between fluorescence signal coming from a fluorophore and a background noise or autofluorescence. This approach can be also employed in FRET experiments. De-excitation process caused by the presence of an acceptor in close proximity of the fluorophore induces shortening of fluorophore lifetime, which allows us to monitor interaction of fluorescent molecules. This technique called FLIM-FRET is described below.

Förster resonance energy transfer (FRET)

Förster resonance energy transfer (FRET), a phenomenon firstly described by Theodor Förster [62], is based on the distance-dependent nonradiative excitation energy transfer from a donor molecule to a suitable acceptor molecule. After excitation, donor molecules undergo a transition from the state S_1 to the ground state S_0, whereby an acceptor is excited from S_0 to S_1. The excited donor molecule returns to the S_0 state without emission of photon, while the acceptor molecule is excited and emits photon when returning to the ground state. For successful energy transfer, the donor emission spectrum must overlap with the excitation spectrum of the acceptor. Simultaneously, both fluorescent molecules must be close enough to each other (typically bellow 10 nm) and have a favorable orientation.

Thanks to the fact that the FRET efficiency depends on the distance between a donor and an acceptor, this technique became popular and widely used in biology as well as in biophysics for precise measuring the distances between molecules in the nanometer range and for the investigation of protein oligomerization or lipid clustering.

There are basically two ways how to measure FRET. The first one is based on measuring donor and acceptor fluorescence intensities, each in separate channels, while exciting only the donor. If FRET occurs, the fluorescence intensity in the donor channel decreases, while the intensity in the acceptor channel increases. The FRET efficiency is then calculated as

$$E = 1 - \frac{I_{DA}}{I_D} \tag{5}$$

where I_{DA} and I_A represent the fluorescence intensity of a donor in the presence or absence of an acceptor, respectively. This approach has several limitations connected with inhomogeneous dye concentrations and photoselection. Thus, quantification of energy transfer is problematic.

The other approach called FLIM-FRET is based on the fact that if energy transfer occurs, the donor is relaxed by radiation-less transfer of the excitation energy to

the acceptor, which results in a shorter donor lifetime. The calculation of FRET efficiency is in this case:

$$E = 1 - \frac{\tau_{DA}}{\tau_D} \tag{6}$$

where τ_{DA} is a lifetime of a donor in the presence of an acceptor and τ_D corresponds to the donor lifetime in the absence of an acceptor. In contrast to the above mentioned approach, FLIM-FRET is not prone to concentration or spectral artifacts. Moreover, we can distinguish more populations of donors that are either surrounded by acceptor molecules, or are in the regions without acceptors.

Principle of MC-FRET (FRET combined with Monte Carlo simulations)

The above mentioned approaches consider energy transfer between a single donor-acceptor pair. However, FRET can also occur in a complex environment with many donors and acceptors, where the donor can transfer the energy to more than one acceptor. Lipid bilayer with incorporated lipid analogues as donors and acceptors is an example of such system. This situation can be mathematically described by Baumann-Fayer model [63]. However, this model presumes homogeneous distribution of the fluorescent probes. If the donors and acceptors are distributed non-homogeneously (for instance, when nanodomains are present in the lipid bilayer), the calculation of the impact of FRET on the donor decay by Baumann-Fayer model becomes difficult. Due to the fact that an appropriate equation describing this situation does not exist, the data have to be analyzed by Monte Carlo simulations. Combination of FLIM-FRET with Monte Carlo simulations, developed in our laboratory, can detect membrane heterogeneities of various kinds, for example, nanodomains or even membrane pores [64]. This method allows us not only to reveal their presence in membranes, but also (in the case of nanodomains) to determine their size in the range between 2 - 50 nm and the area they occupy on the membrane surface. A key factor in this approach is a pair of fluorescent dyes that exhibits either high affinity for nanodomains, or avoids partitioning into these structures. Thus, if nanodomains are formed, both donors and acceptors accumulate within these structures, or outside them. As a result, donors and acceptors get closer to each other, in contrast to homogeneous fluorophore distribution, which results in higher FRET efficiency that can be seen as a shorter time-resolved fluorescence lifetime. The obtained time-resolved fluorescence decays are fitted with simulated decays for various radii and fractional areas occupied by the nanodomains. As a result, we obtain the information about their characteristics (Fig. 12).
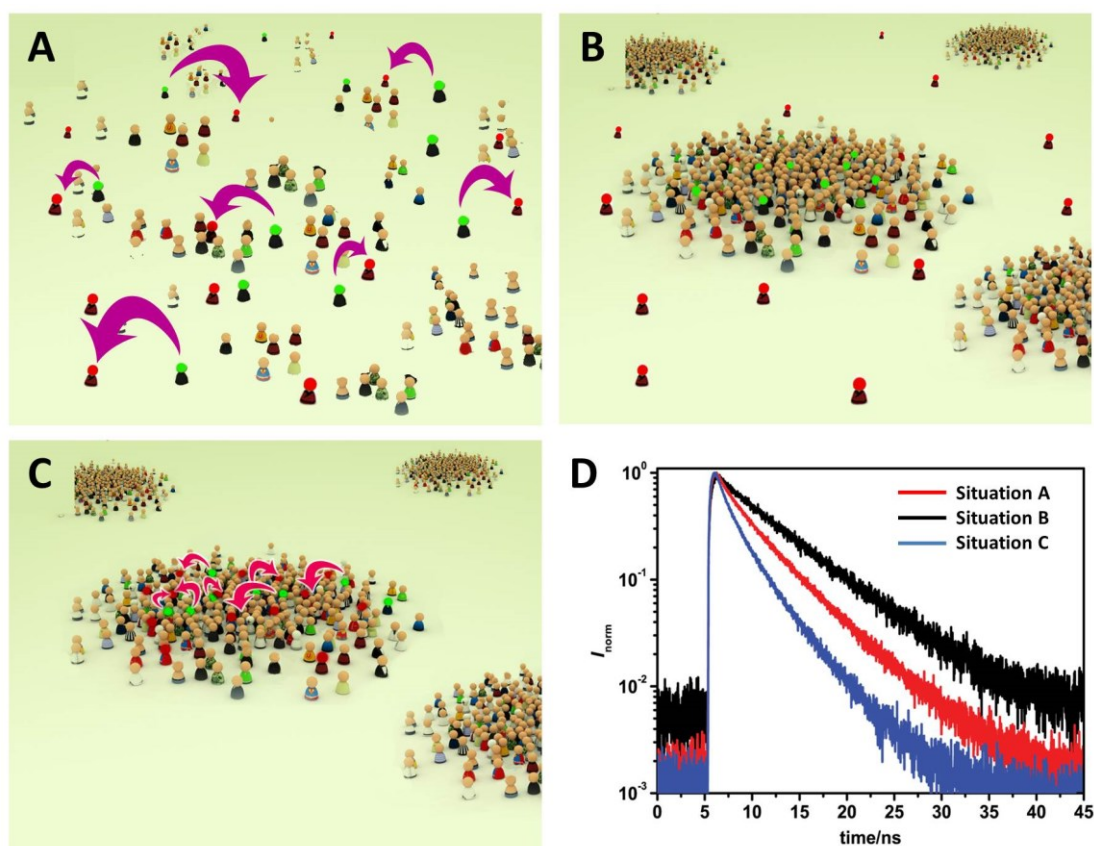
Figure 12. Principles of nanodomains detection by FLIM-FRET.
A) Homogeneous distribution of donors and acceptors. **B)** Donors and acceptors are separated due to their different affinity for the domains. In this case, the FRET efficiency decreases resulting in a longer donor lifetime (black curve in the picture D). **C)** Donors are acceptors accumulate within the nanodomains, which leads to a shorter donor lifetime (blue curve in the picture D). **D)** The experimentally obtained donor decays are fitted with simulated decays for various radii and the area fraction of the nanodomains.

Time-dependent fluorescence shift (TDFS)

Time-dependent fluorescence shift (TDFS) is a fluorescence method based on monitoring the solvent dipole reorientation around the excited fluorescent dye. This technique allows us to characterize hydration and mobility of the lipid bilayer in the vicinity of an excited probe.

The difference between excitation and emission spectra are attributed to losing energy of photons that undergo non-radiative transitions to the lowest vibration level of the S_1 state. In addition, solvent molecules around a fluorophore contribute to the additional loss of energy. Excitation of a fluorescent probe leads to redistribution of its electrons resulting in change of the dipole moment. Dipole moments of surrounding solvent molecules are forced to adapt to the new situation and compensate the dipole moment of an excited probe. Immediately after excitation, the dipoles of a solvent are not in equilibrium with the dipole

moments of the excited probe and the system is in so-called Franck-Condon state. Therefore, the molecules of a solvent gradually rearrange to reach the equilibrium, while the whole system lowers the energy. This process is called solvent relaxation [65] (Fig. 13). It results in additional red shift to the standard Stokes shift. The degree of this effect depends on the polarity of a solvent, viscosity of the environment and the properties of a fluorescent dye. Briefly, the higher the solvent polarity, the greater the red shift. Similarly, the more viscous environment, the slower reorientation of the dipoles. If the dipole reorganization is slower than the fluorescence lifetime, the solvent remains only partially reoriented.

The overall spectral shift caused by the relaxation process can be determined by time-resolved emission spectra (TRES) method. A set of fluorescence intensity decays is recorded by TCSPC method at different wavelengths in the range corresponding to the steady-state emission spectrum of a fluorophore. The measured decays are put together and normalized to the steady-state emission.

Typical dyes used for TDFS are Laurdan, Prodan or Patman. Although they contain the same fluorophore, they differ in the length of hydrophobic chains. Hence, their location in the bilayer is different, which allows measuring polarity and viscosity changes in different depths of the bilayer.
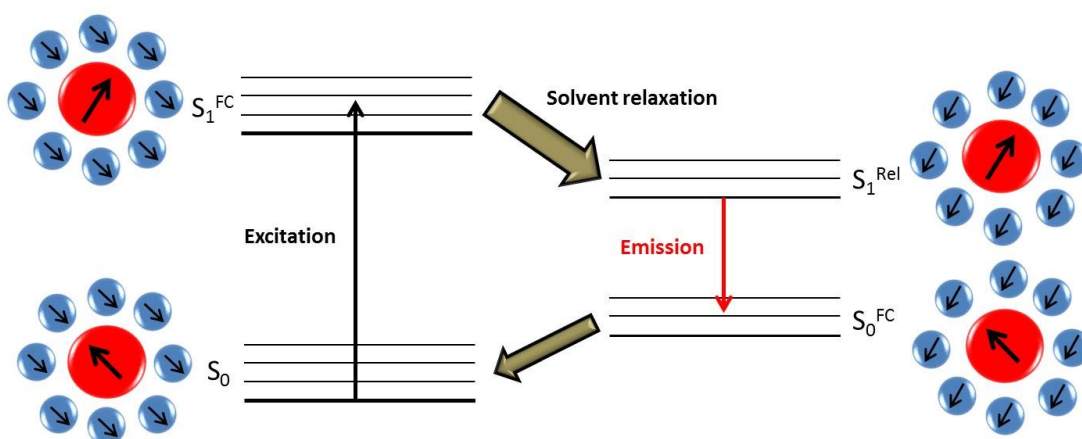
Figure 13. Simplified schematics of solvent relaxation.
Immediately after excitation, the dipole moment of a dye is reoriented, but the orientation of the solvent dipole remains unchanged. Reorientation of solvent molecules leads to lowering of the system energy resulting in the red shift. The encircled black arrows represent the dipole moments of a dye (red circles) and a solvent (blue circles). S_0 – ground state, S_1^{FC} – Franck-Condon excited state, S_1^{Rel} – excited state with relaxed solvent molecules, S_0^{FC} – Franck-Condon ground state.

Research Aims

The aim of this study is to contribute to a better understanding of processes related to biological membranes. We were investigating membrane organization at the nanoscale, examining in which way a small natural molecule interacts with the membrane, or we were trying to enlighten the mechanism of membrane fusion driven by small peptides. For simplicity, this work is divided into three main parts:

Part 1: **Membrane activity of the secondary metabolite didehydro-roflamycoin**

The general objective of this aim was to characterize a novel secondary metabolite 32,33-didehydroroflamycoin in terms of its membrane action as well as to contribute to current knowledge of polyene macrolides mechanism of action in general. Employing simple model membranes (GUVs and LUVs) we were investigating the mode of action of DDHR under various conditions.

Part 2: **Investigation of the nature and size of membrane nanodomains in model lipid membranes**

The existence and nature of heterogeneities in cell membranes is still an open question. The aim of this part was to uncover the existence of lipid nanodomains in binary (DOPC/SM) and ternary (DOPC/Chol/SM) model membranes close to phase separation boundary. Moreover, we also aimed to reveal the properties of GM1 driven nanodomains and to examine binding activity of its ligand cholera toxin B subunit.

Part 3: **Study of the roles of SNARE-mimicking lipopeptides during initial steps of membrane fusion**

Two complementary lipopeptides CP_nK_4 and CP_nE_4 serve as a minimal model for membrane fusion. Employing the system for *in vivo* applications, such as drug delivery or membrane engineering, requires in-depth understanding of molecular mechanism behind the fusion event. The aim of this part was to uncover the roles of lipopeptides during early steps of membrane fusion, (lipo)peptide-membrane and lipopeptide-lipopeptide interactions. Consequently, we aimed on direct observation of the fusion process mediated by these lipopeptides.

List of Publications

This thesis is based on five publications of which three (publication I, II and III) have been published in impacted journals. One (publication IV) is under minor revisions at the time of submission of this thesis. Publication V is a manuscript prepared for submission to Journal of the American Chemical Society. The author's contribution is specified below each reference.

Publication I:

<u>Koukalová A.</u>, Pokorná Š., Fišer R., Kopecký V Jr., Humpolíčková J., Černý J., Hof M. Membrane activity of the pentaene macrolide didehydroroflamycoin in model lipid bilayers. *Biochimica et Biophysica Acta*, Feb; 1848(2):444-52. 2015 (IF$_{2017}$ = 3.44)

> A.K. prepared model lipid membranes for all experiments and carried out spectroscopic measurements, leakage assays, experiments employing BLMs and acquired all the microscopy images. The author interpreted the results and contributed to the writing of the manuscript.

Publication II:

<u>Koukalová A</u>., Amaro M., Aydogan G., Gröbner G., Williamson PTF., Mikhalyov I., Hof M., Šachl R. Lipid Driven Nanodomains in Giant Lipid Vesicles are Fluid and Disordered. *Scientific Reports*, Jul 14; 7(1):5460. 2017 (IF$_{2017}$ = 4.12)

> A.K. prepared the samples in the form of model membranes GUVs, performed majority of FCS and FLIM-FRET measurements, measured K_d values and analyzed the data. She discussed the results and contributed to the writing of the final manuscript.

Publication III:

Šachl R., Amaro M., Aydogan G., **Koukalová A.**, Mikhalyov II., Boldyrev IA., Humpolíčková J., Hof M. On multivalent receptor activity of GM1 in cholesterol containing membranes. *Biochimica et Biophysica Acta*, Apr; 1853(4):850-7. 2015 ($IF_{2017} = 4.65$)

> A.K. was involved in preparation of samples and performance of FLIM-FRET. Further, the author carried out all the experiments with POPC lipid, z-scan FCS measurements of DiD diffusion in the membranes and analyzed FCS and FLIM-FRET data.

Publication IV:

Koukalová A., Pokorná Š., Boyle AL., Mora NL., Kros A., Hof M., Šachl R. Distinct Roles of SNARE-mimicking Lipopeptides during Initial Steps of Membrane Fusion (accepted under minor revisions in Nanoscale) ($IF_{2017} = 7.23$)

> A.K. prepared samples, performed the majority of the experiments and analyzed the data. The author participated in discussion about results and the writing of the manuscript.

Publication V:

Mora NL., Boyle AL., van Kolck B., Rossen A., Pokorná Š., **Koukalová A.**, Šachl R., Hof M. and Kros A. Controlled liposomal membrane fusion triggered by fusogenic coiled-coil peptides assessed by simultaneous dual-color time-lapsed fluorescence microscopy (manuscript prepared for submission to Journal of the American Chemical Society)

> A.K. prepared samples and performed the FCS measurements of lipid and lipopeptide diffusion in the presence or absence of Tween 20, and analyzed the data.

Results

This thesis comprises of three publications published in impacted journals, one manuscript under minor revisions at the time of submission of this thesis and one manuscript ready to submit. According to their main research topics, the publications are divided into three main parts: Membrane activity of the secondary metabolite didehydroroflamycoin, Investigation of the nature and size of membrane nanodomains in model lipid membranes and Study of the roles of SNARE-mimicking lipopeptides during initial steps of membrane fusion. Each publication is introduced by a brief introductory part that provides an insight into a background of a distinct topic. The following "Results and discussion" section is dedicated to discussion of our results with literature. Although each publication itself includes a discussion part, the additional discussion intends to put our findings in a broader context and, if possible, to discuss our results with more recent literature.

Part 1:

Membrane activity of the secondary metabolite didehydroroflamycoin

PUBLICATION I:

Metabolism of living organisms could be divided into primary and secondary metabolism. Primary metabolism generates products that are essential for organism's survival, e.g. proteins, nucleic acids, carbohydrates etc. Secondary metabolism synthetizes compounds called secondary metabolites that are typically unique to a distinct organism providing a tool for defense against competitors and helps the organism to survive in a competitive environment.

Secondary metabolites derived from natural sources are in focus of research for several years because of their bioactivity and broad applications, e.g. in biomedicine. Compounds considered as bioactive can influence the organismal physiology, no matter if the effect is favorable or unfavorable.

A number of organisms (bacteria, fungi, marine organisms etc.) produce a variety of secondary metabolites, but only a small fraction of them are worth further investigation. It has been estimated that more than 300 000 secondary metabolites exist in nature [66]. An alternative way to produce bioactive compounds is combinatorial chemistry. However, this approach is far less effective in terms of overall success rate compared to search and investigation of compounds from natural sources. Potential explanation is that the natural product biosynthesis, including generation of a gene pool involved in particular enzymatic pathways, has evolved over billions of years. Under the strict pressure of natural selection, the secondary metabolites are more prone to exhibit unique biological activities in comparison with synthetic compounds [67].

Despite tremendous variety of available bioactive molecules, there is still a need to introduce new antibiotics. The emergence of bacterial multi-drug resistance increases the urge to search for new metabolites that would broaden the variety of effective drugs. Most of the secondary metabolites used in medicine as antibiotics or chemotherapeutics are produced by bacteria and are an evolutionary consequence of fierce "chemical wars" in the microworld.

One of the most important sources of bioactive compounds are bacteria Actinomycetes, in particular the genus *Streptomyces*. *Streptomyces* are aerobic Gram-positive filamentous bacteria that are commonly found in soil. They produce, besides other secondary metabolites, a range of polyene macrolides. These natural compounds consist of a large lacton ring system made of twelve or

more atoms with series of conjugated double bonds. Macrolides are very effective antifungal agents [68], which are widely used in medicine, although their mechanism of action is still a matter of controversy. Numerous macrolides have been shown to interact with cholesterol in lipid bilayers and form pores, e.g. Amphotericin B (AmB) [69] [70]. Even though polyene antibiotics share the similar structure, mechanism of the interaction with membranes can largely differ and cannot be easily predicted; for instance, while Amphotericin B or nystatin form ion channel pores [71], a pentaene filipin acts as a general disruptor involving formation of membrane protrusions arising from altered phase behaviour [72]. However, the association between macrolides and particular membrane components is a controversial issue, and there is only rare biophysical evidence for direct interactions. The mode of interaction with the membrane could be a key for understanding the molecular mechanism of bioactivity.

It should be noted that polyene macrolides produced by *Streptomyces* are not only very effective antibiotics and antifungal agents (e.g. erythromycin extracted from *Streptomyces erythreus*, nystatin produced by *Streptomyces noursei* or rapamycin by *Streptomyces hygroscopicus*), but they also serve as helpful experimental tools (e.g. filipin extracted from *Streptomyces filipinensis*).

Detailed characterization of the secondary metabolites produced by recently isolated actinomycete *Streptomyces durmitorensis* [73] led to the discovery of a novel compound 32,33-didehydroroflamycoin (DDHR), a new member of the macrolide family. Initial experiments examining biological activity of DDHR showed that DDHR induces cell death in various cancer-derived cell lines (HL60, 4T1, A431, CT26, MDA-MB-231 and HeLa). It was suggested that the mode of action of DDHR is linked to the induction of apoptosis as demonstrated by DNA fragmentation [74]. Recent studies proven toxic effects of DDHR towards *Candida albicans* by inducing membrane disruption but not towards bacteria *Escherichia coli* or *Listeria monocytogenes* [75]. However, its mode of action has not yet been uncovered.

The aim of this work was to investigate the molecular mechanism of membrane associated bioactivity of DDHR employing GUV model membranes. To examine the pore formation ability, we performed several leakage assays, in which we focused especially on the role of cholesterol. The nature of the formed pores was also investigated on black lipid membranes. Furthermore, we tested the ability of DDHR to promote phase separation in bilayers. Supplementary experiments were performed using Amphotericin B and filipin in order to compare the action of DDHR with these structurally related compounds. Due to a rapid photobleaching, we took advantage of multiphoton excitation microscopy to directly visualize DDHR distribution.

RESULTS AND DISCUSSION

In the present work we investigated the membrane interactions of a bioactive compound DDHR aiming to reveal its mode of action. According to literature, related polyene molecules are membrane active compounds with a disruptive impact on the lipid bilayers [76]. In spite of relative similarity of their molecules, it was shown that they differ in the way they permeabilize the membranes [69] [72].

Herein, we performed leakage assays to assess the level of membrane disintegration caused by DDHR and to examine the effect of individual lipid components on the disruptive activity of DDHR. Based on our results, we determined that the formation of membrane protrusions depends on the presence of cholesterol that has been already shown to alter the membrane activity of macrolides [72] [77]. In the absence of cholesterol, GUVs treated with DDHR were leaking much more in the used range of concentrations than cholesterol-containing vesicles. While determining the size of these membrane ruptures, we observed that cholesterol-free vesicles were permeable for molecules of a size between 0.8 and 10 kDa. In contrast, only a minor fraction of larger molecules (3 - 10 kDa) passed through the membranes of vesicles with cholesterol. Thus, it appears that cholesterol enables DDHR to form smaller protrusions than without cholesterol. This prediction has a strong support from the results obtained by current measurements on black lipid membranes. The conductance of these model membranes significantly increased, if DDHR was added to the aqueous phase. On the time curse of the current measured on cholesterol-free membranes we could distinguish either general ruptures, or single opening and closing pores that were similar to those observed for related macrolides [78] [79] [80]. In the case of cholesterol-containing vesicles, the increase of the current evolution was continuous without any distinguishable ruptures or pores. This implies formation of much smaller and very stable pores that are not resolvable even by such a sensitive method.

We calculated that the diameter of the pores in cholesterol-free membranes is approximately 1 nm. In comparison to other pore-forming macrolides [79], the conductance of DDHR-induced pores was considerably lower indicating that although DDHR has a similar chemical structure, it forms much smaller pores. It seems that the presence of cholesterol is not an absolute requirement for the formation of pores as also proposed in the literature for structurally related molecules [81] [82]. In this respect, it is probable that DDHR induces formation of two types of pores with respect to the presence of cholesterol. Similar conclusion was made for AmB forming unstable channels in sterol-free membranes and more stable ones in the sterol-containing membranes [70].

Moreover, cholesterol-containing membranes with incorporated DDHR, unlike those without cholesterol, exhibited significantly higher stability, which means that this compound, in contrast to filipin [83], do not damage the membrane when the cholesterol is present. On the contrary, cholesterol-free membranes collapsed a

short time after addition of DDHR to these membranes. All these results suggest that even though DDHR is, like some other polyenes, a pore-forming agent, corresponding pores are considerably smaller than the pores formed by AmB or nystatin [84]. However, in fact, we observed that even the membranes with cholesterol are permeable to some extent for Atto488 dye; thus, the pores cannot be smaller than 1 nm. Taken into account that elevated concentration of DDHR allows also bigger molecules to pass through the membranes, the size of formed pores is most likely determined predominantly by DDHR amount and cholesterol only stabilizes the pores and keep their size rather small.

In conclusion, we suggest that DDHR induces rather transient pores or temporal ruptures in the membranes without cholesterol that contribute to the overall membrane damage. This effect could be partly attributed to formation of aggregates disrupting the membranes as shown for numerous amphiphilic drugs [85] [86] [87]. The presence of cholesterol promotes formation of small well-defined pores and reduces disruptive activity of DDHR. We assume that cholesterol determines the vertical orientation of the molecule, which could result in less-disruptive activity of DDHR in the cholesterol containing membranes. Very similar effect of sterols has been observed in the case of other polyenes AmB or filipin [72] [77]. AmB has been both computationally and experimentally concluded to reorient in the membranes with cholesterol perpendicularly with respect to the membrane plane [77] [88]. Similar findings were reported also for filipin, whose orientation in membranes is maintained by cholesterol molecules [72]. Our data also indicate that a substantial amount of DDHR is required for formation of pores, because leakage of vesicles was not observed at the lowest 10 μM concentration. This would agree with Venegas' results (2003), assuming a threshold concentration of AmB for its pore-forming activity. However, to get deeper insight into the nature of DDHR induced pores, further investigation is needed.

Moreover, we detected several morphological changes of model membranes generated by DDHR, such as elongation or budding of GUVs. Analogous destabilizing effects on GUVs were observed for another macrolide antibiotic azithromycin. They are supposed to be attributed to the decrease of the interaction energy between lipids resulting in lower elastic moduli of the bilayer upon exposure to a macrolide molecule [89]. Since we observed these effects mainly in cholesterol-free vesicles, they most likely contribute to the leakage of GUVs. Similarly to pore-forming activity, morphological changes are concentration dependent, because 10 μM concentration of DDHR did not induce any morphological changes, unlike its higher concentrations.

Despite limited leakage and morphological changes of cholesterol-containing vesicles, we confirmed that these membranes accommodate significant amount of DDHR molecules as revealed by MPE microscopy. Therefore, the milder impacts of DDHR on the cholesterol-containing membranes cannot be attributed to the lower incorporation efficiency into these membranes.

Surprisingly, DDHR preferentially inserted into highly ordered membrane areas as detected by simultaneous monitoring of distribution of DiD as a marker of L_d phase [90] and the intrinsic fluorescence of DDHR. Moreover, its interaction with membranes led to phase separation even in the simple DOPC/Chol (7/3) and POPC membranes. However, this effect was not noticed for pure DOPC bilayers. It seems that the phase-separating activity of DDHR depends predominantly on the membrane order and cholesterol obviously plays a role in this phase-separating action only as a factor that rigidifies the membrane. Likewise, filipin was shown to have similar unusual property to prefer partitioning into gel crystalline phase [72] as well as to promote formation of ordered and rigid domains [91].

Finally, by FTIR spectroscopy we proved the direct interaction of DDHR with cholesterol, which is most likely responsible for formation of small stable pores and accommodation of a planar molecule DDHR in the L_o phase. These findings are in agreement with previous findings, which indicated interaction of polyene macrolides with sterol containing membranes [72] [76] [77].

From the data presented in this work we can conclude that the effect of DDHR on the membranes is multi-modal. Besides formation of transmembrane pores, it also destabilizes molecular lipid order. Both mechanisms are probably important for the biological activity of DDHR. Overall, biological activity of DDHR is most likely exerted via formation of small pores permeable to ions and small molecules causing disruption of the membrane potential, which ultimately leads to cell death [76].

Part 2:

Investigation of the nature and size of membrane nanodomains in model lipid membranes

PUBLICATION II

In recent years, interest in research focused on membrane organization has increased for several reasons. There is growing evidence that the existence of membrane heterogeneities is essential for many cellular processes such as signaling, trafficking or lateral protein sorting, but they can be also accompanied with pathophysiological conditions. It has been postulated and experimentally proven that the function of several membrane proteins highly depends on their lipid environment [92]. Therefore, there is a great interest to uncover the real membrane organization structure and its impact on protein functions.

It was hypothesized that the membrane heterogeneity in cells arises from the association of saturated lipid acyl chains, such as those of sphingomyelin, with cholesterol resulting in formation of highly ordered domains surrounded by less ordered regions. These domains were named as "lipid rafts" [93]. The indications that "rafts" may exist in cells were supported by the observation that the cellular membranes are not fully solubilizable under certain conditions by mild non-ionic detergents [94]. Thus, the study of "lipid rafts" has been pursued by the analysis of so-called detergent-resistant membranes. According to the initial proposal, these membrane heterogeneities were of a considerable size (from dozens to hundreds of nanometers in diameter), rigid and predominantly stabilized by lipid-lipid interactions resembling floating islands in a fluid sea of lipids. Similar raft-like domains were found in artificial membranes composed of phospholipid-sphingomyelin-cholesterol mixtures, which supported the idea that the membrane areas with L_o phase in both cellular and artificial membranes are of the same nature. However, in fact, such large phase-separated domains have never been directly observed in native cells, even super-resolution microscopy techniques failed to detect "lipid rafts". It raises the question whether these domains really exist in cells. Besides, several cellular processes require rapid changes of the membrane composition, so that it is more efficient for these processes to occur in a dynamic system. Therefore, the formation of rigid and "sharp-edged" domains is not favorable.

As the methods applied for membrane heterogeneity studies became more diverse and sophisticated, the assumed "rafts" have been getting smaller and smaller. Finally, various experimental approaches revealed the existence of sub-diffraction-sized nanodomains [95] [96]. Since the optical resolution of conventional microscopy is insufficient to directly visualize these structures, we have to rely on rather elaborate techniques, for instance, neutron scattering [96], Förster resonance energy transfer [97] or stimulated emission depletion microscopy [98]. Despite employing various detection techniques close to *in vivo* conditions, there are still several limitations resulting in generation of artifacts. For that reason, the nanoscopic cellular membrane organization remains elusive. It is partly caused by the lack of appropriate techniques that would enable us to visualize objects in living cells at the nanoscale, as well as by the absence of suitable model systems that would preserve the cellular membrane complexity.

In cell membranes, distinct raft-like structures were noticed by various microscopic or spectroscopic techniques, for instance, stimulated emission depletion microscopy combined with FCS (FCS-STED) [98] [99] or by employing polarity sensitive probes [100]. However, the physiological nature of such structures is not fully clear.

Nevertheless, unlike L_o domains observed in artificial membranes GUVs, heterogeneities found in cell-derived GPMVs seemed to be less ordered than L_o phase, but more ordered than L_d phase in GUVs [101]. Thus, it suggests that their character is more subtle than previously proposed, which gives rise to an idea that L_o domains found in artificial membranes and raft-like domains in cells are irrelevant to the domains in untouched cells.

Previously mentioned findings led us to the question whether in model membranes can exist similar biologically relevant lipid driven nanoscale domains as well as whether they have L_o or rather less ordered character.

Our aim was to investigate and further characterize the size and nature of nanoscale membrane heterogeneities. We used GUVs made of binary (DOPC/SM) or ternary (DOPC/Chol/SM) lipid mixtures in ratios below the macroscopic phase separation. We were interested especially in the lipid ratios highlighted in red in the phase diagram shown in Figure 14, where the formation of nanodomains was expected. Limitations caused by insufficient resolution of optical microscopes were overcome by employing biophysical non-imaging approaches. Using various fluorescent probes, we combined FLIM-FRET with Monte Carlo simulations to uncover the existence, size and nature of such nanodomains in GUVs. It has been shown that the best way to define the size of nanodomains by this approach is to use fluorescent probes that both prefer either L_o, or L_d phase [102]. However, the list of L_o residing dyes is limited so far and only few probes exhibit the desirable property. We took advantage of a novel BODIPY-FL-headgroup-labeled monosialoganglioside GM1 (g-GM1), whose K_d value was calculated to be suitable for our measurements. Moreover, the size and lipid phase of studied nanodomains was further determined by z-scan FCS and the

magic angle spinning NMR (MAS-NMR) spectroscopy. In addition, attractiveness of this study is also based on the assumption that nanodomains formed in model membranes are expected to be precursors to the formation of macroscopic domains [103].
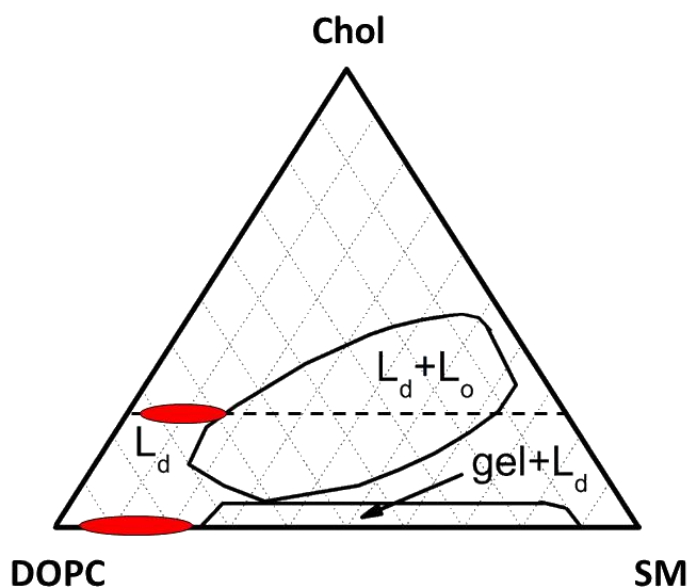
Figure 14. Ternary phase diagram of DOPC/SM/Chol membranes (adapted from [104]).
The phase diagram shows the regions of two phase coexistence, {L_d and L_o} and {gel and L_d}. Red highlighted areas show the regions with expected formation of nanodomains. Note that the $L_d + L_o$ encircled area displays the phase coexistence, which is in size resolvable by conventional optical microscopy.

RESULTS AND DISCUSSION

According to recent findings, the existence of nanoheterogeneities in cellular plasma membrane is more relevant to the reality than previously suggested rigid membrane domains called "rafts" [98] [99]. To overcome the limited resolution of optical microscopy we employed FCS, FLIM-FRET, MAS-NMR and a novel MC-FRET approaches to reveal the size and nature of the nanodomains in model membranes GUVs. As previously mentioned, distribution coefficient K_d of fluorescent probes is a significant factor for determining the nanodomain size. In this work we used fluorescently labelled GM1 (BODIPY-FL-GM1) that has been shown to sufficiently partition into sphingolipid-enriched nano-heterogeneities [105]. Sensitivity of the FRET technique applied in this work along with computational approach enabled us to determine the size of domains and the area they occupy with high accuracy.

Original model of lipid "rafts" is based on preferential interactions between cholesterol and saturated acyl chains of sphingolipids [93]. Likewise, sphingomyelin and cholesterol have been identified as major components of DRMs in cells [106]. Contrary to these findings, we demonstrated that nanodomains are formed not only in ternary DOPC/Chol/SM (70-65/25/5-10 mol%) membranes, but also in the binary DOPC/SM (90-85/10-15 mol%) lipid bilayers below the area of L_o/L_d coexistence [104]. We have shown that the presence of cholesterol is not crucial for nanodomain formation, as they were detected even in binary composition (DOPC/SM) with the content of SM between 10 - 15 mol%. However, it should be noted that cholesterol promotes formation of membrane heterogeneities, because even 5 mol% content of SM was sufficient to detect nanoheterogeneities in these membranes.

Our approach allowed us to determine the size of nanodomains. Their average diameter was calculated to be approximately 9 nm for all compositions with detected nanodomains. Neither diverse content of sphingomyelin, nor the presence of cholesterol changed the size of these heterogeneities, which is in line with the study by Ho et al. [95]. The determined size of nanodomains was roughly in agreement with several recent studies estimating the diameter of nanodomains in the membranes with similar lipid composition approximately between 2 and 15 nm varying with respect to used methods or fluorophores [96] [97] [107] [108]. Nanoheterogeneities in the plasma membrane of living cells were estimated to have less than 20 nm in diameter [98] [99]. More accurate determination of the domain size is challenging due to the resolution limit of available techniques. Nevertheless, the observation of sub-20 nm domains in living cells might point out to similarity between nanodomains in both artificial and plasma membranes.

According to the original model, lipid "rafts" are distinct, highly ordered regions in a sea of fluid lipids occupying relatively small area of the membrane surface [109]. However, our data indicate that membrane heterogeneities cover up to 55 % of the whole membrane surface area. These findings are supported by recent indications that the domain area might, in fact, dominate and cover the majority of the plasma membrane [98] [100].

Moreover, we have demonstrated that the observed nanodomains are fluid and disordered. Three lines of evidence support this contention. Firstly, the calculated number of DOPC molecules by far exceeds the number of SM as well as cholesterol molecules within the nanodomains, which makes the nanodomains fluid. Secondly, fluorescent probes DOPE-Atto488, DOPE-Atto633 and DiD were homogeneously distributed in the nanoheterogeneities-containing membranes, although these probes do not prefer liquid-ordered environments in model membranes. Finally, NMR spectral shift and MAS-NMR spectra measured in the membranes with detected nanoheterogeneities showed characteristics typical for

liquid-disordered phase. Moreover, the obtained results for the area occupied by nanoheterogeneities were in good agreement with above mentioned results from MC-FRET approach. Nevertheless, our findings are in contrast to some of the previous studies where the authors believed to observe L_o nanodomains [96] [97] [108]. However, in fact, the membrane phase of nanodomains has not been experimentally determined in these studies. On the other hand, our findings have a strong support from studies carried out on living cells employing STED-FCS. The authors detected sub-resolution domains that did not have L_o character [98], as the detected domains were accessible for fluorescent probes that strictly avoid L_o phase in model lipid membranes. These results might point out to close nature of nanodomains we observed in model membranes GUVs with those in living cells.

Although we performed the experiments in lipid-only system lacking cytoskeleton or other factors that can possibly influence the membrane character; hence it might not be fully analogous with heterogeneities in the plasma membrane However, the laws of lipid clustering are general and we believe that our findings contribute to the knowledge of a physiological state of plasma membrane organization.

PUBLICATION III

The ganglioside GM1 (a ceramide derived lipid with sialic-acid in a headgroup oligosaccharide chain) is an essential lipid present in all animal cells, although it is predominantly localized in neuronal membranes.

Owing mainly saturated hydrocarbon tails, this lipid is known to segregate laterally resulting in formation of GM1-rich domains enriched also with sphingomyelin and cholesterol [110]. Preferable clustering with sphingomyelin is caused by the interactions of ceramide hydrophobic part of GM1 with the hydrophobic acyl chains of sphingolipids. Clustering is also controlled by glycan-glycan binding forces between headgroup regions of GM1 allowing them to cluster even in the absence of sphingomyelin [111].

Although this lipid is known from 1930s, its role in regulation of biological processes is not yet well understood. It has been shown that GM1 is indispensable for neuronal development and differentiation [112]. Apart from that, accumulation of gangliosides is believed to be related to the development of Alzheimer's or Parkinson's diseases [113] [114].

Lipid GM1 is also considered as the main receptor for pentameric cholera toxin B subunit (CTxB) produced by *Vibrio cholera* that causes massive secretory diarrhea often leading to death. Cholera toxin is composed of two parts, a subunit A and a pentameric subunit B (CTxB). While the subunit B recognizes and interacts with GM1 lipids in the membranes, subunit A needs to be endocytosed

into the host cell to cause disease. Pentameric subunit CTxB is able to specifically interact with five cell surface GM1 molecules, nevertheless, it has been proven that binding only one GM1 molecule is sufficient for toxin activation [115]. It was examined on model supported lipid bilayers that if the density of GM1 is too high, CTxB is not able to bind so effectively as some of the GM1 molecules remain unavailable [116]. Furthermore, membrane environment, such as cholesterol content or membrane fluidity, influences the GM1 recognition [117] [118]. In spite of several studies on CTxB-GM1 binding, the exact mechanism of CTxB binding remains unclear. Thorough understanding of the cholera toxin binding mechanism to the eukaryotic cells is of great importance, as it may help to develop strategies for designing the inhibitory drugs.

The aim of this work was to contribute to current knowledge of binding mechanism and interaction parameters of CTxB by investigation of GM1 clustering. Moreover, we focused on the availability of GM1 for CTxB in the presence or absence of cholesterol. We employed GUV model system as a suitable system and we utilized FRET combined with Monte Carlo simulations and z-scan FCS method. In addition, we employed so called antibunching technique to count the exact number of membrane bound toxins in relation to the number of available GM1 lipids.

RESULTS AND DISCUSSION

Knowledge about GM1 organization is valuable not only it serves as a receptor for a human enterotoxin cholera toxin, but also for its participation in cellular signaling and adhesion.

GM1 molecules have been reported to self-organize into domains [111], but the details about their character are not clear. Analogously to our previously described work, we used a novel fluorescent head-labeled g-GM1 as a donor in FRET studies to investigate clustering of GM1. We demonstrated that the GM1 aggregation occurs in DOPC/GM1 bilayers with the GM1 content between 1 % and 8 %. MC-FRET approach revealed the size of these domains to be 5 - 7 nm in diameter covering 35 - 45 % of the whole bilayer area with no change with increasing content of GM1 molecules. Likewise, the presence of cholesterol did not change neither the size of the domains, nor the area occupied by them. The observation that even 1 mol% of GM1 causes 40 % covering of the bilayer with GM1-driven domains is surprising, nevertheless, studies employing AFM also reported that the area occupying by GM1 domains by far exceeds the amount of GM1 [119]. Therefore, it suggests that the involvement of other lipid molecules in the GM1 domains must be high. This finding can explain our observation that the capacity of these domains seems to be sufficient to accommodate more GM1 molecules with no change in the surface area covered by domains as well as in fluidity of these domains, which was confirmed by z-scan FCS measurements.

Furthermore, we focused on the recognition of GM1 molecules by CtxB. For this study, we employed not only FCS or FLIM-FRET methods, but we also designed fluorescence antibunching experiments to unravel binding activity of CTxB. Our results showed that 4 mol% content of GM1 in the bilayer lowered the binding ability of CTxB in contrast to membranes containing only 1 mol%. Thus, we conclude that the binding sites of CTxB probably do not fit high dense GM1 clusters. Our observations are consistent with previous findings demonstrating that the increased content of GM1 weakens CTxB-GM1 interactions [116].

Cholesterol has been shown to co-localize with GM1 in membrane domains [120]. However, we found out that the presence of cholesterol also lowered the availability of GM1 for CTxB. This result is in agreement with the already published simulation data indicating GM1 headgroup tilting in the presence of cholesterol, which resulted in decreased recognition by CTxB [121]. Besides that, cholesterol is known to play a role in condensing the membrane in general. As a result, the GM1 headgroups can be packed closer, which can result in reduced CTxB binding ability. Thus, the topology and orientation of the GM1 oligosaccharide moiety and the GM1 clustering can represent an important regulatory mechanism for CTxB activity.

Moreover, we revealed that GM1 containing membranes undergo lateral reorganization in response to CtxB binding. Employing FRET experiments between fluorescently labeled CTxB (Alexa488-CTxB) and DiD, we found out that binding of CTxB expels DiD from the vicinity of labeled CTxB, which resulted in lower FRET efficiency. Subsequently, the diffusion of both g-GM1 and DiD decreased. These findings might point out to either the formation of rigid nanosized domains [122], or induction of local membrane curvatures [123].

Ultimately, this study contributes to understanding of the principles underlying formation of GM1-driven nanodomains as well as to revealing the mechanism of CTxB binding.

Part 3:

Study of the roles of SNARE-mimicking lipopeptides during initial steps of membrane fusion

PUBLICATION IV

Cellular membrane fusion is a vital event naturally occurring in all living organisms that has been in focus of research for many years. It is essential for many processes such as import of nutrients, protein transport between intracellular compartments or controlled release of neurotransmitters, but it also assists pathogen entry into host cells. In eukaryotic cells, a non-viral fusion mechanism is mediated by SNARE (soluble N-ethylmaleimide-sensitive factor attachment protein receptor) complex of proteins located on opposing membranes that cooperatively form a stable 4-helical coiled-coil structure [124], which brings the opposing membranes into close proximity. Despite the huge diversity of fusion processes, the fusion cascade consists of three conserved steps: Initially, two membranes are brought into close proximity accompanied by a disruption of lipid continuity at the site of contact. This is followed by fusion of the proximal membrane leaflets involving lipid mixing. Finally, the fusion pore is formed facilitating content mixing of fused vesicles [125] [126] [127]. This process was found to be very efficient, controllable and highly specific due to a perfect interplay of involved proteins [126]. Despite a vast effort, the exact mechanism how SNARE protein complex promotes fusion remains unknown. Its bulky size, complexity, and membrane binding make it handling without danger of artifacts very difficult. Extensive study of original SNARE fusion system [128] [129] served as an inspiration for designing simpler model systems that would have key features of cellular fusion processes. Such systems are based on lipid vesicles decorated with potentially fusogenic molecules, such as DNA-lipid conjugates [130], peptide amphiphiles [131] [132] or small molecules [133] [134] that can act as recognition sites. The system based on complementary peptide amphiphiles, recently developed by the Kros' group [131], was found to be, in comparison to other approaches, highly specific, effective and leakage free [135]. This simplified system designed to mimic naturally occurring SNARE-driven fusogenic process is based on the molecular recognition between coiled-coil forming peptides [136]. The fusogens consist of two complementary amphiphilic coiled-coil forming peptides [(KIAALKE)$_4$] (peptide K$_4$) and [(EIAALEK)$_4$] (peptide E$_4$) coupled to a

cholesterol lipid anchor linked via flexible polyethylene glycol (PEG) (Fig. 15). The latter molecule serves as a linker between the cholesterol anchor and the peptide K_4, or E_4. The cholesterol anchor, in contrast to alternative lipid anchors, has been shown to be the most efficient modification that yields highly fusogenic liposomes [137]. Coiled-coil structures are created by peptide moieties forming several α-helices that wind around each other and finally form stable heterodimer resembling molecular Velcro [138]. If the cationic peptide K_4 is employed, the construct is called CP_nK_4, where n denotes the number of ethylene glycol units, and CP_nE_4 represents the construct containing the anionic peptide E_4.
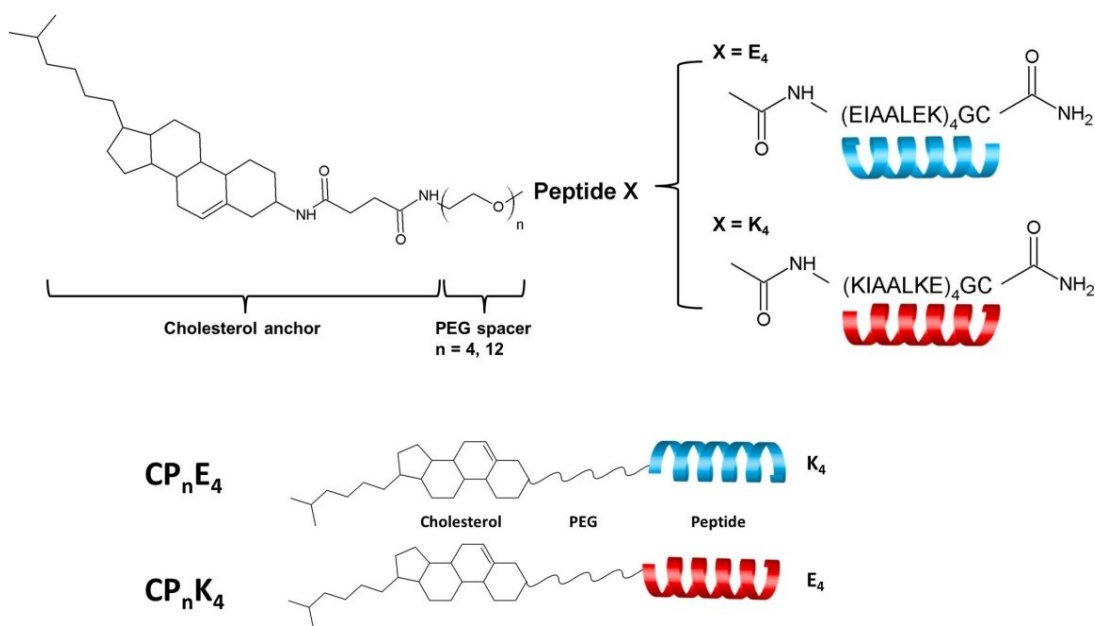

Figure 15. Chemical structures of lipidated amphiphilic peptides CP_nE_4 and CP_nK_4
The lipopeptides consist of a cholesterol tail linked through a polyethylene glycol spacer to the coiled-coil forming peptides E_4, or K_4. The amino acid sequence of E_4 is [(EIAALEK)$_4$] and that of K_4 is [(KIAALKE)$_4$].

The fusion process is forced by CP_nE_4/CP_nK_4 interactions leading to the formation of a coiled-coil motif between peptides K_4 and E_4. This brings both membranes into close proximity, which is followed by their fusion [131] (Fig. 16). In contrast to the conventional strategy of mixing the fusogens with lipids in organic solvents prior to liposome formation, the above mentioned lipopeptides can be efficiently incorporated into artificial as well as into cellular membranes in a facile manner by their addition directly to the solution containing cells or liposomes. Thanks to this fact, such approach opens up new possibilities for *in vivo* applications [139], for example direct drug delivery into the cytosol of living cells [140] or membrane engineering [135].
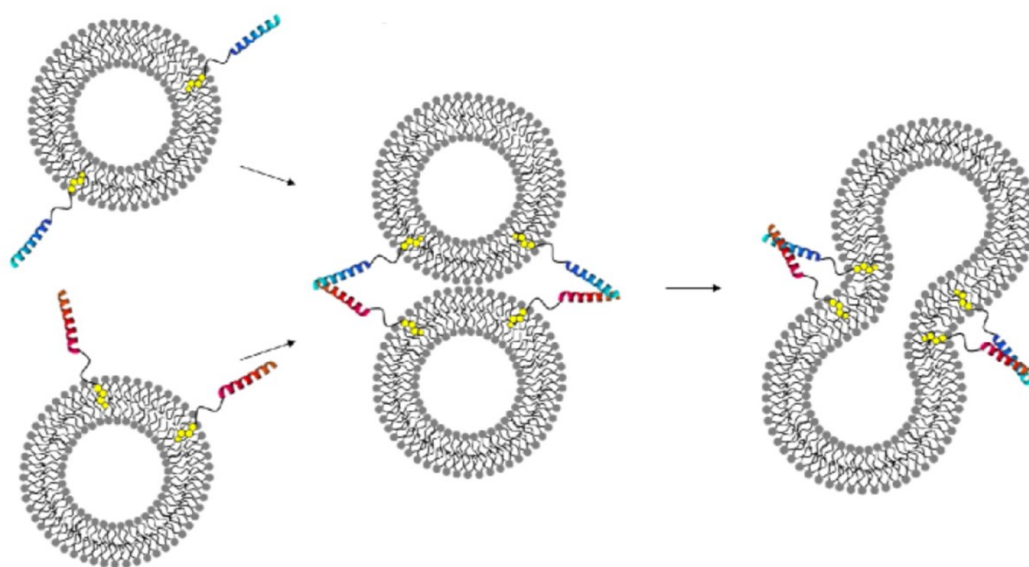
Figure 16. Simple docking model of lipopeptide-driven membrane fusion [137]**.** Lipopeptides are inserted into the lipid vesicles and subsequently form coiled-coil bounds between their complementary partners, which leads to fusion of the lipid vesicles.

However, recent studies have revealed that a simple docking model is not sufficient for description of lipopeptide-induced fusion. It seems that several factors such as lipopeptide concentration or peptide-membrane interactions influence the fusion efficiency [141]. Thus, the exact mechanism of lipopeptide-mediated membrane fusion remains unclear. It has been hypothesized that high local concentration of lipopeptides might lead to formation of homo-coils (K/K or E/E, respectively), which could be responsible for reduced fusion efficiency [141] [142]. However, peptide homocoiling was also suggested as a fusion enhancing factor [137]. Another aspect that should be taken into account is the interaction of lipopetides/peptides with the lipid membrane that might result from their amphipatic nature [143]. This uncertainty about the real mechanism underlying the fusion event, actual state of lipopeptides incorporated into the membranes and their influence on the membrane properties demonstrates the need of thorough

investigation. Design of an efficient fusion system that can be successfully employed *in vivo* requires a detailed understanding of the molecular processes behind lipopeptides mechanism of action.

In the present work, we combined a variety of advanced fluorescent methods including single molecule approaches to study the interactions between peptides K_4 and E_4, or CP_nK_4 and CP_nE_4, respectively, and their influence on physicochemical properties of the lipid bilayer. All experiments were done by using model membranes made of DOPC/DOPE/Chol (50/25/25 mol%) lipid mixture, which is a commonly used lipid composition for fusion experiments [144]. Membrane affinity of peptides to the lipid bilayer was studied by measuring of fluorescence intensity as well as by z-scan FCS. Physicochemical membrane properties were investigated by employing solvent relaxation technique, z-scan FCS or FRET between fluorescently labeled lipid analogues, which allowed us to probe the changes in membrane diffusion or hydration and mobility of the bilayer in the presence of lipopeptides/peptides. Accessibility of lipoeepeptides/peptides for binding to a complementary partner was proven by FCCS and FRET. Based on the studies demonstrating that the PEG linker length influences the fusion efficiency [145], we used two sets of lipopeptides that differ in the length of the linker with either 4 or 12 units of ethylenglycol and we compared their impacts on membrane properties.

RESULTS AND DISCUSSION

Fusion of biological membranes driven by lipopeptides CP_nK_4 and CP_nE_4 is believed to be based on formation of coiled-coil structures between the peptides K_4 and E_4 mediating a close contact of the opposing membranes, for which the set of these molecules has been designed. However, our data show that the role of lipopeptides is more complex. We demonstrated that the peptide K_4, unlike the peptide E_4, interacts strongly with the bilayer composed of DOPC/DOPE/Chol (50/25/25 mol%), which was noticed in the previous research as well [143] [146]. Such effect could stem from the interactions of hydrophobic amino acid residues of leucine, isoleucine and perhaps lysine with the bilayer [146] [147] or from a charge distribution around the hydrophobic part [148] resulting in so called snorkeling effect [147] (Fig. 17).
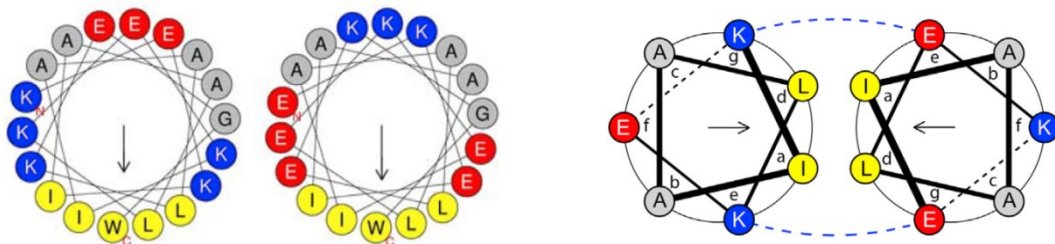
Figure 17. Helical wheel projections of amino acid residues of the peptides E and K [146]**.**
Left) Leucine and isoleucine residues might cause so-called "snorkeling" effect on the membrane surface. **Right)** Coiled-coil binding is mediated by hydrophobic leucine and isoleucine residues. Arrows indicate the direction of the hydrophobic moment, dashed blue lines show supporting electrostatic interactions

Interestingly, our data show that the lipid composition of the membrane plays a fundamental role in the action of the peptides/lipopeptides, as the binding of the peptide K_4 occurs predominantly in DOPE-containing membranes. While the peptide K_4 strongly interacts with the membranes composed of DOPC/DOPE/Chol (50/25/25 mol%), we detected only a minor peptide K_4 binding on the DOPC/Chol (75/25 mol%), pure POPC or pure DPPC bilayers (Fig. 18). Similarly, the effect of DOPE on the peptide K sticking has also been revealed by molecular simulations [149]. However, performing experiments on DOPC/DOPE/Chol membranes is desirable. Thanks to induction of negative curvature by DOPE, this composition is highly efficient and commonly used for fusion experiments [137] [144] [145] [150].
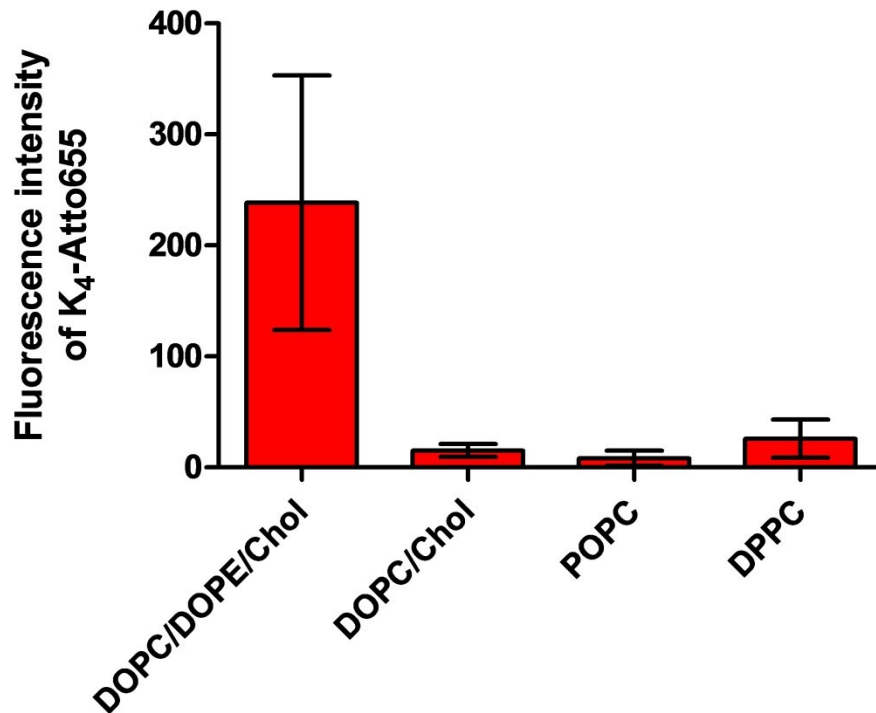
Figure 18. Binding of the peptide K_4 to membranes composed of various lipid mixtures.
Fluorescence intensity (averaged number of photons per area) of the peptide K_4-Atto655 bound to the surface of GUVs composed of various lipid compositions DOPC/DOPE/Chol (50/25/25 mol%), DOPC/Chol (75/25 mol%), pure POPC and pure DPPC provides information about the concentration of the peptides attached on the membrane surface. (The data are not included in the manuscript.)

Originally, lipopeptides CP_nK_4 and CP_nE_4 have been designed to interact with each other via coiled-coil structure to mediate membrane fusion. Based on our examination of fluorescence intensity, we truly demonstrated that peptides E_4 and K_4 strongly interact with the membranes decorated with their complementary lipopeptide partners. Surprisingly, FCCS experiments revealed that the majority of the peptide K_4 does not interact with the lipopeptide CP_4E_4 tethered in the membrane, as the cross-correlation amplitude reached only 30 % of the maxima. *Vice versa*, binding of the peptide E_4 to CP_4K_4 was similarly inefficient. This apparent disagreement in our results might be a proof that the lipopeptide CP_nE_4 functions only as a "handle" for the peptide K_4 that subsequently interacts with the opposing membrane facilitating membrane docking [145]. In contrast to previous works, we did not observe any lipopeptide homo-coiling, which was suggested as a factor decreasing fusion efficiency [141] [142] [151].

The interaction of the peptide K_4 with the bilayer is expected to affect the membrane structure, hydration or mobility. Our TDFS experiments revealed that

the presence of 2 mol% CP_nK_4 in the membrane leads to decreased hydration and increased microviscosity in the headgroup region. Membrane dehydration is mostly accompanied with lipid packing, which expels the water molecules from the bilayer [152]. This effect can be attributed to dense covering of the bilayer surface by peptide segments of the lipopeptide CP_nK_4. Interestingly, even 4 mol% content of the peptide K_4 affects neither membrane mobility, nor membrane hydration in contrast to the case when K_4 was present as a part of CP_nK_4 molecule (the data are not included in the manuscript). This observation could be attributed to the weaker binding of the peptide K_4 to the membrane in comparison to the peptide moiety of membrane tethered CP_4K_4. Similar finding was reported for DOPE-anchored lipopeptide $LP_{12}K_3$ and the peptide K_3 [146]. The binding strength of the peptide K_4 seems not to be sufficient enough to influence the membrane hydration or mobility. In contrast, membrane-tethered CP_4K_4 exhibits stronger interaction with the lipid bilayer and as a result, the membrane properties are influenced by its presence. This finding is, however, in contrast to previous study, where the authors reported disruptive effect of the non-tethered peptide K_3. They showed that the peptide K_3 induces membrane curvature and reorganizes the structure of the membrane by accumulation of PE molecules in its vicinity [146]. Nevertheless, this effect might not be strong enough to affect membrane hydration and mobility, therefore, we did not detect any changes by our approach.

On the other hand, our TDFS data showed that the peptide E_4 as well as the lipopeptide CP_nE_4 did not induce any significant effect on the membrane properties, which perfectly agrees with previous findings indicating that the peptide moiety E is exposed to water [143] [146].

In summary, we suggest that the initial steps of the fusion process might be promoted by cooperative behaviour of both lipopeptides. While the lipopeptide CP_nE_4 acts rather as a "handle" for CP_nK_4 and facilitates formation of coiled-coil structure, which brings the membranes into close contact, peptide K_4 destabilizes the lipid bilayer, which consequently results in full membrane fusion. Thus, we assume that for an efficient fusion there should be equilibrium between K_4/E_4 coiled-coil structures and K_4/membrane interactions.

Our results are in agreement with previously published works suggesting rather asymmetrical role of the peptides during the fusion process [145] [153]. Therefore, the fusion process mediated by lipopeptides CP_nK_4 and CP_nE_4 cannot be explained by originally proposed simple docking model only.

PUBLICATION V

As already mentioned, lipopeptides CP_nK_4 and CP_nE_4 tethered in membranes can mediate membrane fusion. To date, all the vesicle fusion experiments have been performed employing large unilamellar vesicles (LUVs) for their high degree of membrane curvature, which was believed to promote the fusion. However, these vesicles have usually around 100 nm in diameter and it is not possible to visualize them directly using conventional optical microscopy because of their size. By mixing LUVs with much larger GUVs, fusion process driven by coiled-coil forming lipopeptides could be imaged. In addition, this approach is technically close to desired fusion system aiming on delivery of drugs or other compounds encapsulated in vesicles directly to cells. Herein, time-lapse fluorescence microscopy was employed to visualize LUVs/GUVs fusion promoted by lipopeptides CP_nK_4 and CP_nE_4. Lipid mixing as well as content mixing assays were conducted in order to monitor specific recognition of the coiled-coil forming lipopeptides and full membrane fusion.

RESULTS AND DISCUSSION

Designing a leakage-free fusion system remains a challenge. As it has already been reported, employing fusogenic lipopeptides CP_nE_4 and CP_nK_4 could be a successful approach [135]. To date, content mixing assays demonstrating complete fusion process have been performed solely on LUVs that cannot be directly observed by optical microscopy [145] [150] [154]. Most notably, this is the first study to visualize fusion process in the GUVs/LUVs system. We successfully imaged the fusion of vesicles employing a set of fusogenic lipopeptides. In spite of originally proposed symmetry in the CP_nK_4/CP_nE_4 coiled-coil driven fusion, time-lapse lipid-mixing experiments showed earlier docking of CP_4K_4 decorated LUVs to CP_4E_4 decorated GUVs than in the case with interchanged lipopeptides. This effect might be caused by combination of highly curved LUV membranes that promote the fusion [155] with stronger interactions between CP_4K_4-LUVs and CP_4E_4-GUVs. Removing of CP_4E_4 lipopeptides from GUVs and performing the fusion experiments with only CP_4K_4-decorated LUVs and plain GUVs showed a distinct degree of fusion. This finding is in line with the data included in our manuscript in revision (see Publication IV) and previously published results emphasizing that the interaction of the peptide K with the lipid bilayer is a crucial step for fusion process regardless the presence of the lipopeptide CP_nE [145].

Content mixing assays confirmed the results obtained by previously mentioned time-lapse lipid-mixing experiments. However, a considerable amount of GUVs did not exhibit content mixing at all, although a full set of fusogenic molecules CP_4E_4 and CP_4K_4 was employed. Full mixing of LUVs and GUVs content was

observed mainly in small-sized GUVs, which would point out to the necessity of high membrane curvature for coiled-coil driven membrane fusion [156]. In addition, we noted aggregates of LUVs on the surface of unfused GUVs, which probably prevented LUVs from fusion. Disintegration of the LUVs clusters, probably caused by aggregation of CP_nK_4 molecules [151], was performed by incubation with Tween 20 that should weaken peptide-peptide bonds, reduce the aggregates and consequently promote content mixing of liposomes [157]. However, introducing a detergent into the experimental setup might not only reduce lipopeptide aggregates, but it can also soften the membrane, which can subsequently promote fusion [158]. To get deeper insight into Tween 20-promoted reduction of aggregates and to examine its impact on the membrane properties, we employed single-molecule fluorescence approach z-scan FCS. The measured diffusion coefficient of DiD confirmed strong interaction of CP_nK_4 with the membrane in contrast to CP_nE_4 [143] [146]. Increased lateral diffusion of a membrane probe DiD measured in Tween 20-containing membranes in the absence of lipopeptides indicated softening of the membrane. If we consider that diffusion of CP_nK_4 and DiD increased with the same trend, it points out to rather higher mobility of the lipopeptides in a softer and more mobile bilayer than removing of their aggregates. Thus, it is disputable to what extent was the fusion enhanced by peptide-peptide bonds disruption or lipid bilayer softening.

Summary

The aim of this thesis has been to study nanoscale membrane heterogeneities and membrane interacting molecules by employing single-molecule fluorescence approach. All the topics dealt with the interaction of molecules with the lipid bilayer pointed towards investigation of their influence on the membrane properties.

Conclusions related to the aims:

Part 1: The activity of a polyene DDHR was investigated on model lipid membranes. Our results demonstrated the pore-forming activity of DDHR and its preferential partitioning into liquid-ordered phase. The character of the pores is related to the presence or absence of cholesterol. In addition, the insertion of DDHR into the membranes led to phase separation of the membranes. Moreover, direct interaction between DDHR and cholesterol was proven.

Part 2: We revealed that the membranes containing only two common membrane lipids self-organize into nanoscopic islands called nanodomains. We observed the formation of fluid sub-resolution nanodomains in the membranes composed of binary DOPC/SM or ternary DOPC/Chol/SM lipid mixtures below the phase separation boundary. We determined that nanodomains occupy up to 55 % of the membrane surface area while their radius is approximately 9 nm.
Our presented data further revealed that GM1 molecules cluster into fluid sub-resolution nanodomains covering significant area of the lipid bilayer. Moreover, the level of aggregation as well as the presence of cholesterol affects binding of its ligand CTxB.

Part 3: A set of fusogenic lipopeptides CP_nK_4 and CP_nE_4 serves as a minimal model for membrane fusion. We demonstrated that the roles of coiled-coil forming lipopeptides CP_nK_4 and CP_nE_4 in the initial steps of membrane fusion are asymmetrical and differ from their initially proposed mechanism. While the lipopeptide CP_nE_4 functions rather as a "handle" for CP_nK_4, the lipopeptide CP_nK_4 interacts with the membrane and promotes fusion by destabilization of the lipid bilayer. By monitoring of lipid and content mixing of GUVs and LUVs driven by coiled-coil forming lipopeptides, we could directly visualize the fusion process.

List of Symbols and Abbreviations

A	Alanine
AFM	Atomic force microscopy
AmB	Amphotericin B
B7PC	(Me)4bodipy-tail-labeled lipid
BODIPY-FL	4,4-Difluoro-5,7-Dimethyl-4-Bora-3a,4a-Diaza-s-Indacene-3-Propionic Acid
CP_nE_4	Lipidated peptide E_4 composed of cholesterol, polyethylene glycol of variable length and a peptide with amino acid sequence [(EIAALEK)$_4$]
CP_nK_4	Lipidated peptide K_4 composed of cholesterol, polyethylene glycol of variable length and a peptide with amino acid sequence [(KIAALKE)$_4$]
CTxB	Cholera toxin B subunit
Chol	Cholesterol
D	Diffusion coefficient
DDHR	32,33-didehydroroflamycoin
DiD	1,1'-Dioctadecyl-3,3,3',3'-Tetramethylindodicarbocyanine Perchlorate
DRM	Detergent resistant membranes
DOPC	1,2-dioleoyl-sn-glycero-3-phosphocholine
DOPE	1,2-dioleoyl-sn-glycero-3-phosphoethanolamine
DPPC	1,2-dipalmitoyl-sn-glycero-3-phosphocholine
E	Glutamic acid
FCS	Fluorescence correlation spectroscopy
FCS-STED	Stimulated emission depletion microscopy combined with fluorescence correlation spectroscopy
FCCS	Fluorescence cross-correlation spectroscopy
FLIM	Fluorescence lifetime imaging microscopy
FRET	Förster resonance energy transfer
FTIR	Fourier transform infrared
G	Glycine
g-GM1	BODIPY-FL-headgroup-labeled GM1
$G(\tau)$	Autocorrelation function
GFP	Green fluorescent protein
GM1	Monosialotetrahexosylganglioside lipid
GPI	Glycosyl phosphatidylinositol
GPMVs	Giant plasma membrane vesicles
GUVs	Giant unilamellar vesicles
I	Isoleucine
K	Lysine

K_d	Partition/distribution coefficient
L	Leucine
Laurdan	6-lauroyl-2-dimethylaminonaphthalene
LBPA	Lysobisphosphatidic acid
L_d	Liquid disordered phase
L_o	Liquid ordered phase
LUVs	Large unilamellar vesicles
MAS-NMR	Magic angle spinning – nuclear magnetic resonance
MC-FRET	Förster resonance energy transfer combined with Monte Carlo simulations
MPE	Multiphoton excitation microscopy
NADH	Reduced form of Nicotinamide adenine dinucleotide
NBD-cholesterol	22-(N-(7-Nitrobenz-2-Oxa-1,3-Diazol-4-yl)Amino)-23,24-Bisnor-5-Cholen-3β-Ol
NMR	Nuclear magnetic resonance
PEG	Polyethylene glycol
PN	Particle number
POPC	1-palmitoyl-2-oleoyl-sn-glycero-3-phosphocholine
r-GM1	564/570-bodipy-headgroup-labeled GM1
SM	Sphingomyelin
SNARE	Soluble N-ethylmaleimide-sensitive factor attachment protein receptor
SPBs	Supported phospholipid bilayers
SUVs	Small unilamellar vesicles
t	Time
τ	Lag time
$τ_D$	Diffusion time
TCSPC	Time correlated single photon counting
TDFS	Time dependent fluorescent shift
TRES	Time resolved emission spectra
YFP	Yellow fluorescent protein
$ω_0$	Detection volume radius

References

[1] Singer SJ., Nicolson GL., "The fluid mosaic model of the structure of cell membranes," *Science, Feb 18;175(4023):720-31.,* 1972.

[2] Anderson RG., Jacobson K., "A role for lipid shells in targeting proteins to caveolae, rafts, and other lipid domains," *Science, Jun 7;296(5574):1821-5,* 2002.

[3] Spiegel S., "Insertion of ganglioside GM1 into rat glioma C6 cells renders them susceptible to growth inhibition by the B subunit of cholera toxin," *Biochimica et biophysica acta, May 13;969(3):249-56,* 1988.

[4] Fantini J., Maresca M., Hammache D., Yahi N., Delézay O., "Glycosphingolipid (GSL) microdomains as attachment platforms for host pathogens and their toxins on intestinal epithelial cells: activation of signal transduction pathways and perturbations of intestinal absorption and secretion.," *Glycoconjugate journal, Mar-Apr;17(3 -4):173-9.,* 2000.

[5] Simons K., Sampaio JL., "Membrane organization and lipid rafts," *Cold Spring Harbor perspectives in biology, Oct 1;3(10):a004697,* 2011.

[6] Castro-Gómez P., Garcia-Serrano A., Visioli F., Fontecha J., "Relevance of dietary glycerophospholipids and sphingolipids to human health," *Prostaglandins, leukotrienes, and essential fatty acids, Oct;101:41-51,* 2015.

[7] Hung MC., Link W., "Protein localization in disease and therapy," *Journal of cell science, Oct 15;124(Pt 20):3381-92,* 2011.

[8] Dupuy AD., Engelman DM., "Protein area occupancy at the center of the red blood cell membrane," *Proceedings of the National Academy of Sciences of the United States of America, Feb 26;105(8):2848-52,* 2008.

[9] Andersen OS., Koeppe RE 2nd, "Bilayer thickness and membrane protein function: an energetic perspective," *Annual review of biophysics and biomolecular structure, 36:107-30,* 2007.

[10] Chum T., Glatzová D., Kvíčalová Z., Malínský J., Brdička T., Cebecauer M., "The role of palmitoylation and transmembrane domain in sorting of transmembrane adaptor proteins," *Journal of cell science, Jan 1;129(1):95-107,* 2016.

[11] Gupta K., Donlan JAC., Hopper JTS., Uzdravinys P., Landreh M., Struwe WB., Drew D., Baldwin AJ., Stansfeld PJ., Robinson CV., "The role of interfacial lipids in stabilizing membrane protein oligomers," *Nature, Jan 19;541(7637):421-424,* 2017.

[12] Fraenkel G., Hopf HS., "The physiological action of abnormally high temperatures on poikilothermic animals," *Biochemical journal, Jul; 34(7): 1085–1092,* 1940.

[13] van Meer G., Voelker DR., Feigenson GW., "Membrane lipids: where they are and how they behave," *Nature reviews. Molecular cell biology, Feb;9(2):112-24.,* 2008.

[14] Kobayashi T., Beuchat MH., Lindsay M., Frias S., Palmiter RD., Sakuraba H., Parton RG., Gruenberg J. , "Late endosomal membranes rich in lysobisphosphatidic acid regulate cholesterol transport," *Nature cell biology, Jun;1(2):113-8,* 1999.

[15] Asano K., Miwa M., Miwa K., Hanayama R., Nagase H., Nagata S., Tanaka M., "Masking of phosphatidylserine inhibits apoptotic cell engulfment and induces autoantibody production in mice," *The Journal of experimental medicine, Aug 16;200(4):459-67,* 2004.

[16] Nakano M., Fukuda M., Kudo T., Matsuzaki N., Azuma T., Sekine K., Endo H., Handa T., "Flip-flop of phospholipids in vesicles: kinetic analysis with time-resolved small-angle neutron scattering," *The journal of physical chemistry, May 14;113(19):6745-8,* 2009.

[17] Karnovsky MJ., Kleinfeld AM., Hoover RL., Klausner RD., "The concept of lipid domains in membranes," *The journal of cell biology, Jul;94(1):1-6,* 1982.

[18] Okamoto T., Schlegel A., Scherer PE., Lisanti MP., "Caveolins, a family of scaffolding proteins for organizing "preassembled signaling complexes" at the plasma membrane," *The Journal of biological chemistry, Mar 6;273(10):5419-22.,* 1998.

[19] Reverter M., Rentero C., Garcia-Melero A., Hoque M., Vila de Muga S., Alvarez-Guaita S., Conway JR., Wood P., Cairns R., Lykopoulou L., Grinberg D., Vilageliu D., Bosch M., Heeren J., Blasi J., Timpson P., Pol A., Tebar F., Murray RZ., Grewal T., Enrich C, "Cholesterol regulates Syntaxin 6 trafficking at trans-Golgi network endosomal boundaries," *Cell reports, May 8;7(3):883-97,* 2014.

[20] Finkelstein A., Cass A., "Effect of cholesterol on the water permeability of thin lipid membranes," *Nature, Nov 18;216(5116):717-8.,* 1967.

[21] Marsh D., Smith IC., "An interacting spin label study of the fluidizing and condensing effects of cholesterol on lecithin bilayers," *Biochimica et biophysica acta, Mar 16;298(2):133-44.,* 1973.

[22] Takishita K., Chikaraishi Y., Tanifuji G., Ohkouchi N., Hashimoto T., Fujikura K., Roger AJ., "Microbial Eukaryotes that Lack Sterols," *The journal of eukaryotic microbiology, Nov;64(6):897-900,* 2017.

[23] Wei JH., Yin X., Welander PV., "Sterol Synthesis in Diverse Bacteria," *Frontiers in microbiology, Jun 24;7:990,* 2016.

[24] Gorter E., Grendel F., "ON BIMOLECULAR LAYERS OF LIPOIDS ON THE CHROMOCYTES OF THE BLOOD," *The Journal of experimental medicine, Mar 31;41(4):439-43,* 1925.

[25] Danielli JF., Davson H., "A contribution to the theory of permeability of thin films," *Journal of cellular and comparative physiology, May:495–508, ,* 1935.

[26] Green DE, Perdue JF., "Membranes as expressions of repeating units," *Proceedings of the National Academy of Sciences of the United States of America, May;55(5):1295-302,* 1966.

[27] Jain MK., White HB. 3rd, "Long-range order in biomembranes," *Advances in lipid research, 15:1-60,* 1977.

[28] Honigmann A., Sadeghi S., Keller J., Hell SW., Eggeling C., Vink R., "A lipid bound actin meshwork organizes liquid phase separation in model membranes," *eLife, Mar 18;3:e01671,* 2014.

[29] Kusumi A., Suzuki KG., Kasai RS., Ritchie K., Fujiwara TK., "Hierarchical mesoscale domain organization of the plasma membrane," *Trends in biochemical sciences, Nov;36(11):604-15,* 2011.

[30] Mouritsen OG., Bloom M., "Mattress model of lipid-protein interactions in membranes," *Biophysical journal, Aug;46(2):141-53,* 1984.

[31] Sharpe HJ., Stevens TJ., Munro S., "A comprehensive comparison of transmembrane domains reveals organelle-specific properties," *Cell, Jul 9;142(1):158-69,* 2010.

[32] Kaiser HJ., Orlowski A., Róg T., Nyholm TK., Chai W., Feizi T., Lingwood D., Vattulainen I., Simons K., "Lateral sorting in model membranes by cholesterol-mediated hydrophobic matching," *Proceedings of the National Academy of Sciences of the United States of America, Oct 4;108(40):16628-33,* 2011.

[33] Simons K., van Meer G., "Lipid sorting in epithelial cells," *Biochemistry, Aug 23;27(17):6197-202,* 1988.

[34] Brown DA., London E., "Structure and function of sphingolipid- and cholesterol-rich membrane rafts," *The Journal of biochemical chemistry, Jun 9;275(23):17221-4.,* 2000.

[35] Horejsi V., Hrdinka M., "Membrane microdomains in immunoreceptor signaling," *FEBS letters, Aug 1;588(15):2392-7,* 2014.

[36] Klammt C., Lillemeier BF., "How membrane structures control T cell signaling," *Frontiers in immunology, Sep 21;3:291,* 2012.

[37] Pike LJ., "Rafts defined: a report on the Keystone Symposium on Lipid Rafts and Cell Function," *Journal of lipid research, Jul;47(7):1597-8,* 2006.

[38] Kabeche R., Madrid M., Cansado J., Moseley JB., "Eisosomes Regulate Phosphatidylinositol 4,5-Bisphosphate (PI(4,5)P2) Cortical Clusters and Mitogen-activated Protein (MAP) Kinase Signaling upon Osmotic Stress," *The journal of biological chemistry, Oct 23;290(43):25960-73,* 2015.

[39] Doughty DM., Dieterle M., Sessions AL., Fischer WW., Newman DK., "Probing the subcellular localization of hopanoid lipids in bacteria using NanoSIMS," *PLoS one, Jan 7;9(1):e84455,* 2014.

[40] Ikonen E., "Roles of lipid rafts in membrane transport," *Current opinion in cell biology, Aug;13(4):470-7,* 2001.

[41] Bayburt TH., Sligar SG., "Self-assembly of single integral membrane proteins into soluble nanoscale phospholipid bilayers.," *Protein science: a publication of the Protein Society, Nov;12(11):2476-81.,* 2003.

[42] Kucharska I., Edrington TC., Liang B., Tamm LK., "Optimizing nanodiscs and bicelles for solution NMR studies of two β-barrel membrane proteins," *Journal of biomolecular NMR, Apr;61(3-4):261-74,* 2015.

[43] Brown RE., Brockman HL., "Using monomolecular films to characterize lipid lateral interactions.," *Methods in molecular biology, 398:41-58,* 2007.

[44] Przybylo M., Sykora J., Humpolickova J., Benda A., Zan A., Hof M., "Lipid diffusion in giant unilamellar vesicles is more than 2 times faster than in supported phospholipid bilayers under identical conditions.," *Langmuir, Oct 24;22(22):9096-9.,* 2006.

[45] Hennesthal C., Steinem C., "Pore-Spanning Lipid Bilayers Visualized by Scanning Force Microscopy," *Journal of the American Chemical Society, Aug 122 (33), 8085–8086,* 2000.

[46] Hennesthal C., Drexler J., Steinem C., "Membrane-suspended nanocompartments based on ordered pores in alumina," *Chemphyschem: a European journal of chemical physics and physical chemistry, Oct 18;3(10):885-9,* 2002.

[47] Bordag N., Keller S., "Alpha-helical transmembrane peptides: a "divide and conquer" approach to membrane proteins," *Chemistry and physics of lipids, Jan;163(1):1-26,* 2010.

[48] Larsen J., Hatzakis NS., Stamou D., "Observation of inhomogeneity in the lipid composition of individual nanoscale liposomes," *Journal of the American Chemical Society, Jul 20;133(28):10685-7,* 2011.

[49] Chiantia S., Schwille P., Klymchenko AS., London E., "Asymmetric GUVs prepared by MβCD-mediated lipid exchange: an FCS study," *Biophysical journal, Jan 5;100(1):L1-3,* 2011.

[50] Baumgart T., Hammond AT., Sengupta P., Hess ST., Holowka DA., Baird BA., Webb WW., "Large-scale fluid/fluid phase separation of proteins and lipids in giant plasma membrane vesicles.," *Proceedings of the National Academy of Sciences of the United States of America, Feb 27;104(9):3165-70,* 2007.

[51] "Une vision moléculaire du vivant," Institute de Biologie Structurale, [Online]. Available: http://www.ibs.fr/research/research-groups/dynamics-and-kinetics-of-molecular-processes-group-m-weik/pixel/photophysics-of-fluorescent/.

[52] Miller RG., "The use and abuse of filipin to localize cholesterol in membranes," *Cell biology international reports, Jul;8(7):519-35,* 1984.

[53] Drabikowski W., Lagwinska E., Sarzala MG., "Filipin as a fluorescent probe for the location of cholesterol in the membranes of fragmented sarcoplasmic reticulum," *Biochimica et biophysica acta, Jan 2;291(1):61-70,* 1973.

[54] Šachl R., Boldyrev I., Johansson LB., "Localisation of BODIPY-labelled phosphatidylcholines in lipid bilayers," *Physical chemistry chemical physics: PCCP, Jun 21;12(23):6027-34,* 2010.

[55] Baumgart T., Hunt G., Farkas ER., Webb WW., Feigenson GW., "Fluorescence probe partitioning between Lo/Ld phases in lipid membranes," *Biochimica et biophysica acta, Sep;1768(9):2182-94,* 2007.

[56] Egger MD., Petráň M., "New reflected-light microscope for viewing unstained brain and ganglion cells," *Science, Jul 21;157(3786):305-7,* 1967.

[57] Elson EL., Magde D., "Fluorescence correlation spectroscopy. I. Conceptual basis and theory," *Biopolymers, 13: 1-27,* 1974.

[58] Ries J., Schwille P., "Fluorescence correlation spectroscopy," *BioEssays: news and reviews in molecular, cellular and developmental biology, May;34(5):361-8,* 2012.

[59] Sýkora j., Kaiser K., Gregor I., Bönigk W., Schmalzing G., Enderlein J., "Exploring fluorescence antibunching in solution to determine the stoichiometry of molecular complexes," *Analytical chemistry, Jun 1;79(11):4040-9,* 2007.

[60] Benda A., Beneš M., Mareček V., Lhotský A., Hermens WT., Hof M., "How to determine diffusion coefficients in planar phospholipid systems by confocal fluorescence correlation spectroscopy," *Langmuir, 19, 4120–4126,* 2003.

[61] Becker W., "Principle of Time-Correlated Single Photon Counting," in *The bh TCSPC Handbook, Seventh Edition*, Berlin, Becker & Hickl GmbH, 2017, p. 87.

[62] Förster T., "Zwischenmolekulare Energiewanderung und Fluoreszenz," *Annalen der physik, 2, (1-2), 55-75,* 1948.

[63] Baumann J., Fayer MD., "Excitation transfer in disordered two-dimensional and anisotropic three-dimensional systems: effects of spatial geometry on time-resolved observables," *The journal of chemical physics, 85.7: 4087-4107,* 1986.

[64] Šachl R., Johansson LB., Hof M., "Förster resonance energy transfer (FRET) between heterogeneously distributed probes: application to lipid nanodomains and pores," *International journal of molecular sciences, Nov 30;13(12):16141-56,* 2012.

[65] Jurkiewicz P., Sýkora J., Olzynska A., Humpolíčková J., Hof M., "Solvent relaxation in phospholipid bilayers: principles and recent applications," *Journal of fluorescence, Nov;15(6):883-94,* 2005.

[66] McMurry JE., "Organic Chemistry: With Biological Applications," Cengage Learning, 2010, p. 1016.

[67] Lahlou M., "The Success of Natural Products in Drug Discovery," *Pharmacology & Pharmacy, 4: 17-31,* 2013.

[68] Zotchev SB., "Polyene macrolide antibiotics and their applications in human therapy," *Current medicinal chemistry, Feb;10(3):211-23,* 2003.

[69] Hartsel SC., Benz SK., Ayenew W., Bolard J., "Na+, K+ and Cl- selectivity of the permeability pathways induced through sterol-containing membrane vesicles by amphotericin B and other polyene antibiotics," *European biophysics journal: EBJ, 23(2):125-32.,* 1994.

[70] Cohen BE., "The Role of Signaling via Aqueous Pore Formation in Resistance Responses to Amphotericin B," *Antimicrobial agents and chemotherapy, Aug 22;60(9):5122-9,* 2016.

[71] Coutinho A., Prieto M., "Cooperative partition model of nystatin interaction with phospholipid vesicles.," *Biophysical journal, May;84(5):3061-78.,* 2003.

[72] Lopes SC., Goormaghtigh E., Cabral BJ., Castanho MA., "Filipin orientation revealed by linear dichroism. Implication for a model of action," *Journal of the American Chemical Society, May 5;126(17):5396-402.,* 2004.

[73] Savic M., Bratic I., Vasiljevic B., "Streptomyces durmitorensis sp. nov., a producer of an FK506-like immunosuppressant," *International journal of systematic and evolutionary microbiology, Sep;57(Pt 9):2119-24.,* 2007.

[74] Stodulkova E., Kuzma M., Hench IB., Cerny J., Kralova J., Novak O., Chudickova M., Savic M., Djokic L., Vasiljevic B., Flieger M., "New polyene macrolide family produced by submerged culture of Streptomyces durmitorensis," *Journal of Antibiotics 64: 717-722,* 2011.

[75] Stankovic N., Senerovic L., Bojic-Trbojevic Z., Vuckovic I., Vicovac L., Vasiljevic B., Nikodinovic-Runic J., "Didehydroroflamycoin pentaene macrolide family from Streptomyces durmitorensis MS405(T) : production optimization and antimicrobial activity," *Journal of applied microbiology, Dec;115(6):1297-306,* 2013.

[76] Bolard J., "How do the polyene macrolide antibiotics affect the cellular membrane properties?," *Biochimica et biophysica acta, Dec 22;864(3-4):257-304,* 1986.

[77] Grudzinski W., Sagan J., Welc R., Luchowski R., Gruszecki WI, "Molecular organization, localization and orientation of antifungal antibiotic amphotericin B in a single lipid bilayer," *Scientific reports, Sep 13;6:32780,* 2016.

[78] Grigorjev PA., Bezrukov SM., "Hofmeister effect in ion transport: reversible binding of halide anions to the roflamycoin channel," *Biophysical journal, Dec;67(6):2265-71,* 1994.

[79] Shahmoradi T., Sepehry H., Ashrafpour M., "pH regulation of amphotericin B channels activity in the bilayer lipid membrane," *Journal of natural science, biology, and medicine, Jan-Jun;7(1):85-8,* 2016.

[80] Venegas B., González-Damián J., Celis H., Ortega-Blake I., "Amphotericin B channels in the bacterial membrane: role of sterol and temperature," *Biophysical journal, Oct;85(4):2323-32,* 2003.

[81] Huang W., Zhang Z., Han X., Tang J., Wang J., Dong S., Wang. E, "Ion channel behavior of amphotericin B in sterol-free and cholesterol- or ergosterol-containing supported phosphatidylcholine bilayer model membranes investigated by electrochemistry and spectroscopy," *Biophysical journal, Dec;83(6):3245-55,* 2002.

[82] Cotero BV., Rebolledo-Antúnez S., Ortega-Blake I., "On the role of sterol in the formation of the amphotericin B channel," *Biochimica et biophysica acta, Oct 15;1375(1-2):43-51,* 1998.

[83] Behnke O., Tranum-Jensen J., van Deurs B., "Filipin as a cholesterol probe. II. Filipin-cholesterol interaction in red blood cell membranes," *European journal of cell biology, Nov;35(2):200-15,* 1984.

[84] Holz R., Finkelstein A., "The water and nonelectrolyte permeability induced in thin lipid membranes by the polyene antibiotics nystatin and amphotericin B," *The journal of general physiology, Jul;56(1):125-45,* 1970.

[85] Sosnik A., "Drug self-assembly: A phenomenon at the nanometer scale with major impact in the structure–biological properties relationship and the treatment of disease," *Progress in materials science, Sep 82;39-82.,* 2016.

[86] Gagos M., Koper R., Gruszecki WI., "Spectrophotometric analysis of organisation of dipalmitoylphosphatidylcholine bilayers containing the polyene antibiotic amphotericin B.," *Biochimica et biophysica acta, Mar 9;1511(1):90-8,* 2001.

[87] Wasko P., Luchowski R., Tutaj K., Grudzinski W., Adamkiewicz P., Gruszecki WI., "Toward understanding of toxic side effects of a polyene antibiotic amphotericin B: fluorescence spectroscopy reveals widespread formation of the specific supramolecular structures of the drug.," *Molecular pharmaceutisc, May 7;9(5):1511-20,* 2012.

[88] Neumann A., Wieczor M., Zielinska J., Baginski M., Czub J., "Membrane Sterols Modulate the Binding Mode of Amphotericin B without Affecting Its Affinity for a Lipid Bilayer," *Langmuir, Apr 12;32(14):3452-61,* 2016.

[89] Fa N., Lins L., Courtoy PJ., Dufrene Y., Van Der Smissen P., Brasseur R., Tyteca D., Mingeot-Leclercq MP., "Decrease of elastic moduli of DOPC bilayers induced by a macrolide antibiotic, azithromycin," *Biochimica et biophysica acta, Jul;1768(7):1830-8,* 2007.

[90] Chiantia S., Ries J., Kahya N., Schwille P., "Combined AFM and two-focus SFCS study of raft-exhibiting model membranes," *Chemphyschem: a European journal of chemical physics and physical chemistry, Nov 13;7(11):2409-18,* 2006.

[91] Milhaud J., Mazerski J., Bolard J., Dufourc EJ., "Interaction of filipin with dimyristoylphosphatidylcholine membranes studied by 2H-NMR, circular dichroism, electronic absorption and fluorescence," *European biophysics journal: EBJ, 17(3):151-8,* 1989.

[92] Cheng PC., Brown BK., Song W., Pierce SK., "Translocation of the B cell antigen receptor into lipid rafts reveals a novel step in signaling," *Journal of Immunology, Mar 15;166(6):3693-701,* 2001.

[93] Simons K., Ikonen E., "Functional rafts in cell membranes," *Nature, Jun 5;387(6633):569-72,* 1997.

[94] Brown DA., Rose JK., "Sorting of GPI-anchored proteins to glycolipid-enriched membrane subdomains during transport to the apical cell surface," *Cell, Feb 7;68(3):533-44,* 1992.

[95] Ho CS., Khadka NK., Pan J., "Sub-ten-nanometer heterogeneity of solid supported lipid membranes determined by solution atomic force microscopy," *Biochimica et biophysica acta, Feb;1858(2):181-8,* 2016.

[96] Petruzielo RS., Heberle FA., Drazba P., Katsaras J., Feigenson GW., "Phase behavior and domain size in sphingomyelin-containing lipid bilayers," *Biochimica et biophysica acta, Apr;1828(4):1302-13,* 2013.

[97] Pathak P., London E., "The Effect of Membrane Lipid Composition on the Formation of Lipid Ultrananodomains," *Biophysical journal, Oct 20;109(8):1630-8,* 2015.

[98] Honigmann A., Mueller V., Ta H., Shcoenle A., Sezgin E., Hell SW., Eggeling C., "Scanning STED-FCS reveals spatiotemporal heterogeneity of lipid interaction in the plasma membrane of living cells," *Nature communications, Nov 20;5:5412,* 2014.

[99] Eggeling C., Ringemann C., Medda R., Schwarzmann G., Sandhoff K., Polyakova S., Belov VN., Hein B., von Middendorff C., Schönle A., Hell SW., "Direct observation of the nanoscale dynamics of membrane lipids in a living cell," *Nature, Feb 26;457(7233):1159-62.,* 2009.

[100] Owen DM., Williamson DJ., Magenau A., Gaus K., "Sub-resolution lipid domains exist in the plasma membrane and regulate protein diffusion and distribution," *Nature communications, 3:1256.,* 2012.

[101] Sezgin E., Gutmann T., Buhl T., Dirkx R., Grzybek M., Coskun Ü., Solimena M., Simons K., Levental I., Schwille P., "Adaptive lipid packing and bioactivity in membrane domains," *PloS one, Apr 23;10(4),* 2015.

[102] Šachl R., Humpolíčková J., Štefl M., Johansson LB., Hof M., "Limitations of electronic energy transfer in the determination of lipid nanodomain sizes," *Biophysical journal, Dec 7;101(11):L60-2,* 2011.

[103] Heberle FA., Wu J., Goh SL., Petruzielo RS., Feigenson GW., "Comparison of three ternary lipid bilayer mixtures: FRET and ESR reveal nanodomains," *Biophysical journal, Nov 17;99(10):3309-18,* 2010.

[104] Smith AK., Freed JH., "Determination of tie-line fields for coexisting lipid phases: an ESR study," *The journal of biophysical chemistry, Mar 26;113(12):3957-71,* 2009.

[105] Amaro M., Šachl R., Aydogan G., Mikhalyov II., Vácha R., Hof M., "GM1 Ganglioside Inhibits β-Amyloid Oligomerization Induced by Sphingomyelin," *Angewandte chemie, Aug 1;55(32):9411-5,* 2016.

[106] Ahmed SN., Brown DA., London E., "On the origin of sphingolipid/cholesterol-rich detergent-insoluble cell membranes: physiological concentrations of cholesterol and sphingolipid induce formation of a detergent-insoluble, liquid-ordered lipid phase in model membranes," *Biochemistry, Sep 9;36(36):10944-53,* 1997.

[107] de Almeida RF., Loura LM., Fedorov A., Prieto M., "Lipid rafts have different sizes depending on membrane composition: a time-resolved fluorescence resonance energy transfer study," *Journal of molecular biology, Mar 4;346(4):1109-20,* 2005.

[108] Armstrong CL., Marguardt D., Dies H., Kučerka N., Yamani Z., Harroun TA., Katsaras J., Shi AC., Rheinstädter MC., "The Observation of Highly Ordered Domains in Membranes with Cholesterol," *PLoS One, Jun 18;8(6):e66162,* 2013.

[109] Schütz GJ., Kada G., Pastushenko VP., Schindler H., "Properties of lipid microdomains in a muscle cell membrane visualized by single molecule microscopy," *The EMBO journal, Mar 1;19(5):892-901,* 2000.

[110] Yuan C., Furlong J., Burgos P., Johnston LJ., "The size of lipid rafts: an atomic force microscopy study of ganglioside GM1 domains in sphingomyelin/DOPC/cholesterol membranes," *Biophysical journal, May;82(5):2526-35,* 2002.

[111] Bertoli E., Masserini M., Sonnino S., Ghidoni R., Cestaro B., Tettamanti G., "Electron paramagnetic resonance studies on the fluidity and surface dynamics of egg phosphatidylcholine vesicles containing gangliosides," *Biochimica et biophysica acta, Oct 2;647(2):196-202,* 1981.

[112] Yu RK., Tsai YT., Ariga T., "Functional roles of gangliosides in neurodevelopment: an overview of recent advances," *Neurochemical research, Jun;37(6):1230-44,* 2012.

[113] Yanagisawa K., Odaka A., Suzuki N., Ihara Y., "GM1 ganglioside-bound amyloid beta-protein (A beta): a possible form of preamyloid in Alzheimer's disease," *Nature medicine, Oct;1(10):1062-6,* 1995.

[114] Schneider JS., Cambi F., Gollomp SM., Kuwabara H., Brašic JR., Leiby B., Sendek S., Wong DF., "GM1 ganglioside in Parkinson's disease: Pilot study of effects on dopamine transporter binding," *Journal of the neurological sciences, Sep 15;356(1-2):118-23,* 2015.

[115] Jobling MG., Yang Z., Kam WR., Lencer WI., Holmes RK., "A single native ganglioside GM1-binding site is sufficient for cholera toxin to bind to cells and complete the intoxication pathway," *mBio, Oct 30;3(6),* 2012.

[116] Shi J., Yang T., Kataoka S., Zhang Y., Diaz AJ., Cremer PS., "GM1 clustering inhibits cholera toxin binding in supported phospholipid membranes," *Journal of the American Chemical Society, May 9;129(18):5954-61,* 2007.

[117] Mahfoud R., Manis A., Binnington B., Ackerley C., Lingwood CA., "A major fraction of glycosphingolipids in model and cellular cholesterol-containing membranes is undetectable by their binding proteins," *The Journal of biological chemistry, Nov 12;285(46):36049-59,* 2010.

[118] Sezgin E., Levental I., Grzybek M., Schwarzmann G., Mueller V., Honigmann A., Belov VN., Eggeling C., Coskun U., Simons K., Schwille P., "Partitioning, diffusion, and ligand binding of raft lipid analogs in model and cellular plasma membranes," *Biochimica et biophysica acta, Jul;1818(7):1777-84,* 2012.

[119] Frey SL., Chi EY., Arratia C., Majewski J., Kjaer K., Lee KY., "Condensing and fluidizing effects of ganglioside GM1 on phospholipid films," *Biophysical journal, Apr 15;94(8):3047-64,* 2008.

[120] Lozano MM., Hovis JS., Moss FR 3rd, Boxer SG., "Dynamic Reorganization and Correlation among Lipid Raft Components," *Journal of the American Chemical Society, Aug 10;138(31):9996-10001,* 2016.

[121] Lingwood D., Binnington B., Róg T., Vattulainen I., Grzybek M., Coskun U., Lingwood CA., Simons K., "Cholesterol modulates glycolipid conformation and receptor activity," *Nature chemical biology, May;7(5):260-2,* 2011.

[122] Štefl M., Šachl R., Humpolíčková J., Cebecauer M., Macháň R., Kolářová M., Johansson LB., Hof M., "Dynamics and size of cross-linking-induced lipid nanodomains in model membranes," *Biophysical journal, May 2;102(9):2104-13,* 2012.

[123] Pezeshkian W., Nabo LJ., Ipsen JH., "Cholera toxin B subunit induces local curvature on lipid bilayers," *FEBS open bio, Oct 10;7(11):1638-1645,* 2017.

[124] Suedhof TC., Rothman JE., "Membrane fusion: grappling with SNARE and SM proteins," *Science, Jan 23;323(5913):474-7,* 2009.

[125] Weber T., Zemelman BV., McNew JA., Westermann B., Gmachl M., Parlati F., Söllner TH., Rothmann JE., "SNAREpins: minimal machinery for membrane fusion," *Cell, Mar 20;92(6):759-72,* 1998.

[126] Jahn R., Lang T., Südhof TC., "Membrane fusion," *Cell, Feb 21;112(4):519-33,* 2003.

[127] Jahn R., Fasshauer D., "Molecular machines governing exocytosis of synaptic vesicles," *Nature, Oct 11;490(7419):201-7,* 2012.

[128] Chen YA., Scales SJ., Scheller RH., "Sequential SNARE assembly underlies priming and triggering of exocytosis," *Neuron, Apr;30(1):161-70,* 2001.

[129] Han J., Pluhackova K., Böckmann RA., "The Multifaceted Role of SNARE Proteins in Membrane Fusion," *Frontiers in physiology, Jan 20;8:5,* 2017.

[130] van Lengerich B., Rawle RJ., Bendix PM., Boxer SG., "Individual vesicle fusion events mediated by lipid-anchored DNA," *Biophysical journal, Jul 16;105(2):409-19.,* 2013.

[131] Robson MH., Elbers NA., Bomans PH., Sommerdijk NA., Kros A., "A reduced SNARE model for membrane fusion," *Angewandte Chemie, 48(13):2330-3,* 2009.

[132] Meyenberg K., Lygina AS., van den Bogaart G, Jahn R., Diederichsen U., "SNARE derived peptide mimic inducing membrane fusion," *Chemical communications, Sep 7;47(33):9405-7,* 2011.

[133] Gong Y., Luo Y., Bong D., "Membrane activation: selective vesicle fusion via small molecule recognition," *Journal of the American Chemical Society, Nov 15;128(45):14430-1,* 2006.

[134] Richard A., Marchi-Artzner V., Lalloz MN., Brienne MJ., Artzner F., Gulik-Krzywicki T., Guedeau-Boudeville MA., Lehn MJ., "Fusogenic supramolecular vesicle systems induced by metal ion binding to amphiphilic ligands," *Proceedings of the National Academy of Sciences of the United States of America, Oct 26;101(43):15279-84,* 2004.

[135] Mora NL., Bahreman A., Valkenier H., Li H., Sharp TH., Sheppard DN., Davis AP., Kros A., "Targeted anion transporter delivery by coiled-coil driven membrane fusion," *Chemical Science, Mar 1;7(3):1768-1772,* 2016.

[136] Litowski JR., Hodges RS., "Designing heterodimeric two-stranded alpha-helical coiled-coils. Effects of hydrophobicity and alpha-helical propensity on protein folding, stability, and specificity," *The journal of biological chemistry, Oct 4;277(40):37272-9,* 2002.

[137] Versluis F., Voskuhl J., van Kolck B., Zope H., Bremmer M., Albregtse T., Kros A., "In situ modification of plain liposomes with lipidated coiled coil forming peptides induces membrane fusion," *Journal of the American Chemical Society, May 29;135(21):8057-62,* 2013.

[138] Marsden HR., Korobko AV., van Leeuwen N., Pouget EM., Veen SJ., Sommerdijk NA., Kros A., "Noncovalent triblock copolymers based on a coiled-coil peptide motif," *Journal of the American Chemical Society, Jul 23;130(29):9386-93,* 2008.

[139] Zope HR., Versluis F., Ordas A., Voskuhl J., Spaink JP., Kros A., "In vitro and in vivo supramolecular modification of biomembranes using a lipidated coiled-coil motif," *Angewandte chemie, Dec 23;52(52):14247-51,* 2013.

[140] Yang J., Bahreman A., Daudey G., Bussmann J., Olsthoorn RC., Kros A., "Drug Delivery via Cell Membrane Fusion Using Lipopeptide Modified Liposomes," *ACS central science, Sep 28;2(9):621-630,* 2016.

[141] Robson Marsden H., Korobo VA., Zheng T., Voskuhl J., Kros A., "Controlled liposome fusion mediated by SNARE protein mimics," *Biomaterials Science, 1, 1046,* 2013.

[142] Pähler G., Lorenz B., Janshoff A., "Impact of peptide clustering on unbinding forces in the context of fusion mimetics," *Biochemical and biophysical research communications, Jan 18;430(3):938-43,* 2013.

[143] Rabe M., Schwieger C., Zope HR., Versluis F., Kros A., "Membrane interactions of fusogenic coiled-coil peptides: implications for lipopeptide mediated vesicle fusion," *Langmuir, Jul 8;30(26):7724-35,* 2014.

[144] Marsden HR., Tomatsu I., Kros A., "Model systems for membrane fusion," *Chemical society reviews, Mar;40(3):1572-85,* 2011.

[145] Daudey GA., Zope HR., Voskuhl J., Kros A., Boyle AL., "Membrane-Fusogen Distance Is Critical for Efficient Coiled-Coil-Peptide-Mediated Liposome Fusion," *Langmuir, Oct 31;33(43):12443-12452,* 2017.

[146] Rabe M., Aisenbrey C., Pluhackova K., de Wert V., Boyle AL, Bruggeman DF., Kirsch SA, Bockmann RA., Kros A., Raap J., Bechinger B. , "A Coiled-Coil Peptide Shaping Lipid Bilayers upon Fusion," *Biophysical journal, Nov 15;111(10):2162-2175,* 2016.

[147] Strandberg E., Killian JA., "Snorkeling of lysine side chains in transmembrane helices: how easy can it get?," *FEBS letters, Jun 5;544(1-3):69-73,* 2003.

[148] Mishra MK., Palgunachari MN., "Interaction of model class A1, class A2, and class Y amphipathic helical peptides with membranes," *Biochemistry, Aug 27;35(34):11210-20,* 1996.

[149] Woo SY., Lee H., "All-atom simulations and free-energy calculations of coiled-coil peptides with lipid bilayers: binding strength, structural transition, and effect on lipid dynamics," *Scientific reports, Mar 1;6:22299,* 2016.

[150] Versluis F., Dominquez J., Voskuhl J., Kros A., "Coiled-coil driven membrane fusion: zipper-like vs. non-zipper-like peptide orientation," *Faraday discussions, 166:349-59,* 2013.

[151] Tomatsu I., Marsden HR., Rabe M., Versluis F., Zheng T., Zope H., Kros A., "Influence of pegylation on peptide-mediated liposome fusion," *Journal of materials chemistry, 21, 18927-18933,* 2011.

[152] Jurkiewicz P., Cwiklik L., Jungwirth P., Hof M., "Lipid hydration and mobility: an interplay between fluorescence solvent relaxation experiments and molecular dynamics simulations," *Biochimie, Jan;94(1):26-32,* 2012.

[153] Rabe M., Zope HR., Kros A., "Interplay between Lipid Interaction and Homo-coiling of Membrane-Tethered Coiled-Coil Peptides," *Langmuir, Sep 15;31(36):9953-64,* 2015.

[154] Zheng T., Voskuhl J., Versluis F., Zope HR., Tomatsu I., Marsden HR., Kros A., "Controlling the rate of coiled coil driven membrane fusion," *Chemical communications (Cambridge, England), May 7;49(35):3649-51,* 2013.

[155] Hernandez JM., Stein A., Behrmann E., Riedel D., Cypionka A., Farsi Z., Walla PJ., Raunser S., Jahn R., "Membrane fusion intermediates via directional and full assembly of the SNARE complex," *Science, Jun 22;336(6088):1581-4,* 2012.

[156] Hernandez JM., Kreutzberger AJ., Kiessling V., Tamm LK., Jahn R., "Variable cooperativity in SNARE-mediated membrane fusion," *Proceedings of the National Academy of Sciences of the United States of America, Aug 19;111(33):12037-42,* 2014.

[157] Kreilgaard L., Jones LS., Randolph TW., Frokjaer S., Flink JM., Manning MC., Carpenter JF., "Effect of Tween 20 on freeze-thawing- and agitation-induced aggregation of recombinant human factor XIII," *Journal of pharmaceutical sciences, Dec;87(12):1597-603,* 1998.

[158] Otten D., Brown MF., Beyer K., "Softening of Membrane Bilayers by Detergents Elucidated by Deuterium NMR Spectroscopy," *The Journal of physical chemistry, Nov 104 (51), 12119–29,* 2000.

Appendix: Publications

Membrane activity of the pentaene macrolide didehydroroflamycoin in model lipid bilayers

CrossMark

Membrane activity of the pentaene macrolide didehydroroflamycoin in model lipid bilayers

Alena Koukalová [a,b], Šárka Pokorná [a], Radovan Fišer [b,c], Vladimír Kopecký Jr. [d], Jana Humpolíčková [a,*], Jan Černý [b], Martin Hof [a]

[a] J. Heyrovský Institute of Physical Chemistry, Academy of Sciences of the Czech Republic, v.v.i., Dolejškova 2155/3, 182 23 Prague 8, Czech Republic
[b] Faculty of Science, Charles University in Prague, Albertov 6, 128 43 Prague 2, Czech Republic
[c] Institute of Microbiology, Academy of Sciences of the Czech Republic, v.v.i., Vídeňská 1083, 142 20 Praha 4-Krč, Czech Republic
[d] Institute of Physics, Faculty of Mathematics and Physics, Charles University in Prague, Ke Karlovu 5, 121 16 Prague 2, Czech Republic

ARTICLE INFO

ABSTRACT

Didehydroroflamycoin (DDHR), a recently isolated member of the polyene macrolide family, was shown to have antibacterial and antifungal activity. However, its mechanism of action has not been investigated. Antibiotics from this family are amphiphilic; thus, they have membrane activity, their biological action is localized in the membrane, and the membrane composition and physical properties facilitate the recognition of a particular compound by the target organism. In this work, we use model lipid membranes comprised of giant unilamellar vesicles (GUVs) for a systematic study of the action of DDHR. In parallel, experiments are conducted using filipin III and amphotericin B, other members of the family, and the behavior observed for DDHR is described in the context of that of these two heavily studied compounds. The study shows that DDHR disrupts membranes via two different mechanisms and that the involvement of these mechanisms depends on the presence of cholesterol. The leakage assays performed in GUVs and the conductance measurements using black lipid membranes (BLM) reveal that the pores that develop in the absence of cholesterol are transient and their size is dependent on the DDHR concentration. In contrast, cholesterol promotes the formation of more defined structures that are temporally stable.

© 2014 Elsevier B.V. All rights reserved.

1. Introduction

Polyene macrolides are biologically active metabolites isolated from *Streptomyces* [1]. Due to their antifungal activity, some of them, e.g., amphotericin B (AmB) or nystatin, have been used in human medicine to treat fungal infections for several decades [2]. Their mode of action is assumed to heavily involve biological membranes [3]. Although polyene antibiotics share a similar structure, the mechanism of the interaction with the membrane can substantially differ and cannot be easily predicted. For instance, AmB and nystatin form ion channel pores [3], but the pentaene filipin III acts as a general disruptor through membrane protrusions that arise from altered phase behavior [4–6]. The action of most polyenes strongly depends on the presence of sterols in membranes [7–10]. Furthermore, a target organism can be identified by the sterol composition of its membrane [11], and despite the importance of sterols, the involvement of sterols is not thoroughly understood. Pore formation occurs even in sterol-free bilayers, indicating that sterols merely facilitate the incorporation of antibiotics into the membrane via modulation of the membrane mechanical properties [6,12]. In contrast,

specific interactions of the mycosamine moiety of AmB have been proposed to be crucial for the interaction with ergosterol [13].

In this manuscript, we investigate the membrane interactions of a recently isolated polyene macrolide, 32,33-didehydroroflamycoin (DDHR, Fig. 1) [14]. To date, the only known aspect of its mechanism of action is associated with the dose-dependent hemolysis of red blood cells [15].

In this study, leakage assays were used to study the creation of pores, as well as other membrane formations (buds, non-spherical shape), in well-defined, free-standing model membranes of giant unilamellar vesicles (GUVs). In particular, we focus on the role of cholesterol and its participation in the enhancement/attenuation of membrane disruption. By combining these assays with conductance measurements of black lipids membranes (BLMs), we demonstrate that the pores formed in cholesterol-containing bilayers are defined in size and temporally stable. In contrast, the pores formed in the absence of cholesterol resemble general membrane disruptions, which are transient and whose size depends on the concentration.

Furthermore, we study membranes consisting of coexisting fluid phases and the ability of DDHR to promote these phases in a homogeneous bilayer. Additionally, experiments are also performed using filipin III and AmB (Fig. 1), other members of the polyene macrolide

* Corresponding author. Tel.: +420 266 053 142; fax: +420 286 58 2 307.
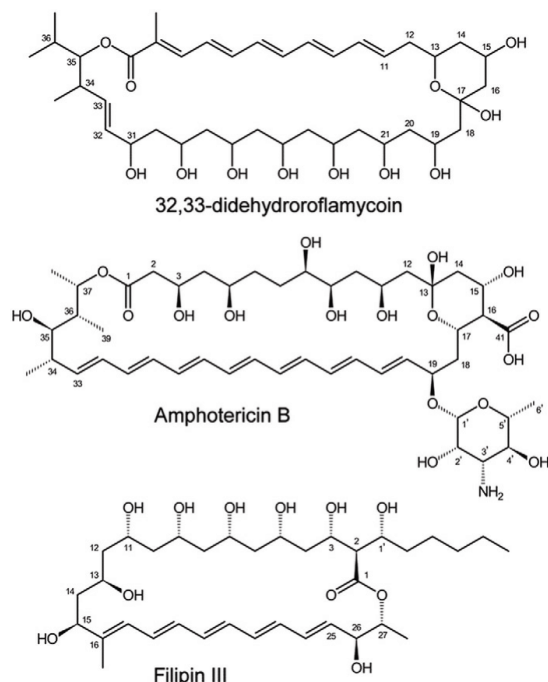E-mail address: jana.humpolickova@jh-inst.cas.cz (J. Humpolíčková).

Fig. 1. Structures of the polyene macrolides 32,33-didehydroflamycoin, amphotericin B and filipin III.

family. The similarities and differences in their action are demonstrated, showing that although cholesterol substantially participates in the action of all the presented antibiotics, its final effect on the fate of a membrane and potentially on the fate of a cell may be very different.

2. Materials and methods

2.1. Extraction of DDHR and other macrolides

Dry DDHR powder was kindly gifted by the Laboratory of Fungal Genetics and Metabolism (Institute of Microbiology, Academy of Sciences of the Czech Republic v.v.i., Prague, Czech Republic). The extraction procedure has been described elsewhere [14]. The dry DDHR powder was kept in the dark at −20 °C. A stock solution of 5 mM DDHR was prepared by dissolving the DDHR powder in methanol. This solution was stored as aliquots at −80 °C and was protected from light. Pure methanol was used as a solvent due to the poor solubility of DDHR in water. Additionally, 5 mM stock solutions of AmB and filipin III were prepared in methanol.

2.2. Solvent and reagents

1,2-Dioleoyl-sn-glycero-3-phosphocholine (DOPC), porcine brain sphingomyelin (Sph) and cholesterol were purchased from Avanti Polar Lipids Inc. (Alabaster, AL). All lipids were used without purification after the phospholipid purity was confirmed using thin-layer chromatography. Stock solutions were prepared in chloroform using standard quantitative techniques. Atto488 was purchased from ATTO-Tec (Siegen, Germany) and prepared as a stock solution in 105 mOsm glucose buffer. DiIC18(5) (DiD), AlexaFluor®488-labeled dextran 3000 and dextran 10 000 were purchased from Life Technologies Corporation

(Carlsbad, CA), and the dextrans were dissolved in 105 mOsm glucose buffer. Filipin III and AmB were purchased from Sigma-Aldrich (St. Louis, MO).

2.3. GUV formation

GUVs were prepared using a modified electroformation method originally developed by Angelova [16]. Lipid mixtures were prepared from stock solutions in chloroform. The total amount of all lipids (100 nmol in approximately 200 μL of chloroform) together with DiD (0.1 mol%) was spread onto two hollowed titanium plates, which were placed on a heater plate at approximately 50 °C to facilitate solvent evaporation, and the mixture was subsequently placed in high vacuum for at least 1 h for evaporation of the remaining solvent traces. The lipid-coated plates were assembled using one layer of Parafilm for insulation [17]. The electroswelling chamber was filled with 1 mL of preheated sucrose solution (100 mM sucrose, osmolarity of 103 mOsm/kg) and sealed with Parafilm. An alternating electrical field of 10 Hz that increased from 0.02 V to 1.1 V (peak-to-peak voltage) during the first 45 min was applied and was then maintained at 1.1 V for an additional 2.5 h at 55 °C; this field was followed by 30 min of 4 Hz and 1.3 V to detach the formed liposomes. Finally, approximately 40 μL of the GUV suspension was placed in a microscopy chamber containing 360 μL of glucose buffer (~80 mM glucose, 10 mM HEPES and 10 mM NaCl, pH 7.2) with an osmolarity of 103 mOsm/kg. The presence of glucose in the final solution allowed the liposomes to sediment and decreased the vesicle movement.

For all the experiments, DDHR, filipin III and AmB were added to the glucose buffer prior the addition of GUVs. For the leakage assays, the glucose buffer also contained Atto488, labeled dextrans or methanol in the desired concentration. The leaking vesicles were counted after 1 h of incubation. All the measurements were performed at room temperature.

Simultaneously with the leakage experiments, control experiments were conducted. Instead of DDHR or the other investigated polyenes, methanol in the same volume as the volume of the polyene solution was added. The maximum methanol volume fraction was 1%. The control GUVs were stable, as shown in Table 1.

2.4. LUV formation

For LUV formation, an appropriate mixture containing 10^{-6} mol of lipids was prepared in chloroform. Chloroform was evaporated using a rotary evaporator, and the lipid film was rehydrated using 1 mL of buffer solution (10 mM HEPES, 150 mM NaCl and 2 mM EDTA, pH 7). A turbid solution containing the multilamellar vesicles was extruded 10 times using 100 nm filters in a LIPEX extruder (Northern Lipids Inc., Canada) [18].

2.5. Absorption/emission spectra

Absorption spectra were measured on a UV2600 UV–VIS spectrophotometer (Shimadzu Corporation, Kyoto, Japan). Emission spectra were monitored using a FluoroLog 3 steady-state fluorescence spectrometer (model FL3-11; Horiba Jobin Yvon Inc., Edison, NJ). DDHR was excited by 370 nm light.

2.6. Confocal microscopy

Confocal microscopy imaging was performed on an FV1000 (Olympus, Hamburg, Germany), and the microscope was equipped with a UPLSAPO 60× W N.A. 1.20 objective lens. Atto488, AlexaFluor®488 and DiD were excited using the 488 and 632 nm laser lines, respectively. DDHR and filipin III was excited by a Coherent Chameleon Vision II titanium:sapphire laser (Coherent, Santa Clara, CA) using multiphoton excitation at 800 and 750 nm, respectively.

Table 1
Percentage of leaking GUVs exposed to three different concentrations of DDHR (mean $\pm$ standard deviation) and the control experiments. The numbers in parenthesis indicate the number of analyzed GUVs/number of independent measurements. The mean values and standard deviations are calculated from subsets of the analyzed GUVs (100 GUVs each).

	10 μM DDHR		30 μM DDHR				50 μM DDHR		Controls			
	DOPC	DOPC/Chol (7/3)	DOPC	POPC	DOPC/Chol (7/3)	DOPC/Sph/Chol (2/2/1)	DOPC	DOPC/Chol (7/3)	DOPC	POPC	DOPC/Chol (7/3)	DOPC/Sph/Chol (2/2/1)
Atto488	12 ± 8 (>600/2)	6 ± 4 (>600/2)	84 ± 13 (>1100/4)	99 ± 1 (>600/1)	42 ± 23 (>1700/5)	56 ± 16 (>300/1)	—	—	11 ± 6 (>2800/9)	8 ± 3 (>600/1)	9 ± 7 (>2600/8)	2 ± 1 (>300/1)
Dextran 3000	—	—	6 ± 5 (>600/2)	—	6 ± 5 (>600/2)	—	78 ± 10 (>300/1)	12 ± 1 (>300/1)	6 ± 4 (>600/2)	—	3 ± 4 (>600/2)	—
Dextran 10 000	—	—	9 ± 5 (>600/2)	—	6 ± 5 (>600/2)	—	87 ± 9 (>300/1)	12 ± 9 (>300/1)	4 ± 2 (>300/1)	—	9 ± 4 (>300/1)	—

2.7. Analysis of confocal images

The obtained images were analyzed both qualitatively and quantitatively. Qualitatively, the characteristic vesicle behavior in the presence of DDHR was assigned to various patterns. This determination was based on a continuous observation of the fluorescence of the components for the first 30 min after the vesicle transfer. The images of the vesicle remained focused at the equatorial plane.

The confocal images and movies were quantitatively analyzed using ImageJ. Vesicles that appeared multilamellar or aggregated and those that had a diameter of less than 10 μm were not analyzed. When the fluorescence intensity of either Atto488 or labeled dextrans inside of the GUVs was greater than 20% of the intensity outside of the GUVs, the GUV was considered a leaking GUV. This choice corresponds to the control experiments, where up to a leaking efficiency of up to 20% was found for majority of GUVs.

2.8. FTIR spectroscopy

Infrared spectra were recorded on a Vector 33 FTIR spectrometer (Bruker Optik GmbH, Ettlingen, Germany) using a standard MIR source, KBr beamsplitter and MCT detector. The spectrometer was purged using dry air. Four thousand scans were collected at a spectral resolution 2 cm^{-1} with a Blackman-Harris 3-term apodization function. The samples were measured at room temperature (20 °C) in a CaF$_2$ cell with an 8-μm path length. The spectral contribution of the buffer was corrected using a standard algorithm [19], and the FTIR spectrum of water vapor was subtracted. The FTIR difference spectrum was calculated in the following manner—the spectrum of DDHR with cholesterol in complex was taken as a reference, and the spectra of the DDHR and cholesterol solution were fit to it together with a polynomial correction (7th grade) of the background. The data processing was performed using GRAMS/AI 9.1 software (Thermo Scientific, Waltham, MA, USA).

Samples were prepared for FTIR by dissolving dry DDHR powder and cholesterol in deionized water containing SDS. The final concentrations in the sample were 40 mM DDHR and cholesterol 80 mM SDS. The mixtures were vortexed well to create proper micelles.

2.9. Electrophysiology

Measurements on planar lipid bilayers (black lipid membranes) were performed in Teflon cells separated by a diaphragm with a circular hole (diameter: 0.5 mm) bearing the membrane. DDHR was added to the grounded *cis* compartment that had a positive potential. The membrane was formed using the painting method with a 3% lipid solution in *n*-decane:butanol (9:1 *v/v*) using soybean phosphatidyl choline alone (type IIS, asolectin; Sigma-Aldrich, St. Louis, MO) or in a mixture with 30% (*w/w*) cholesterol (Sigma-Aldrich, St. Louis, MO). Both compartments contained 2 mL of 10 mM Tris and 1 M KCl at pH 7.4. The membrane current was recorded using Ag/AgCl electrodes (Theta) with salt bridges (applied voltage: 70 mV), amplified using LCA-4k-1G or LCA-200-100G amplifiers (Femto, Berlin, Germany) and digitized using a KPCI-3108 card (Keithly, Cleveland, OH) and BLM2 software

(Assoc. Prof. Jiří Bok, Charles University in Prague, Czech Republic). The signal was processed using a Perl script and QuB software (http://www.qub.buffalo.edu/). The single-channel recordings were electronically filtered using a 30 Hz low-pass filter.

3. Results and discussion

3.1. Spectroscopic properties

The polyene motif in DDHR, as well in most other members of the family, is responsible for the fluorescence of these molecules. The absorption and emission spectra of DDHR in DOPC LUVs are shown in Fig. 2. No significant difference in the absorption/emission spectra were observed between the cholesterol-containing and cholesterol-free LUVs. This result suggests that no cholesterol-induced aggregation of DDHR occurs in the investigated concentration range (up to 50 μM), in contrast to the results for filipin III [20] and Nystatin [21]. The fluorescence signal of DDHR in buffer solution is several orders of magnitudes weaker than its signal in LUVs. This difference probably stems from a high tendency of the amphiphilic molecules to self-aggregate in polar solvents.

When visualizing GUVs containing DDHR, we utilized its fluorescence properties and two-photon excitation for imaging.

3.2. Pore-formation activity of DDHR

The main action of macrolide antibiotics is assumed to occur at the membrane surface and is attributed to the formation of membrane disruptions, specifically pores. Their structural properties may be very different, ranging from the well-defined barrel-shaped structures formed by AmB [22] to the general disruptions formed by filipin III
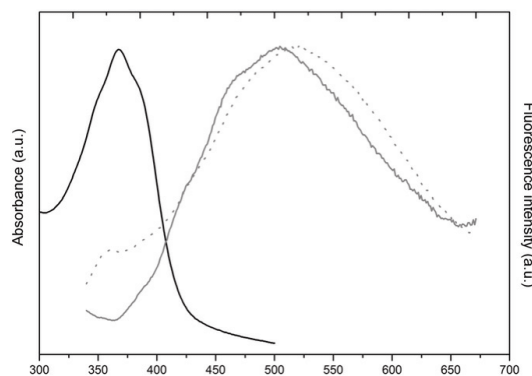

Fig. 2. Absorption (black line) and emission (grey line) spectra of DDHR in DOPC LUVs for concentrations ranging from 10 to 50 μM. The total lipid concentration was 1 mM. The dotted line shows the normalized fluorescence spectra of DDHR in HEPES buffer (very low fluorescence signal).

that have an undefined nature [6]. Because we cannot provide detailed insight into their shapes and sizes, we will concentrate on their actions, as revealed by vesicle leaking. The formation of these pores is generally dependent on the presence of sterols. Our attention therefore mainly focuses on the role of cholesterol in the pore formation at various concentrations of DDHR.

To determine the ability of DDHR to disrupt lipid membranes, we performed a leakage assay that followed the penetration of the fluorescent dye Atto488 and various sizes of labeled dextrans into GUVs composed either of pure DOPC, POPC or DOPC/cholesterol (7:3, mol/mol) upon the addition of DDHR. After the GUVs were treated with DDHR, the percentage of leaking vesicles was counted using confocal microscopy (see Table 1). The percentage of leaking GUVs reflects how prone the membrane is to disruption by the amphiphile.

The results shown in Table 1 allow for the following conclusions: first, at all tested concentrations of DDHR (30–50 μM), the GUVs that consist of pure DOPC or POPC displayed much more leaking than that of the cholesterol-containing GUVs. The leakage assays were also performed for AmB and filipin III (Table 2). The action of filipin III occurred at a much lower concentration than did the actions of DDHR and AmB. At a decreased level of filipin III (10 μM), there was almost no action in the cholesterol-free membranes, whereas the cholesterol-containing GUVs were torn into pieces and not observable any more. The action of AmB confirmed the effect of cholesterol on membrane disruption, as indicated by the elevated number of leaking GUVs in the presence of cholesterol. This finding suggests that for DDHR, cholesterol reduces leaking, in contrast to the results for the other polyene macrolides (AmB, filipin III).

Fig. 3**A** shows the distribution of the leaking efficiency (amount of intrinsic fluorescence with respect to the outside fluorescence) in the analyzed ensemble of GUVs. Both AmB and DDHR can cause leaking in cholesterol-free GUVs (nearly 100%). However, in the cholesterol-containing membranes, the leaking efficiency decreases; for AmB, the effect is only small, if any, and for DDHR, the leaking efficiency drops to 25%. This finding is most likely related to the size of the pores, which prevents the penetration of some fluorescent probes that do not have a suitable orientation when they encounter the membrane pore.

To determine whether the altered leaking properties in the system containing cholesterol can be attributed exclusively to the presence of cholesterol or whether the change arises from the increased membrane rigidity that results from the presence of sterol, we also performed an experiment using POPC GUVs. Table 1 shows that the POPC membrane, which is more ordered than the DOPC membrane [23], displays the same leaking properties as the DOPC membrane. These findings suggest that cholesterol does indeed have a specific role in pore formation.

Table 2
Percentage of leaking GUVs (mean ± standard deviation) for a comparison of the actions of filipin III and AmB with those of DDHR in cholesterol-containing and cholesterol-free GUVs. The numbers in parenthesis stand for the number of analyzed GUVs/number of independent measurements. The mean values and standard deviations are calculated from subsets of analyzed GUVs (100 GUVs each).

	DOPC	DOPC/Chol (7/3)
10 μM filipin	16 ± 5 (>300/1)	Not-measurable
30 μM AmB	44 ± 6 (>300/1)	73 ± 6 (>300/1)
50 μM AmB	76 ± 5 (>300/1)	85 ± 3 (>300/1)
10 μM DDHR	12 ± 8 (>600/2)	6 ± 4 (>600/2)
30 μM DDHR	84 ± 13 (>1100/4)	42 ± 23 (>1700/5)
Controls	11 ± 6 (>2800/9)	9 ± 7 (>2600/8)

Second, the leakage assay was performed at various concentrations of DDHR (10, 30, 50 μM). At the lowest concentration (10 μM), no significant changes in the vesicle leakage were detected compared with that in the control experiments; however, in the solution containing 30 μM DDHR, a large amount of leaking GUVs were found (~90% for pure DOPC membranes). This suggests that a certain threshold concentration must be exceeded for pore formation. Below that concentration (10 μM), DDHR incorporates into the membrane, as indicated by 2-photon microscopy, but the pores are either not created or are smaller than the size of Atto488, the dye that was used.

Third, to determine the size of the pores, we used labeled molecules with different sizes – Atto488-COOH (800 Da), dextran 3 000 (3 kDa) and dextran 10 000 (10 kDa). The results of these experiments are shown in Table 1. Different behaviors are clearly observed for the GUVs containing cholesterol and the cholesterol-free membranes. In pure DOPC, larger dextrans can penetrate the membrane when the DDHR concentration increases; however, in the GUVs containing cholesterol, neither of the two dextrans can pass through the bilayer even at increased levels of DDHR. This finding suggests that the pores formed in the presence of cholesterol have well-defined structures, whereas the pores formed in the cholesterol-free membranes are more general membrane ruptures. Fig. 3C and D shows the distributions of the leaking efficiency for differently large molecules in the cholesterol-free and cholesterol-containing membranes, respectively. The size dependence is nicely illustrated in the 30 μM DDHR system that does not contain cholesterol (Fig. 3C): Atto488 performs almost 100% leaking efficiency, but the 3 kDa dextran molecules are significantly less effective, and the 10 kDa molecules do not penetrate the membrane at all.

3.3. Pore formation observed using conductance measurements

The channel formation caused by DDHR was also examined by measuring the membrane current/conductance in BLMs. In accordance with the leakage assays, the pore formation also strongly depended on the presence of cholesterol. Notably, the stability of the BLMs without cholesterol in the presence of DDHR was already significantly lowered than that of the cholesterol-containing BLMs. The BLMs without cholesterol usually collapsed a few minutes after their creation, whereas with cholesterol the membrane was stable, at least in the time range of tens of minutes, and its conductance far exceeded the level reached in the cholesterol-free membranes. The fast collapses of the cholesterol-free BLMs occur on the same timescale as the budding-fission cycles in GUVs described in the following section; thus, we may attribute these two observations to the same phenomena. Fig. 4 depicts the time evolution of the electric current across the membrane in a pure asolectin bilayer and in an asolectin/cholesterol system. In the former case, individual pores (ion channels) are clearly distinguishable, causing defined current fluctuations when opening and closing (Fig. 5). These channels most likely contribute to the overall leaking observed in GUVs for the cholesterol-free bilayers. In the latter case, the increase in the current is continuous, and the single opening-closing events are not observable even at the initial times. This finding allows us to conclude that pores are formed transiently in the absence of cholesterol, but cholesterol-containing pores are either much smaller or temporally stable or a combination of both. The average pore conductance in the system with no cholesterol is 25 pS, which corresponds to the conductance for pores that are approximately 1 nm in diameter. The leakage assays suggest that the pores in both systems are permeable to the organic fluorophore Atto488 (in the cholesterol-containing membranes, the leaking efficiency is significantly reduced, but leaking still occurs, Fig. 3). Therefore, the cholesterol-containing pores cannot be significantly smaller than 1 nm in diameter; opening and closing events are not observed, which most likely causes the prolonged temporal stability of the pores. This explanation is consistent with the conclusion drawn from the leakage assays that
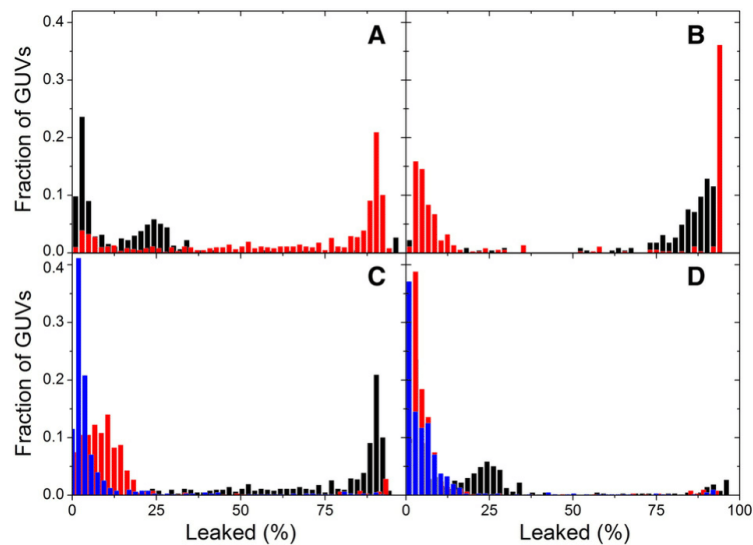
Fig. 3. Distributions of the leaking efficiency among the analyzed GUVs. A,B) Leaking of Atto488 through cholesterol-free membranes (red) and cholesterol-containing membranes (black) caused by A) 30 μM DDHR, and B) 30 μM AmB. C, D) Leaking of molecules of increasing size (Atto488: black, dextran 3 000: red, and dextran 10 000: blue) through DOPC and DOPC/chol membranes, respectively.

suggested the creation of defined complexes between DDHR and cholesterol-containing pores.

In BLMs, cholesterol seems to promote transmembrane ion transport through pores/channels; however, the leakage assays suggest lower leaking efficiency in the cholesterol-containing GUVs. The BLMs lacking cholesterol were much less stable and often ruptured early after the BLM formation. Thus, the conductance was much higher in the cholesterol-containing BLMs than in the cholesterol-free bilayer. As discussed in the following section, an additional leaking mechanism associated with morphological changes of GUVs and follow-up budding/vesicle fission cycles is most likely responsible for the overall greater disruption of the cholesterol-free membranes.

Fig. 4. Typical electrical current recordings showing the membrane conductance induced by 21 μM DDHR in (A) asolectin/cholesterol (7:3, *w/w*) or in (B) asolectin membranes. (C) A control trace without DDHR. The current was recorded at 70 mV in 1 M KCl and 10 mM Tris, pH 7.4.

3.4. DDHR-driven morphological changes of GUVs

At the lowest DDHR concentration, the vesicles did not undergo any deformations; however, in the higher concentration range (30 or 50 μM), the GUVs only remained spherical for a few minutes after their transfer into the measuring chambers. Later, various membrane formations evolved in the cholesterol-free GUVs. Numerous vesicles were not spherical anymore; instead, they became irregularly elongated, asymmetric and not stable in shape (Fig. 6B). However, the most commonly observed formations were groups of small disorganized spheres (Fig. 6A). The process of their formation was directly observable during the experiment. In the beginning, the small spheres were formed as individual buds, followed by their fission from the membrane of the mother GUV. This cycle repeated several times, and as additional smaller spheres evolved, the GUVs leaked more rapidly. This behavior was not observed for either AmB of filipin III.

Morphological changes and sphere formation are often attributed to an asymmetric localization of the amphiphile [24]. When the amphiphile inserts into the outer leaflet, it causes membrane stress. This stress calls for an effective translocation mechanism that allows access to the
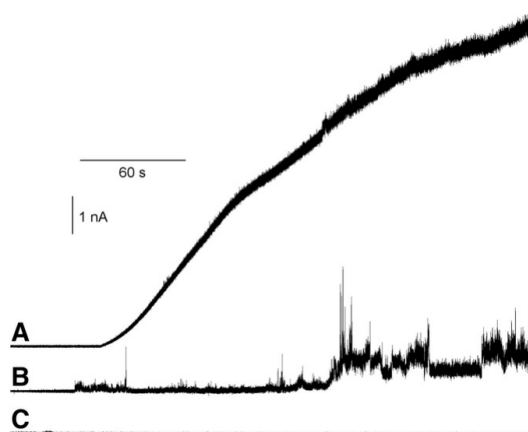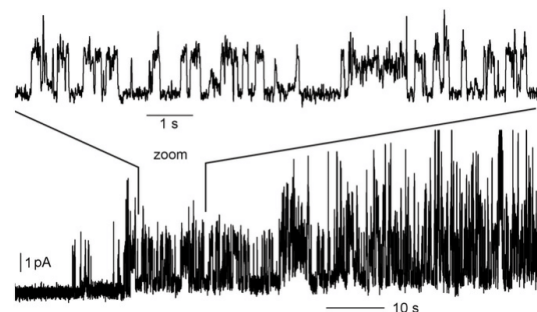

Fig. 5. Representative single-channel recording of 14 μM DDHR in asolectin membranes. The current was recorded at 70 mV in 1 M KCl and 10 mM. The average pore conductance was 25 pS.
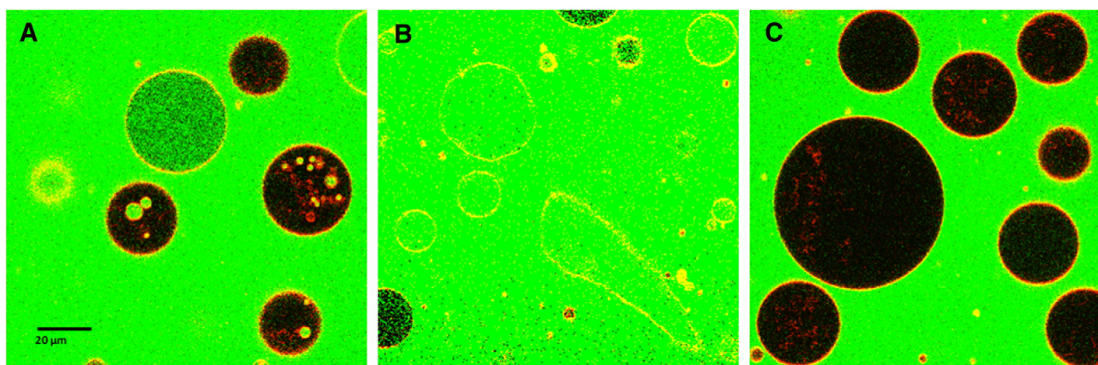
Fig. 6. Effect of DDHR on the shape of GUVs. The figure shows the most common morphological changes of GUVs that occurred at 30 μM DDHR. (A) Groups of small disorganized spheres observable inside the DOPC GUVs. (B) Irregularly elongated and asymmetric GUVs. (C) Stable DOPC/cholesterol GUVs without any significant changes in their shape or the formation of small spheres inside the vesicles. The green color represents the fluorescent probe (Atto488) used for the leakage assays.

inner leaflet. If the translocation is not favorable, spontaneous membrane curvature is established, compensating for the different area requirements of the two leaflets. Shape changes similar to those induced by DDHR have also been reported for azithromycin [25]. The authors showed a significant decrease in the elastic moduli of a DOPC bilayer upon the addition of azithromycin, and this decrease was accompanied by an increased area per DOPC headgroup. Computer modeling provides an explanation: azithromycin is horizontally located at the phospholipid acyl chain/headgroup interface. This results in an expansion of the outer leaflet and a decrease in DOPC–DOPC interactions, followed by the formation of buds. Thus, the observation of increased leaking after budding–fission cycles suggests another effective mechanism for membrane penetration in parallel to the mechanism of pore formation.

The cholesterol-containing GUVs remained stable at all concentrations of DDHR without any significant changes in their shape and the formation of small spheres inside the GUVs (Fig. 6C). Apparently, cholesterol prevents DDHR from imposing membrane curvature because cholesterol most likely provides DDHR with a translocation mechanism. The decreased leaking of cholesterol-containing GUVs upon DDHR treatment can also be attributed to the fact that the cholesterol-mediated stabilization of the bilayer does not allow other methods of membrane penetration except for pore formation, i.e., no leaking during the fission steps. The pores mediated by DDHR are less effective than the pores formed by AmB, which may be related to the ability of the mycosamine moiety to facilitate interactions between AmB and cholesterol [22].

In the cholesterol-containing GUVs, the presence of DDHR does not lead to the morphological changes observed in the DOPC bilayer; however, its action in the simple binary system of DOPC/Chol (7/3) is demonstrated by the phase separation of the bilayer. Fig. 7 shows a complementary pattern of DiD (L_d marker) and DDHR. To understand whether the phenomenon is caused by the generally higher ordering of the membrane or whether it arises from the favorable interaction between DDHR and cholesterol that seems to participate in the formation of pores, we also investigated the DDHR action in a pure POPC bilayer. The POPC bilayer displays a higher level of ordering that is not due to the presence of cholesterol but is due to the higher level of chain saturation. Surprisingly, as shown in Fig. 7, the phase separation also occurred in the POPC bilayer, providing clear evidence that the domains are not formed by a specific interaction with cholesterol but are formed due to the general physical properties of the membrane. Eventually, the morphological formations observed in DOPC GUVs were also observed in the POPC membrane. The extent of the formations was

smaller; we mainly observed the loss of the round shape, and buds were not formed.

For the action of filipin III, a filipin-induced phase separation of cholesterol-containing membranes has been proposed [6] and has been observed using atomic force microscopy [5]. The phase separation of cholesterol-containing DOPC membranes can also be observed using fluorescence measurements in the presence of a much lower concentration (0.3 μM) of filipin III than in the case of the leakage experiments. However, Fig. 7 shows that the formation of DDHR-containing phases (or clusters) is not followed by the complementary changes in the DiD pattern, suggesting that the origin of the DDHR-induced changes differs from that for the filipin III observations, which were reported [26,27] to be driven by an interaction with cholesterol. No separation occurred when the system was treated with AmB.

3.5. Localization of DDHR in membranes

In the previous section, we discussed the involvement of DDHR in pore formation and the specific role of cholesterol. Here, we would like to examine the issue of DDHR partitioning into more rigid L_o lipid areas that are rich in cholesterol. GUVs composed of mixtures of unsaturated phosphatidylcholine, Sph and cholesterol are known for limited lipid miscibility and for phase separation [28].

To identify the preferential localization of DDHR, fluorescence images of DDHR were compared with images of the lipid tracer DiD, which has been shown to prefer the L_d phase [29]. Fig. 7 indicates that the localization of the two fluorescence molecules is complementary. The increased preference for the L_o phase itself is notable. It has been shown that most tail-labeled lipids, as well as organic dye molecules, preferentially segregate to the L_d phase [30]. This separation is attributed to the fact that more organized areas do not accommodate molecules, which would require the loss of the membrane order. The increased L_o partitioning is always attributed to a favorable spatial "matching" or even a specific interaction between the molecules of interest and the constituents of the L_o phase. Therefore, the L_o preference of DDHR, which is a relatively bulky molecule, would imply an interaction between DDHR and cholesterol. In contrast, in the case of AmB and filipin III, it has been proposed that sterols are merely responsible for a modulation of the bilayer properties that allow the bilayer to better accommodate the antibiotics [6,12]. It has to be admitted, however, that the direct interaction with cholesterol remains controversial.

We examined the DDHR distribution between two coexisting liquid phases in GUVs (the L_o and L_d phases) in vesicles made of ternary lipid
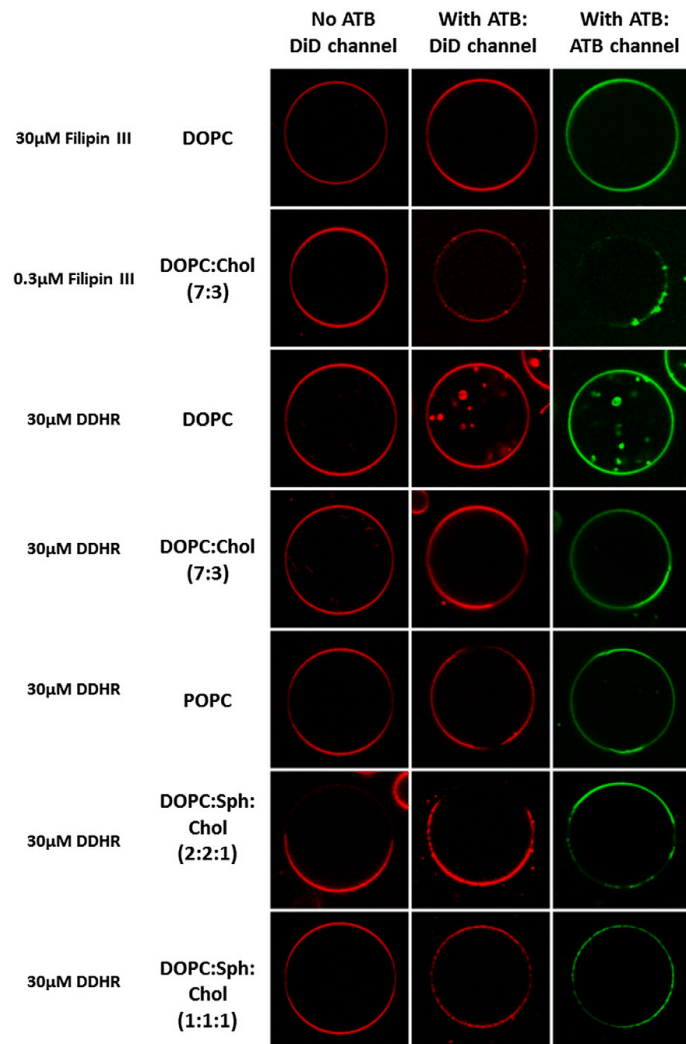
Fig. 7. Equatorial images of GUVs composed of various lipid mixtures. Images before and after the addition of selected antibiotics (ATB). The fluorescence recorded is in red for the DiD channel (L_d marker) and green for the ATB channel. Images of the green and red channels could not be taken simultaneously (the green and red channels are approximately 10 s delayed) due to the microscope setup used; thus, the images may correspond to slightly different z-optical sections and/or be moved in the xy-direction. Incubation time: 10 min.

mixtures (DOPC:Sph:cholesterol) in three different ratios—1:1:1, 1.5:1.5:1 and 2:2:1.

At larger amounts of Sph (the ratios 1.5:1.5:1 and 2:2:1), the GUVs exhibited a clear phase separation represented by the signal of DiD. DDHR localized in the areas without DiD fluorescence and did not appear to affect the size or geometry of the phases.

In GUVs with a lipid composition of 1:1:1 DOPC:Sph:cholesterol, no phase separation was observed before DDHR was added to the system. DiD was equally distributed over the entire surface of the vesicles. The addition of DDHR to the samples promoted the phase separation, and relatively small domains developed (Fig. 7). Thus, DDHR seems to substitute for the lack of Sph and facilitate the formation of the domains. The fact that the domains are small in size and also do not fuse suggests that DDHR stabilizes the domains at the L_d/L_o interface.

It is worth comparing the distribution coefficients of DDHR between the phases with and without Sph (DOPC/cholesterol). The values, which were calculated as the ratio of the mean DDHR fluorescence intensities in the two coexisting phases, are given in Fig. 8. The figure shows that for the larger Sph/cholesterol ratio, the contrast in the DDHR fluorescence between the cholesterol-rich and cholesterol-poor lipid phases is higher than that for the system consisting of only DOPC and cholesterol. This finding indicates that the DDHR localization is driven not only by the presence of sterols but also by the overall membrane properties.

The formation of membrane pores investigated by the leakage assay for the 1:1:1 composition is summarized in Table 1. Obviously, the presence of the L_o phases that recruit the majority of DDHR lowers the amount of leaking GUVs compared with that in the GUVs that are exclusively formed by DOPC.
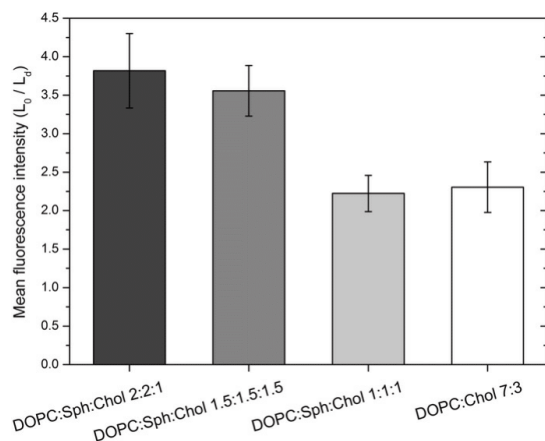
Fig. 8. The graph displays the ratio of mean of the DDHR fluorescence intensities in the coexisting Lo and Ld phases in GUVs with various compositions.

3.6. Interaction between DDHR and cholesterol

The measured FTIR spectra of DDHR in SDS clearly reflect the DDHR structure (Fig. 9) and show infrared bands similar to those of some related molecules, e.g., filipin III [31] or amphotericin B [32]. The DDHR infrared spectrum is dominated by strong bands for CH_2 stretching and CH_2–OH vibrations at approximately 2924 cm^{-1}, carbonyl stretching vibrations at 1707 cm^{-1}, a region of CH_2 and CH_3 bending vibrations at approximately 1437 cm^{-1}, ester vibrations at ~1104 cm^{-1} and stretching vibrations of C–O–C in the pyranose ring at 1030 cm^{-1} (for the detailed band assignment, see Table **S1** in the Supplementary information).

The infrared spectrum after the addition of cholesterol to the buffer containing DDHR and SDS remains dominated by the DDHR spectrum (cf. Fig. 9A and B curves) because the infrared bands of cholesterol are less intense and prominent (Fig. **S1**). The FTIR difference spectrum, after the subtraction of the spectra of the independent components measured at the same conditions, clearly shows interactions between DDHR and cholesterol (Fig. 9C). (An independent subtraction without the baseline modification has been performed using the second derivative, which can identify overlapping components, with similar results—Fig. S2 in the Supplementary information.)

The difference is dominated by changes in the DDHR bands. The most intense changes at 1642 cm^{-1} and 1575 cm^{-1} are associated with stretching C=O and C=C vibrations, respectively. An up-shift at 1276–1293 cm^{-1}, which most likely shows bending OH vibrations, an intensity change in the stretching C–O–C vibrations for the ester group at approximately 1164 cm^{-1} and bending CH vibrations at ca. 996 cm^{-1} are observed. The stretching CH_2 vibrations at 2849 cm^{-1} were downshifted, and the stretching CH_2–OH vibrations at 2927 cm^{-1} were also affected by the binding. However, the interaction led to distinguishable band shifts for the cholesterol molecule. The most prominent cholesterol band at 1468 cm^{-1}, corresponding to bending CH_2 vibrations, and the band of stretching C–C vibrations of the aliphatic chain at 1066 cm^{-1} were shifted to higher wavenumbers.

Considering all these FTIR spectral changes that occur when DDHR interacts with cholesterol in the SDS buffer, we may conclude that cholesterol most likely primarily binds to the ester part of the DDHR molecule, helping the DDHR molecule to organize itself into a more planar and rigid molecule. Nevertheless, subsequent interactions of the more rigid DDHR with other free DDHR molecules cannot be excluded.
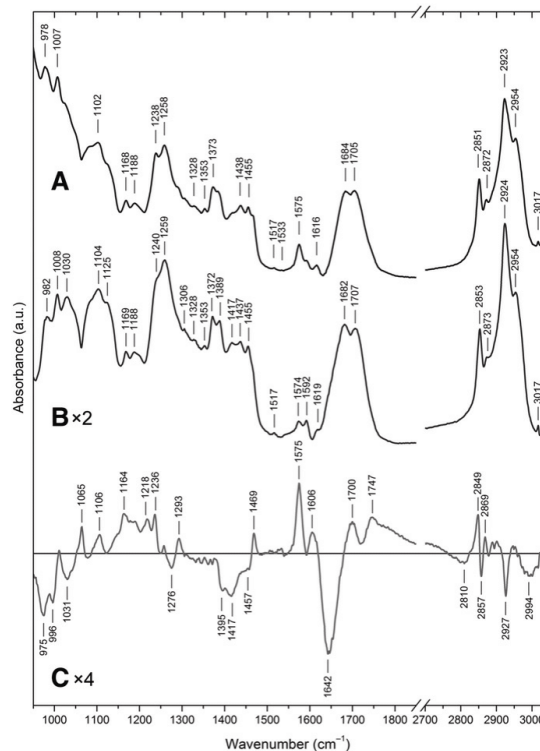

Fig. 9. The FTIR spectra of (A) 40 mM DDHR with 40 mM cholesterol in 80 mM SDS buffer and (B) 40 mM DDHR in 80 mM SDS buffer. (C) The difference of (A) minus (B) and minus the FTIR spectrum of 40 mM cholesterol in 80 mM SDS buffer (Fig. S1 in Supplementary information) and the polynomial fit of a 7th grade. (The zero level is marked for the difference.)

The FTIR experiments require concentrations of the investigated compounds that are more than three orders of magnitude higher than those for the microscopy experiment. Performing these experiments in lipid vesicles with similar lipid-to-cholesterol ratios would not be feasible; therefore, SDS is required to solubilize the compounds. Therefore, the FTIR data cannot prove that DDHR interacts with cholesterol in the biological membrane. These data can, however, indicate what vibrations would most likely participate in that interaction. Our leakage experiments strongly suggest that cholesterol plays a distinct role in the formation of DDHR pores, and this formation may be mediated by the interaction observed in the FTIR measurements.

4. Conclusions

In this work, we have investigated the membrane action of a newly isolated member of the polyene macrolide family, DDHR. In particular, we have focused on its involvement in pore formation, the morphological changes it imposes on model GUV membranes, its partitioning between various fluid lipid phases and its ability to initiate the formation of these phases. In addition, we have studied the role of cholesterol in all the specified issues.

Our leakage assays show that DDHR triggers pore formation independently of the presence of cholesterol. However, the pores only seem to have a distinct size and temporal stability in the cholesterol-containing bilayers. Without cholesterol, the pore size depends on the DDHR concentration, and the pores are transient, as suggested by the

conductance measurements of BLMs. Moreover, the leakage in the absence of cholesterol is also dependent on other leaking mechanisms, as indicated by the budding/fission-associated permeation. Although the formation of buds becomes suppressed in membranes that have higher rigidity irrespective of the presence of cholesterol, the formation of pores has a distinct, cholesterol-specific character.

DDHR preferentially inserts into membrane areas that have higher lipid order, and in addition, the insertion leads to phase separation in membranes with a lipid composition close to the phase separation boundary (DOPC/Sph/Chol 1/1/1). Surprisingly, however, the phase separation also occurs in DOPC/Chol (7/3) and pure POPC membranes. This result demonstrates a highly organizing effect of DDHR that requires a certain degree of membrane rigidity, but this effect is not associated solely with the presence of cholesterol.

Acknowledgments

Appendix A. Supplementary data

Supplementary data to this article can be found online at http://dx. doi.org/10.1016/j.bbamem.2014.10.038.

References

[1] J.F. Aparicio, P. Caffrey, J.A. Gil, S.B. Zotchev, Polyene antibiotic biosynthesis gene clusters, Appl. Microbiol. Biotechnol. 61 (2003) 179–188.
[2] J. Bolard, How do the polyene macrolide antibiotics affect the cellular membrane-properties, Behav. Ecol. Sociobiol. 864 (1986) 257–304.
[3] A. Coutinho, M. Prieto, Cooperative partition model of nystatin interaction with phospholipid vesicles, Biophys. J. 84 (2003) 3061–3078.
[4] J. Milhaud, Permeabilizing action of filipin-III on model membranes through a filipin-phospholipid binding, Behav. Ecol. Sociobiol. 1105 (1992) 307–318.
[5] N.C. Santos, E. Ter-Ovanesyan, J.A. Zasadzinski, M. Prieto, M.A.R.B. Castanho, Filipin-induced lesions in planar phospholipid bilayers imaged by atomic force microscopy, Biophys. J. 75 (1998) 1869–1873.
[6] S.C.D.N. Lopes, E. Goormaghtigh, B.J.C. Cabral, M.A.R.B. Castanho, Filipin orientation revealed by linear dichroism. Implication for a model of action, J. Am. Chem. Soc. 126 (2004) 5396–5402.
[7] D. Gottlieb, H.E. Carter, J.H. Sloneker, A. Ammann, Protection of fungi against polyene antibiotics by sterols, Science 128 (1958) 361-361.
[8] J.O. Lampen, E.R. Morgan, A. Slocum, P. Arnow, Absorption of nystatin by microorganisms, J. Bacteriol. 78 (1959) 282–289.
[9] G. Weissman, G. Sessa, Action of polyene antibiotics on phospholipid-cholesterol structures, J. Biol. Chem. 242 (1967) 616.
[10] Hamilton-Miller J.M., Chemistry and biology of polyene macrolide antibiotics, Bacteriol. Rev. 37 (1973) 166–196.
[11] J.O. Lampen, P.M. Arnow, R.S. Safferman, Mechanism of protection by sterols against polyene antibiotics, J. Bacteriol. 80 (1960) 200–206.
[12] B. Venegas, J. Gonzalez-Damian, H. Celis, I. Ortega-Blake, Amphotericin B channels in the bacterial membrane: role of sterol and temperature, Biophys. J. 85 (2003) 2323–2332.
[13] N. Matsumori, Y. Sawada, M. Murata, Mycosamine orientation of amphotericin B controlling interaction with ergosterol: sterol-dependent activity of conformation-restricted derivatives with an amino-carbonyl bridge, J. Am. Chem. Soc. 127 (2005) 10667–10675.
[14] E. Stodulkova, M. Kuzma, I.B. Hench, J. Cerny, J. Kralova, P. Novak, M. Chudickova, M. Savic, L. Djokic, B. Vasiljevic, M. Flieger, New polyene macrolide family produced by submerged culture of *Streptomyces durmitorensis*, J. Antibiot. 64 (2011) 717–722.
[15] N. Stankovic, L. Senerovic, Z. Bojic-Trbojevic, I. Vuckovic, L. Vicovac, B. Vasiljevic, J. Nikodinovic-Runic, Didehydroroflamycoin pentaene macrolide family from *Streptomyces durmitorensis* MS405(T): production optimization and antimicrobial activity, J. Appl. Microbiol. 115 (2013) 1297–1306.
[16] M.I. Angelova, S. Soleau, P. Meleard, J.F. Faucon, P. Bothorel, Preparation of giant vesicles by external Ac electric-fields—kinetics and applications, Trends Colloid Interf. Sci. VI 89 (1992) 127–131.
[17] V. Weissig, Liposomes: methods and protocols, Biological Membrane Models, vol. 2, Humana Press, New York, 2010.
[18] M.J. Hope, M.B. Bally, L.D. Mayer, A.S. Janoff, P.R. Cullis, Generation of multilamellar and unilamellar phospholipid-vesicles, Chem. Phys. Lipids 40 (1986) 89–107.
[19] F. Dousseau, M. Therrien, M. Pezolet, On the spectral subtraction of water from the Ft-Ir spectra of aqueous-solutions of proteins, Appl. Spectrosc. 43 (1989) 538–542.
[20] M.A.R.B. Castanho, A. Coutinho, M.J.E. Prieto, Absorption and fluorescence-spectra of polyene antibiotics in the presence of cholesterol, J. Biol. Chem. 267 (1992) 204–209.
[21] A. Coutinho, L. Silva, A. Fedorov, M. Prieto, Cholesterol and ergosterol influence nystatin surface aggregation: relation to pore formation, Biophys. J. 87 (2004) 3264–3276.
[22] D.S. Palacios, I. Dailey, D.M. Siebert, B.C. Wilcock, M.D. Burke, Synthesis-enabled functional group deletions reveal key underpinnings of amphotericin B ion channel and antifungal activities, Proc. Natl. Acad. Sci. U. S. A. 108 (2011) 6733–6738.
[23] C.D. Stubbs, T. Kouyama, K. Kinosita, A. Ikegami, Effect of double-bonds on the dynamic properties of the hydrocarbon region of lecithin bilayers, Biochemistry 20 (1981) 4257–4262.
[24] M. Nazari, M. Kurdi, H. Heerklotz, Classifying surfactants with respect to their effect on lipid membrane order, Biophys. J. 102 (2012) 498–506.
[25] N. Fa, L. Lins, P.J. Courtoy, Y. Dufrene, P. Van Der Smissen, R. Brasseur, D. Tyteca, M.P. Mingeot-Leclercq, Decrease of elastic moduli of DOPC bilayers induced by a macrolide antibiotic, azithromycin, Biochim. Biophys. Acta Biomembr. 1768 (2007) 1830–1838.
[26] A.W. Norman, Vandeene Ll, B. Dekruyff, R.A. Demel, Journal of Biological Chemistry, Studies on biological properties of polyene antibiotics—evidence for direct interaction of filipin with cholesterol, J. Biol. Chem. 247 (1972) 1918.
[27] M. Castanho, M. Prieto, Filipin fluorescence quenching by spin-labeled probes—studies in aqueous-solution and in a membrane model system, Biophys. J. 69 (1995) 155–168.
[28] S.L. Veatch, S.L. Keller, Miscibility phase diagrams of giant vesicles containing sphingomyelin, Phys. Rev. Lett. 94 (2005) 148101.
[29] S. Chiantia, J. Ries, N. Kahya, P. Schwille, Combined AFM and two-focus SFCS study of raft-exhibiting model membranes, ChemPhysChem 7 (2006) 2409–2418.
[30] E. Sezgin, I. Levental, M. Grzybek, G. Schwarzmann, V. Mueller, A. Honigmann, V.N. Belov, C. Eggeling, U. Coskun, K. Simons, P. Schwille, Partitioning, diffusion, and ligand binding of raft lipid analogs in model and cellular plasma membranes, Biochim. Biophys. Acta Biomembr. 1818 (2012) 1777–1784.
[31] G.B. Whitfield, T.D. Brock, A. Ammann, D. Gottlieb, H.E. Carter, Filipin, an antifungal antibiotic—isolation and properties, J. Am. Chem. Soc. 77 (1955) 4799–4801.
[32] M. Gagos, M. Arczewska, FTIR spectroscopic study of molecular organization of the antibiotic amphotericin B in aqueous solution and in DPPC lipid monolayers containing the sterols cholesterol and ergosterol, Eur. Biophys. J. Biophys. Lett. 41 (2012) 663–673.
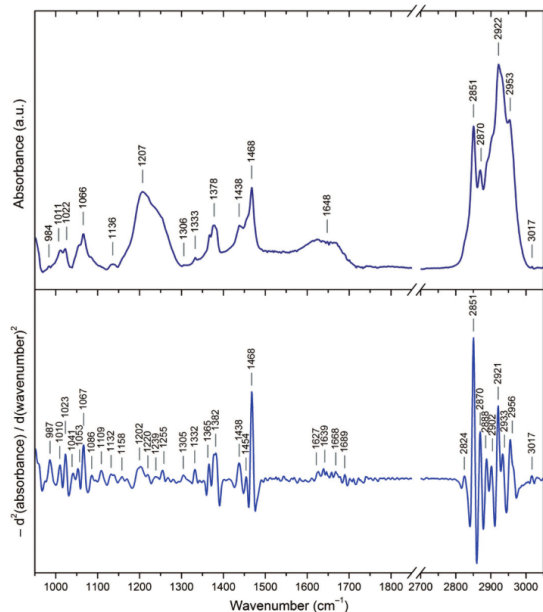
Fig. S1. FTIR absorption spectrum of 40 mM cholesterol in 80 mM SDS buffer (upper) and its negative second derivative (dawn) calculated using Savitzky–Golay smoothing [1] over 15 points (ca. 13 cm⁻¹).

Table S1

Infrared absorption bands identified in the FTIR spectrum of 40 mM DDHR in 80 mM SDS with their estimated assignment according to ref. [2–5].

Wavenumber (cm⁻¹)	Assignment*
982 m	δ(=C–H)
1008 m-s	δ(C–C–H) in plane, δ(–CH) out of plane
1030 m-s, br	ν_{sym}(C–O–C) in pyranose ring
1104 m-s, br	ν_{asym}(C–O)
~1125 m-s, sh	ν(C–O–C) for ester + δ(OH)
1169 m	
1188 m	ν(C–O–C=O)
~1240 s, sh	
1259 s, br	δ(–CH₂)
1306 m	δ(OH)
1328 m	δ(CH₃) + δ(OH)
1353 m	
1372 m	δ_{sym}(CH₂)
1389 m	δ_{sym}(CH₂)
1417 m	δ_{sym}(CH₃)
1437 m	δ_{asym}(CH₃, CH₃)
1455 m	δ_{asym}(CH₂, CH₃)
1517 vw	
1574 w	ν(C=C)
1592 w	ν(C=C)
1619 w	ν(C=C)
1682 m	ν_{asym}(C=O) for ester
1707 m	ν_{asym}(C=O) for ester
2853 m	ν_{sym}(CH₂, CH₃) + ν(CH) in polyene
2873 m	ν_{sym}(CH₂, CH₃) + ν(CH) in polyene
2924 vs	ν_{asym}(CH₂) + ν_{sym}(CH₂–OH)
2954 s	ν_{asym}(CH₂) + ν_{asym}(CH₂–OH)
3017 w	

* ν, stretching mode; δ, bending mode; *sym*, symmetric vibrations; *asym*, asymmetric vibrations; *br*, broad band; *sh*, shoulder; *vs*, *s*, *m-s*, *m*, *m-w*, *w*, *vw*, very strong, strong, medium to strong, medium, medium to weak, weak, very weak, respectively (according to ref. [6]).
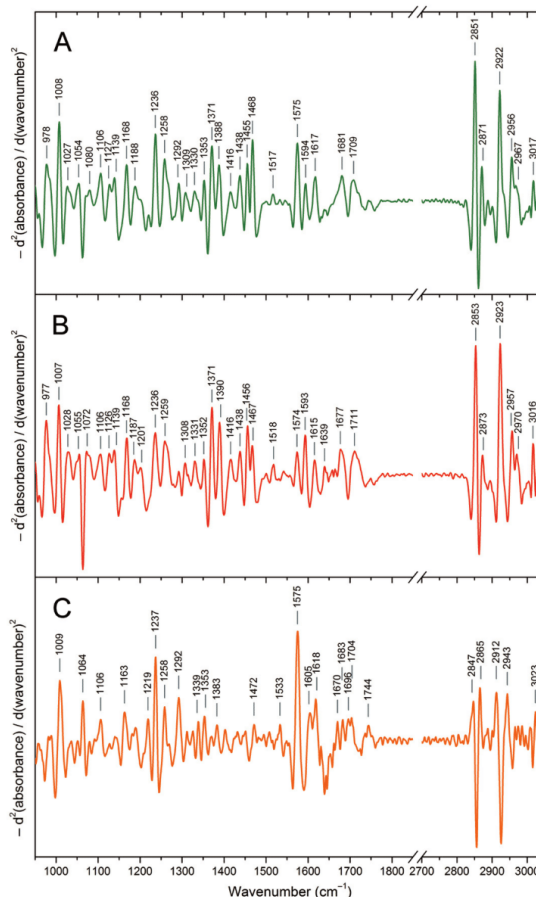

Fig. S2. The negative second derivatives of (A) FTIR spectrum of 40 mM DDHR with 40 mM cholesterol in 80 mM SDS buffer, (B) FTIR spectrum of 40 mM DDHR in 80 mM SDS buffer. (C) represents the difference of second derivatives (A) minus (B) and minus the second derivative of 40 mM cholesterol in 80 mM SDS buffer (see Fig. S1). The second derivatives were calculated using Savitzky–Golay smoothing [1] over 15 points (ca. 13 cm⁻¹).

References

[1] A. Savitzky, M. J. E. Golay, Smoothing and differentiation of data by simplified least squares procedures, Anal. Chem. 36 (1964) 1627–1639.

[2] G. Socrates, Infrared and Raman Characteristics Group Frequencies. Wiley, Chichester 2006, 3rd edition.

[3] M. Garoś, M. Arczewska, Spectroscopic studies of molecular organization of antibiotic amphotericin B in monolayers and dipalmitoylphosphatidylcholine lipid multibilayers. Biochim. Biophys. Acta 1798 (2010) 2124–2130.

[4] M. Garoś, M. Arczewska, Influence of K⁺ and Na⁺ ions on the aggregation processes of antibiotic amphotericin B: electronic absorption and FTIR spectroscopic studies. 34 (1995) 5440–5451. J. Phys. Chem. B 115 (2011) 3185–3192.

[5] M. Garoś, M. Arczewska, FTIR spectroscopic study of molecular organization of the antibiotic amphotericin B in aqueous solution and in DPPC lipid monolayers containing the sterols cholesterol and ergosterol. Eur. Biophys. J. 41 (2012) 663–673.

[6] P. Vandenabeele, L. Moeans, Some ideas on the definition of Raman spectroscopic detection limits for the analysis of art and archaeological objects. J. Raman Spectrosc. 43 (2012) 1545–1550.

Lipid Driven Nanodomains in Giant Lipid Vesicles are Fluid and Disordered

SCIENTIFIC REP⚙RTS

OPEN

Lipid Driven Nanodomains in Giant Lipid Vesicles are Fluid and Disordered

Alena Koukalová[1], Mariana Amaro [1], Gokcan Aydogan[1], Gerhard Gröbner[2], Philip T. F. Williamson [3], Ilya Mikhalyov[4], Martin Hof [1] & Radek Šachl[1]

It is a fundamental question in cell biology and biophysics whether sphingomyelin (SM)- and cholesterol (Chol)- driven nanodomains exist in living cells and in model membranes. Biophysical studies on model membranes revealed SM and Chol driven micrometer-sized liquid-ordered domains. Although the existence of such microdomains has not been proven for the plasma membrane, such lipid mixtures have been often used as a model system for 'rafts'. On the other hand, recent super resolution and single molecule results indicate that the plasma membrane might organize into nanocompartments. However, due to the limited resolution of those techniques their unambiguous characterization is still missing. In this work, a novel combination of Förster resonance energy transfer and Monte Carlo simulations (MC-FRET) identifies directly 10 nm large nanodomains in liquid-disordered model membranes composed of lipid mixtures containing SM and Chol. Combining MC-FRET with solid-state wide-line and high resolution magic angle spinning NMR as well as with fluorescence correlation spectroscopy we demonstrate that these nanodomains containing hundreds of lipid molecules are fluid and disordered. In terms of their size, fluidity, order and lifetime these nanodomains may represent a relevant model system for cellular membranes and are closely related to nanocompartments suggested to exist in cellular membranes.

The original definition of rafts as sphingomyelin (SM)- and cholesterol (Chol)-enriched platforms in cellular plasma membranes emerged over 20 years ago[1]. The postulation of such heterogeneities found support in experiments where detergent resistant membranes biochemically isolated from cells were shown to be enriched in SM and Chol[1,2]. This was supported by biophysical studies on model membranes (i.e. giant unilamellar vesicles; GUVs) composed of SM, Chol and phosphatidylcholine which revealed micrometer-sized liquid-ordered (L_o) domains. Recently, another valuable model membrane system was developed and characterised. The so-called giant plasma membrane vesicles (GPMVs) are formed directly from cells and thus the formed membrane contains multiple essential components of the cellular plasma membrane[3]. Interestingly, fluorescence experiments performed on those GPMVs indicated that physicochemical properties of the cell-derived membranes differ significantly from those with synthetic lipid composition[4,5]. The micrometer-sized ordered phase of GPMVs seems less ordered than L_o phase of GUVs and in analogy to that the disordered phase of cell-derived membranes is more ordered than L_d phase of GUVs[6]. This suggests that differences between domain and non-domain parts of biological membranes are rather subtle and not so extreme as between L_o and L_d phase of GUVs formed from synthetic lipids.

The search for L_o phase domains in cellular plasma membranes was brought by an attempt to draw analogies between the SM and Chol enriched microdomains and the postulated plasma membrane rafts. Experiments using super-resolution fluorescence imaging techniques[7,8] or indirect approaches using polarity sensitive probes[9–11] suggest that heterogeneity of cellular plasma membranes exists. However, those heterogeneities seem to occur on the nano- rather than on the micro-scale[7,9,12,13]. The failure to directly detect domains in cellular membranes by super-resolution fluorescence imaging techniques with a resolution of about 40 nm[7,8] and the recent results

[1]Department of Biophysical Chemistry, J. Heyrovský Institute of Physical Chemistry of the A.S.C.R. v.v.i., Prague, Czech Republic. [2]Department of Chemistry, University of Umeå, SE-901 87, Umeå, Sweden. [3]Centre for Biological Sciences/Institute for Life Sciences, University of Southampton, Southampton, SO17 1BJ, United Kingdom. [4]Shemyakin-Ovchinnikov Institute of Bioorganic Chemistry of the Russian Academy of Science, Moscow, GSP-7, Russian Federation. Alena Koukalová and Mariana Amaro contributed equally to this work. Correspondence and requests for materials should be addressed to R.Š. (email: radek.sachl@jh-inst.cas.cz)
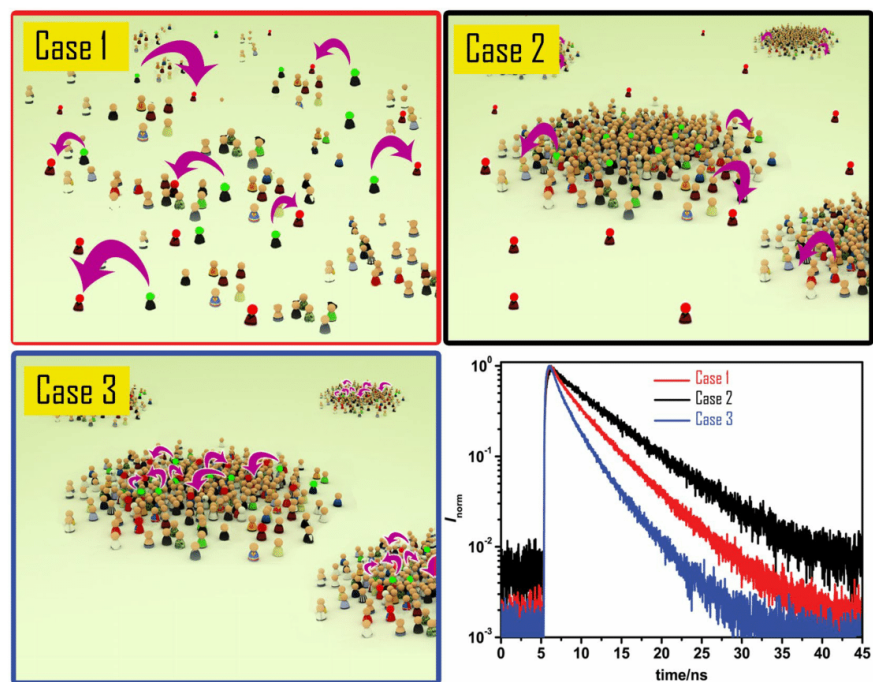
Figure 1. Figure depicting the basic principles underlining the detection of domains by FRET. When donors (green) and acceptors (red) are homogeneously distributed on a plane at sufficiently high acceptor concentration (Case 1) FRET occurs and speeds up the relaxation of the donors back to the ground state. If formation of domains influences the distribution of probes, i.e. when the probes possess different affinity for the domains and the remaining part of the bilayer, two scenarios are possible: Case 2 where the donors accumulate in the domains and acceptors are excluded from them leading to separation of the donors from the acceptors and thus to a decrease in the FRET efficiency and consequently to slower relaxation to the ground state (compare the black with the red decay in the bottom right corner); Case 3 where the accumulation of the donors and acceptors in the nanodomains results in more efficient FRET and consequently to faster relaxation to the ground state (compare the blue with the red decay in the bottom right corner). Bottom right: Examples of the fluorescence decays of the donors in each case. The decays are influenced by the size of the domains, the fractional area occupied by the domains and by the affinity of the probes for the domains; the readouts which can be determined by fitting the experimental decays by using MC-FRET method.

concerning properties of biological membranes question the biological relevance of the L_o phase microdomains found in model membranes. The assumption that experiments on model membranes can reveal biologically relevant information leads us to two central questions: firstly, can lipid driven domains in model membranes be smaller than 40 nm and secondly if so, do such nanodomains have a L_o character?

In this work we used MC-FRET in combination with novel monosialoganglioside GM_1 fluorescent probes to uncover the existence of nanodomains in lipid bilayers that should be in a homogeneous liquid disordered (L_d) phase according to published phase diagrams[14, 15]. FRET has been frequently used in the past to reveal micro- to nano-scale heterogeneities in lipid membranes[16–18] but mostly on a qualitative level. Combination of FRET with MC simulations enabled us quantifying the sizes of domains down to a few nanometers and the fractional area occupied by these domains. To assess the fluidity and phase of the nanodomains we employed solid state wide-line and high resolution MAS (magic angle spinning) NMR spectroscopy, two-color z-scan fluorescence correlation spectroscopy (FCS)[19] and FRET.

Determination of nanodomain size and fractional bilayer area by MC-FRET.

Description of the MC-FRET approach. FRET between a single donor and a single acceptor occurs at distances between 1 to 10 nm and can be used as a molecular ruler within this accessible range. The situation is different when FRET occurs in a lipid bilayer that contains nanodomains and an ensemble of heterogeneously distributed donors and acceptors. Here, the formation of nanodomain structures forces a homogeneous distribution of donors and acceptors (Fig. 1, case 1) into a heterogeneous one (Fig. 1, cases 2 and 3) when using appropriate fluorescent probes that possess either an increased or decreased affinity for such nanodomains. This causes a change

DOPC (mol%)	SM (mol%)	Chol (mol%)	Domain radius (nm)	Domain area (%)	FRET pair	$K_D(D)$**	$K_D(A)$**	E_{rel}***
100, 75, 70	0	0, 25, 30	Homogeneous distrib.		g-GM$_1$/r-GM$_1$	-----*	-----*	1.00
95, 92	5, 8	0	Homogeneous distrib.		g-GM$_1$/r-GM$_1$	-----*	-----*	1.00
90, 88, 85	10, 12, 15	0	8 ± 1	37 ± 10	g-GM$_1$/r-GM$_1$	≈ 10	≈ 10	1.03
			12 ± 3	55 ± 10				
95, 92, 90, 88	5, 8, 10, 12	0	Homogeneous distrib.		CF-PEG-DSPE/Rh-PEG-DSPE	≈ 1	≈ 1	1.00
70, 67, 65	5, 8, 10	25	9 ± 1	45 ± 5	g-GM$_1$/r-GM$_1$	≥ 20	≥ 20	1.12
63	12	25	Homogeneous distrib.		g-GM$_1$/r-GM$_1$	-----*	-----*	1.00
70, 67	5, 8	25	Homogeneous distrib.		CF-PEG-DSPE/Rh-PEG-DSPE	≈ 1	≈ 1	1.00
65, 63	10, 12	25	8 ± 1	55 ± 5	CF-PEG-DSPE/Rh-PEG-DSPE	≈ 5	≈ 5	1.10
60	10	30	9 ± 1	45 ± 5	g-GM$_1$/r-GM$_1$	≥ 20	≥ 20	1.12

Table 1. The average radius and fractional bilayer area of the nanodomains, distribution constants K_D and relative FRET efficiencies E_{rel} (for definition see Materials and Method section) for two different donor-acceptor pairs in DOPC/SM and DOPC/Chol/SM mixtures. All lipid mixtures that are given in the same row provided overlapping fluorescence decays. For this reason, the same values are determined for these parameters in the mentioned bilayers. The output parameters were determined by MC-FRET. The total amount of D/A molecules was 1 mol% at max. *no nanodomains detected at the given bilayer compositions; **as determined by MC-FRET; ***the estimated error in Erel was below 1%.

Donor	K_D for L$_o$ micro domains*	Acceptor	K_D for L$_o$ micro domains*	Implications for FRET in the presence of L$_d$ nanodomains	Implications for FRET in the presence of L$_o$ nanodomains
g-GM$_1$	2.5 ± 0.28	r-GM$_1$	1.6 ± 0.63	Increased**,***	Slightly increased**,***
CF-PEG-DSPE	1.5 ± 0.54	Rh-PEG-DSPE	3.5 ± 0.90	Slightly increased**,***	Slightly increased**,***
g-GM$_1$	2.5 ± 0.28	DiD	0.1 ± 0.01	No change**	Decreased**
Atto 488-DOPE	0.29 ± 0.115	Atto 633-DOPE	0.03 ± 0.013	No change**	Increased**

Table 2. Distribution constants K_D of probes for L$_o$ microdomains and implications for FRET in the presence of L$_d$ or L$_o$ domains. Note that K_D for L$_d$ nanodomains are shown in Table 1. *Determined by intensity measurements (see SI) in L$_d$/L$_o$ phase separated bilayers of DOPC/Chol/SM (55/25/20); **as compared to FRET obtained in a homogeneous bilayer; ***this conclusion is drawn based on K_Ds given in Table 1.

in FRET efficiency that can be seen in the recorded fluorescence decays (Fig. 1, bottom right corner). In these cases, the range of accessible distances (domain radii) that can be determined is significantly broader (2–50 nm)[20] and lies exactly in the region where other techniques become less efficient. The remarkably broad range of accessible distances is a consequence of FRET that occurs at the boundary of the nanodomains and of the fact that the length of that boundary depends on the nanodomain radius R_D. The entire process of energy transfer can be modeled using MC simulations under certain assumptions (see Materials and Methods for details). The simulated decay curves were fitted to the experimental data by varying the radius of the nanodomains R_D, the fractional bilayer area occupied by the nanodomains Ar (which is proportional to nanodomain concentration c_D by $c_D = Ar/(\pi R_D)$) and the distribution constants of donors $K_D(D)$ and acceptors $K_D(A)$ (defined as $K_D(D) = [D_{inside}]/[D_{outside}]$, $K_D(A) = [A_{inside}]/[A_{outside}]$).

MC-FRET can detect various kinds of membrane heterogeneities, such as domains or pores[21, 22]. However, its resolution significantly depends on both $K_D(D)$ and $K_D(A)$. If the probes possess equal affinity for the nanodomains and the remaining bilayer, then the formation of heterogeneities in a bilayer will not induce a heterogeneous probe distribution and therefore no change in FRET efficiency will occur. Consequently, such heterogeneities will not be 'seen' by FRET and the selected probes. Thus, Donor/Acceptor (D/A) pairs with suitable K_D have to be chosen. Based on literature[23] and our previous work[24, 25] we used two different D/A pairs for the detection of lipid driven nanodomains. The first one consisted of ganglioside GM$_1$ molecules labeled at the headgroup with either FL-BODIPY (g-GM$_1$) or 564/570-BODIPY (r-GM$_1$). Both g-GM$_1$ and r-GM$_1$ show increased affinity for the L$_o$ microdomains but also to less ordered fluid nanodomains (refs 24 and 25 and as shown on Table 1 and Table 2). Importantly, these GM$_1$ probes do not intrinsically self-aggregate at the concentrations used in the FRET experiments (see SI and ref. 26). The second D/A pair consisted of 1,2-distearoyl-sn-glycero-3-phosphoethanolamine-N-[amino (Polyethyleneglycol) 2000] labeled at the end of the Polyethyleneglycol chain with either carboxyfluorescein (CF-PEG-DSPE) or Rhodamine101 (Rh-PEG-DSPE). PEG-DSPE lipids were shown to have increased affinity for the L$_o$ phase[23], which is confirmed by this work (Table 2). In addition, here we demonstrate that these probes preferentially partition to the nanodomains that are rich in Chol and SM but still maintain their liquid-disordered character.

Nanodomains outside the L$_d$/gel phase coexistence region in DOPC/SM. These mixtures phase-separate at 23 mol% of SM (L$_d$ + gel phase coexistence) and are fully converted into the gel phase at 81 mol% of SM at room
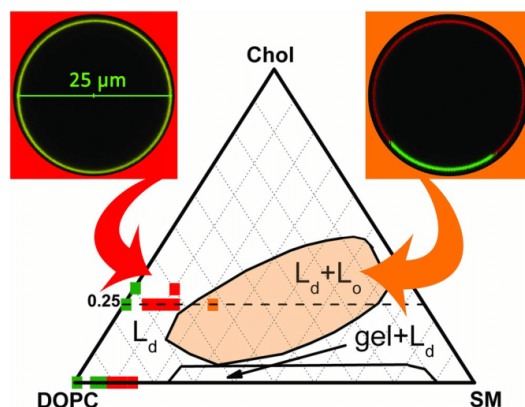
Figure 2. The DOPC/Chol/SM ternary phase diagram. The boundaries for the L_d/L_o and gel/L_d regions of phase coexistence were taken from refs 14 and 15. Selected points mark the compositions at which homogeneous bilayers (green squares), bilayers with liquid-disordered (L_d) nanodomains (red squares) or with microscopic liquid-ordered (L_o) phase domains (orange square) were found. The fluorescent microscopy images at the top show the apparent homogeneous nature of the bilayers containing nanodomains and the microscopic heterogeneity of mixtures in the L_d/L_o phase coexistence region. The images were obtained by using g-GM_1 (green) and DiD (red) probes. The details concerning microscope setup are described in the Materials and Method section.
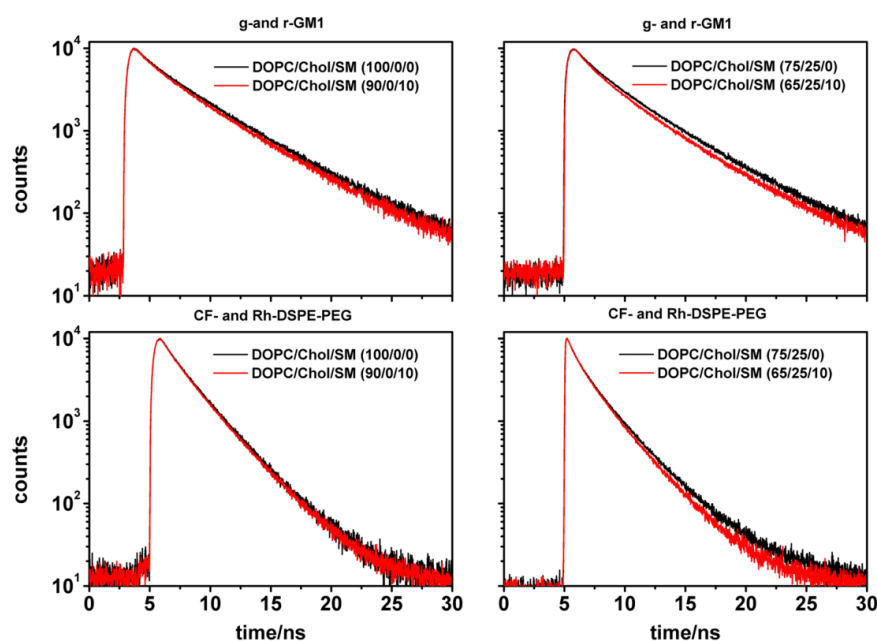

Figure 3. Experimental time-resolved fluorescence decays of the donor for the two D/A pairs and selected lipid mixtures with and without nanodomains (red and black fluorescence decays, respectively).

temperature (Fig. 2)[27, 28]. To detect and characterize nanodomains in this binary system we performed MC-FRET experiments in the range 0–15 mol% of SM with g-GM_1/r-GM_1 and CF-PEG-DSPE/Rh-PEG-DSPE D/A pairs. All bilayers appeared homogeneous in confocal images (see an example in Fig. 2). MC-FRET results obtained using g-GM_1/r-GM_1 D/A pair indicated that the bilayers were homogeneous at DOPC/SM (100–92/0–8), while at (90–85/10–15) we were able to detect nanodomains (Table 1). The presence of nanodomains is reflected in an enhanced relative FRET efficiency (see Table 1 for results and Materials and Methods for definition) and a faster

fluorescence decay of the donor g-GM$_1$ in the presence of r-GM$_1$ (compare the two decays in the top left panel of Fig. 3). Determination of average domain radius yielded two global minima at $R_D = (8 \pm 1)$ nm, $Ar = (37 \pm 10)$ % and $R_D = (12 \pm 3)$ nm, $Ar = (55 \pm 10)$ %. The best fit was obtained for $K_D = 10$, showing a high affinity of the GM$_1$ probes for the domains. In contrast, the distribution of the CF-PEG-DSPE/Rh-PEG-DSPE D/A pair in the bilayer was not affected by the presence of nanodomains ($K_D(D,A) = 1$), which did not allow for the detection of nanodomains by means of this D/A pair (see Table 1 and overlapping decays in the bottom left panel of Fig. 3).

It is worth noting that binary DOPC/Chol mixtures exhibit different behavior. We showed previously that lipid mixtures of DOPC/Chol (65/35) were homogeneous as determined by FRET[24]. Transient nanodomains were found for this binary mixture only close to the phase separation boundary by other methods[29, 30] where miscibility of Chol with DOPC is low[28] and Chol starts to phase-separate into anhydrous and monohydrate crystals[31].

Nanodomains outside the L_d/L_o phase coexistence region in DOPC/Chol/SM.   Addition of 25 mol% of Chol to the DOPC/SM bilayers promoted the formation of nanodomains. Here nanodomains were detected at DOPC/Chol/SM (70–65/25/5–10) by g-GM$_1$/r-GM$_1$ D/A pair. The enhanced relative FRET efficiency as compared to the homogeneous DOPC/Chol/SM (75/25/0) bilayer and the time resolved fluorescence decays of the donor g-GM$_1$ can be seen in Table 1 and Fig. 3, respectively. Determination of domain sizes by MC-FRET yielded an average R_D (9 ± 1) nm and $Ar = (45 \pm 5)$ %. Deep chi-squared minima were only reached when $K_D(D)$ and $K_D(A)$ were at least 20, demonstrating that the GM$_1$ probes were highly localized in the nanodomains (see Fig. SI4). Moreover, the nanodomains were also detected by the CF-PEG-DSPE/Rh-PEG-DSPE DA pair at DOPC/Chol/SM (65/25/10) and (63/25/12) (Table 1 and Fig. 3). The affinity of the PEG-DSPE probes for the domains was lower ($K_D(D)$ and $K_D(A) \approx 5$), but sufficient to cause a change in the relative FRET efficiency and enable the determination of domain sizes at the higher SM amounts. The determined average $R_D = (8 \pm 1)$ nm and $Ar = (55 \pm 5)$ % are in good agreement with the parameters determined using the g-GM$_1$/r-GM$_1$ pair.

Supportive evidence for nanodomain existence by z-scan FCS.   Our FRET measurements indicate that the nanodomains occupy up to 55% of the entire bilayer area in binary DOPC/SM as well as ternary DOPC/Chol/SM lipid mixtures and exhibit an average radius of approximately 10 nm. According to our previous work focusing on MC simulations of molecular probe diffusion in a lipid bilayer[32], the presence of stable (ca. >10 ms) nanodomains at such high domain concentration slows down the diffusion of fluorescently labeled lipids (=probes, Fig. 4). The extent to which the diffusion of the probes is slowed down depends in particular on their K_D, the size of the nanodomains, the diffusion coefficient of the nanodomains themselves D (nanodomain), and the diffusion coefficient of the probes within those nanodomains D (probe). The strongest impact on probe diffusion occurs when the nanodomains are immobile and the probes have high affinity for them. When using classical FCS (where the focal waist is much larger than the nanodomains, about 300 nm vs. 10 nm) the presence of nanodomains is reflected in a slower diffusion behavior of the probe that can still be described by the free diffusion model (for example at $K_D(\text{probe}) = 25$, domain radius = 50 nm and diffusion coefficient of nanodomains = $0.8\,\mu\text{m}^2$/s probe diffusion is 5 times slower)[32]. However, considering the small size of the nanodomains described in this manuscript, it can be expected that they are mobile. In such case their impact on probe diffusion is less pronounced but still significant in most cases (for details see ref. 32). When probes avoid entering the nanodomains ($K_D < 1$, panel A of Fig. 4) their diffusion is slowed down as well and does not exhibit any deviations from free diffusion as seen by classical FCS. In general, their sensitivity to the presence of nanodomains is smaller compared to probes that partition mostly towards nanodomains.

Considering the high affinity of g-GM$_1$ for nanodomains (Table 1), we used it as a probe to detect nanodomains by FCS. For comparison, we also used the DiD probe. It can be inferred from FRET experiments using g-GM$_1$ and DiD (Fig. SI3), that DiD is homogeneously distributed between the nanodomains and the remaining bilayer. Therefore, the expected impact of nanodomains on its diffusion will be smaller.

In DOPC/SM lipid mixtures (panel B of Fig. 4) the dependence of the diffusion of g-GM$_1$ on SM content in the lipid bilayer could be divided into two regimes: In the first regime, at DOPC/SM (100–92/0–8), the diffusion coefficients were constant within the error of the FCS measurement. In this regime, our FRET experiments showed a homogeneous bilayer. At DOPC/SM (90–85/10–15), where FRET detected nanodomains, the g-GM$_1$ diffusion coefficient decreased. A similar trend but with slightly less distinct differences between the two regimes was obtained for DiD. According to panel B of Fig. 4, the diffusion of g-GM$_1$ was on average about 5% slower in bilayers with nanodomains than in homogeneous bilayers, whereas the diffusion of DiD slowed down on average about 3%. In order to judge the significance of the decrease in the diffusion coefficient D a t-test was performed (see Table SI2 and SI3 in SI). *P*-values lower than 0.1 determine a significant difference between two sets of data. In case of g-GM$_1$ the change in D in respect to the composition DOPC/SM (100/0), which contains no nanodomains, was significant for the compositions (90/10) and (85/15) and insignificant for (88/12). In case of DiD the drop was significant only for (85/15).

The impact of nanodomains on the diffusion of g-GM$_1$ was much stronger in DOPC/Chol/SM mixtures (panel C of Fig. 4), where g-GM$_1$ partitioned into the nanodomains more efficiently (see Table 1 for K_Ds), compared to the DOPC/SM bilayers. A significant drop in the diffusion of g-GM$_1$ (see Table SI3 in SI) occurred already at (70/25/5), where nanodomains were detected by FRET. The diffusion slowed down further as more SM was accumulated into the nanodomains (note that the average domain radius and area coverage remain the same (Table 1) as SM content is increased). Based on the similarity of the hydrophobic molecular regions of SM and g-GM$_1$, and the results of the MC simulation of probe diffusion in the presence of nanodomains[32] this can be explained by more efficient entrapment (longer dwell-time) of g-GM$_1$ in the SM-rich nanodomains. The abrupt increase in the diffusion coefficient at (63/25/12) occurred due to formation of microscopically phase-separated domains and concentration of Chol and SM into such domains. The bilayer was very close to the L_d/L_o phase separation boundary at this composition. Here, there is an increased risk of measurements being unintentionally
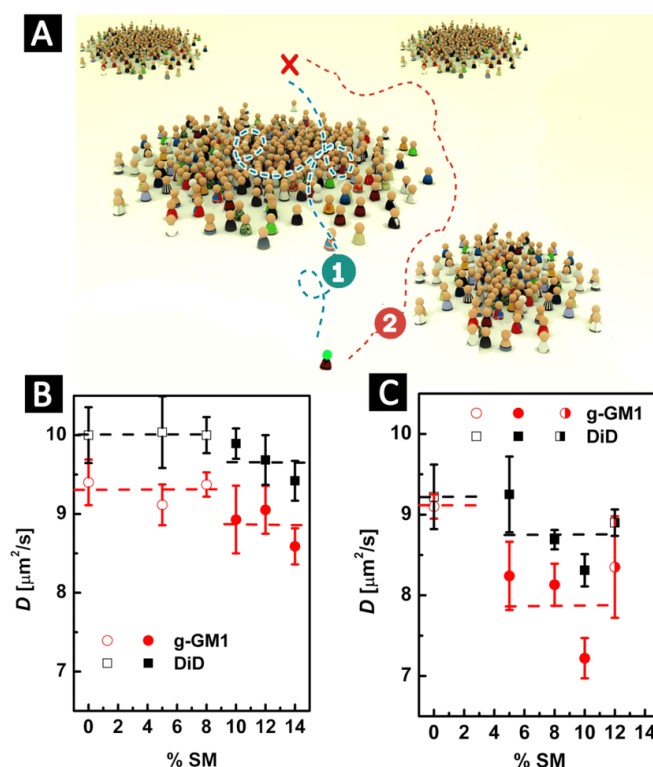
Figure 4. This figure demonstrates the impact of nanodomains on the diffusion of fluorescent probes. (**A**) Two scenarios are possible: the probes diffuse through the nanodomains (case 1); the probes avoid entering the nanodomains (case 2). At sufficiently high domain concentration, the probes diffuse significantly slower as compared to the case where the probes diffuse freely in a homogeneous bilayer[32]. Panels (B) and (C) show experimental results of two-colour z-scan FCS measurements performed on GUVs. The diffusion coefficients of g-GM$_1$ and DiD are presented as a function of SM content in bilayers of DOPC/SM [(100 − x)/x] (panel B) or DOPC/Chol/SM [(75 − x)/25/x] (panel C). Empty vs. filled symbols mark bilayer mixtures where a homogeneous bilayer vs. a bilayer with nanodomains was detected by FRET. Microscopically phase-separated bilayers are marked by the half-filled symbol. Error bars are the standard deviation within the sample of results (measurements on 5 to 10 different GUVs) obtained for each composition.

performed on phase-separated GUVs, where the diffusion in the L$_d$ phase is fast[33]. This is also reflected in the large standard deviation error bar associated with this data point (panel C of Fig. 4). A similar pattern of diffusion coefficients was obtained for DiD. For comparison, the diffusion coefficient of g-GM$_1$ decreased on average about 14% in bilayers containing nanodomains, whereas DiD diffusion was slowed down on average about 5%. Of note, the decrease in D of DiD in (67/25/8) and (65/25/10) bilayers was determined to be significant by the t-test (Table SI3).

Nanodomain fluidity. According to the published phase diagrams[27, 28], the investigated bilayers (Table 1) should be homogeneous and in a neat liquid-disordered state. However, we observed nanodomains under these conditions, thus, we questioned to which extent these nanodomains were fluid and disordered. We calculated the number of individual lipid molecules in the nanodomains assuming an equal distribution of DOPC between domains and remaining bilayer and an exclusive localization of Chol and SM within the nanodomains (see SI for details of this calculation). In DOPC/SM (90/10) bilayers the nanodomains contained on average approximately 94 SM and 390 DOPC molecules. This results in a SM to DOPC molar ratio within the nanodomains of 1:4. In DOPC/Chol/SM (65/25/10) bilayers, the nanodomains are estimated to contain 228 DOPC, 195 Chol and 78 SM molecules. This yields a 1:3 SM to DOPC molar ratio and a 1:2.5 SM to Chol molar ratio. In both DOPC/SM and DOPC/Chol/SM the number of DOPC molecules by far exceeds the number of SM molecules in the nanodomains. This makes the nanodomains fluid and disordered. Even in the case of the ternary mixture, where Chol molecules also contribute by a large fraction, the large amount of DOPC maintains the fluidity and disorder of the nanodomains. Moreover, since the DOPC/Chol/SM bilayer phase-separates at (60/25/15), these given numbers
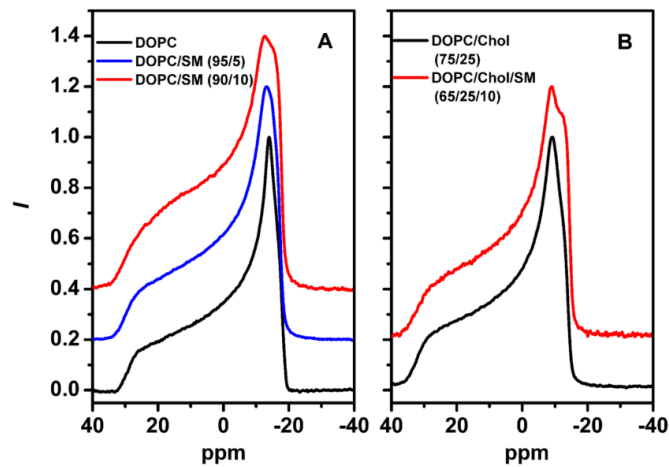
Figure 5. Static ^{31}P NMR spectra of multilamellar vesicles composed of (left panel) DOPC (black), DOPC/SM 95/5 (red) and DOPC/SM 90/10 (blue) or (right panel) DOPC/Chol 75/25 (black) and DOPC/Chol/SM 65/25/10 (red) at 298 K.

represent the approximate highest ratios of SM/DOPC and SM/Chol at which liquid disordered nanodomains could still be formed.

FRET experiments between two additional D/A pairs consisting of DOPE labeled at the headgroup by Atto-488 or Atto-633 (Atto-488-DOPE/Atto-633-DOPE), respectively, and between g-GM$_1$ and the lipid tracer DiD further confirmed the liquid-disordered character of the nanodomains (Figs SI2 and SI3 in SI). These experiments are based on the assumption that by knowing the affinity of donors and acceptors for microscopically phase separated L$_o$ domains, for which K_Ds can be determined easily, one can draw conclusions about the L$_o$ character of nanodomains of similar composition by simple time-resolved FRET measurements (see SI). Here we are under the assumption that the lipid compositions, which are slightly different between the microscopic and nanoscopic domains, do not change K_Ds of probes. As shown in Table 2, Atto-488-DOPE, Atto-633-DOPE and DiD partition preferably into the L$_d$ phase and are efficiently expelled from microscopic L$_o$ domains in DOPC/Chol/SM (55/25/20) bilayers. This composition is close in the phase diagram (Fig. 2) to those where nanodomains are observed (e.g. DOPC/Chol/SM 65/25/10). Based on these results, one expects that these probes should be driven out of nanodomains with L$_o$ character. This would change the relative FRET efficiency for both D/A pairs (see Table 2 for implications in FRET in the presence of L$_d$ or L$_o$ nanodomains). On the other hand, formation of L$_d$ nanodomains would not change either the distribution of the probes or the relative FRET efficiency for both DA pairs. As Figs SI2 and SI3 show, the kinetics of fluorescent relaxation of the donors remained the same for all the cases. This indicates that the relative FRET efficiency for both D/A pairs remained constant in all investigated bilayer compositions, with and without nanodomains. This finding supports our hypothesis that the nanodomains have a L$_d$ character.

To obtain further insight at a molecular level into the organization and dynamics of the lipid bilayers studied here, additional solid-state wide-line and high-resolution MAS ^{31}P NMR experiments were performed[34, 35]. Wide-line NMR spectra obtained for pure DOPC bilayers (Fig. 5) exhibited a "powder-like" lineshape at 298 K, which is typical for a lamellar PC bilayer in its liquid-crystalline L$_d$-phase[36, 37]. Under these conditions, the individual lipid molecules in the bilayer undergo fast rotational dynamics, which causes the typical shape and reduced width of the obtained NMR spectra. Analysis of the lineshapes revealed a chemical shift anisotropy, $\Delta\sigma$, where $\Delta\sigma = \sigma_\parallel - \sigma_\perp$ is the width of NMR spectrum, of approximately 45.3 ppm, which is typical for this phase. Addition of 25 mol% of cholesterol to the DOPC bilayers generated a spectrum representative for a lamellar bilayer system at 298 K (Fig. 5B) with a hint of a second subspectrum, i.e. showing a homogeneous bilayer with perhaps a small fraction of a second, slightly more ordered subdomain. In contrast, the sample composed of DOPC/SM (90/10) resulted in significant changes in the corresponding NMR lineshape (Fig. 5A). The NMR spectrum is clearly composed of two sub-spectra, the main component with an intense 90° edge at −14.6 ppm and a second at −18.3 ppm. As SM is a minor component (10%) in the lipid bilayer, we attribute these two sub-spectra to DOPC in two different dynamic environments. Fitting the lineshape to two axially symmetric powder patterns reveals that the first sub-spectrum, characterized by a chemical shift anisotropy of 38.4 ppm, contributes approximately 47% of the total intensity. This component reflects a lipid environment with a slightly increased disorder in the headgroup region of the DOPC lipids. The second sub-spectrum with an intense 90° edge at 16 ppm, is characterized by a larger chemical shift anisotropy of approximately 49.0 ppm. This increase indicates a different membrane environment with the lipid headgroup regions (and presumably the whole lipid molecules) undergoing reduced dynamics (with less motional averaging of the chemical shift anisotropy) presumably due to the close proximity of stiff SM molecules. In summary, the DOPC/SM (90/10) membranes appear to consist of two different
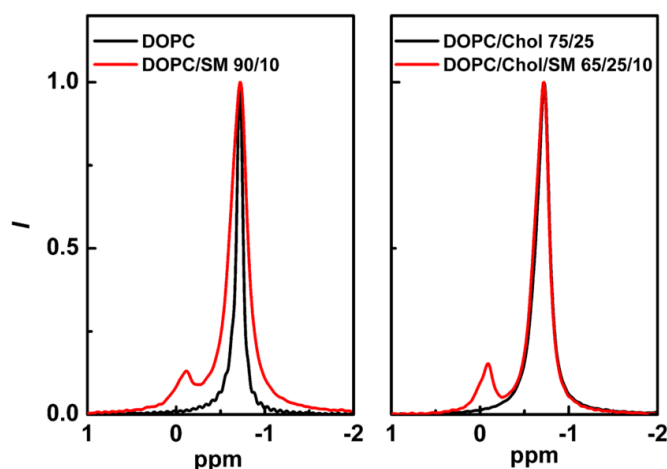
Figure 6. Change in the MAS ^{31}P NMR spectra after addition of 10% of SM into DOPC (left panel) or DOPC/Chol (75/25) (right panel) lipid mixtures.

environments: 47% of the bilayer was presumably SM free, fluid and disordered whereas the rest of the bilayer was richer in SM with DOPC lipids in direct contact with SM molecules. Such estimation is in agreement with our MC-FRET results, according to which the SM rich domains occupied 37% or 55% (two global chi-squared minima) of the entire bilayer area (Table 1). Also in agreement with FRET data, 5 mol% SM was not able to induce nanodomains as seen in Fig. 5A, which would have been visible as a second NMR sub-spectrum characterized by a larger chemical shielding anisotropy.

For the ternary systems composed of DOPC/Chol/SM (70,65/25/5,10) lipid mixtures, static NMR spectra were clearly composed of two sub-spectra with different widths (Fig. 5B). Although multiple components (sub-spectra) are present in the system the spectral properties of each are inconsistent with the broader spectra that would be expected of lipids in their gel phase. The broader of these two components has an intense 90° edge at −14 ppm, whilst the remaining component has a smaller chemical shift anisotropy similar to that of DOPC/Chol bilayers in the absence of SM. Fitting the lineshape to two axially symmetric powder patterns indicates that the SM rich contributes approximately 44% of the entire spectral intensity in good agreement with MC-FRET results.

Our MAS ^{31}P NMR results further confirm the L_d character of the nanodomains found in the studied bilayers. As seen in Fig. 6, the isotropic NMR signal occurred at −0.71 ppm, which is the isotropic chemical shift value expected for DOPC bilayers. Upon addition of SM, or Chol and SM, the variations in this value were minor (upfield to −0.74 ppm) but the NMR linewidth increased dramatically from 15 Hz to 45 Hz. Despite the increase in the linewidth, the resonances remained relatively narrow, supporting the disordered character of the lipid headgroups within the domains. The lipids are undergoing fast dynamics and the isotropic lineshapes of the MAS spectra are influenced by exchange processes. Such behaviour is also typical for L_d phase. The isotropic linewidths in the MAS ^{31}P NMR spectra of lipids are largely dominated by the spin-spin/transverse relaxation times which are sensitive to motion on the ms to μs timescale[38]. The similarity of the linewidths obtained for DOPC in the presence of SM, Chol or both SM and Chol indicates that both species are likely to interact with DOPC head-groups, slowing down the motions on the ms to μs timescale and resulting in reduction of the T_2 and an increase in the corresponding linewidth. The absence of more significant changes in the ^{31}P powder lineshape reflects that the exchange processes occurring do so from populations of lipids exhibiting similar isotropic and anisotropic chemical shielding suggesting that both populations exhibit similar dynamic properties.

The fact that the nanodomains were detected both by NMR and FCS helps to restrict the range of possible nanodomain lifetimes. The readouts of both techniques are influenced by processes that occur on the micro- to millisecond time scale. Therefore, the lifetimes of nanodomains should be roughly in this range. The broadening that is present in the SM/DOPC MAS ^{31}P NMR spectra (Fig. 6, red colour) together with the underlying broad subspectrum (ranging from 0.3 to −1.5 ppm) indicates that the DOPC is in exchange between different environments on the NMR timescale (ms/μs) in a manner analogous to that reported by e.g. by Bonev et al.[39]. This observation is consistent with SM lipids forming a dynamic complex with multiple DOPC molecules over the timescale of the NMR experiment (ms/μs). Interestingly, g-GM$_1$, r-GM$_1$, CF-DSPE-PEG and Rh-PEG-DSPE probes seem to exhibit increased affinity for this dynamic complex (see Table 1 for K_ps). Preferable localization of these probes in the nanodomains originates presumably from structural similarity of hydrophobic regions of these probes with SM and allows for determination of nanodomain sizes by MC-FRET.

Of note, transient and dynamic heterogeneities of much shorter lifetime, about 100 ns, and size of 10 nm were revealed by neutron scattering[29, 40] and MARTINI simulations[41]. These were reported to exist in DPPC/Chol and DMPC/Chol bilayers close to the phase separation boundary where Chol crystals start to form. Moreover, longer lived fluctuations in composition of about 0.8 ms were observed in ternary mixtures of high and low melting

Composition of the lipid bilayer			Nanodomains detected YES/NO						Area covered by the nanodomains [%]	
			FRET				**FCS**			
DOPC [%]	**SM [%]**	**Chol [%]**	**g-GM$_1$/r-GM$_1$**	**CF-PEG- DSPE/Rh-PEG-DSPE**	**NMR**	**g-GM$_1$**	**DiD**	**FRET**	**NMR**
100, 95, 92	0, 5, 8	0	NO	NO	NO	NO	NO	no nanodomains	
90, 88, 85	10, 12, 15	0	YES	NO ($K_D \approx 1$)[a]	YES	YES	NO/YES[b]	37, 55	53
75	0	25	NO	NO	NO	NO	NO	no nanodomains	
70, 67	5, 8	25	YES	NO ($K_D \approx 1$)[a]	—	YES	NO/YES[c]	45	—[d]
60	10	25	YES	YES	YES	YES	YES	45–55[e]	44
63	12	25	NO ($K_D \approx 1$)	YES	—[d]	YES	NO	45	—[d]

Table 3. Nanodomains as detected by FRET and two different D/A pairs, solid-state NMR and z-scan FCS. [a]This D-A pair is equally distributed between the nanodomains and the remaining bilayer and thus the existence of the nanodomains does not have an effect on the FRET phenomenon; [b]the decrease in D, which indicates the presence of nanodomains, was only significant (p < 0.1) for the bilayers composed of 15% SM; [c]only for 8% SM; [d]not determined; [e]45% with GM$_1$ pair, 55% with DSPE pair.

temperature lipids near miscibility critical points[42]. In this work, on the contrary to the above mentioned cases, the nanodomains are found further away from the phase separation boundaries (Fig. 2).

Although the mechanism of how these nanodomains are formed is not yet well understood, we expect that the process is facilitated by the following factors. First, geometrical factors result in different packing preferences of DOPC and SM. Consequently, SM tends to be surrounded by other SM rather than DOPC molecules. Moreover, it has been documented by a variety of experimental approaches that SM and Chol preferably interact with each other (for a review see ref. 43). It is also known that Chol promotes segregation of different PC components at low Chol contents whereas it suppresses the segregation at higher concentrations (above 50 mol%)[44]. All these interactions seem to be re-enforced by hydrogen bonding between –NH group of SM and hydroxyl group of Chol and between SM and DOPC[43, 45–47]. In addition, temporal thermal fluctuations and fluctuations in concentration may perhaps be involved in the formation of nanodomains[41]. Groupings of three to five molecules have been found even in ideal binary mixtures with only nearest neighbor interactions[48]. Thus, hypothetically, it is possible that these temporal fluctuations function as seeds for the liquid disordered nanodomains in a similar way as nanodomains work as formation platforms for microscopic L$_o$ phase domains.

Implications for the raft theory. So far, scientists have frequently used L$_o$ microdomains as a model system for rafts despite insufficient experimental evidence for the existence of such domains in cells. The size and physical properties of such microdomains are extreme in the context of the plasma membrane, but they are still used as a model system for putative nano-scale rafts in cellular membranes. In respect to the complex composition of a cellular plasma membrane where sharp and well-defined phase transitions can hardly be expected, differences between various local environments are presumably more subtle than the differences between the L$_d$ and L$_o$ phases encountered in model systems. To bridge the gap between the extremes of L$_d$ or L$_o$ phase bilayers in artificial model systems and the plasma membrane of living cells scientists started using giant plasma membrane vesicles (GPMVs) as an intermediate model system that more or less preserve biological complexity of native plasma membranes[5, 49]. Similarly to the synthetic model membranes of GUVs, GPMVs may phase separate into two distinct microscopic phases. However, the differences between the L$_d$ and L$_o$ phase are significantly smaller to those observed in GUVs, presumably better corresponding to what is encountered in plasma membranes of living cells. A disadvantage might be a worse control of the GPMVs' composition[6] and phase behaviour which is dependent on the detergent used[49].

The L$_d$ nanoscale domains that have been found and characterized in this work have in analogy to the L$_o$ microdomains encountered on GUVs a very simplified composition. However, in terms of domain sizes and their physical properties the nanodomains seem to represent a good model system for cellular rafts. Moreover, the plasma membrane of a living cell is permanently changing. Thus, rafts can be expected to form and disappear or change their properties during their lifetime. In this context, the transient nature of the L$_d$ nanodomains may also correspond better to the properties of cellular rafts.

Summary. In this work, we discovered and characterized nanodomains in binary DOPC/SM and ternary DOPC/Chol/SM bilayers of compositions that should result in homogeneous bilayers according to published phase diagrams. The results of our MC-FRET, solid-state NMR and z-scan FCS experiments are summarized in the phase diagram of Fig. 2 and in Table 3. Briefly, all three methods indicate that binary mixtures DOPC/SM (100–92/0–8) are homogeneous and that DOPC/SM (90–85/10–15) exhibit nanodomains. In the ternary lipid mixtures containing Chol, nanodomains were revealed at DOPC/Chol/SM (70–65/25/5–10).

The nanodomains of approximately 10 nm can be estimated to consist of roughly 400 to 500 molecules, are enriched in SM but still contain a high amount of DOPC molecules, which is sufficient to maintain the nanodomains fluid and disordered. Despite their L$_d$ character the nanodomains exhibit subtle differences on average environment and dynamics as compared to the surrounding. The nanodomains appear long-lived with a lifetime in the range of microseconds to several milliseconds. In terms of their size, fluidity, order and lifetime these nanodomains may represent a relevant model system for cellular membranes and perhaps be more closely related to heterogeneities, e.g. nanocompartments, observed in cellular plasma membranes.

Methods

GUV preparation. GUVs were prepared by the electroformation method as described previously by Angelova *et al.*[50]. All lipid mixtures were made from stock solutions in chloroform. The lipid mixture (100 nmol in approximately 200 μL of chloroform) containing the additional labelled lipids was spread onto two hollowed titanium plates. These were placed on a heating plate at approximately 47 °C to facilitate solvent evaporation. The plates were subsequently put under vacuum for at least 1 h to evaporate remaining solvent traces. The lipid-coated plates were assembled using one layer of Parafilm as an insulating material. The electroswelling chamber was filled with 1 ml of preheated sucrose solution (with the osmolarity of 103 mOsm/kg) and sealed with Parafilm. An alternating electrical field of 10 Hz rising from 0.02 V to 1.1 V (peak-to-peak voltage) during the first 45 min was applied and kept at 1.1 V and 47 °C for additional 1.5 h. This sequence was followed by a so-called detaching phase at 4 Hz and 1.3 V for 30 min. Finally, the GUVs were added to a microscope chamber containing glucose buffer (~80 mM glucose, 10 mM HEPES and 10 mM NaCl, pH 7.2) at the osmolarity of 103 mOsm/kg. All lipid mixtures contained 2 mol% of biotinyl-PE to immobilize the GUVs on the bottom of a chamber coated with BSA-biotin/streptavidin.

For the FCS experiments, the probe-to-lipid ratio was 1:100000 whereas for the FRET experiments, the donor (acceptor)-to-lipid ratio was 1:1000 (1:200) in case of g-GM$_1$/DiD pair and 1:200 (1:200) in case of g-GM$_1$/r-GM$_1$ pair, respectively.

Sample preparation for NMR experiments. The lipid mixtures were prepared by dissolving the appropriate lipids in a 2/1 vol/vol HCCl$_3$/MeOH solution, followed by evaporation, resuspending in water and freeze-drying, as described previously[51]. To produce multilamellar vesicles, appropriate amounts (around 20 mg) of dry lipid powder was then rehydrated using in the same buffer as used above (except D$_2$O was used here instead) at a one-to-one weight ratio, followed by several freeze-thaw cycles and vortexing. Finally the membrane suspensions were pelleted into 4 mm MAS NMR rotors (Bruker, Germany) and measured immediately or kept at −20 °C prior NMR experiments.

FCS and FLIM-FRET measurements. Both types of measurements were performed on a home-built confocal microscope consisting of an inverted confocal microscope body IX71 (Olympus, Hamburg, Germany) and pulsed diode lasers (LDH-P-C-470, 470 nm, and LDH-D-C-635, 635 nm PicoQuant, Berlin, Germany) operated at 10 MHz repetition rate. The lasers were pulsing alternatively to avoid artifacts caused by signal bleed-through. The laser light was coupled to a polarization maintaining single mode optical fiber and re-collimated at the output with an air space objective (UPLSAPO 4X, Olympus). The light was up-reflected to a water immersion objective (UPLSAPO 60x, Olympus) with a 470/635 dichroic mirror. The signal was split between two single photon avalanche diodes using 515/50 and 697/58 band pass filters (Chroma Rockingham, VT) for green and red channel, respectively.

z-scan measurements were conducted on the top of selected GUVs. First, a membrane was placed to the waist of a laser, moved 1.5 μm below the waist afterwards and finally, scanned vertically in 20 steps (150 nm spaced). A 60 second long measurement was performed at each step. The laser intensity at the back aperture of the objective was around 6 μW for each laser line. To obtain the average diffusion coefficients presented in Fig.4 z-scan FCS measurements on 5–10 different GUVs were performed. Further details of the data analysis are given elsewhere[19].

FLIM-FRET measurements were done by acquiring an image (512 × 512 pixels, 0.6 ms/pixel) of a GUV at its cross-section. The experimental fluorescence decay of the donor that was taken for further analysis was obtained by summing up the measured fluorescence decays from at least five different GUVs. However, variability between fluorescence decays obtained from individual GUVs was negligible (see Fig. SI6). Laser intensity of 1 μW for the 470 nm laser was chosen low enough to avoid pile-up effect for the FLIM-FRET measurements. The experiments were performed at 25 °C.

NMR experiments. All ^{31}P NMR experiments were acquired using a 500 MHz Avance III spectrometer (Bruker, Switzerland). Static wideline NMR spectra of multilamellar vesicles were acquired at 298 K using a Hahn echo pulse sequence with a single π/2 pulse of 7.8 μs pulse length, an inter-pulse delay of 50 μs and a recycle rate of 4 s. During acquisition, TPPM proton decoupling[52] was used (40 W) and ca. 10000 scans were accumulated. For high-resolution MAS NMR spectra, the samples were spun at 5 kHz and a single pulse excitation followed by proton decoupling (parameters as for static NMR experiments) was used. Between 200 to 600 scans were accumulated.

NMR data was processed in matNMR[53], with all spectra zero-filled to 4096 pts and 30 Hz line-broadening added prior to Fourier transform. Powder lineshapes were analyzed by fitting to one or two axially symmetric powder patterns, using the fitting routines within matNMR.

Analysis of FLIM-FRET data. Förster resonance energy transfer (FRET) was analyzed from fluorescence lifetime images (FLIM). Each pixel contains information on the arrival times of individual photons. These times are used to construct the fluorescence decay, whose shape can be modified by FRET. Analysis of the decay by an appropriate mathematical model yields further information. In this work, the so-called Baumann-Fayer (BF) model was used (see SI) to (i) determine the experimental surface concentration of the acceptors, which was required as one of the input parameters for the MC simulations; (ii) obtain information about how donors and acceptors were distributed in the lipid bilayer. Relative FRET efficiency E_{rel} used in the manuscript is defined as the ratio between FRET efficiency[54] for a heterogeneous bilayer E_{hetero} (with nanodomains) and the FRET efficiency for a homogeneous bilayer E_{homo} (without nanodomains). Homogeneous bilayers were selected to contain 0% of SM and the same amount of Chol as the heterogeneous bilayers.

The determination of nanodomain sizes was performed by analyzing the experimental fluorescence decay with Monte Carlo simulations. Two sets of GUVs are always prepared: the first set contains GUVs with homogeneous bilayers and is used to calculate the number of acceptors in the GUVs by the Baumann-Fayer model (see SI). The number of acceptors is assumed to be the same in the other set of GUVs, where nanodomains with unknown

dimensions might exist. This is done in order to reduce the number of optimized parameters. The entire fitting procedure was described in detail elsewhere[24] and is shortly summarized in what follows. A defined number of donors, acceptors and circular domains with a given radius R_D was generated in the lipid bilayer. Whereas the number of donors was kept at a sufficiently high value for statistical reasons, the number of acceptors had to be determined by the BF model (SI) to correspond to the actual experimental conditions. First, the donors and acceptors were distributed according to the distribution constants defined as $K_D(D) = [D_{inside}]/[D_{outside}]$, $K_D(A) = [A_{inside}]/[A_{outside}]$. In the next step, a donor was randomly excited and the time at which an energy transfer event took place calculated. This process was random and modulated by the overall energy transfer rate Ω_i according to $\Delta t_i = -ln\gamma/\Omega_i$ where γ is a randomly generated number between 0–1. The outcome of each simulation step was the time interval Δt_i between the excitation and the energy transfer event. To achieve good statistics, each generated configuration was used 100 times before a new configuration was generated. The total number of all excitation events was 3×10^5. By constructing a histogram of Δt_i intervals the total survival probability function $G(t)$ was obtained and the simulated decay of donors quenched by the acceptors calculated. The simulated decay was fitted to the experimental one by varying the input simulation parameters, i.e. the domain radius R_D, the area fraction the domains occupied Ar and $K_D(D,A)$. The global minimum was found by scanning the chi-squared space of physically acceptable parameters R_D, Ar, and $K_D(D,A)$. Because of structural similarity between donors and acceptors and a weak dependence of R_D and Ar on the actual values of K_D, $K_D(D)$ was kept identical to $K_D(A)$.

Analysis of z-scan FCS data has been described many times before[19, 55] and is briefly summarized in SI.

References

1. Simons, K. & Ikonen, E. Functional rafts in cell membranes. *Nature* **387**, 569–572 (1997).
2. Brown, D. A. & London, E. Structure and origin of ordered lipid domains in biological membranes. *J. Membr. Biol.* **164**, 103–114 (1998).
3. Baumgart, T. *et al.* Large-scale fluid/fluid phase separation of proteins and lipids in giant plasma membrane vesicles. *Proc. Natl. Acad. Sci. USA* **104**, 3165–3170 (2007).
4. Lingwood, D. & Simons, K. Lipid rafts as a membrane-organizing principle. *Science* **327**, 46–50 (2010).
5. Levental, I., Grzybek, M. & Simons, K. Raft domains of variable properties and compositions in plasma membrane vesicles. *Proc. Natl. Acad. Sci. USA* **108**, 11411–6 (2011).
6. Sezgin, E. *et al.* Adaptive lipid packing and bioactivity in membrane domains. *PLoS One* **10**, 1–14 (2015).
7. Eggeling, C. *et al.* Direct observation of the nanoscale dynamics of membrane lipids in a living cell. *Nature* **457**, 1159–1162 (2009).
8. Bernardino de la Serna, J., Schütz, G. J., Eggeling, C. & Cebecauer, M. There Is No Simple Model of the Plasma Membrane Organization. *Front. Cell Dev. Biol.* **4**, 1–17 (2016).
9. Owen, D. M., Williamson, D. J., Magenau, A. & Gaus, K. Sub-resolution lipid domains exist in the plasma membrane and regulate protein diffusion and distribution. *Nat. Commun.* **3**, 1256 (2012).
10. Kreder, R. *et al.* Solvatochromic Nile Red Probes with FRET Quencher Reveal Lipid Order Heterogeneity in Living and Apoptotic Cells. *ACS Chem. Biol.* **10**, 1435–1442 (2015).
11. Sanchez, S. A., Tricerri, M. A. & Gratton, E. Laurdan generalized polarization fluctuations measures membrane packing micro-heterogeneity *in vivo*. *Proc. Natl. Acad. Sci. USA* **109**, 7314–9 (2012).
12. Ritchie, K., Iino, R., Fujiwara, T., Murase, K. & Kusumi, A. The fence and picket structure of the plasma membrane of live cells as revealed by single molecule techniques (Review). *Mol. Membr. Biol.* **20**, 13–18 (2003).
13. Varma, R. & Mayor, S. GPI-anchored proteins are organized in submicron domains at the cell surface. *Nature* **394**, 798–801 (1998).
14. Smith, A. K. & Freed, J. H. Determination of Tie-Line Fields for Coexisting Lipid Phases: An ESR Study. *J. Phys. Chem. B* **113**, 3957–3971 (2009).
15. Farkas, E. R. & Webb, W. W. Precise and millidegree stable temperature control for fluorescence imaging: Application to phase transitions in lipid membranes. *Rev. Sci. Instrum.* **81** (2010).
16. Loura, L. M. S., Fernandes, F. & Prieto, M. Membrane microheterogeneity: Forster resonance energy transfer characterization of lateral membrane domains. *Eur. Biophys. J. with Biophys. Lett.* **39**, 589–607 (2010).
17. Loura, L. M., Fedorov, A. & Prieto, M. Fluid-fluid membrane microheterogeneity: a fluorescence resonance energy transfer study. *Biophys. J.* **80**, 776–788 (2001).
18. Bader, A. N. *et al.* Homo-FRET imaging as a tool to quantify protein and lipid clustering. *ChemPhysChem* **12**, 475–483 (2011).
19. Benda, A. *et al.* How to determine diffusion coefficients in planar phospholipid systems by confocal fluorescence correlation spectroscopy. *Langmuir* **19**, 4120–4126 (2003).
20. Šachl, R., Johansson, L. B.-Å. & Hof, M. Förster resonance energy transfer (FRET) between heterogeneously distributed probes: Application to lipid nanodomains and pores. *Int. J. Mol. Sci.* **13**, 16141–16156 (2012).
21. Šachl, R. *et al.* Distribution of BODIPY-labelled phosphatidylethanolamines in lipid bilayers exhibiting different curvatures. *Phys. Chem. Chem. Phys.* **13**, 11694–11701 (2011).
22. Štefl, M. *et al.* Dynamics and size of cross-linking-induced lipid nanodomains in model membranes. *Biophys. J.* **102**, 2104–2113 (2012).
23. Honigmann, A. *et al.* Scanning STED-FCS reveals spatiotemporal heterogeneity of lipid interaction in the plasma membrane of living cells. *Nat. Commun.* **5**, 5412 (2014).
24. Šachl, R. *et al.* On multivalent receptor activity of GM1 in cholesterol containing membranes. *Biochim. Biophys. Acta* **1853**, 850–7 (2015).
25. Amaro, M. *et al.* GM1 Ganglioside Inhibits b-amyloid Oligomerization Induced by Sphingomyelin. *Angew. Chemie* **55**, 9411–9415 (2016).
26. Marushchak, D., Gretskaya, N., Mikhalyov, I. & Johansson, L. B.-Å. Self-aggregation - an intrinsic property of GM₁ in lipid bilayers. *Mol. Membr. Biol.* **24**, 102–112 (2007).
27. Nyholm, T. K. M., Lindroos, D., Westerlund, B. & Slotte, J. P. Construction of a DOPC/PSM/cholesterol phase diagram based on the fluorescence properties of trans-parinaric acid. *Langmuir* **27**, 8339–50 (2011).
28. Veatch, S. L. & Keller, S. L. Miscibility Phase Diagrams of Giant Vesicles Containing Sphingomyelin. *Phys. Rev. Lett.* **94**, 148101 (4pp) (2005).
29. Rheinstädter, M. C. & Mouritsen, O. G. Small-scale structure in fluid cholesterol-lipid bilayers. *Curr. Opin. Colloid Interface Sci.* **18**, 440–447 (2013).
30. Leidy, C., Wolkers, W. F., Jørgensen, K., Mouritsen, O. G. & Crowe, J. H. Lateral Organization and Domain Formation in a Two-Component Lipid Membrane System. *Biophys. J.* **80**, 1819–1828 (2001).
31. Epand, R. M. *et al.* Novel properties of cholesterol-dioleoylphosphatidylcholine mixtures. *Biochim. Biophys. Acta - Biomembr.* **1616**, 196–208 (2003).

32. Šachl, R., Bergstrand, J., Widengren, J. & Hof, M. Fluorescence correlation spectroscopy diffusion laws in the presence of moving nanodomains. *J. Phys.D Appl. Phys.* **49**, 114002 (11pp) (2016).
33. Korlach, J., Schwille, P., Webb, W. & Feigenson, G. W. Characterization of Lipid Bilayer Phases By Confocal Microscopy and Fluorescence Correlation Spectroscopy. *Proc. Natl. Acad. Sci.* **96**, 8461–8466 (1999).
34. Dufourc, E. J., Mayer, C., Stohrer, J., Althoff, G. & Kothe, G. Dynamics of phosphate head groups in biomembranes. Comprehensive analysis using phosphorus-31 nuclear magnetic resonance lineshape and relaxation time measurements. *Biophys. J.* **61**, 42–57 (1992).
35. Holland, G. P., McIntyre, S. K. & Alam, T. M. Distinguishing individual lipid headgroup mobility and phase transitions in raft-forming lipid mixtures with 31P MAS NMR. *Biophys. J.* **90**, 4248–4260 (2006).
36. Lindström, F., Williamson, P. T. F. & Gröbner, G. Molecular insight into the electrostatic membrane surface potential by $^{14}N/^{31}P$ MAS NMR spectroscopy: nociceptin-lipid association. *J. Am. Chem. Soc.* **127**, 6610–6616 (2005).
37. Cullis, P. R. & De Kruijff, B. Lipid polymorphism and the functional roles of lipids in biological membranes. *Biochim. Biophys. Acta - Rev. Biomembr.* **559**, 399–420 (1979).
38. Ernst, R. R., Bodenhausen, G. & Wokaun, A. *Principles of Nuclear Resonance in One and Two Dimensions*. (Oxford University Press, 1987).
39. Bonev, B. B., Chan, W. C., Bycroft, B. W., Roberts, G. C. K. & Watts, A. Interaction of the lantibiotic nisin with mixed lipid bilayers: A 31P and 2H NMR study. *Biochemistry* **39**, 11425–11433 (2000).
40. Armstrong, C. L. *et al*. The Observation of Highly Ordered Domains in Membranes with Cholesterol. *PLoS One* **8**, 1–10 (2013).
41. Baoukina, S., Mendez-Villuendas, E., Bennett, W. F. D. & Tieleman, D. P. Computer simulations of the phase separation in model membranes. *Faraday Discuss*. 63–75, doi:10.1039/c2fd20117h (2013).
42. Honerkamp-Smith, A. R. R. Machta, B., Benjamin, B. & Keller, S. Experimental Observations of Dynamic Critical Phenomena in a Lipid Membrane. *Phys. Rev. Lett*. **108**, 265702 (5pp) (2012).
43. Ohvo-Rekilä, H., Ramstedt, B., Leppimäki, P. & Peter Slotte, J. Cholesterol interactions with phospholipids in membranes. *Prog. Lipid Res.* **41**, 66–97 (2002).
44. Silvius, J. R., Del Giudice, D. & Lafleur, M. Cholesterol at different bilayer concentrations can promote or antagonize lateral segregation of phospholipids of differing acyl chain length. *Biochemistry* **35**, 15198–15208 (1996).
45. Slotte, J. P. Sphingomyelin-cholesterol interactions in biological and model membranes. *Chem. Phys. Lipids* **102**, 13–27 (1999).
46. Boggs, J. M. Lipid intermolecular hydrogen bonding: influence on structural organization and membrane function. *Biochim. Biophys. Acta - Rev. Biomembr.* **906**, 353–404 (1987).
47. Hyvonen, M. T. *et al*. Molecular dynamics simulation of sphingomyelin bilayer. *J. Phys. Chem. B* **107**, 9102–9108 (2003).
48. Huang, J. & Feigenson, G. W. Monte Carlo simulation of lipid mixtures: finding phase separation. *Biophys. J.* **65**, 1788–1794 (1993).
49. Sezgin, E. *et al*. Elucidating membrane structure and protein behavior using giant plasma membrane vesicles. *Nat. Protoc.* **7**, 1042–51 (2012).
50. Angelova, M., Soleau, S. & Meleard, P. Preparation of Giant Vesicles by External AC Electric Fields - Kinetics and Applications. *Trends Colloid Interface Sci. VI* **89**, 127–131 (1992).
51. Wallgren, M., Lidman, M., Pham, Q. D., Cyprych, K. & Gröbner, G. The oxidized phospholipid PazePC modulates interactions between Bax and mitochondrial membranes. *Biochim. Biophys. Acta - Biomembr.* **1818**, 2718–2724 (2012).
52. Bennett, A. E., Rienstra, C. M., Auger, M., Lakshmi, K. V. & Griffin, R. G. Heteronuclear decoupling in rotating solids. *J. Chem. Phys.* **103**, 6951–6958 (1995).
53. van Beek, J. D. matNMR: A flexible toolbox for processing, analyzing and visualizing magnetic resonance data in Matlab? *J. Magn. Reson.* **187**, 19–26 (2007).
54. Valeur, B. Molecular Fluorescence Principles and Applications (2001).
55. Macháň, R. & Hof, M. Recent Developments in Fluorescence Correlation Spectroscopy for Diffusion Measurements in Planar Lipid Membranes. *Int. J. Mol. Sci.* **11**, 427–457 (2010).

Acknowledgements

Author Contributions

R.Š. and M.H. conceived and designed the research. A.K., M.A., R.Š. and G.A. performed FRET and FCS experiments and analyzed the results. G.G. performed all NMR experiments and did the analysis of NMR results together with PTFW. I.M. synthesized the GM_1 probes. R.Š. and M.H. wrote the manuscript with the help of other authors.

Additional Information

Competing Interests: The authors declare that they have no competing interests.

Publisher's note: Springer Nature remains neutral with regard to jurisdictional claims in published maps and institutional affiliations.

Lipid Driven Nanodomains in Giant Lipid Vesicles

Are Fluid and Disordered: Supporting Information

Alena Koukalová, Mariana Amaro, Gokcan Aydogan, Gerhard Gröbner, Philip T.F. Williamson,

Ilya Mikhalyov, Martin Hof and Radek Šachl

Baumann-Fayer model[1] describes a situation where donors and acceptors are homogeneously distributed in two parallel planes of a bilayer. In such a case, FRET occurs within one bilayer leaflet (*intra*-FRET) as well as between two parallel planes (*inter*-FRET). By assuming dynamic limit conditions the survival probability function for *intra*-FRET G_{intra} can be expressed as

$$ln\, G_{intra}(t) = -C_2 \Gamma\left(\frac{2}{3}\right)\left(\frac{t}{\tau}\right)^{1/3}, \qquad (1)$$

where C_2 is the reduced surface concentration of the acceptors, which represents the average number of acceptors surrounding a donor within an area of πR_0^2, Γ is the gamma function and τ the average lifetime of the donors. The survival probability for *inter*-FRET, G_{inter}, depends on C_2 but also the bilayer thickness d and is expressed as

$$ln\, G_{inter}(t) = -\frac{C_2}{3}\left(\frac{d}{R_0}\right)^2 \left(\frac{2\mu}{3}\right)^{1/3} \int_0^{2/3\mu}(1 - e^{-s})s^{-4/3}ds, \qquad (2)$$

where θ_r is the angle between the bilayer normal and the vector connecting the locations of the donor and acceptor dipoles, $\mu = 3t\left(\frac{R_0}{d}\right)^6 \frac{1}{2\tau}$ and $s = 2\mu \cos^6\frac{\theta_r}{3}$. Both *inter*- and *intra*-FRET may occur simultaneously in a lipid bilayer. Therefore, the total survival probability of the donors is

given by the joint probability $G(t) = G_{\text{intra}}(t)G_{\text{inter}}(t)$ and the fluorescence intensity $F(t)$ of the donors in the presence of the acceptors described as

$$F(t) = G(t) \sum_i \alpha_i \, exp\left(-\frac{t}{\tau_i}\right), \qquad (3)$$

where $\sum_i \alpha_i \, exp(-t/\tau_i)$ represents the donor decay in the absence of FRET.

Table SI1: Comparison of the acceptor to lipid ratios determined by the Baumann-Fayer model with the expected acceptor to lipid ratios gives information about clustering of fluorescent probes.

DOPC	SM	Chol	Fluorescent probe	Acceptor to lipid ratio obtained by fitting	Expected acceptor to lipid ratio
100, 95, 92	0, 5, 8	0	r-GM$_1$	1:279*	1:200
75	0	25	r-GM$_1$	1:196	1:200

*The following lipid compositions provided identical time-resolved fluorescence decays. Therefore, one value is presented for more than one lipid composition.

FRET excludes intrinsic self-aggregation of GM₁ probes at the concentrations used. One way to exclude self-aggregation of GM$_1$ probes is to use the Baumann-Fayer model (see above). This model provides a parameter called reduced surface concentration of acceptors (C_2), which gives the number of the acceptors in a circle determined by R_0 and can be recalculated to yield the acceptor to lipid ratio. This value is a priori known by mixing lipids and probes with each other and can be compared with the value obtained by fitting. According to [2] aggregation leads to significantly (2.5 to 5 times) larger C_2 values obtained by fitting as compared with the expected values. In our experiments GUVs were prepared at the acceptor to lipid ratio 1:200. Self-aggregation can be excluded because values close to this number were obtained by fitting.

Results are summarized in Table SI1. Of note, this approach can be used only for probes distributed in homogeneous bilayers where Baumann-Fayer model can be applied.

In heterogeneous bilayers a qualitative approach which is based on FRET can be used instead. Here the concentration of donors is varied while keeping a constant concentration of acceptors. If no aggregation occurs overlapping time-resolved fluorescence decays should be obtained. According to Fig. SI1 no aggregation of GM_1 probes in DOPC/Chol/SM (65/25/10) bilayers that contain nanodomains occurs because all decays overlap perfectly.

In conclusion, these experiments indicate that GM_1 probes do not intrinsically self-aggregate at the lipid bilayers and concentrations we have used.
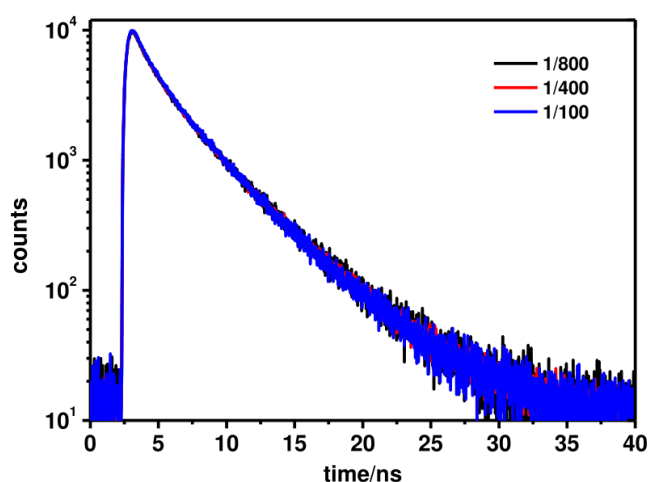

Fig. SI1: Time-resolved fluorescence decays of g-GM_1 in the presence of r-GM_1 acceptors in DOPC/Chol/SM (65/25/10) bilayers. The g-GM_1 to lipid ratio was varied from 1:100 to 1:800.

Determination of the distribution constant K_D between the L_o microdomains and the remaining bilayer. The probe preferences for L_o vs. L_d were determined on microscopically phase

separated giant unilamellar vesicles (GUVs) by fluorescence intensity measurements[3]. The fluorescence intensity was extracted from individual pixels that either belonged to L_o or L_d phase and averaged out to obtain the average fluorescence intensity for L_d, F_{Ld}, or L_o phase, F_{Lo}, respectively. Assuming that F is proportional to the dye concentration in the membrane, the following equation can be used for the calculation of K_D (for K_D definition see the manuscript)

$$K_D = \frac{F_{Lo}}{F_{Ld} + F_{Lo}}. \qquad (4)$$

According to[3], the correction for different brightness in L_d vs. L_o plays a minor role and was consequently not performed in this work, where a rough K_D determination was sufficient.

Nanodomain fluidity and order influences distribution of fluorescent probes. The affinity of fluorescent probes for the domains and the remaining bilayer usually differs. If the probe preferences (given by the partition coefficient K_D) are known *a priori* and under the assumption that the lipid composition does not influence K_Ds at least in a narrow range of lipid concentrations, the fluidity and order of the nanodomains can be characterized. For this purpose, we used two different donor-acceptor (D-A) pairs in this work:

1) Atto-488-DOPE/Atto-633-DOPE: According to Table 2 in the manuscript, both donors and acceptors have very low affinity for L_o microdomains. Formation of L_o nanodomains should therefore be manifested by an increased FRET efficiency because Atto-488-DOPE donors would come into more frequent contact with Atto-633-DOPE acceptors as the donors and acceptors would be more concentrated in the remaining L_d phase. However, the existence of nanodomains did not change the FRET efficiency (Fig. SI2), which implies that the distribution of donors and acceptors had to remain homogeneous. Not surprisingly, it followed from the MC-FRET analysis

that $K_D(D, A) = 1$, confirming the homogeneous distribution of the probes and the disordered character of the nanodomains.
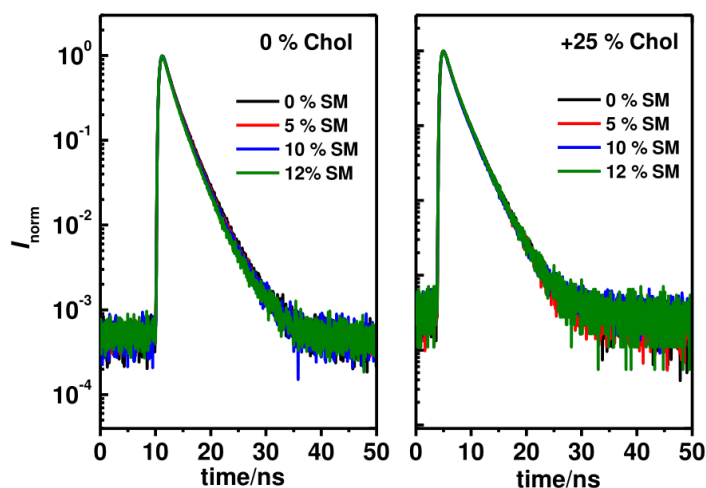

Figure SI2. Time-resolved fluorescence decays for Atto-488-DOPE in the presence of Atto-633-DOPE in DOPC/SM (100-x/x) (left panel) or DOPC/Chol/SM (75-x/25/x) (right panel) lipid mixtures with variable amounts of SM.

2) g-GM$_1$/DiD: Here, donors are accumulated in L$_o$ regions of the bilayer whereas acceptors are efficiently excluded from them (Table 2 in the manuscript). Therefore, existence of L$_o$ nanodomains should significantly decrease FRET efficiency, as the donors are driven apart from the acceptors. No such behavior was found in the time resolved fluorescence decays (Fig. SI3) as SM content in the bilayer was increased; thus further supporting the disordered character of the nanodomains.
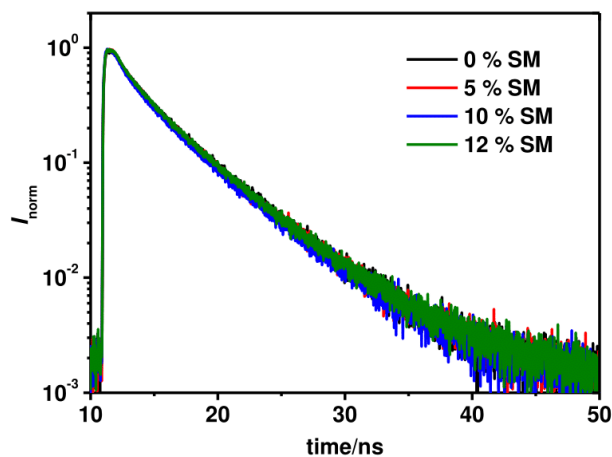
Figure SI3. Time-resolved fluorescence decays for g-GM$_1$ in the presence of DiD acceptors. The GUVs consisted of DOPC/Chol (75/25) (no nanodomains, black) or DOPC/Chol/SM (70-63/25/5-12) (containing nanodomains, red, blue, olive), respectively.

FRET as an indicator of bilayer condensation/expansion. It is important to realize that condensation of the lipid bilayer as well as accumulation of the probes in the nanodomains brings donors and acceptors closer to each other. As seen by FRET, these two phenomena may interfere with each other. For this reason, condensation of the lipid bilayer has to be considered when drawing conclusions about the nanodomain sizes and concentrations. In this work, no condensation of the bilayer occurred when SM content in the bilayer increased and the nanodomains formed. Therefore, no special corrections were necessary. This is documented by the constant FRET efficiency between Atto-488-DOPE and Atto-633-DOPE and between g-GM$_1$ and DiD as shown in Figs. SI2 and SI3.

FRET as a tool to measure size and concentration of the nanodomains. As described in detail in the manuscript as well as in[4], the MC-FRET approach is based on fitting time-resolved fluorescence decays with simulated decays whose shape depends, among other input simulation parameters, on the size and concentration of the nanodomains and K_Ds. Representative chi-squared maps are shown in Figs. SI4 and SI5. The maps in Fig. SI4 were made for such K_D for which the best fit to the experimental data was obtained. Minima in the chi-squared parameter were found in DOPC/Chol/SM (65/25/10) bilayer at the nanodomain radius $R_D = 9$ nm and the fractional domain area $Ar = 45$ % when using g-GM$_1$/r-GM$_1$ or at $R_D = 8$ nm and $Ar = 55$ % when using CF-PEG-DSPE/Rh-PEG-DSPE donor-acceptor pair. The maps of Fig. SI6 show the chi-squared values for four different K_Ds, demonstrating a fact that the position and depth of the global chi-squared minimum for the GM$_1$ probes in DOPC/Chol/SM (65/25/10) bilayers is practically constant for K_D ≥ 20.
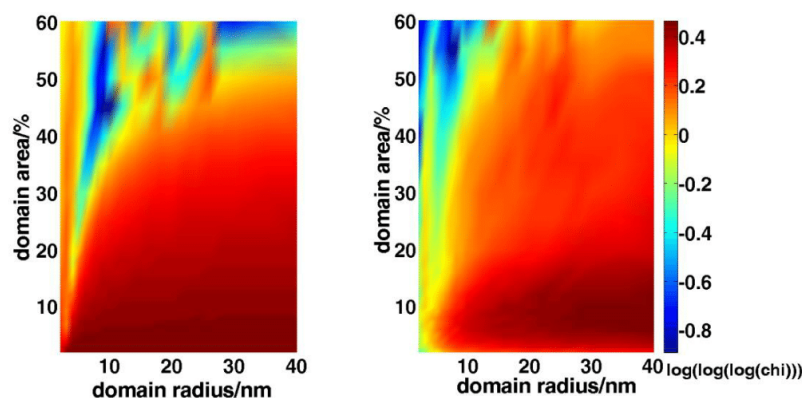

Figure SI4. Chi-squared maps obtained after fitting experimental decays by the MC-FRET approach. The lipid mixture consisted of DOPC/Chol/SM (65/25/10). The domain sizes and concentration were determined by either g-GM$_1$/r-GM$_1$ (left panel) or CF-PEG-DSPE/Rh-PEG-DSPE (right panel) donor-acceptor pair. The chi-squared maps are shown for K_D(g-GM$_1$, r-GM$_1$)

= 1000 and K_D(CF-PEG-DSPE, Rh-PEG-DSPE) = 10, i.e. for such K_D values for which the best fit to the experimental data was obtained. To improve visibility of the chi-squared minima, *chi*, log(log(log(*chi*))) is displayed in the figure.
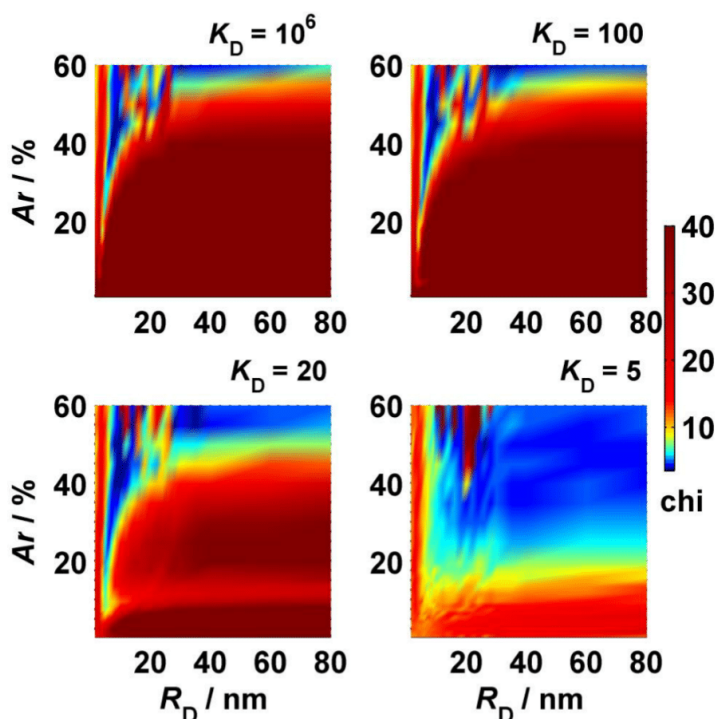

Fig. SI5: chi-squared minima (chi) for a set of different distribution coefficients K_D of g-, r-GM$_1$ probes. Specifically, the global minimum in chi-squared for K_D = 20 is only about 0.5 % lower than the minimum for K_D = 1000. The lipid mixture consisted of DOPC/Chol/SM (65/25/10).

Variability of nanodomain size and the fractional area occupied by the nanodomains between individual GUVs. Interestingly, variability in the nanodomain size and concentration between individual GUVs was extremely low. This can be documented by overlapping time-resolved fluorescence decays obtained from different GUVs of the same sample (see Fig. SI6). These decays were used to calculate the size and fractional area of the nanodomains in lipid
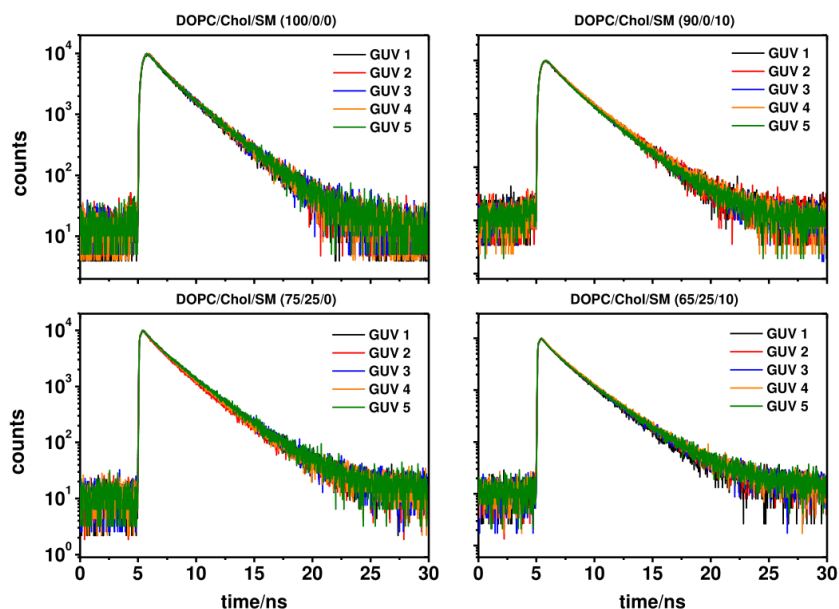
bilayers

Figure SI6: Time-resolved fluorescence decays of CF-DSPE-PEG in the presence of Rh-DSPE-PEG acceptors obtained from individual GUVs for four different bilayer compositions.

How many DOPC, Chol and SM molecules does a single nanodomain contain? Since nothing was *a priori* known about the distribution of individual lipids between the nanodomains and the remaining bilayer, two extreme situations were assumed: 1) Lipids are distributed equally between the nanodomains and the rest of the bilayer; 2) Lipid molecules of a given type are exclusively localized inside the nanodomains. The calculation of the number of lipid molecules in a domain is straightforward in both cases:

Situation 1: $N_{\text{inside}}^{i} = \pi R_D^2 A r x^i / a_0$ (5)

Situation 2: $N_{\text{inside}}^i = \pi R_D^2 x^i / a_0$ (6)

N_{inside}^i is the number of lipid molecules of type i inside a domain, R_D is the domain radius, Ar the total area occupied by the domains, x^i the molar ratio of the i-th lipid and, finally, a_0 the average lipid headgroup area. In this rough estimate, a constant value of a_0 was assumed for each different type of lipid.

Analysis of z-scan FCS data. Z-scan FCS is a technique by which absolute diffusion coefficients D in a planar bilayer can be obtained. This is achieved by measuring fluorescence autocorrelation functions (ACF) at well-defined positions along the optical axis of the microscope (the z axis). The acquired ACFs are fitted to a model that assumes Brownian diffusion of a dye in a two-dimensional surface and transition of the dye to the triplet state[5]

$$G(\tau) = 1 + \frac{1}{PN} \frac{1}{1+(\tau/\tau_D)} \frac{1-T+T\exp(-\tau/\tau_T)}{1-T} \qquad (7)$$

Here τ is a so-called lag-time, PN is the particle number, τ_D the dye diffusion time, T the fraction of the dye in the triplet state and τ_T the lifetime of the triplet state. Due to the Gaussian beam profile, τ_{2D} and PN values follow a parabolic dependence with Δz, which allows for the determination of D according to[6]

$$\tau_{2D} = \frac{w_0^2}{4D} \left(1 + \frac{\lambda^2 \Delta z^2}{\pi^2 n^2 w_0^4}\right) \qquad (8)$$

where n is the refractive index, λ is the excitation wavelength and Δz the distance between the actual sample position and a reference position z_0.

t-test confirms the significance of the desrease in the diffusion coefficient due to the presence of nanodomains. To test the significance of the drop in the diffusion coefficient after

nanodomains were formed a so-called t-test was performed (Tables SI2 and SI3). This test can be used to determine if two sets of data are significantly different from each other. It provides a parameter called p-value, which determines the significance of the drop in D. p-values lower than 0.1 or 0.05, respectively, determine a significant change in D. In Tables SI2 and SI3 D in a homogeneous bilayer (no nanodomains) is compared with D in a heterogeneous bilayer (with nanodomains). For instance, the lipid mixture DOPC/Chol/SM (100/0/0) is compared with the mixtures DOPC/Chol/SM (90,88,85/0/10,12,15).

Table SI2: Statistical test (t-test) of the significance of the drop in the diffusion coefficient that was caused by the formation of nanodomains in DOPC/SM (90-85/10-15) mixtures (compare with Fig. 4 in the manuscript). The drop is considered significant when the p-value obtained from the t-test is lower than 0.1.

DOPC	Chol	SM	nanodomains	probe	$D[\mu m^2/s]$	p-value	drop in D
100	0	0	NO	g-GM$_1$	9.4 ± 0.29	-	-
90	0	10	YES	g-GM$_1$	8.9 ± 0.43	0.0752	Significant
88	0	12	YES	g-GM$_1$	9.1 ± 0.30	0.1451	Insignificant
85	0	15	YES	g-GM$_1$	8.6 ± 0.23	0.0016	Significant
100	0	0	NO	DiD	10.0 ± 0.35	-	-
90	0	10	YES	DiD	9.9 ± 0.19	0.7073	Insignificant
88	0	12	YES	DiD	9.7 ± 0.32	0.2814	Insignificant
85	0	15	YES	DiD	9.4 ± 0.25	0.0697	Significant

Table SI3: Statistical test (t-test) of the significance of the drop in the diffusion coefficient that was caused by the formation of nanodomains in DOPC/Chol/SM (70-65/25/5-10) mixtures (compare with Fig. 4 in the manuscript). The drop is considered significant when the p-value obtained from the t-test is lower than 0.1.

DOPC	Chol	SM	nanodomains	probe	$D[\mu m^2/s]$	p-value	drop in D
100	25	0	NO	g-GM$_1$	9.1 ± 0.15	-	-
70	25	5	YES	g-GM$_1$	8.2 ± 0.42	0.0036	Significant
67	25	8	YES	g-GM$_1$	8.1 ± 0.26	0.0000	Significant
90	25	10	YES	g-GM$_1$	7.2 ± 0.25	0.0000	Significant
63	25	12	unstable comp.	g-GM$_1$	8.35 ± 0.63	0.0270	Significant
100	25	0	NO	DiD	9.2 ± 0.40	-	-
70	25	5	YES	DiD	9.3 ± 0.47	0.3533	Insignificant
67	25	8	YES	DiD	8.7 ± 0.12	0.0028	Significant
90	25	10	YES	DiD	8.3 ± 0.20	0.0002	Significant
63	25	12	unstable comp.	DiD	8.9 ± 0.16	0.3200	Insignificant

As follows from Tables SI2 and SI3, formation of nanodomains both in DOPC/SM and DOPC/Chol/SM mixtures leads except of one case to a significant decrease in D when using g-GM$_1$ probes. Diffusion of these probes is influenced by the presence of the nanodomains to a large extent because they are localized preferentially in the nanodomains. On the other hand, DiD probes are distributed equally between the nanodomains and the remaining bilayer, which hampers any impact of the nanodomains on the diffusion.

Synthesis of Rh-PEG-DSPE. 5 mg (1.7 μmole) DSPE-PEG2000 were dissolved in 100 μl of dried chloroform and mixed with a solution of rhodamine 101 (0.2 mg, 0.3 μmole) in 50 μl of dried chloroform, 10 μl (10 μl /100 μl of chloroform) of triethylamine and 1 mg (0.3 μmole) BOP. The reaction mixture was stirred for 1.5 h at 4 °C and kept at 0 °C overnight. The reaction mixture was evaporated and dissolved in 100 μl of chloroform. Rh-PEG-DSPE was separated by column chromatography (Silica gel 60, Merck) in chloroform : methanol : H$_2$O, 65:25:1 (v/v). After evaporation, 0.42 mg (0.13 μmol, 38 %) of Rh-DSPE-PEG2000 was obtained as a red powder.

Chemicals. 1,2-dioleoyl-*sn*-glycero-3-phosphocholine (DOPC), GM$_1$ ganglioside (Ovine brain sodium salt), N-stearoyl-D-erythro-sphingosylphosphorylcholine (SM), cholesterol, 1,2-

dipalmitoyl-*sn*-glycero-3-phosphoethanolamine-N-(cap biotinyl) (biotinyl-PE) and 1,2-distearoyl-*sn*-glycero-3-phosphoethanolamine-N-poly(ethyleneglycol)2000 labelled in the headgroup region by carboxyfluorescein (CF-PEG-DSPE) were purchased from Avanti Polar Lipids (Alabaster, AL, U.S.A.) and used without further purification. DiIC18(5)-DS (DiD) was purchased from Invitrogen (Carlsbad, CA) whereas Streptavidin and biotin labeled bovine serum albumin (biotin-BSA) were purchased from Sigma (St. Louis, MO). DOPE labeled in the headgroup region by Atto-488 (Atto-488-DOPE) or by Atto-633 (Atto-633-DOPE), respectively, was bought from ATTO-TEC GmbH. Synthesis of FL-BODIPY-GM$_1$ (g-GM$_1$)[7] and of 564/570-BODIPY-GM$_1$ (r-GM$_1$)[8] has already been described previously. The synthesis of 1,2-distearoyl-*sn*-glycero-3-phosphoethanolamine-N-poly(ethyleneglycol)2000 labeled in the headgroup region by Rhodamine-101 (Rh-PEG-DSPE) is described in SI. The following compounds were used for the synthesis: 1,2-distearoyl-*sn*-glycero-3-phosphoethanolamine-N-[amino(Polyethyleneglycol)2000]ammonium salt (DSPE-PEG2000, purchased from Avanti Polar Lipids), Rhodamine 101 perchlorate (Lambda Physik, Germany), triethylamine (Fluka), benzotriazol-1-yloxytris-(dimethylamino)-phosphonium hexafluorophosphate (BOP, purchased from Fluka) and silica gel 60 (40-63 μm, purchased from Merck GmbH). All solvents used here were of at least analytical grade.

References

1. Johansson, L. B.-Å., Engström, S. & Lindberg, M. Electronic-Energy Transfer in Anisotropic Systems. 3. Monte-Carlo Simulations of Energy Migration in Membranes. *J. Chem. Phys.* **96,** 3844–3856 (1992).
2. Marushchak, D., Gretskaya, N., Mikhalyov, I. & Johansson, L. B.-Å. Self-aggregation - an intrinsic property of G(M1) in lipid bilayers. *Mol. Membr. Biol.* **24,** 102–112 (2007).
3. Sezgin, E. *et al.* Partitioning, diffusion, and ligand binding of raft lipid analogs in model and cellular plasma membranes. *Biochim. Biophys. Acta - Biomembr.* **1818,** 1777–1784 (2012).
4. Šachl, R., Johansson, L. B.-Å. & Hof, M. Förster resonance energy transfer (FRET) between heterogeneously distributed probes: Application to lipid nanodomains and pores.

Int. J. Mol. Sci. **13,** 16141–16156 (2012).

5.   Widengren, J., Mets, Ü. & Rigler, R. Fluorescence Correlation Spectroscopy of Triplet States in Solution: A Theoretical and Experimental Study. *J.Phys.Chem.* **99,** 13368–13379 (1995).

6.   Benda, A. *et al.* How to determine diffusion coefficients in planar phospholipid systems by confocal fluorescence correlation spectroscopy. *Langmuir* **19,** 4120–4126 (2003).

7.   Bergström, F. *et al.* Dimers of dipyrrometheneboron difluoride (BODIPY) with light spectroscopic applications in chemistry and biology. *J. Am. Chem. Soc.* **124,** 196–204 (2002).

8.   Marushchak, D., Gretskaya, N., Mikhalyov, I. & Johansson, L. B.-Å. Self-aggregation - an intrinsic property of G(M1) in lipid bilayers. *Mol. Membr. Biol.* **24,** 102–112 (2007).

On multivalent receptor activity of GM1 in cholesterol containing membranes

On multivalent receptor activity of GM1 in cholesterol containing membranes ☆

Radek Šachl [a,1], Mariana Amaro [a,1], Gokcan Aydogan [a], Alena Koukalová [a,c], Ilya I. Mikhalyov [b], Ivan A. Boldyrev [b], Jana Humpolíčková [a,*], Martin Hof [a]

[a] Department of Biophysical Chemistry, J. Heyrovsky Institute of Physical Chemistry of the Academy of Sciences of the Czech Republic, Dolejškova 2155/3, Prague 8, Cz-182 23, Czech Republic
[b] Shemyakin- Ovchinnikov Institute of Bioorganic Chemistry of the Russian Academy of Science, Ul. Miklukho-Maklaya, 16/10, 117997 Moscow, GSP-7, Russian Federation
[c] Faculty of Science, Charles University in Prague, Albertov 6, 128 43, Prague 2, Czech Republic

ABSTRACT

Gangliosides located at the outer leaflet of plasma membrane are molecules that either participate in recognizing of exogenous ligand molecules or exhibit their own receptor activity, which are both essential phenomena for cell communication and signaling as well as for virus and toxin entry. Regulatory mechanisms of lipid-mediated recognition are primarily subjected to the physical status of the membrane in close vicinity of the receptor. Concerning the multivalent receptor activity of the ganglioside GM1, several regulatory strategies dealing with GM1 clustering and cholesterol involvement have been proposed. So far however, merely the isolated issues were addressed and no interplay between them investigated. In this work, several advanced fluorescence techniques such as Z-scan fluorescence correlation spectroscopy, Förster resonance energy transfer combined with Monte Carlo simulations, and a newly developed fluorescence antibunching assay were employed to give a more complex portrait of clustering and cholesterol involvement in multivalent ligand recognition of GM1. Our results indicate that membrane properties have an impact on a fraction of GM1 molecules that is not available for the ligand binding. While at low GM1 densities (~1 %) it is the cholesterol that turns GM1 headgroups invisible, at higher GM1 level (~4 %) it is purely the local density of GM1 molecules that inhibits the recognition. At medium GM1 content, cooperation of the two phenomena occurs. This article is part of a Special Issue entitled: Nanoscale membrane organisation and signalling.

© 2014 Elsevier B.V. All rights reserved.

1. Introduction

Glycosphingolipids (GSLs), ceramide-derived lipid moieties with an oligosaccharide attached to the headgroup, are often localized on cell surfaces where they act as receptor molecules for various protein ligands. Therefore GSLs are often involved in cellular signaling and communication as well as in virus or toxin entry. GSLs (ganglioside GM1 in particular) serve not only as receptor molecules directly but were also found to modulate function of other membrane receptors usually by association with the particular membrane protein [1].

Apart from the regulation of receptor ligand recognition occurring at the level of GSL expression, several regulatory mechanisms based on membrane lipid-lipid interactions have been proposed.

GSLs due to the ceramide hydrophobic moiety are known to preferably interact with sphingomyelins which results in their segregation into liquid ordered (L_o) phase in model membranes or into the so called lipid "rafts" in living cells. This potentially gives rise to the biophysical, lipid-mediated origin of a signaling regulatory mechanism. For example, clustering of GM1 containing lipid rafts has been shown to signal β1 integrins in T-cells and by that activate strengthening of their adhesion [2].

Furthermore, cholesterol has been indicated to have an essential role in regulating the receptor activity of GSLs [3]. Cholesterol-related "masking" of GSLs turning them unavailable for ligands has been related to a tilt of glycolipid headgroup. Cholesterol was predicted to make the oligosaccharide moiety lean over the membrane surface instead of sticking out of the bilayer, which reduces the surface recognition capacity. This was, for example, demonstrated to work during sperm activation [4].

☆ This article is part of a Special Issue entitled: Nanoscale membrane organisation and signalling.
 * Corresponding author. Tel.: +420 266053142; fax: +420 28658 2307.
  E-mail addresses: radek.sachl@jh-inst.cas.cz (R. Šachl), mariana.amaro@jh-inst.cas.cz (M. Amaro), gokcan.aydogan@jh-inst.cas.cz (G. Aydogan), alenakoukalova@seznam.cz (A. Koukalová), ilya.mikhalyov@gmail.com (I.I. Mikhalyov), ivan@lipids.ibch.ru (I.A. Boldyrev), jana.humpolickova@jh-inst.cas.cz (J. Humpolíčková), martin.hof@jh-inst.cas.cz (M. Hof).
 [1] Contributed equally to this work.

Apart from the interactions of the aglycone there is also a significant contribution of the glycane-glycane binding in the headgroup region. The network of hydrogen bonds stabilizes the cooperative interactions between the sugar residues allowing them to cluster even in phosphatidylcholine bilayers. The clustering itself can serve as a regulatory mechanism of ligand recognition becoming especially important when the multivalent ligand-receptor interaction is discussed. In the work of Shi et al. [5], the regulation of pentavalent carbohydrate-protein binding, represented by GM1 – cholera toxin B (CTxB), is demonstrated on the model system of supported lipid bilayers. In the GM1 clusters the distance between GM1 molecules was concluded to not fit the binding sites of CTxB anymore and thus some GM1 became unavailable.

As indicated, strategies regulating ligand recognition use various mechanisms and apparently, in the complex system of cellular plasma membrane, interplay between them most probably occurs resulting from local variations in cholesterol, saturated lipids and/or GSLs content. The aim of this manuscript is to shed light on two aspects of the regulation, particularly on cholesterol driven changes in GM1 availability and on the tendency of GM1 molecules to cluster. The clustering ability of GM1 is promoted by oligo-saccharide moieties in the headgroup region. Thus, in order to address specifically the sugar related behavior, we have performed our experiments on DOPC containing membranes, where tail-to-tail interaction are lowered compared to mixtures containing saturated lipids. In the model system of giant unilamellar vesicles (GUVs) consisting of DOPC/cholesterol (Chol)/GM1, we utilize i) Förster resonance energy transfer (FRET) between various FRET pairs in combination with Monte Carlo (MC) simulations, and ii) Z-scan fluorescence correlation spectroscopy (FCS) [6] in order to characterize the size and nature of GM1 clusters in cholesterol containing and cholesterol free membranes.

Next, we develop a binding assay based on the counting of individual emitters via a fluorescence antibunching technique [7], which allows for measuring the number of GM1 lipids in the membrane as well as the number of bound toxins.

By this we can clearly demonstrate that clustering of GM1 occurs even in bilayers containing solely DOPC and, in addition to that, it is completely independent on the cholesterol content. While cholesterol does not seem to have an impact on the aggregation of GM1 molecules, its content is still essential for GM1 recognition by CTxB. We show however that the GM1 clusters change their nature at increased GM1 levels (~4 %) as the GM1 molecules become denser and thus prevent sugar headgroups from being available for the binding of the pentavalent CTxB ligand. At this stage, it is the clustering mechanism that prevails over the cholesterol modulation of GM1 and cholesterol is no longer involved in the ligand recognition.

Eventually we explore the role of the ligand in GM1 organization. We show that upon CTxB binding, the character of the nano-clusters changes substantially. While their size remains the same, their rigidness and permeability becomes significantly affected resulting from an increased GM1/DOPC ratio.

2. Materials and methods

2.1. Chemicals

1,2-dioleoyl-sn-glycero-3-phosphocholine (DOPC), GM1 Ganglioside (Ovine brain sodium salt), cholesterol, and 1,2-dipalmitoyl-*sn*-glycero-3-phosphoethanolamine-N-(cap biotinyl) (biotinyl Cap PE) were purchased from Avanti Polar Lipids (Alabaster, AL, U.S.A.) and used without further purification. DilC$_{18}$(5)-DS (DiD), Alexa Fluor® 488 labeled CTxB (CTxB-488) were purchased from Invitrogen (Carlsbad, CA). Streptavidin, biotin labeled bovine serum albumin (biotin-BSA), and CTxB were purchased from Sigma (St. Louis, MO). DOPE was covalently labeled by Atto655-NHS-ester (Siegen, Germany) and purified by adsorption

chromatography on silica gel column Kieselgel 60 (Merck, Whitehouse Station, NJ, U.S.A.) in chloroform/methanol/water (60/25/4) eluent. Synthesis of FL-BODIPY-GM1 and of 564/570-bodipy-GM1 is described elsewhere [8].

2.2. GUV preparation

GUVs for fluorescence microscopy were prepared by the electroformation method using titanium chambers as described by Angelova et al. [9] Lipid mixtures were made from stock solutions in chloroform. The overall amount of all lipids (100 nmol in approximately 200 μL of chloroform) together with the labeled lipids was spread onto two hollowed titanium plates which were placed on a heater plate at approximately 50 °C to facilitate solvent evaporation and subsequently put under high vacuum for at least 1 h for evaporation of remaining traces of solvent. The lipid-coated plates were assembled using one layer of Parafilm for insulation [10]. The electroswelling chamber was filled with 1 ml preheated sucrose solution (100 mM sucrose, and osmolarity of 103 mOsm/kg) and sealed with Parafilm. An alternating electrical field of 10 Hz rising from 0.02 V to 1.1 V (peak-to-peak voltage) in the first 45 min was applied and then kept at 1.1 V for additional 2.5 h at 55 °C, followed by 30 min of 4 Hz and 1.3 V to detach the formed liposomes. Finally, the GUVs were placed in a microscopy chamber containing glucose buffer (~80 mM glucose, 10 mM HEPES and 10 mM NaCl, pH 7.2) with an osmolarity of 103 mOsm/kg. All lipid mixtures contained 2 mol % of biotinyl Cap PE for immobilization of GUVs on BSA-biotin/streptavidin coated bottom of the chamber.

For the FCS experiments probe-to-lipid ratio was around 1:100000, *i.e.* 0.0001 %. For the FRET experiments the donor(acceptor)-to-lipid ratio 1:1000, *i.e.* 0.01 % (1:200, *i.e.* 0.5 %) was chosen in the case of g-GM1/DiD pair; and 1:200, *i.e.* 0.5 % for both donor- and acceptor-to-lipid ratio in the case of g-GM1/r-GM1 pair.

2.3. LUV preparation

For LUV formation the appropriate mixture containing 10^{-6} mol of DOPC/Chol (at given ratio) and 10^{-8} to 4×10^{-8} mol of GM1 was prepared in chloroform. GM1 contained a labelled lipid (Atto655-DOPE) in a well-defined ratio (GM1/Atto655-DOPE, 606:1) in order to be able to estimate the amount of GM1 via antibunching. The chloroform was evaporated using a rotary evaporator and the lipid film re-hydrated with 1 mL buffer solution (~80 mM glucose, 10 mM HEPES and 10 mM NaCl, pH 7.2). The turbid solution containing multilamellar vesicles was extruded 10 times with use of 100 nm filters in a LIPEX extruder (Northern Lipids Inc, Canada) [11].

2.4. FCS and FLIM-FRET

Both types of measurements were performed on a home-built confocal microscope consisting of an inverted confocal microscope body IX71 (Olympus, Hamburg, Germany). Pulsed diode lasers (LDH-P-C-470, 470 nm, and LDH-D-C-635, 635 nm PicoQuant, Berlin, Germany) with 10 MHz repetition rate each were used. The lasers were pulsing alternatively in order to avoid artifacts caused by signal bleed-through. The laser light was coupled to a polarization maintaining single mode optical fiber and at the output re-collimated with an air space objective (UPLSAPO 4X, Olympus). The light was up-reflected to a water immersion objective (UPLSAPO 60x, Olympus) with a 470/635 dichroic mirror. The signal was split between two single photon avalanche diodes using 515/50 and 697/58 band pass filters (Chroma Rockingham, VT) for green and red channel, respectively. In the case of FCS measurements, laser intensity at the back aperture of the objective was around 10 μW for each laser line. The z-scan was performed on the top of selected unilamellar liposomes. Membrane was first placed to the laser beam waist, then moved 1.5 μm below the waist and consequently vertically scanned in 20 steps (150 nm spaced). At every position a 60 second

measurement was performed. Details of the data analysis are given elsewhere [6b]. For the FLIM-FRET measurements the lasers' intensities were chosen low enough to avoid pile-up effect, i.e. around 1 μW for 470 nm and less than 0.1 μW for 635 nm. Each GUV was scanned at the cross-section and an image of 512 × 512 pixels (0.6 ms/pixel) was acquired. Details of the MC simulations are given in SI.

2.5. Antibunching

The confocal setup for antibunching was the same as for FCS measurements. Either 470 nm or 635 nm pulsed diode laser was used for excitation with repetition frequency 20 MHz. To achieve detection of two nanosecond and sub-nanosecond delayed consecutive photons the signal was split between two independent detectors connected to independent electronic circuits (Hydraharp, PicoQuant, Germany). Two identical emission filters were placed in front of each detector (515/50 for green emission and 697/58 in combination with a 775 short pass filter, to block the far IR light, for red emission) to prevent detector afterglow. The autocorrelation function is calculated by crosscorrelating the signal from the two detectors. Correlation and subsequent data analysis was done with home-written scripts in Matlab (Mathworks, Natick, MA). Details are given in SI.

2.6. Binding assay

100 nm LUVs consisting of DOPC/Chol/GM1 in a given ratio were prepared. Stock solution of GM1 contained a defined fraction of Atto655-DOPE. Number of Atto655-DOPE was measured via antibunching. This allowed for estimating how many GM1 molecules were present in a single LUV. Then the LUV solution was titrated with a mixture of Alexa488-labeled/non-labeled CTxB (1/60). During the titration the number of labeled CTxB was evaluated. Once the surface became fully saturated by CTxB the maximum of labeled toxin per LUV was reached and the average number of emitters per complex started to drop due to contribution of unbound labeled CTxB from the solution. Eventually, information on the amount of available GM1 and amount of bound toxin was obtained.

3. Results and discussion

3.1. Clustering of GM1 in presence/absence of cholesterol

3.1.1. FRET combined with MC simulations

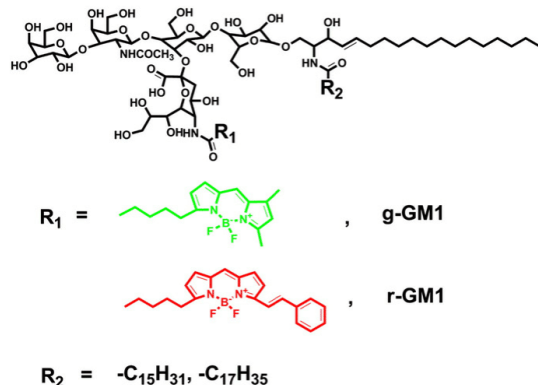To address the issue of GM1 clustering, FRET between FL- and 564/570-BODIPY-head-labeled GM1 (g-GM1 = green-GM1, r-GM1 = red-GM1) [8a,12] molecules was investigated. The structures of the donor and acceptor are given in Fig. 1.

As long as donors (g-GM1) and acceptors (r-GM1) are homogeneously distributed in the membrane, the donor fluorescence decay becomes shortened as a result of donor-acceptor interactions occurring at various distances within the same membrane leaflet as well as across the membrane. Such situation, assigning every donor-acceptor distance a certain probability of energy transfer, is described analytically via the Baumann-Fayer (B-F) model [13]. The electric dipole moments of the probes are supposed to be randomly distributed or reorient fast with respect to FRET. As long as the donor decay can be reconstituted with the B-F model and providing reasonable acceptor concentrations the distribution of donors and acceptors can be, within the resolution capability of FRET [14], considered homogenous. Once the GM1 containing clusters (domains) are formed, g- and r-GM1 molecules are dragged closer to one another, the level of FRET increases and fails to follow the B-F model. Instead, MC simulations [15] accounting for an inhomogeneous distribution of donors and acceptors are carried out providing information on the size of the clusters and overall percentage of the bilayer occupied by those clusters.

Both the DOPC and DOPC/Chol (70/30) GUVs were labeled with a 1:1 mixture of g-GM1 and r-GM1 (1 % of both lipids in total). The donor fluorescence decay was in both the discussed cases well described by the B-F model suggesting a homogeneous distribution of g- and r-GM1 molecules. Upon adding non-labeled GM1 molecules the donor decay becomes significantly faster, i.e. FRET between the g-GM1 and r-GM1 increases suggesting that GM1 containing domains are formed (Fig. 2a, Fig. S4a). The donor decay changes upon addition of 1 % of GM1 and then remains unchanged up to relatively high content of GM1 (~8 %). The fact that the change in FRET occurs instantly in narrow range of added GM1 and is not followed by further development suggests: i) labeled GM1 molecules do not constitute domains on their own, yet interact with them once they are established; ii) the formed domains do not change in size and overall amount when excess of GM1 is added, suggesting that their nature is affected by the increasing GM1 content.

To confirm i), we have used an alternative FRET pair consisting of green (Me)₄bodipy-tail-labeled lipid (B7PC) [16] as a donor and r-GM1 as an acceptor. Use of this FRET pair allowed us for reducing the amount of labeled GM1 to one half (0.5 %). B7PC most probably does not show any preference in partitioning (similar to DiD, see further). Therefore, when domains are formed, contributions from the domains (increased FRET) and from the outside membrane region (lowered FRET) are to be expected. The latter one would prevail as more B7PC molecules are involved. The change in FRET occurs already at 0.5 % added GM1 and does not significantly develop with further increase of GM1 (see Fig. S6
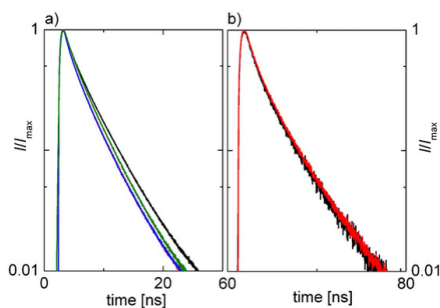

Fig. 1. Structures of FL- and 564/570-BODIPY-head-labeled GM1 (g-GM1, r-GM1).

Fig. 2. Donor fluorescence decays of g-GM1. a) FRET between g-GM1 (1/200, 0.5 %) and r-GM1 (1/200, 0.5 %) in DOPC bilayer at 0 % (black), 1 % (red), 4 % (blue) added unlabeled GM1, saturation with CTxB (olive). b) FRET between g-GM1 (1/1000, 0.1 %) and DiD (1/100, 1 %) in DOPC bilayer at 0 % (black), 2 % (red) added unlabeled GM1. Ratio given in brackets corresponds to the donor (acceptor) – lipid ratio.

and the corresponding discussion). All together it turns out, that the amount of labeled GM1 does not impact the changes occurring when non-labeled GM1 is added, i.e. it is evident the labeled GM1 does not constitute the domains, but becomes incorporated in them when they are established. In addition to that, the experiment proves that GM1 clustering occurs already at concentrations below 1 %, which can be barely but still visible with the g-GM1/r-GM1 pair as the amount of the label necessary exceeds the amount of the added GM1 (see Fig. S5 in SI).

Considering the g-GM1/r-GM1 pair, the donor decays displaying FRET enhancement were analyzed by means of MC simulations (Table 1). The size as well as the average area domains occupy does not change with increasing level of GM1. Both the domain radius of around 5-7 nm and the area they occupy (~40 %), as well as the fact that there is no change of the two parameters when more GM1 is present seems to be in accordance with the available AFM data acquired for supported lipid bilayers [5]. The study of Shi et al give the AFM based diameters of the domains as follow: 13.6 nm for 1 % GM1, 15.3 nm for 3 % GM1, and 18.6 nm for 5 % GM1, which we find well corresponding to our results of the FRET data. Furthermore, visual inspection of the AFM images given in the discussed work also suggests that the overall domain area exceeds significantly the GM1 content in the bilayer.

The experiment was also performed with POPC replacing the DOPC lipid (see Fig. S7 in SI). The extent of the FRET change upon GM1 addition is slightly lower when POPC is used. Fit results in Table 1 suggest that the domains are larger in both the cholesterol free and cholesterol containing systems. While the difference between POPC and DOPC is rather small, it suggests that the increasing level of saturated lipids stabilize the domains in the tail region. While at low level of saturated lipids, the domains formation is solely driven by GM1 and its sugar-related behavior, at larger level of lipid saturation, it will be the saturated lipids that would govern domain creation and their properties.

Table 1 provides also estimated number of individual lipids present in the domains. The estimation assumed that all GM1 molecules are present in the domains, that cholesterol fraction is the same in the domains and outside of them, that the average area per lipid is 72 Å^2 for cholesterol free bilayer and 64 Å^2] for bilayer containing 30 % of cholesterol [17]. GM1 contribution to the overall area was neglected.

The overall surface covered by domains, which reaches around 40 % even in the systems containing only 1 % of GM1, is worth discussion. The area the domains occupy is largely subjected to partitioning of the labeled GM1 between the GM1 domains and the outside bilayer. Since such knowledge would be hard to obtain, we run our MC simulations for several values of K_d. The endeavor to obtain lower, intuitively more appropriate, domain areas failed as fitting provided us with shallow chi^2 minima or did not converge at all. Moreover, not only MC-FRET but also literature available AFM images of GM1 containing membranes suggest the presence of domains with overall area largely exceeding the

amount of GM1 in the membrane [5]. The evidence that 10 % GM1 causes formation of flower-shaped domains spanning over more than 40 % of DPPC/GM1 monolayer [18] confirms the high involvement of PC molecules in the discussed structures.

Assuming that all GM1 molecules compose the GM1 domains, the ratio DOPC/GM1 in the domains can be roughly estimated. It starts at about ~ 20/1 at 1 % GM1 and continues down to 4/1 at 8 % GM1 (see Table 1). Literature suggests non ideal mixing of GM1 and phosphatidylcholines (PCs) resulting in condensing effect of GM1 [18]. This has been attributed to the complexes GM1 forms with PCs with a stoichiometry of about 3 PC molecules to 1 GM1. With regard to the literature and as well as to the geometry of GM1, the ratios we observe far exceed theoretical number of PCs that may be stabilized by single GM1 molecule. A computational study of GM1 in fully hydrated DOPC bilayer [19] shows that GM1 molecules not only condense headgroup area of DOPC molecules in the first coordination sphere of GM1 (containing 2-3 DOPC molecules) but also shift the average mass of DOPC inside the bilayer due to the sugar moiety buried in the headgroup region of PCs. This results in a locally perturbed membrane that may require several DOPC molecules to accommodate such a perturbation to the remaining bilayer, which might explain the higher involvement of DOPC. Eventually merging of GM1-caused perturbations may be promoted in order to minimize the overall energetic penalty spent on the accommodation of the whole pool of GM1 rather than individuals. The fact that increasing amount of GM1 does not cause further development in FRET efficiency suggests that the pools of stabilized GM1 perturbations can accommodate more GM1 molecules as long as the ratio between DOPC and GM1 is below the stoichiometry of a complex of GM1 and PCs in the first coordination sphere (~2-3).

The idea that GM1 domains in DOPC and DOPC/Chol mixtures are rich in PC molecules is further supported by FRET experiments made on a pair consisting of g-GM1 (donor) and DiD (acceptor). Fig. 2b (Fig. S4b) shows that energy transfer from g-GM1 to DiD is insensitive to the presence of extra unlabeled GM1 revealing that the acceptor distribution has not been altered upon domain formation. No preferential partitioning of DiD (as well as of Atto655-DOPE, for which the very same result was observed with g-GM1 as acceptor, data not shown) indicates high permeability of the GM1 domains that can only be maintained if they are mainly composed of PC molecules, considering that GM1 is a ceramide derivative preferring higher lipid ordering.

FRET experiments (g-GM1/r-GM1, g-GM1/DiD) performed in GUVs composed of DOPC and cholesterol (up to 30 %) showed a behavior very similar to the one observed for cholesterol free GUVs (see Table 1). No evidence that cholesterol has an impact on GM1 clustering also indirectly supports the mentioned idea of GM1 pools containing almost isolated GM1 molecules. If GM1 molecules were in closer contact, cholesterol with its inverse cone-like structure would stabilize the locally enhanced number of GM1 cones, which would most probably result in a GM1 dependency of the overall domain area. As this does not occur, it follows

Table 1
Values of radii and overall domain areas obtained from MC-simulated fitting of FRET data for various donor-acceptor pairs at different membrane compositions, before and after CTxB binding. Number of lipids/CTxB molecules estimated for domains of a given radius and overall area.

DOP POPC*/%	Chol/%	Added GM1/%	CTxB	FRET pair	Radius/nm	Area/%	Number of lipids/toxin molecules in the domains. Number of lipids holds for both leaflets.						
							DOPC POPC*	Chol	GM1	labeled GM1	total GM1	CTxB pentamer	DOPC POPC*/all GM1
100	0	1;4;8	0	g-/r-GM1	5-7	35-45	314	0	8; 31; 63	8	16; 39; 72	NA	20; 8; 4
70	30	1;4;8	0	g-/r-GM1	5-7	35-45	247	106	9; 35; 71	9	18; 44; 80	NA	14; 6; 3
100*	0	4	0	g-/r-GM1	10	45	872*	0	78	19	97	NA	9*
70*	30	4	0	g-/r-GM1	7-8	45-55	386*	166	44	11	55	NA	7*
100	0	4	saturated	g-/r-GM1	8	55	558	0	39	10	49	2-3	11
70	30	4	saturated	g-/r-GM1	8	55	440	188	44	11	55	2-3	8
100	0	1	saturated	Alexa488-CTxB/DiD	7	50	427	0	9	0	9	1	47
70	30	1	saturated	Alexa488-CTxB/DiD	4,5	35	139	60	6	0	6	1	23
100	0	4	saturated	Alexa488-CTxB/DiD	6	45	314	0	28	0	28	2-3	11
70	30	4	saturated	Alexa488-CTxB/DiD	6	45	247	106	32	0	32	2-3	8

* Values obtained for POPC.

that DOPC remains the main partner of GM1 even when cholesterol is available.

3.1.2. Diffusion measurements

Z-scan FCS measurements were performed to investigate changes in diffusion of g-GM1 and DiD once the GM1 domains are established. Fig. 3 shows that at approximately 2 % of GM1 the diffusion of both labeled molecules significantly decreases. This confirms the conclusions made when discussing the FRET data: labeled GM1 as well as DiD – a lipid tracer which is known to strongly avoid partitioning into ordered lipid areas – interact with pools of GM1 molecules causing their diffusion to slow down. The drop in diffusion is observed independently on the presence of cholesterol, which is in accord with the FRET experiments. Below 2 % GM1 we do not observe changes in diffusion. This however does not exclude domain formation at even lower level of GM1 as we most probably get to the resolution limit of our approach.

The diffusion of g-GM1 shows no change with the increase of GM1 concentration from 2 % to 4 %. This suggests, and is supported by the FRET data, that the domains can accommodate the increasing number of GM1 molecules without significant changes in GM1 diffusion. GM1 molecules still move relatively independent of each other inside the domain.

3.2. Receptor activity of GM1

Recognition of multivalent ligands (CTxB) by GM1 molecules could be lowered if some GM1 molecules are "hidden" on the surface and thus are not available for binding. As suggested in previous works, this may arise from clustering [5] of the receptor and/or tilting of its headgroup [4]. In order to relate the overall number of GM1 to the number of CTxB bound to the GM1 containing surface we have designed a fluorescence antibunching based binding assay. In this case we apply the antibunching experiment (i.e. detecting photon pairs delayed by less than their fluorescence lifetime, details are given in SI) on freely diffusing molecular complexes of emitters in solution. The final histogram of the lag-times between two consecutive photons is an ensemble average of all transits of the individual complexes through the focal volume. When approaching zero lag-times the probability of detecting a photon pair decreases since one of the emitters in the complex, once it has emitted a photon, is turned off for several nanoseconds. The depth of the zero lag-time decrease provides a read-out on the number of emitters in the molecular complex.

The binding assay in this study is the following: large unilamellar vesicles (LUVs) containing a given amount of GM1 in an investigated lipid mixture are prepared. GM1 stock solution contains Atto655-DOPE in a given defined ratio, which serves as a GM1 tracer allowing for determination of the amount of GM1 per LUV. The ratio was optimized so that each LUV contains maximum ~ 10 labeled lipids. With the help of antibunching, labeled tracer molecules per LUV are counted
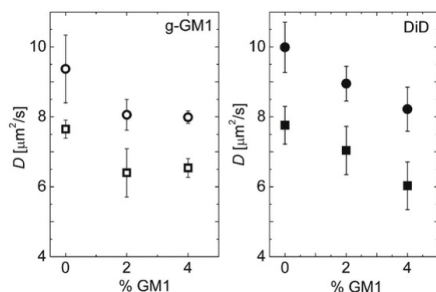
which provides a good overview on the amount of total GM1 in the LUVs. At the used concentration range the number of tracer molecules per LUV linearly scaled with increasing concentration of the tracer. This confirms that LUVs are molecular complexes large enough to prevent processes such as singlet-singlet annihilation that would "mask" some emitters [20]. The antibunching experiment done with the tracer molecule additionally confirms the unilamellar character of the LUVs, as the number of the tracer molecules per LUV detected by antibunching is in agreement with the estimated number assuming the unilamellarity. Further, the unilamellarity was tested by quenching experiments (see Fig. S3).

Then, the LUVs are titrated with a mixture of labeled/non-labeled CTxB and in every titration step the total number of emitting CTxB per LUV is counted. Since the dissociation constant for GM1-CTxB complexes is very low ($\sim 10^{-11}$ – 10^{-12} mol/L) [21], the GM1 containing surface is first fully saturated with the toxin and then, when no binding sites are available, free toxin appears in the solution. The titration curve (i.e. the dependence of emitting CTxB per LUV on the amount of added CTxB mixture) passes a maximum when all available GM1 lipids are involved and is followed by a sharp decrease caused by the contribution of non-complexed CTxB molecules from the solution to the fluorescence signal. Finally, the total number of receptor molecules as well as the total number of bound ligands is obtained.

Eventually, the performed titration experiments can also be evaluated in classical FCS-based manner, the results are in perfect agreement with the evaluation of antibunching (Fig. S2 in SI and corresponding discussion).

Antibunching was performed on LUVs containing 1 % of GM1. As we have shown already, at this level GM1 molecules are organized into domains but the amount of neighboring DOPC molecules is still high keeping them independent from one another. Fig. 4a depicts titration curves obtained for samples of LUVs containing various amounts of GM1. While the x-axis displays consumption of CTxB relative to the amount of GM1 added at sample preparation, the y-axis gives the ratio between the number of the toxin bound emitters (Alexa488) per molecular complex (LUV) and the number of GM1-tracing molecules (Atto655-DOPE) per LUV, both measured by antibunching. In other words, y-axis serves as a measure of capacity of LUV surface to bind the ligand which refers to the availability of GM1 for the recognition process. Both the toxin consumption as well as the titration maximum suggest that at 1 %
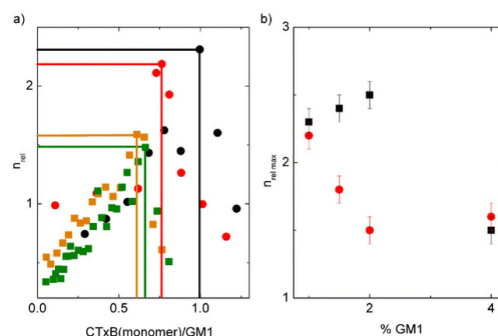

Fig. 4. a) Titration curves of GM1 containing LUVs with CTxB. x-axis stays for the ratio between overall added CTxB and GM1 concentrations. y-axis (n_{rel}) depicts number of antibunching-counted Alexa488 emitters (CTxB) divided by the number of tracer molecules per LUV, for each investigated lipid mixture. Maximum n_{rel} is directly proportional to the capacity of GM1 on the LUVs' surface to bind CTxB. The following lipid mixtures were investigated: DOPC + 1 % GM1 (DOPC/Chol/GM1 = 99/0/1 mol %) (black circles), DOPC/Chol (70/30) + 1 % GM1 (DOPC/Chol/GM1 = 69.3/29.7/1 mol %) (red circles), DOPC + 4 % GM1 (DOPC/Chol/GM1 = 96.2/0/3.8 mol %) (green squares), DOPC/Chol (70/30) + 4 % GM1 (DOPC/Chol/GM1 = 67.3/28.8/3.8 mol %) (orange squares). b) Maximum of the titration curve depicted as a function of the GM1 content for system without (black squares) and with cholesterol (red circles).

Fig. 3. Dependence of diffusion coefficient of g-GM1 (left) and DiD (right) on the amount of GM1 for DOPC (circles) and DOPC/Chol (70/30) (squares) bilayer.

GM1 the cholesterol containing LUVs bind less CTxB than LUVs that are cholesterol free.

The situation becomes different at 4 % GM1 because i) cholesterol content does not play role any more, CTxB binding is cholesterol insensitive; and ii) the availability of GM1 at 4 % is reduced compared to 1 %. This suggests that upon further addition of GM1 molecules the arrangement of the gangliosides becomes tighter causing a poorer match to the binding sites of the ligand which is also no longer sensitive to the presence of cholesterol.

Fig. 4b shows the dependence of the titration maxima as a function of GM1 content. Apparently below 2 % of GM1 in the cholesterol free LUVs, the GM1 availability remains unaltered with increasing GM1 density. However, with cholesterol the GM1 availability is lowered. This suggests that the presence of cholesterol act cooperatively with the effect of GM1 density as increasing density promotes the cholesterol impact. The role of cholesterol seems to comprise not only the suggested issue of the headgroup tilt[4] but also several other general aspects such as cholesterol condensing effect [17]. It is well known that not only cholesterol but also GM1 condenses lipid bilayers [18,19], and it has been shown that GM1 and cholesterol tend to co-localize [22]. Therefore cholesterol together with higher GM1 content may be responsible for high GM1 density in the domains and possibly also for high level of ordering. As it is the GM1 density that matters generally (also in the bilayer that does not contain cholesterol), it is very likely that cholesterol amplifies its impact. Also, reduced GM1 mobility in cholesterol containing membrane may render GM1 molecules less adaptable to the ligand binding sites.

In summary, the binding assays reveal that while cholesterol does not seem to impact the size and amount of GM1 domains its role in binding recognition is yet significant. The effect of cholesterol is subjected to the spatial density of clustered GM1 molecules. At low GM1 densities (1 %), a relatively little effect of cholesterol is observed, which could be assigned to cholesterol's ability to keep GM1 headgroups in the tilted conformation [4]. At increasing GM1 levels (1-2 %) cholesterol causes a drop in GM1's availability. Eventually, at even tighter GM1 arrangements (corresponding to 4 %), GM1 density takes control of its recognition behavior.

3.3. Ligand induced changes

Even though GM1 organization apparently affects its ability to recognize the ligand, bound ligands in response significantly rearrange the bilayer in the vicinity of GM1.

In order to address the impact of the ligand on GM1 organization we carried out more FRET experiments on GUVs. First, we employed a FRET pair consisting of Alexa488 labeled CTxB as a donor and DiD as an acceptor. As shown in the previous discussion, irrespective of GM1 domains, DiD is homogeneously distributed in the GUVs' bilayer. However, Fig. 5 shows that upon saturating all available GM1 molecules with ligands (mixture of labeled and non-labeled CTxB) the donor fluorescence decay exhibits lowered FRET compared to the situation when only less than 1 % of all GM1 was bound to a fluorescent ligand. This most importantly suggests that upon binding of the ligand the character of the GM1 domains is changed because in this new situation DiD is expelled from them, i.e. the domains are no longer fully permeable for the lipid tracer.

Parameters resulting from the MC simulations of the FRET decays as well as the estimation of number of individual lipids in the domains are given in Table 1. It further predicts number of toxin molecules that can at maximum bind to a domain, when number of GM1 in the domains and/or size of the domains would be taken as a limiting factor. Assuming that the used excess of CTxB is guaranteeing that all GM1 localized at the outer surface of the GUVs is associated with the CTxB-lipid domains, our data indicates that i) size of the domains as well as the area they occupy does not significantly change upon CTxB binding; ii) at 1 % GM1 the overall area occupied by toxin containing domains is lowered in the
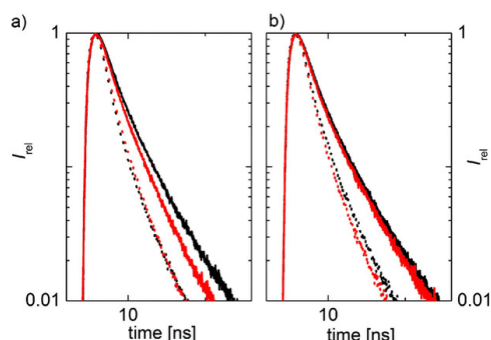

Fig. 5. FRET experiments made with Alexa488-labeled CTxB (donor) and DiD (acceptor) in GUVs. Donor fluorescence decays in systems containing a) 1 % GM1, and b) 4 % GM1. Decays for system without cholesterol (black) and with 30 % of cholesterol (red); CTxB (monomer)-to-lipid ratio 0.0001 (no change caused by CTxB) (dotted curves), fully saturated GM1 surface (solid curves).

presence cholesterol, while at 4 % GM1 cholesterol has no impact on the final distribution of donors and acceptors. The cholesterol effect on the domain parameters is in accord with the binding assays performed on LUVs.

Second, as a result of GM1 – ligand interaction the diffusion of DiD and g-GM1 decrease upon CTxB addition (Table 2). Most probably the observed fluorescent moieties keep interacting with the CTxB-GM1 complexes at the interface, where molecules may experience curvature which CTxB is known to impose on the bilayer [23].

More detailed analysis of the diffusive motion given in Fig. S8 shows that the slower diffusion of lipids upon CTxB binding represented by an apparent diffusion coefficient given in Table 2 accounts for a different type of motion than free diffusion. The dependence of the residence time on mean square displacement suggests a trapped diffusion, i.e. random walk interrupted by staying still in the potential trap [24].

4. Conclusions

In this manuscript the availability of ganglioside GM1 for multivalent receptor-ligand recognition is discussed. A portrait unifying two usually solely considered aspects of GM1 receptor activity such as its clustering and cholesterol involvement is given.

We show that GM1 tends to cluster even in bilayers consisting of pure DOPC at concentration lower than 1 %. There is moreover no evidence that cholesterol would affect this behavior. MC simulations of FRET predict domains of 5-7 nm radius that are extended over more than 35 % of the entire bilayer area regardless of the amount of GM1 present (up to ~ 8 %). This indicates that especially at lower GM1 concentrations these domains contain more than 3 DOPC molecules per GM1, which are predicted to occupy the first coordination sphere of GM1 [19]. The excess of PCs in the GM1 domains suggests that PCs are required to accommodate GM1 perturbed regions to the remaining bilayer. Consequently the domains cannot be considered to be of liquid ordered nature but rather more as fluid pools containing almost isolated GM1 molecules at low GM1 concentrations (below ~ 1 %).

The fact that GM1 molecules are confined in the pools allows for fine tuning of local GM1 density even at very low overall GM1 content (1 – 4 %) resulting in a powerful regulation of the multivalent recognition. Significant reduction of GM1 availability for the ligands can be accomplished by only a few percent elevation of GM1 content which makes GM1 molecules already too dense for being efficiently recognized by the ligand.

R. Šachl et al. / Biochimica et Biophysica Acta 1853 (2015) 850–857

Table 2
Diffusion coefficients of g-GM1 and DiD measured by Z-scan FCS for 4 % GM1 containing membranes in absence and presence (30 %) of cholesterol, before and after CTxB is added.

	$D_{g\text{-}GM1}$ [$\mu m^2/s$]	St. dev. [$\mu m^2/s$]	D_{DiD} [$\mu m^2/s$]	St. dev. [$\mu m^2/s$]
DOPC + 4 % GM1 DOPC/Chol/GM1 = 96.2/0/3.8 mol %	8.02	2.74	8.28	2.55
DOPC + 4 % GM1 + CTxB DOPC/Chol/GM1 = 96.2/0/3.8 mol %	6.47	0.48	5.18	0.95
DOPC/Chol + 4 % GM1 DOPC/Chol/GM1 = 67.3/28.8/3.8 mol %	6.77	0.64	5.96	0.78
DOPC/Chol + 4 % GM1 + CTxB DOPC/Chol/GM1 = 67.3/28.8/3.8 mol %	4.50	0.50	4.38	0.24

Cholesterol involvement in the regulation of GM1 availability is subjected to the density of GM1. While at low GM1 contents cholesterol reduces the recognition activity of GM1 (perhaps due to the suggested tilted conformation [4] which is not suitable for binding), at higher GM1 densities (~4 %) cholesterol ceases to have any impact on GM1-ligand interaction. At medium GM1 densities (1-2 % GM1) the cholesterol effect on down regulation of GM1 recognition activity gets amplified which indicates cooperation between the two aspects. The cholesterol content facilitates increase of GM1 density together with reduction of its mobility within the GM1 pools which apparently disqualifies it from effective ligand recognition.

The nature of GM1 domains is severely affected upon binding of the ligand. Seemingly, various labeled lipids (DiD) are no longer residing in the domains bound by CTxB suggesting loss in permeability and much tighter packing of the molecules inside the domains, accompanied by lower DOPC level and reduction of the overall domain area. Cholesterol present in the bilayer does not have an impact on GM1-ligand domains at 4 % of GM1 at all. At lower GM1 level (~1 %) presence of cholesterol mainly affects the overall area GM1-ligand domains occupy while their size is not significantly altered.

Physiological relevance of the clustering shown in this paper as well as in the earlier work of Shi et al. [5] depends on the level of GM1 that is naturally present in plasma membrane of living cells. The highest level of GSLs (from which GM1 is the most frequent) was reported in cells of nervous system, where they constitute almost 6 % of lipids [25]. The results drawn on GM1, as they are related to the general phenomena of an oligo-saccharide moiety in the headgroup region, may be possibly extended also on other GSLs that may act with GM1 in a cooperative manner.

Eventually it is of note that despite the fact that our experiments show significant changes in receptor activity of GM1 upon clustering and when cholesterol is involved, the activity is only reduced and never completely turned off. We hypothesize that apart from the clustering of GM1 and the cholesterol role we address here, various other aspects such as the presence of unsaturated lipids or membrane thickness can have a synergistic impact on the ganglioside recognition. All our experiments were undertaken in highly fluid, liquid disordered bilayers. However, in real biological membranes, which are much more rigid and ordered, all aspects affecting ganglioside organization may have much larger impact as they are less disturbed by diffusion.

Acknowledgement

Appendix A. Supplementary data

Supplementary data to this article can be found online at http://dx.doi.org/10.1016/j.bbamcr.2014.07.016.

References

[1] (a) G.S. Wu, Z.H. Lu, A.G. Obukhov, M.C. Nowycky, R.W. Ledeen, Induction of calcium influx through TRPC5 channels by cross-linking of GM1 ganglioside associated with alpha 5 beta 1 integrin initiates neurite outgrowth, J. Neurosci. 27 (28) (2007) 7447–7458;
(b) A.J. Yates, A. Rampersaud, Sphingolipids as receptor modulators - An overview, Sphingolipids Signal. Modulators Nerv. Syst. 845 (1998) 57–71.

[2] J.S. Mitchell, W.S. Brown, D.G. Woodside, P. Vanderslice, B.W. McIntyre, Clustering T-cell GM1 lipid rafts increases cellular resistance to shear on fibronectin through changes in integrin affinity and cytoskeletal dynamics, Immunol. Cell Biol. 87 (4) (2009) 324–336.

[3] R. Mahfoud, A. Manis, B. Binnington, C. Ackerley, C.A. Lingwood, A Major Fraction of Glycosphingolipids in Model and Cellular Cholesterol-containing Membranes Is Undetectable by Their Binding Proteins, J. Biol. Chem. 285 (46) (2010) 36049–36059.

[4] D. Lingwood, B. Binnington, T. Rog, I. Vattulainen, M. Grzybek, U. Coskun, C.A. Lingwood, K. Simons, Cholesterol modulates glycolipid conformation and receptor activity, Nat. Chem. Biol. 7 (5) (2011) 260–262.

[5] J.J. Shi, T.L. Yang, S. Kataoka, Y.J. Zhang, A.J. Diaz, P.S. Cremer, GM(1) clustering inhibits cholera toxin binding in supported phospholipid membranes, J. Am. Chem. Soc. 129 (18) (2007) 5954–5961.

[6] (a) D. Magde, E.L. Elson, W.W. Webb, Fluorescence Correlation Spectroscopy. 2.Experimental Realization, Biopolymers 13 (1) (1974) 29–61;
(b) A. Benda, M. Benes, V. Marecek, A. Lhotsky, W.T. Hermens, M. Hof, How to determine diffusion coefficients in planar phospholipid systems by confocal fluorescence correlation spectroscopy, Langmuir 19 (10) (2003) 4120–4126.

[7] J. Sykora, K. Kaiser, I. Gregor, W. Bonigk, G. Schmalzing, J. Enderlein, Exploring fluorescence antibunching in solution to determine the stoichiometry of molecular complexes, Anal. Chem. 79 (11) (2007) 4040–4049.

[8] (a) D. Marushchak, N. Gretskaya, I. Mikhalyov, L.B.A. Johansson, Self-aggregation - an intrinsic property of G(M1) in lipid bilayers, Mol. Membr. Biol. 24 (2) (2007) 102–112;
(b) I. Mikhalyov, N. Gretskaya, L.B.A. Johansson, Fluorescent BODIPY-labelled G(M1) gangliosides designed for exploring lipid membrane properties and specific membrane-target interactions, Chem. Phys. Lipids 159 (1) (2009) 38–44.

[9] M.I. Angelova, S. Soleau, P. Meleard, J.F. Faucon, P. Bothorel, Preparation of Giant Vesicles by External Ac Electric-Fields - Kinetics and Applications, Trends Colloid Interf. Sci. Vi 89 (1992) 127–131.

[10] V. Weissig, Liposomes: Methods and Protocols, *Biological Membrane Models.*, Vol. 2, Humana Press, New York, 2010.

[11] M.J. Hope, M.B. Bally, L.D. Mayer, A.S. Janoff, P.R. Cullis, Generation of Multilamellar and Unilamellar Phospholipid-Vesicles, Chem. Phys. Lipids 40 (2–4) (1986) 89–107.

[12] F. Bergstrom, I. Mikhalyov, P. Hagglof, R. Wortmann, T. Ny, L.B.A. Johansson, Dimers of dipyrrometheneboron difluoride (BODIPY) with light spectroscopic applications in chemistry and biology, J. Am. Chem. Soc. 124 (2) (2002) 196–204.

[13] J. Baumann, M.D. Fayer, Excitation Transfer In Disordered Two-Dimensional And Anisotropic 3-Dimensional Systems - Effects Of Spatial Geometry On Time-Resolved Observables, J. Chem. Phys. 85 (7) (1986) 4087–4107.

[14] R. Sachl, J. Humpolickova, M. Stefl, L.B.A. Johansson, M. Hof, Limitations of Electronic Energy Transfer in the Determination of Lipid Nanodomain Sizes, Biophys. J. 101 (11) (2011) L60–L62.

[15] (a) S. Engstrom, M. Lindberg, L.B.A. Johansson, Monte-Carlo Simulations Of Electronic-Energy Transfer In 3-Dimensional Systems - A Comparison With Analytical Theories, J. Chem. Phys. 89 (1) (1988) 204–213;
(b) L.B.A. Johansson, S. Engstrom, M. Lindberg, Electronic-energy transfer in anisotropic systems.3. Monte-carlo simulations of energy migration in membranes, J. Chem. Phys. 96 (5) (1992) 3844–3856.

[16] I.A. Boldyrev, J.G. Molotkovsky, A synthesis and proper-ties of new 4,4-difluoro-3a,4a-diaza-s-indacene (BODIPY)-labeled lipids, Russ. J. Bioorg. Chem. 32 (1) (2006) 78–83.

[17] J.J. Pan, S. Tristram-Nagle, J.F. Nagle, Effect of cholesterol on structural and mechanical properties of membranes depends on lipid chain saturation, Phys. Rev. E. 80 (2) (2009).

[18] S.L. Frey, E.Y. Chi, C. Arratia, J. Majewski, K. Kjaer, K.Y.C. Lee, Condensing and fluidizing effects of ganglioside G(M1) on phospholipid films, Biophys. J. 94 (8) (2008) 3047–3064.

[19] P. Jedlovszky, M. Sega, R. Vallauri, GM1 Ganglioside Embedded in a Hydrated DOPC Membrane: A Molecular Dynamics Simulation Study, J. Phys. Chem. B 113 (14) (2009) 4876–4886.

[20] P. Tinnefeld, K.D. Weston, T. Vosch, M. Cotlet, T. Weil, J. Hofkens, K. Mullen, F. C. De Schryver, M. Sauer, Antibunching in the emission of a single tetrachromophoric dendritic system, J. Am. Chem. Soc. 124 (48) (2002) 14310–14311.

[21] G.M. Kuziemko, M. Stroh, R.C. Stevens, Cholera toxin binding affinity and specificity for gangliosides determined by surface plasmon resonance, Biochemistry 35 (20) (1996) 6375–6384.

[22] M.M. Lozano, Z. Liu, E. Sunnick, A. Janshoff, K. Kumar, S.G. Boxer, Colocalization of the Ganglioside G(M1) and Cholesterol Detected by Secondary Ion Mass Spectrometry, J. Am. Chem. Soc. 135 (15) (2013) 5620–5630.

[23] H. Ewers, W. Romer, A.E. Smith, K. Bacia, S. Dmitrieff, W.G. Chai, R. Mancini, J. Kartenbeck, V. Chambon, L. Berland, A. Oppenheim, G. Schwarzmann, T. Feizi, P. Schwille, P. Sens, A. Helenius, L. Johannes, GM1 structure determines SV40-induced membrane invagination and infection, Nat. Cell Biol. 12 (1) (2010) 11-U36.

[24] (a) L. Wawrezinieck, H. Rigneault, D. Marguet, P.F. Lenne, Fluorescence correlation spectroscopy diffusion laws to probe the submicron cell membrane organization, Biophys. J. 89 (6) (2005) 4029–4042;
    (b) M. Stefl, R. Sachl, J. Humpolickova, M. Cebecauer, R. Machan, M. Kolarova, L.B.A. Johansson, M. Hof, Dynamics and Size of Cross-Linking-Induced Lipid Nanodomains in Model Membranes, Biophys. J. 102 (9) (2012) 2104–2113;
    (c) C. Eggeling, C. Ringermann, R. Medda, G. Schwarzmann, K. Sandhoff, S. Polyakova, V.N. Belov, B. Hein, C. von Middendorff, A. Schoenle, S.W. Hell, Direct observation of the nanoscale dynamics of membrane lipids in a living cell, Nature 457 (7233) (2009) 1159-U121.

[25] (a) J.C.M. Holthuis, T. Pomorski, R.J. Raggers, H. Sprong, G. Van Meer, The organizing potential of sphingolipids in intracellular membrane transport, Physiol. Rev. 81 (4) (2001) 1689–1723;
    (b) J.M. Berg, J.L. Tymoczko, L. Stryer, G.J. Gatto, Biochemistry, 7th ed W H Freeman & Co, 2010.

On Multivalent Receptor Activity of GM1 in Cholesterol Containing Membranes

Radek Šachl, Mariana Amaro, Gokcan Aydogan, Alena Koukalová, Ilya I. Mikhalyov,
Ivan A. Boldyrev, Jana Humpolíčková, Martin Hof

Supporting Information

Fluorescence antibunching

The antibunching experiment deals with decreased probability of photon pair detection at lag times shorter than the fluorescence lifetime of observed fluorophores. The antibunching technique is commonly applied to immobilized molecular complexes in order to determine the emitters' lifetime and/or their aggregation status. Since the probability of detecting a sub-nanosecond spaced photon pairs is usually very low the overall number of photons needs to be high, which is incompatible with low photostability of most fluorescing molecules. The approach chosen here switches from temporal to ensemble averaging and therefore can be directly applied to diffusing molecular complexes in solution. This allows for long (~tens of minutes) measurements and sufficient number of collected photons.

In our work we use a pulsed laser with repetition period of 100 ns which is a sufficiently long time for all fluorophores in S1 state to emit a photon and return back to the ground state. The signal is collected with two independent detectors connected to independent electronic circuits so that detection of the first photon from the pair would not prevent the second photon from being detected due to instrumental dead time.
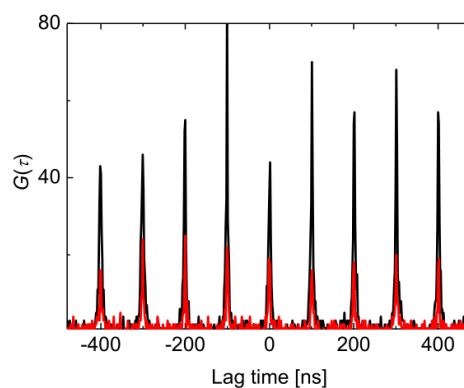

Figure S1. Example of ns-scale autocorrelation curve used for fluorescence antibunching.

The signals from the two detectors are crosscorelated (Fig.S1) for short lagtimes (over 11 laser periods): $g(\tau) = \langle I(t)I(t+\tau) \rangle_t$ The crosscorrelation between the detector I and the detector II is assigned positive lag time, while the crosscorrelation between the detector II and the detector I is assigned negative lag time. Individual peaks reflecting

pulses of the laser are separated by the laser period. The zero peak corresponds to all the "photon pair events" that occurred after a single pulse of the laser (i.e. two photons arrived within one pulse period). The side peaks correspond to the situation where the first photon and the second photon arrive after different pulses of the laser, spaced by the number of pulsed period equal to the position of said side peak from the zero peak.

The area of the zero peak g_{n-1} depends on the overall concentration of the molecular complexes c, the number of emitters in the complex n, brightness of a single emitter κ and the background signal b:

$$g_{n-1} \propto \left(c*n*(n-1)*\left\langle \kappa^2(\vec{r})\right\rangle_r + \left(cn\left\langle \kappa(\vec{r})\right\rangle_r + b\right)^2 \right). \tag{1}$$

This reflects the fact that the same emitter in the complex cannot provide two photons as a response to a single picosecond laser pulse due to the time the emitter needs to spend in the excited state, i.e. the second photon can only be provided by n-1 emitters.

The area below the side peaks g_n corresponds to the "photon pair events" than can be generated by the same emitter since the delay between the two photons is sufficiently long:

$$g_n \propto \left(c*n*n*\left\langle \kappa^2(\vec{r})\right\rangle_r + \left(cn\left\langle \kappa(\vec{r})\right\rangle_r + b\right)^2 \right). \tag{2}$$

Furthermore, a correlation curve with 1 second offset is calculated: $g(\tau + 1s) = \left\langle I(t)I(t+\tau+1s)\right\rangle_t$ (Fig. S1). At these lag times, photon antibunching due to sub-nanosecond scale photon exclusivity as well as photon bunching due to micro- to millisecond dwelling of the fluorophore within the laser focus diminishes, photon stream becomes stochastic and the nanosecond pattern reflects only the periodic pulsing of the laser. Each of the peaks merely reflects the overall signal and the background:

$$g_\infty \propto \left(cn\left\langle \kappa(\vec{r})\right\rangle_r + b\right)^2. \tag{3}$$

Eventually, the number of emitters per complex can be withdrawn: $n = \dfrac{g_n - g_\infty}{g_n - g_{n-1}}$.

The situation becomes more difficult when the emitter undergoes fast (microsecond) photophysics such as formation of the triplet state. In that case the $<\kappa^2(\mathbf{r})>_r$ in Eq. 1 has to be recalculated to the time when the photophysical relaxation diminishes. Detailed insight into the theory behind the techniques is given in.[1]

Antibunching assay: alternative data treatment
The antibunching assay as described in the manuscript is a titration of GM1 molecules on the surface of LUVs with a mixture of labeled and unlabeled CTxB. The measurement principally does not differ from classical FCS experiment, therefore obtained data can be also treated in the sense of FCS: correlating the intensity trace, fitting the correlation function to a model accounting for two kinds of freely diffusing particles (slow: LUVs, fast: free labeled CTxB).

The fraction of a slow diffusing species can be plotted as a function of added CTxB. The addition of CTxB corresponding to the situation when the fraction of slow diffusing species starts to drop exactly corresponds to the maximum emitters per LUV,

i.e. full surface saturation. The comparison of the two way of treating the data is given in Fig. S2:
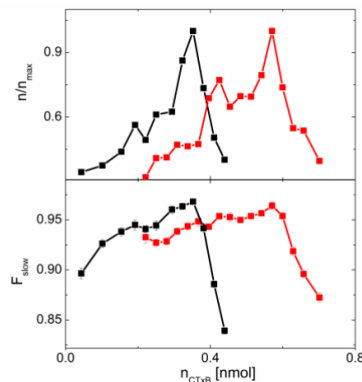

Figure S2. Comparison of data treatment via antibunching (upper part) and classical FCS (lower part). Upper part: dependence of a number of Alexa488 emitters on CTxB (normalized) on the amount of added CTxB. Lower part: dependence of fraction of slow moving particles (LUVs) on the amount of labeled CTxB. Data obtained for LUVs containing 1.5 % of GM1 in pure DOPC (red) and in DOPC/Chol (70/30) mixture.

Quenching experiments on LUVs

In order to exclude multilamellar character of LUVs used for the antibunching assays, we have performed quenching of g-GM1 in the LUVs with potassium iodide. The quenching experiments did not reveal any non-linearity in Stern-Volmer plot referring on an inaccessible fraction of GM1 while its fluorescence dropped almost to a half (see Fig. S3). This indicates that LUVs used for the binding assay were unilamellar.
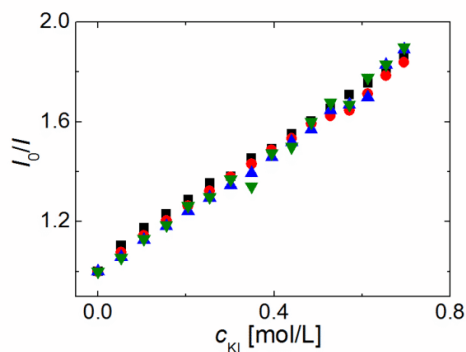

Figure S3. Stern-Volmer plot for g-GM1 in LUVs (g-GM1/lipid 1/400) quenched by potassium iodide. Lipid composition of the used LUVs: DOPC/Chol (100/0) + 0 % GM1 (black), DOPC/Chol (70/30) + 0 % GM1 (red), DOPC/Chol (100/0) + 1 % GM1 (blue), DOPC/Chol (70/30) + 1 % GM1 (green).

Baumann-Fayer model

3

The Baumann-Fayer model accounts for Förster resonance energy transfer (FRET) between homogenously distributed donors (D) and acceptors (A) in a lipid bilayer. Analytical equations have been derived for several geometrical arrangements and for both static and dynamic limit conditions. Since D and A were localized at the lipid water interface in our case, it is reasonable to assume that the dynamic limit conditions have been fulfilled. When FRET occurs within one bilayer leaflet this process is referred to as *intra*-FRET and the survival probability $G_{intra}(t)$, *i.e.* the probability that the excited donor is still in the excited state after time t, can be expressed as:[2]

$$\ln\left(G_{intra}(t)\right) = -C_2\Gamma(2/3)(t/\tau)^{1/3}$$
(4)

Here C_2 is a so called reduced surface concentration of acceptors corresponding to the average number of acceptors within a circle limited by the Förster radius of the donor (R_0), Γ is the gamma function and τ is the average lifetime of the donor. When the excitation energy is transferred across the lipid bilayer between two parallel leaflets that are separated by the distance d, the process is called as *inter*-FRET and the survival probability $G_{inter}(t)$ can be calculated as:[2]

$$\ln\left(G_{inter}(\mu)\right) = -\frac{C_2}{3}(d/R_0)^2(2\mu/3)^{1/3}\int_0^{2/3\mu}(1-e^{-s})s^{-4/3}ds$$
(5)

In Eq. 5, $\mu = 3t(R_0/d)^6/2\tau$ and $s = 2\mu\cos^6\theta_r/3$, where θ_r denotes the angle between the bilayer normal and the vector $\boldsymbol{r}$ which connects the locations of the donor and acceptor dipoles. When both *inter*- and *intra*-FRET occur simultaneously the total survival probability is given by $G(t) = G_{intra}(t)G_{inter}(t)$ and the fluorescence intensity of a donor in the presence of acceptors $F(t)$ decays according to

$$F(t) = G(t)\sum_i A_i \exp\left(-\frac{t}{\tau_i}\right),$$
(6)

where A_i and τ_i describe the donor fluorescence in the absence of acceptors.

Estimation of cluster sizes by means of FRET-Monte Carlo simulations
The following workflow has been used for the determination of cluster/domain sizes:[3] 1) Circular domains of radius R and occupying a certain fraction of the total bilayer area f are randomly generated in the lipid bilayer. 2) Donors and acceptors are distributed at the lipid water interface according to the distribution constant defined as $K_{D,A}$ = [donors (acceptors) within]/[donors (acceptors) outside]). 3) In the next step, a donor is randomly excited. 4) The time Δt_i when the energy transfer event takes place is calculated. This event is a random process but is modulated by the overall energy transfer rate Ω_i according to Δt_i = -lnα/Ω_i, where α is a randomly generated number between 0-1. 5) Steps 1-4 are repeated many times in order to obtain good statistics. Each generated step is used about 100 times before a new one is generated. The total number of excitation events is usually higher than 3.10^5. 6) A histogram, which corresponds to the total survival probability function $G(t)$, is constructed from the energy transfer events Δt_i. 7) The generated decay, which is obtained from the $G(t)$ function by means of Eq. 6, is

4

compared to the experimental one. 8) Finally, steps 1-7 are repeated by varying the input parameters R and f until the generated decay fits the experimental one.

Parameters used for FRET-MC simulations
For performing the MC simulations several input parameters are required, such as Förster radius, distribution coefficients and donor decay characteristics in the absence of acceptors. The parameters used for the pairs in this work are given in the Table S1.

donor	acceptor	K_D	K_A	R_0/nm	$<\tau_D>$/ns
g-GM1	r-GM1	1000	1000	5.9	5.5
Alexa-CTxB	DiD	1000	0.001	5.4	3.5

Table S1. Input parameters for the FRET MC simulations used in this work. K_{DA} stands for donor/acceptor distribution coefficient, R_0 is the Förster radius, $<\tau_D>$ is the mean fluorescence lifetime.

In all the simulations domains coupled through the membrane leaflets were taken into account. Intra-leaflet contributions to the final decay are usually less significant than the inter-leaflet ones, therefore domain coupling through the membrane usually provides similar results as if the domains were not coupled (this was tested for the g-GM1/r-GM1 pair). Uncoupled domains require optimizing of more fitting parameters which results in lower reliability of the fit. Ch^2 surface does not have deep minima but rather shallow valleys suggesting that several combinations of fitting parameters correspond equally well to the experimental data.

Data obtained in presence of cholesterol
Fig. S4a and S4b show data obtained with g-GM1/r-GM1, g-GM1/DiD FRET pair, respectively in the membrane containing 30 % of cholesterol. The changes in FRET are almost identical to the changes observed without cholesterol shown in Fig. 2 of the manuscript.
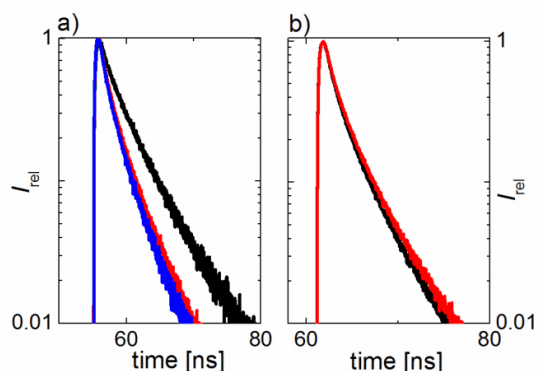

Figure S4. a) Donor fluorescence decays of g-GM1. a) FRET between g-GM1 (1/200, 0.5 %) and r-GM1 (1/200, 0.5 %) in DOPC/Chol (70/30) bilayer at 0 % (black), 2 % (red), 4 % (blue) added unlabeled GM1. b)

FRET between g-GM1 (1/1000, 0.1 %) and DiD (1/100, 1 %) in DOPC/Chol (70/30) bilayer at 0 % (black), 2 % (red) added unlabeled GM1. Ratio given in brackets corresponds to the donor (acceptor) – lipid ratio.

g-GM1/r-GM1 FRET pair: below 1 % of GM1
In order to approach a concentration threshold, below which the GM1 domains are not formed, we lowered the amount of added non-labelled GM1 to the GUVs containing DOPC and the g-GM1/r-GM1 FRET pair (1 % in total) to 0.5 %, *i.e.* below concentration of the two labels. The subtle change in FRET was observed even under these conditions (Fig. S5).
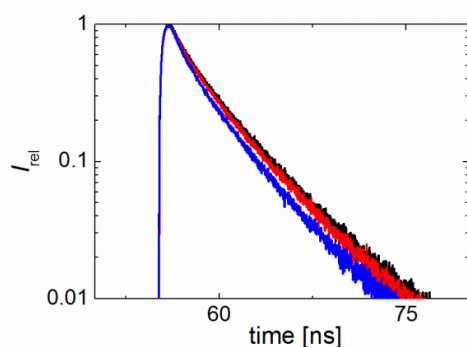
Figure S5. FRET on g-GM1/r-GM1 pair (0.5 % each). Donor fluorescence decays for g-GM1 in GUVs consisting of DOPC with 0 % (black), 0.5 % (red) and 1 % (blue) added non labeled GM1.

It has to be kept in mind that here the concentration of the studied non-labelled GM1 dropped below the concentration of the labels. Therefore necessarily, most of the labels are not incorporated in the domains (as we show that they do not constitute the domains on their own). As a result, the change in FRET is less pronounced due to the interfering signal of the donors that do not experience the domains. Unfortunately, concentration of the labels cannot be significantly lower as for FRET, high enough number of acceptors is needed in the donor vicinity (1 acceptor per 200 lipids is almost a limiting situation). The concentration of donors cannot be lowered either as we have to make sure that the signal of acceptor in the donor channel is negligible in comparison to the signal of donor.
A possibility to circumvent the issue of the reasonably high labelling at least partially is to use a different donor (see Fig. S6).

FRET between B7PC and r-GM1
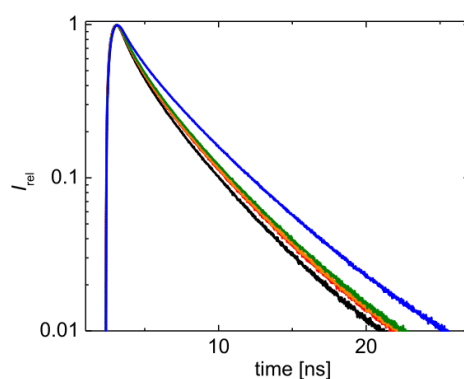FRET experiment between (Me)$_4$bodipy-tail-labelled lipid (B7PC)[4] and r-GM1 are given in Fig. S2.

Figure S6. FRET between B7PC (0.5 %) and r-GM1 (0.5 %). Donor decays: a) no extra added GM1 (black), b) 0.5 % unlabelled GM1 (red), c) 1 % unlabelled GM1 (orange), d) 2 % unlabelled GM1 (olive), e) 2 % unlabelled GM1, fully saturated with toxin (blue)

In this case, B7PC is most probably homogeneously distributed in the membrane (similar to DiD) in all investigated compositions while r-GM1 segregates to the domains once they are formed. When CTxB is added domains become stiffer, B7PC gets expelled out of them and FRET further decreases.

This pair allows for reducing the overall concentration of labeled GM1 (0.5 %) compared to g-GM1/r-GM1 pair and for observing FRET behavior at a lower GM1 concentration level. Fig. S2 displays FRET being reduced upon GM1 addition. Apparently even at the decreased concentration of labeled GM1 the only thing that matters is the addition of non-labeled ganglioside. Similarly to the g-GM1/r-GM1 pair, the main change in FRET occurs upon the initial addition of unlabeled GM1 (0.5 %) and no further significant change follows. This indicates that the amount of labeled GM1 does not have an impact on the domain formation and thus serves merely as their marker.

FRET between g-GM1 and r-GM1: DOPC vs POPC
The impact of lipid saturation on the GM1 domains was investigated by exchanging the unsaturated DOPC for partially saturated POPC. The FRET data (donor decays of g-GM1) show decreased extend to the change in FRET between the GM1 not-containing and containing GUVs. The POPC impact was observed both for the cholesterol free and cholesterol containing bilayers.
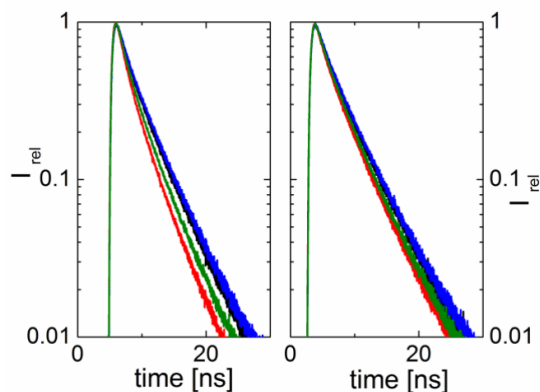
Figure S7. FRET between g-GM1/r-GM1 in the GUVs composed of: Left: DOPC + 0 % GM1 (black), DOPC + 4 % GM1 (red), POPC + 0 % GM1 (blue), POPC + 4 % GM1 (green); Right: DOPC/Chol + 0 % GM1 (black), DOPC/Chol + 4 % GM1 (red), POPC/Chol + 0 % GM1 (blue), POPC/Chol + 4 % GM1 (green). DOPC/Chol and POPC/Chol ratio was 70/30. All GUVs contained g-GM (1/200, 0.5 %) and r-GM1 (1/200, 0.5 %).

Detailed analysis of the change in DiD diffusion in the DOPC bilayer (4 % GM1) upon saturation with CTxB

The slowed lipid motion in the bilayer containing GM1 upon saturation with CTxB was further investigated by means of Z-scan approach[5] combined with plotting of the residence time as a function of illuminated area,[6] *i.e.* plotting average time that a fluorophore spends in the illuminated membrane area as a function of the area size. The positive offset of the dependence is usually attributed to the trapped motion, i.e. random walk interrupted by dwelling of the fluorophore at a certain position. The results clearly showing the positive offset in the $\tau - PN/PN_0$ dependence that appears when CTxB is added are summarized in the Fig. S8.
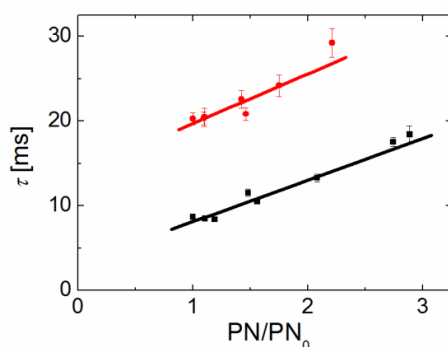

8

Figure S8. Dependence of mean residence time of DiD on the relative size of the illumination spot (PN/PN_0) in SLBs composed of DOPC with 4 % of GM1 before (black) and after (red) saturation with CTxB.

This experiment was carried out on supported lipid bilayers (SLBs) in order to avoid photobleaching issues occurring on GUVs. Preparation of SLBs was done as described elsewhere.[5]

1.   Sykora, J.; Kaiser, K.; Gregor, I.; Bonigk, W.; Schmalzing, G.; Enderlein, J., *Exploring fluorescence antibunching in solution to determine the stoichiometry of molecular complexes. Analytical Chemistry* **2007,** *79 (11), 4040-4049.*
2.   Baumann, J.; Fayer, M. D., *Excitation transfer in disordered two-dimensional and anisotropic 3-dimensional systems - effects of spatial geometry on time-resolved observables. J Chem Phys* **1986,** *85 (7), 4087-4107.*
3.   (a) Johansson, L. B. A.; Engstrom, S.; Lindberg, M., *Electronic-energy transfer in anisotropic systems. 3. Monte-Carlo simulations of energy migration in membranes. J Chem Phys* **1992,** *96 (5), 3844-3856; (b) Bergenstahl, B. A.; Stenius, P., Phase-Diagrams of Dioleoylphosphatidylcholine with Formamide, Methylformamide, and Dimethylformamide. Journal of Physical Chemistry* **1987,** *91 (23), 5944-5948; (c) Stefl, M.; Sachl, R.; Humpolickova, J.; Cebecauer, M.; Machan, R.; Kolarova, M.; Johansson, L. B. A.; Hof, M., Dynamics and Size of Cross-Linking-Induced Lipid Nanodomains in Model Membranes. Biophys J* **2012,** *102 (9), 2104-2113.*
4.   Boldyrev, I. A.; Molotkovsky, J. G., *A synthesis and proper-ties of new 4,4-difluoro-3a,4a-diaza-s-indacene (BODIPY)-labeled lipids. Russian Journal of Bioorganic Chemistry* **2006,** *32 (1), 78-83.*
5.   Benda, A.; Benes, M.; Marecek, V.; Lhotsky, A.; Hermens, W. T.; Hof, M., *How to determine diffusion coefficients in planar phospholipid systems by confocal fluorescence correlation spectroscopy. Langmuir* **2003,** *19 (10), 4120-4126.*
6.   (a) Humpolickova, J.; Gielen, E.; Benda, A.; Fagulova, V.; Vercammen, J.; Vandeven, M.; Hof, M.; Ameloot, M.; Engelborghs, Y., *Probing diffusion laws within cellular membranes by Z-scan fluorescence correlation spectroscopy. Biophys J* **2006,** *91 (3), L23-L25; (b) Wawrezinieck, L.; Rigneault, H.; Marguet, D.; Lenne, P. F., Fluorescence correlation spectroscopy diffusion laws to probe the submicron cell membrane organization. Biophys J* **2005,** *89 (6), 4029-4042.*

Distinct Roles of SNARE-mimicking Lipopeptides during Initial Steps of Membrane Fusion

Under minor revisions in Nanoscale

Distinct Roles of SNARE-mimicking Lipopeptides during Initial Steps of Membrane Fusion

Alena Koukalová,[†a] Šárka Pokorná,[†a] Aimee L. Boyle,[b] Nestor Lopez Mora,[b] Alexander Kros,[b] Martin Hof [a] and Radek Šachl *[a]

[a]Department of Biophysical Chemistry, J. Heyrovský Institute of Physical Chemistry of the Academy of Sciences of the Czech Republic, Prague, 182 23, Czech Republic, E-mail: radek.sachl@jh-inst.cas.cz,

[b]Supramolecular and Biomaterials Chemistry, Leiden Institute of Chemistry, Leiden University, P.O. Box 9502, 2300 RA Leiden, The Netherlands

†AK:á and ŠP contributed equally to this work.

Abstract

A model system for membrane fusion, inspired by SNARE proteins and based on two complementary lipopeptides CP_nE_4 and CP_nK_4, has been recently developed. It consists of cholesterol (C), a polyethylene glycol linker (P_n) and either a cationic peptide K_4 (KIAALKE)$_4$ or an anionic peptide E_4 (EIAALEK)$_4$. In this paper, fluorescence spectroscopy is used to decipher distinct but complementary roles of these lipopeptides during early stages of membrane fusion. Molecular evidence is provided that different distances of E_4 in CP_nE_4 and K_4 in CP_nK_4 from the bilayer represent an important mechanism, which enables fusion. Whereas E_4 is exposed to the bulk and solely promotes membrane binding of CP_nK_4, K_4 loops back to the lipid-water interface where it fulfills two distinct roles: it initiates bilayer contact by binding to CP_nE_4 containing bilayers; and it initiates fusion by modulating the bilayer properties. The interaction between CP_nE_4 and CP_nK_4 is severely down-regulated by binding of K_4 to the bilayer and possible only if the lipopeptides approach each other as constituents of different bilayers. When the complementary lipopeptides are localized in the same bilayer, hetero-coiling is disabled. These data provide crucial insights as to how fusion is initiated and highlight the importance of both peptides in this process.

Keywords

membrane fusion, lipopeptides, SNARE, FRET, FCS

Introduction

Fusion of cellular membranes has recently attracted considerable scientific attention, not only for being ubiquitous and vital in living organisms, but also for its potential to be used for *in vivo* applications. Fusion of membranes in living cells is crucial for a number of cellular functions, e.g. the controlled release of neurotransmitters, fertilization, communication, and material exchange in eukaryotic cells.[1,2] In eukaryotic cells, this process is mediated by so-called SNARE proteins (soluble N-ethyl-maleimide-sensitive factor attachment protein receptor), which have been proposed to be involved in all intracellular events of membrane fusion.[3] The fusing membranes are brought into contact by the formation of a tetrameric coiled-coil between three different membrane-tethered SNARE proteins. This so-called coiled-coil interaction is established by α-helical portions of the proteins interacting with each other in a specific manner resulting in the formation of a stable complex.[4,5]

Despite the huge diversity of systems where fusion can occur, the fusion cascade shares a few common features: first, contact between two membranes is developed and accompanied by disruption of the contact site. This is followed by fusion of the proximal leaflets and lipid mixing, which culminates in opening of a fusion pore and content mixing.[1,6,7] Attempts to mimic and understand the mechanism of membrane fusion *in vivo* has led to the development of several artificial model systems using various strategies, e.g. double stranded DNAs, covalent or hydrogen-bonding motifs and coiled-coil interactions between two complementary α-helices.[8–11] Recently, a model system inspired by the molecular recognition of native SNARE proteins has been developed.[12] The fusogens consist

of a set of two complementary lipopeptide molecules (**Figure 1**). Each of these lipopeptides contains a recognition domain comprising one of the complementary coiled-coil-forming peptides E or K, cholesterol which serves as a membrane anchor and a polyethylenglycol (P) of variable length. The latter molecule serves as a linker between the cholesterol anchor and the peptide. If the cationic peptide K_4 (KIAALKE)$_4$ is employed, the construct is known as CP_nK_4, where n denotes the number of ethylene glycol units, and CP_nE_4 represents the construct containing the anionic peptide E_4 (EIAALEK)$_4$. The lipopeptides CP_nK_4 and CP_nE_4 interact with each other by the formation of a coiled-coil motif resulting from the interaction of peptide E_4 and K_4. This coiled-coil is strong enough to bring the two opposing membranes into close contact and induce effective and leakage-free fusion *in vitro*.[12,13] Both lipopeptides can be incorporated in artificial as well as plasma membranes of living cells in a facile manner by adding the lipopeptides directly to either liposomes or cells. This strategy opens up new possibilities for *in vivo* applications.[13,14,15] However, the exact mechanism of lipopeptide-mediated membrane fusion still remains unknown. In this paper, we employ single molecule FCS (fluorescence correlation spectroscopy) and FCCS (fluorescence cross-correlation spectroscopy) techniques and FRET (Förster resonance energy transfer) to uncover distinct but complementary roles of CP_nE_4 and CP_nK_4 lipopeptides during the initial steps of membrane fusion. We show for the first time that the interaction between the complementary lipopeptides, which is a pre-requisite for establishing a membrane contact between two approaching bilayers, is strongly down-regulated by the looping-back of K_4 to the lipid bilayer. The majority of CP_nK_4 is in fact needed to stimulate the bilayer for undergoing fusion whereas only a minor fraction of CP_nK_4 is then used to bind CP_nE_4 on an approaching bilayer. Conversely, E_4 in CP_n-E_4 is largely exposed to the bulk and works solely as a handle for CP_nK_4. This paper provides molecular evidence that different distances, facilitated by different PEG-spacer lengths, of E_4 in CP_nE_4 and K_4 in CP_nK_4 from the lipid-water interface represent an important mechanism which enables efficient fusion.
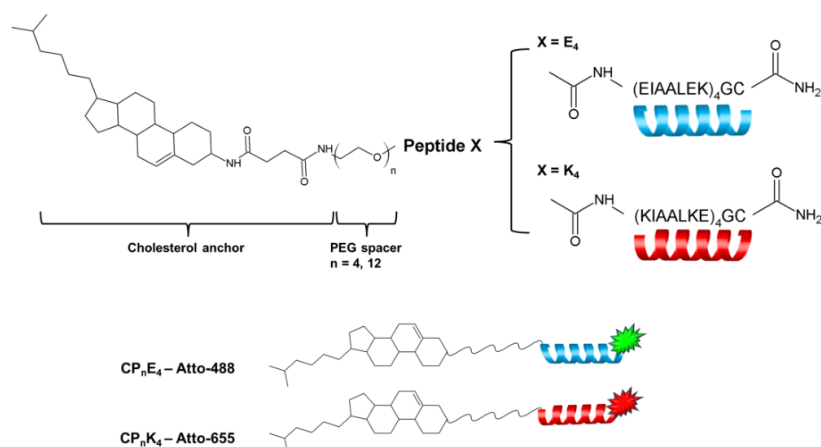

Figure 1. Chemical structures of CP_nE_4 and CP_nK_4 lipopeptides. A lipopeptide consists of a cholesterol moiety (C), a flexible polyethylenglycol (PEG) linker of either 4 or 12 PEG units (P_4 or P_{12}) and one of the complementary peptides E or K. The lipopeptides were fluorescently labelled with either Atto-488 or Atto-655 at the C terminus of the peptide by a thiol-maleimide coupling.

Results and Discussion

Strong binding of K_4 to the bilayer hampers a direct interaction of E_4 with K_4

In alignment with previous studies, we worked with 1,2-dioleoyl-*sn*-glycero-3-phosphocholine/1,2-dioleoyl-*sn*-glycero-3-phosphoethanolamine/Cholesterol (DOPC/DOPE/Chol) (50/25/25 mol%) lipid mixtures as fusion of such DOPE rich membranes was found to be highly efficient due to induction of positive curvature by the DOPE lipids.[16–19] The extent of membrane binding was determined by measuring the fluorescence intensity of the peptides bound to the bilayer of giant unilamellar vesicles (GUVs) and confirmed by z-scan FCS diffusion measurements (see SI). The GUVs incubated solely with a fluorescent peptide K4-Atto-655 exhibited approximately 6.5 times higher intensity than those incubated with the same concentration of E4-Atto-655, showing a higher affinity of K4 to the lipid bilayer (Figure 2). The situation changed drastically when the vesicles were decorated with one of the complementary lipopeptides prior to addition of either E4-Atto-655 or K4-Atto-655 (**Figure 2**). Binding of both E4-Atto-655 and K4-Atto-655 significantly improved, which demonstrates the mutual affinity of the complementary peptides.
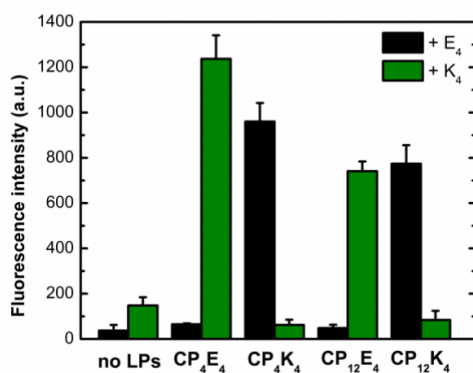

Figure 2. Fluorescence intensities (averaged number of photons per area) of fluorescently labelled peptides K4-Atto-655 (olive) and E4-Atto-655 (black) adsorbed on the surface of DOPC/DOPE/Chol (50/25/25 mol%) GUVs give information about the surface concentration of the peptides at the lipid bilayer. The GUVs were prepared either with or without 1 mol% of one of the complementary lipopeptides (LPs) (type of the lipopeptide is further specified below the *x* axis). GUVs were scanned 30 minutes after the addition of the peptide (0.4 mol%).

To understand how binding of the peptides to the complementary lipopeptides progresses at the molecular level, fluorescence correlation spectroscopy (FCS) experiments were conducted. An output of an FCS measurement is an autocorrelation function (G_{auto}), which contains information about diffusion of fluorescently labelled molecules (**Figure 3A**). The diffusion coefficient D of K4-Atto-655 in bilayers with and without 1 mol% of CP4E4 remained almost the same and was similar to the diffusion coefficient of fluorescently labelled DOPE-Atto-655 lipids in the presence of 1 mol% of K4 (**Table 1**). Moreover, the diffusion of K4-Atto-655 in the presence of 1 mol% of CP4E4 was slightly higher than the diffusion of CP4E4-Atto-488 in the presence of 1 mol% of K4. The last two observations would indicate that a considerable fraction of K4-Atto-655 stays in the bilayer unbound to CP4E4-Atto-488. The amount of unbound K4-Atto-655 was further quantified by fluorescence cross-correlation spectroscopy (FCCS) experiments between K4-Atto-655 and CP4E4-Atto-488 (see SI for further details). In **Figure 3B** the measured cross-correlation amplitude $G_{\mathrm{cross}}(0)$ was normalized (yielding $G_{\mathrm{cross}}^{\mathrm{norm}}(0)$) and plotted against the concentration of K4-Atto-655 in the bilayer (see SI for details). Then, $G_{\mathrm{cross}}^{\mathrm{norm}}(0) = 1$ should be obtained if all K4-Atto-655 binds to CP4E4-Atto-488 molecules. $G_{\mathrm{cross}}^{\mathrm{norm}}(0)$ in Figure 3B grows with increasing concentration of K4-Atto-655 until it reaches a maximum value of about 25 %. Thus, considerable fractions of K4-Atto-655 and CP4E4-Atto-488 do not bind to each other in the lipid bilayer.

Similarly, diffusion of E4-Atto-655 in the presence of CP4K4-Atto-488 significantly differed from the diffusion of CP4K4-Atto-488 in in the presence of 1 mol% of E4 (Table 1). Moreover, the diffusion of E4-Atto-

655 in pure DOPC/DOPE/Chol (50/25/25 mol%) bilayers was much faster than the previously reported diffusion of K_4-Atto-655. Both observations point to a weaker interaction of peptide E_4 with the bilayer. Interestingly, it follows from the FCCS analysis of CP_4K_4-Atto-488 and E_4-Atto-655 (Figure 3B) that only 35 % of the maximum value of $G_{\mathrm{cross}}(0)$ were reached in this case. In summary, we show that membrane embedded CP_4E_4 and CP_4K_4 do form hetero-coils with the complementary K_4 and E_4, but the fraction of stable hetero-coils is low. It appears that the direct interaction of E_4 with K_4 is hampered by preferable interactions of K_4 with the bilayer. In the case when K_4 binds to CP_4E_4 containing vesicles, CP_4E_4 works only as a handle which brings K_4 close to the lipid bilayer where K_4 prefers to interact with the bilayer rather than with CP_4E_4. In the other case when E_4 is approaching CP_4K_4-containing vesicles E_4 can bind only by means of CP_4K_4. This lipopeptide is, however, unable to bind E_4 efficiently because of its high affinity to the bilayer.
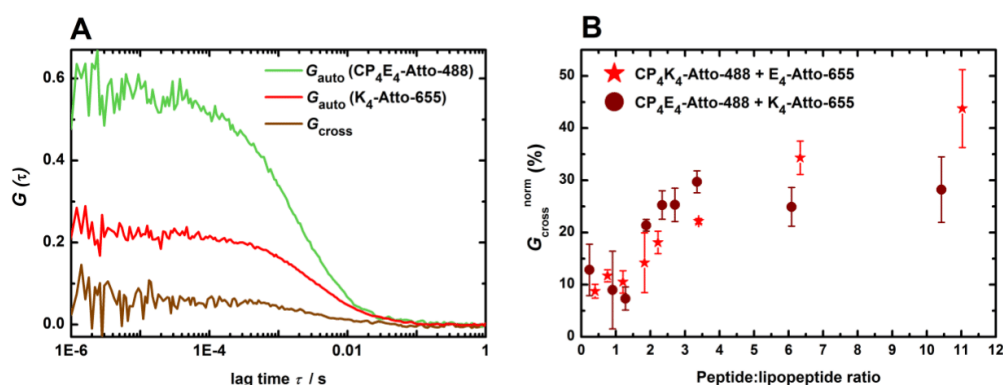

Figure 3. (Left): Demonstrative auto-correlation functions G_{auto} for CP_4E_4-Atto-488 and K_4-Atto-655 obtained from an FCS measurement and the corresponding cross-correlation function (G_{cross}) obtained from a parallel FCCS measurement. (Right): The normalized cross-correlation amplitude, which reports on the extent of interaction between one of the peptides and the complementary lipopeptide, as a function of the peptide to lipopeptide ratio on DOPC/DOPE/Chol (50/25/25 mol%) bilayers. The average value of $G_{\mathrm{cross}}^{\mathrm{norm}}$ was calculated based on measurements on at least 5 GUVs.

Table 1. Diffusion coefficients (D) for K_4-Atto-655 and E_4-Atto-655 peptides adsorbed on DOPE/DOPC/Chol (50/25/25 mol%) bilayers. The GUVs were pre-incubated with 1 mol% of one of the (lipo)peptides specified in the first column. Furthermore, the table shows D for a DOPE-Atto-488 reference probe.

GUVs pre-incubated with 1 mol% of	D ($\mu m^2/s$)				
	K_4-Atto-655	E_4-Atto-655	CP_4K_4-Atto-488	CP_4E_4-Atto-488	DOPE-Atto-488
No LPs	(9.13 ± 0.63)	(132 ± 13)	-	-	9.85 ± 0.36
K_4	-	-	-	(7.9 ± 0.55)	9.73 ± 0.54
CP_4E_4	(9.27 ± 0.32)	-	-	-	-
E_4	-	-	(5.67 ± 0.75)	-	10.09 ± 0.58
CP_4K_4	-	(10.24 ± 0.95)	-	-	-

Different distances of the peptide segments E_4 or K_4 from the lipid water interface prevent lipopeptides from hetero-coiling

Importantly, no detectable hetero-coiling occurs when both lipopeptides CP_nE_4 and CP_nK_4 are reconstituted in the same bilayer at roughly the same concentration. This is documented by the cross-correlation amplitude for CP_4E_4-Atto-488 and CP_4K_4-Atto-655 equal to zero at low lipopeptide concentrations (<< 1 mol %, $G_{cross}(0) = 0$, **Figure 4A**) but also by FRET at considerably higher lipopeptide concentrations (about 1 mol %, **Figure 4B**), at which fusion normally progresses. The efficiency of FRET E depends on the average distance of the donors from the acceptors. For the case of homogeneously distributed donors and acceptors in a lipid bilayer, the dependence of E on the acceptor to lipid ratio can be obtained from a model derived by Baumann and Fayer (black line in Figure 4): it is steep at low acceptor to lipid ratios and flattens off typically at ratios exceeding 2 mol% of the acceptors.[20] Clustering of the donors with the acceptors (i.e. hetero-coiling of CP_4E_4-Atto-488 with CP_4K_4-Atto-655) brings the donors effectively closer to the acceptors, enhancing the efficiency of FRET in comparison to the expected theoretical value for a given acceptor to lipid ratio. The hetero-coiling of lipopeptides should thus lead to a steeper dependence of E on the acceptor to lipid ratio than would correspond to a homogeneous distribution of the labelled lipopeptides. The experimental dependency shown in Figure 4B perfectly follows the theoretical one (to understand in more detail how the theoretical dependence is calculated see SI). This means that hetero-coils of the lipopeptides in the membrane are not formed at higher, and in terms of fusion more relevant, concentrations either (up to 1.2 mol%). Such behaviour might suggest the two following scenarios: 1) hetero-coiling of lipopeptides is outcompeted by the formation of homo-coils or 2) the peptide segments of the complementary lipopeptides cannot come close enough to each other to facilitate hetero-coiling.
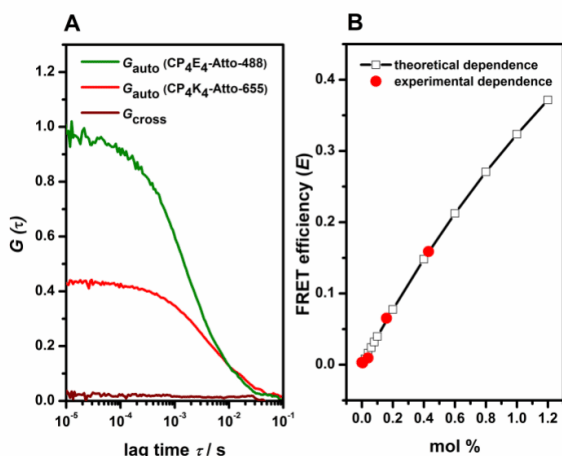

Figure 4. (A): Demonstrative auto-correlation functions (G_{auto}) for CP_4E_4-Atto-488 and CP_4K_4-Atto-655 and the corresponding cross-correlation function (G_{cross}); (B): FRET efficiency E as a function of the acceptor to lipid ratio. The donor/acceptor pair consisted of CP_4E_4-Atto-488/CP_4K_4-Atto-655 fluorescently labelled lipopeptides. The experimental data are displayed as solid red points. A theoretical dependence is shown for reference (black line with empty black squares). It was assumed in this dependence that the donors were homogeneously distributed in two parallel planes (separated by the distance $d_{l-l}(CP_4E_4$-Atto-488$) = d + 2d_{l-m}(CP_4E_4$-Atto-488$)$) whereas acceptors were distributed in two other parallel planes (separated by the distance $d_{l-l}(CP_4K_4$-Atto-655$) = d + 2d_{l-m}(CP_4K_4$-Atto-655$)$). See Figure S1 for further explanation. The donor to lipid ratio was 0.3 mol%.

Scenario 1), i.e. homo-coiling of CP_nE_4 with CP_nE_4, or CP_nK_4 with CP_nK_4 has already been shown to impair membrane fusion.[21] It has also been shown that aggregation of homo- and hetero-coils might enhance the efficiency of fusion or that it can induce membrane curvature and rupture, which might in turn mediate fusion.[2,16,17,19,22–24] However, neither our FCCS or brightness experiments conducted at low lipopeptide concentrations, nor FRET experiments performed at higher lipopeptide concentrations pointed to the presence of CP_nE_4 or CP_nK_4 homo-coils (see SI for results). Despite an obvious absence of stable homo-coils

in the DOPC/DOPE/Chol (50/25/25 mol%) bilayer, individual lipopeptide molecules do 'feel' each other when present at fusion-relevant concentrations. This follows from the observation that after addition of 1 mol % of the lipopeptides to the bilayer, the diffusion of a lipopeptide labelled by Atto-488 is slowed down more than the diffusion of a lipid-like reference probe DiD (1,1'-Dioctadecyl-3,3,3',3'-Tetramethylindodicarbocyanine-5,5'-Disulfonic Acid, D(lipopeptide)/D(DiD) < 1, see the upper panel of **Figure 5**). It is likely that the relatively bulky headgroups of the lipopeptides consisting of a polyethyleneglycol chain and a peptide moiety E_4 or K_4 interfere with each other and cannot therefore move freely. According to Šachl et al., the diffusion under such conditions may still appear free although it is impeded, depending on the overall concentration of the obstacles.[25] In other words, individual CP_4K_4 or $CP_{12}K_4$ molecules can act as obstacles for each other at such elevated concentrations.

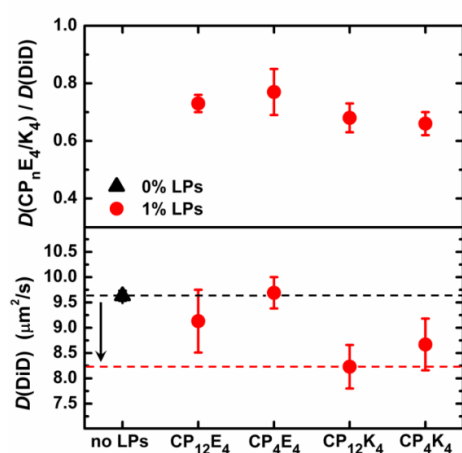**Figure 5.** The diffusion coefficients D of lipopeptides (LPs) CP_nE_4 or CP_nK_4 normalized by the diffusion coefficient of DiD (upper panel) and the diffusion coefficient of the membrane marker DiD (lower panel) shown for the lipopetide concentration of 1 mol% in DOPC/DOPE/Chol (50/25/25 mol%) GUVs.

Scenario 2) could happen if the positions of the peptide segments of the lipopeptides differed so much that the peptides would not 'see' each other. This hypothesis can be tested by FRET.[26] By assuming that the donors (peptide segments of CP_nE_4-Atto-488/CP_nK_4-Atto-488) were found in one plane whereas the acceptors (DiD) were localized at the lipid-water interface in the plane parallel to the first one, the distance between these planes could be determined (**Figure 6**). As shown in panel A of Figure 6, the average time-resolved fluorescence decays of $CP_{12}E_4$-Atto-488 and $CP_{12}K_4$-Atto-488 differ from each other significantly. Because the surface concentration of the acceptors was kept at a constant level the observed differences could have only been caused by different distances of the peptide segments from the interface. Fitting the decays with a model derived by Baumann and Fayer yielded quantitative information regarding the distances.[20] The distance d_{CPK-m} of Atto-488 attached to peptide K_4 in CP_nK_4 was found, on average, $2.2 - 2.3$ nm from the acceptor plane (= the lipid-water interface). The estimated maximal theoretical distances of Atto-488 from this plane were calculated to be 6.5 nm for CP_4K_4 and 9.3 nm for $CP_{12}K_4$, respectively. Comparison of these values with the measured distance suggests 'looping back' of the peptide segments in CP_4K_4 and $CP_{12}K_4$ to the lipid-water interface. This finding is in line with previous findings, which reported the tendency of peptide K_3 and the peptide segment CP_nK_3 to snorkel in the lipid bilayer.[17,19] Conversely, the distance d_{CPE-m} of Atto-488 attached to CP_nE_4 from the bilayer surface equalled on average (6.7 ± 0.6) nm for CP_4E_4 nm or (6.0 ± 0.5) nm for $CP_{12}E_4$, respectively (Figure 6D). This means that CP_nE_4 is in contrast to CP_nK_4 largely exposed to the bulk. Furthermore, as indicated by different time-resolved fluorescence decays obtained from individual GUVs (Figure 6B and **S5**) the peptide segments of both lipopeptides are broadly distributed around the corresponding average distances from the lipid-

water interface. In summary, E_4 in CP_nE_4, which is found more apart from the bilayer, has practically no chance to interact with K_4 in CP_nK_4, which is in contrast localized close to the lipid-water interface. Hetero-coils can apparently be formed only when CP_nE_4 and CP_nK_4 approach each other as constituents of opposing membranes.
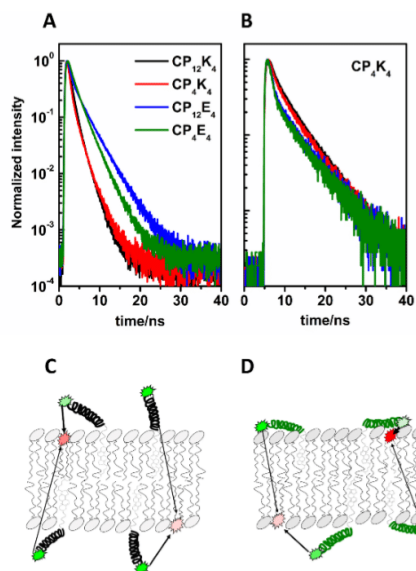

Figure 6. (A) Average normalized time-resolved fluorescence decays of CP_nE_4-Atto-488 and CP_nK_4-Atto-488 donors in the presence of DiD acceptors. (B) An example of varying decays of CP_4K_4-Atto-488 in the presence of DiD obtained for a set of different GUVs. (C-D) Schematic pictures outlying the proposed orientations of CP_nK_4 (C) and CP_nE_4 (D) with respect to the lipid bilayer. The arrows point to the directions in which FRET can occur: within the same leaflet as well as across the lipid bilayer.

Peptide K as an essential modulator of the lipid bilayer

The different distances of the peptide segments of CP_nE_4 and CP_nK_4 from the membrane strongly suggest that K_4 will influence the DOPC/DOPE/Chol (50/25/25 mol%) bilayer more than E_4. Disruptive behaviour has already been reported for the lipopeptide CP_nK_3 and peptide K_3, which are shorter peptides. It was shown that K_3 reorganizes the membrane composition in its vicinity, induces positive membrane curvature, and enhances the probability of lipid tail protrusions.[17] All of these effects are fusion relevant.[27] Here we show by diffusion and Time-Dependent Fluorescence Shift (TDFS) measurements that CP_4K_4 and $CP_{12}K_4$ in contrast to CP_4E_4 and $CP_{12}E_4$ influence the bilayer at least to the level of carbonyls. TDFS provides information about hydration and mobility of the molecules that are found in the immediate vicinity of an excited probe. Both the hydration and mobility can be quantified by the total spectral shift ($\Delta\nu$) and the mean solvent relaxation time (τ_r), respectively. It has been shown that, for Laurdan located at the fully hydrated carbonyl level of a phospholipid bilayer, $\Delta\nu$ is directly proportional to the hydration and τ_r to the rigidity of the lipid bilayer at the level of the carbonyls.[28,29] As follows from **Figure 7**, 2 mol% of CP_4E_4 and $CP_{12}E_4$ were not able to induce any significant changes in hydration or mobility; and as follows from the lower panel of Figure 5, the diffusion of a fluorescent lipid analog DiD remained unaffected by addition of 1 mol % of CP_4E_4 or $CP_{12}E_4$. On the other hand, addition of 2 mol% of both CP_4K_4 and $CP_{12}K_4$ resulted in the prolongation of τ_r between 11 and 15 %, a decrease in $\Delta\nu$ from 4350 to 4250 cm^{-1} and an impeded diffusion of DiD (Figure 5 and 6). Prolongation of τ_r is usually accompanied in TDFS experiments by the decrease in $\Delta\nu$ because of the increase in bilayer rigidity, mostly caused by denser lipid packing, and this

often leads to dehydration as water molecules are expelled to the bulk.[30–32] In summary, CP_4K_4 and $CP_{12}K_4$ do affect the bilayer by increasing bilayer viscosity and by dehydrating the bilayer down to the carbonyl level.
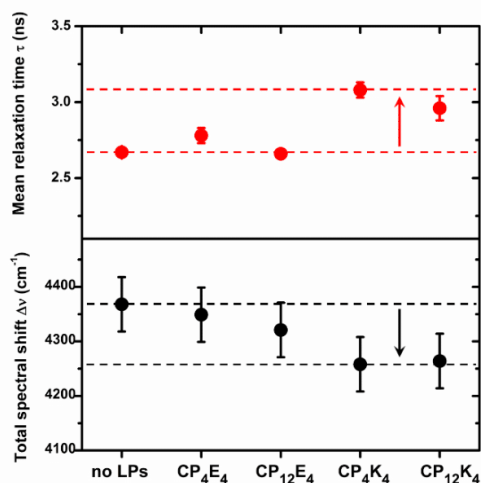

Figure 7. The solvent relaxation time τ_r and the spectral shift Δv of Laurdan in DOPC/DOPE/Chol (50/25/25 mol%) LUVs containing 2 mol% of lipopeptides (LPs).

Consequences for the initial steps of fusion

Fusion of lipid bilayers driven by complementary lipopeptides CP_nE_4 and CP_nK_4 is based on coiled-coil formation between peptides E_4 and K_4. The formation of this coiled-coil is intended to mediate close contact of opposing membranes that the peptides are anchored in. We have already shown that K_4, in contrast to E_4, interacts strongly with DOPC/DOPE/Chol (50/25/25 mol%) bilayers. Such strong binding is probably facilitated by the specific positioning of lysine residues and respective charge distribution within the primary sequence of peptide K_4.[19] Amphipathic helices with this charge distribution pattern are classified as class A1 amphipathic helices and are known to interact with zwitterionic lipids.[33,34] Both CP_nE_4 and CP_nK_4 have been found in DOPC/DOPE/Chol (50/25/25 mol%) bilayers as monomers. Neither FCCS nor FRET experiments revealed any detectable amount of stable homo-oligomers in DOPC/DOPE/Chol (50/25/25 mol%) bilayers at a broad range of lipopeptide concentrations 0.05 -1.2 mol%. Such oligomers might potentially reduce the number of monomeric peptides which are available for binding to a complementary lipopeptide. Formation of homo-oligomers was suggested by previous studies employing circular dichroism spectroscopy. Increased α-helicity, commonly attributed to the homo-coil formation, was shown for peptides in solution and for lipopeptides incorporated in model lipid bilayers at concentration spanning the range at which the fusion normally occurs (1-3 mol%).[12,13,18,35–37] According to a recent study, elevated α-helicity of $CP_{12}K_3$ does not reflect the peptide homo-coiling, but rather membrane snorkelling of K_3 moiety into the lipid bilayer.[16] In contrast to $CP_{12}K_3$, no such interaction was shown for $CP_{12}E_3$, which was reported to exist in equilibrium between unfolded monomers and folded homo-coils at 2 mol%. Although we could not reveal any stable homo-clusters below 1.2 mol% by our methods, it follows from FCS diffusion measurements that the lipopeptides need to 'know' about each other because the diffusion of all lipopeptides is slowed down just because of the presence of the lipopeptides more than the diffusion of DiD. Interactions of CP_nE_4 with CP_nK_4 are happening in a dense sea of neighbouring lipopeptides. Such a dense environment of surrounding lipopeptides might modulate homo- and hetero-coiling of CP_nE_4 and CP_nK_4.

Importantly, binding of K_4 to E_4 is not efficient. According to single molecule FCCS experiments, the majority of CP_4E_4 and K_4 remain unbound to each other when up to a 10-fold excess of K_4 is added to CP_4E_4

containing GUVs. Of note, the cross-correlation amplitude reaches about 30 % of the maximum value that could be reached. Furthermore, binding of K_4 to CP_nE_4 rich GUVs is 6 times stronger than to CP_nE_4 deficient GUVs, and as indicated by diffusion measurements, K_4 sticks to the bilayer, where it diffuses with almost the same speed as the surrounding lipids. Therefore, our FCCS experiments directly prove the exclusive function of CP_nE_4, which is to 'invite' peptide K_4 to the bilayer. Once K_4 attaches to the bilayer it prefers staying there without a need to interact with CP_nE_4. Similarly, it appears from FCCS experiments that significant amounts of CP_4K_4 and E_4 stay unbound to each other when up to a 10-fold excess of E_4 is incubated with CP_4K_4 containing GUVs. The cross-correlation amplitude is even lower in this case as compared to the previous one. This occurs because only a fraction of the entire population of CP_4K_4 is available for binding to E_4 as a result of its preferable interactions with the lipid bilayer. E_4 behaves differently to K_4 in that it interacts with the bilayer exclusively by means of the complementary lipopeptide CP_nK_4. Therefore, the function of CP_nK_4 is actually two-fold: firstly it brings the fusing bilayers into close contact; and secondly it strongly interacts with the lipid bilayer.

Surprisingly, CP_nE_4 and CP_nK_4 do not form hetero-coils so efficiently with each other when reconstituted in the same bilayer. The efficiency of hetero-coiling is in fact so low that FCCS was not able to reveal any detectable amount of CP_4E_4-Atto-488/CP_4K_4-Atto-655 pairs (see above). This can be rationalized by the fact that CP_nK_4 and CP_nE_4 are localized at different distances from the lipid-water interface with a low chance of meeting/interacting with each other. The different localization of the peptides along the bilayer normal may represent an important mechanism by which the number of free CP_nE_4 and CP_nK_4 molecules potentially available for binding to an opposing membrane is kept on a high level, enabling efficient fusion. Furthermore, it follows from the FRET experiments we performed that the transverse distribution of K_4 and E_4 peptide moiety of CP_nK_4/CP_nE_4 molecules is rather broad. Whereas the peptide segment of CP_nE_4 is exposed to the bulk, a considerable fraction of CP_nK_4 is because of the broad transverse distribution imbedded in the bilayer. Previous experiments showed that fusion of CP_nE_3 or CP_nK_3 containing LUVs occurs only if the length of the polyethyleneglycol linker of CP_nE_3 is so long that it can reach the lipid-water interface of the opposing bilayer where majority of CP_nK_4 is imbedded.[38] Therefore, it appears crucial for the fusion that the peptide segment of CP_nE_4 is sufficiently long and exposed to the bulk.

Lipopeptides CP_nE_4 in contrast to CP_nK_4 do not have any observable impact on DOPC/DOPE/Chol (50/25/25 mol%) bilayers. The peptide segments K_4 of CP_nK_4 molecules densely cover the surface of the bilayer at 2 mol% of CP_nK_4, which leads to increased microviscosity and decreased polarity of the carbonyl region of the lipid bilayer. Similar effects were shown to play an important role during membrane fusion.[39,40] Moreover, the diffusion of the lipid analogue DiD becomes impeded by 1 mol% of CP_nK_4. These findings are in line with a peptide insertion model with the helical peptide inserted in parallel to the membrane surface and with the hydrophobic face penetrating into the hydrophobic core of the bilayer.[17] From the macroscopic point of view, the insertion of K_4 was reported to be accompanied by local membrane deformations, which are manifested by an altered bilayer curvature and lipid tail protrusions. These initial steps of membrane fusion are followed by fusion of the proximal leaflets and lipid mixing culminated by opening of a fusion pore and content mixing. However, how these later stages of membrane fusion occur still remains a question.

Conclusions

Fusion of intracellular membranes in nature is mediated by so-called SNARE proteins. A minimal model system for membrane fusion inspired by these proteins consists of cholesterol serving as a lipid membrane anchor, a polyethylene glycol linker and either a cationic peptide K_4 or its counterpart an anionic peptide E_4. The behaviour of the complementary lipopeptides CP_nE_4 and CP_nK_4 is in many ways different, which fits with their previously uncovered distinct roles during fusion. The lipopeptide molecules CP_nK_4 exist in lipid bilayers predominantly as monomers where they strongly interact with the lipid bilayer. During the initial steps of membrane fusion, the main role of CP_nK_4 is to disrupt the bilayer and stimulate it for undergoing fusion. On the other hand, CP_nE_4 molecules work as lipid anchors. The peptide moieties are exposed to the bulk, where they search for the complementary CP_nK_4 molecules, inviting them to their own bilayer. The efficiency of hetero-coil formation is very low and possible only when the lipopeptides approach each

other as constituents of different bilayers. When the complementary lipopeptides are incorporated in the same bilayer the formation of hetero-coils is disabled by different localization of the peptides along the normal of the lipid bilayer. This mechanism keeps the number of monomeric lipopeptides that can hetero-coil with a complementary lipopeptide on the neighbouring bilayer at a high level, enabling efficient fusion. All these facts represent important findings that need to be taken into account when a model for later stages of fusion is developed.

Methods

General. Details of all chemicals, synthesis of the (lipo)peptides and formation of GUVs can be found in the supporting information.

Sample preparation for FCS (fluorescence correlation spectroscopy) and FCCS (fluorescence cross-correlation spectroscopy). The lipopeptides dissolved in methanol were added to the GUVs by keeping the volume of added solvent below 1% of the total volume. Prior to a measurement, the GUVs were incubated with the lipopeptides for at least 30 minutes. Finally, 40 µl of GUVs were added to a microscope chamber (Nunc® Lab-Tek® Chamber) filled with 360 µl of phosphate buffer (25mM PBS, 100mM KCl, 1mM EDTA, pH 7.4, 255 mOsm) and precoated with BSA-biotin/streptavidin for immobilization of the GUVs at the bottom of the microscope chamber. The probe to lipid ratio was between 0.1% and 0.005 %. The bilayer of GUVs contained in addition a lipophilic marker DiD at 0.001 mol%.

Sample preparation for FLIM-FRET (fluorescence lifetime imaging of Förster resonance energy transfer). The preparation procedure was similar to that one described in the previous section except that the lipopeptides were mixed with the lipids already before the formation of GUVs. 40 µl of GUVs were added to a microscope chamber (Nunc® Lab-Tek® Chamber), filled with 360 µl of phosphate buffer (25mM PBS, 100mM KCl, 1mM EDTA, pH 7.4, 255 mOsm) and precoated with BSA-biotin/streptavidin. Prior to a measurement, the GUVs were left for about 15 min to settle down at the bottom of a chamber.

Sample preparation for Time-Dependent Fluorescence Shifts (TDFS) of Laurdan. Appropriate volumes of lipids dissolved in $CHCl_3$ and Laurdan dissolved in MetOH were mixed in glass tubes and dried under nitrogen stream. To get rid of the remaining organic solvents the lipid films were left in vacuum for at least two hours. The resulting lipid films were resuspended in phosphate buffer (25mM PBS, 100mM KCl, 1mM EDTA, pH 7.4). Large unilamellar vesicles (LUVs) were formed by extrusion through filters with a defined pore size of 100 nm (Avestin, Ottawa, Canada). Final concentrations of lipids and Laurdan were 1mM and 0.01mM, respectively. The samples were equilibrated for at least 15 minutes prior to a measurement.

FLIM-FRET, FCS and FCCS measurements were performed on a home build confocal microscope consisting of an inverted confocal microscope body IX71 (Olympus, Hamburg, Germany). The samples were excited by pulsed diode lasers (LDH-P-C-470, λ = 470 nm and LDH-D-C-635, λ = 635 nm, both produced by Picoquant, Germany) with the repetition rate of 12.5 MHz for each of the laser lines. The laser light was pulsed alternatively to avoid artefacts caused by signal bleed-through. The light was up-reflected to a water immersion objective (UPLSAPO 60x, Olympus) with a 470/635 nm dichroic mirror. The signal was detected by two single photon avalanche diode detectors equipped with 515/50 and 685/50 nm band pass filters (Chroma Rockingham, VT).

Z-scans were conducted at the top of a single GUV. The membrane was scanned vertically in 15 steps separated 150 nm apart from each other. 60-seconds-long intensity trace was recorded at each position. To obtain the average diffusion coefficients measurements on at least five different GUVs were done. Further details on the analysis of data can be found for instance in [41]. During acquisition of FLIM-FRET data, GUVs were scanned at the cross-section with the resolution of 512 x 512 pixels (0.6 ms/pixel). Decays from at least five different GUVs were summed up and used for further analysis. The temperature was kept at 25°C. The analysis of FLIM-FRET, FCS and FCCS is described in more detail in supporting information (SI) of this paper.

TDFS measurements. Steady-state emission spectra were measured on Fluorolog-3 spectrofluorometer (model FL3–11; Jobin Yvon Inc., Edison, NJ, USA) equipped with a xenon-arc lamp whereas time-resolved fluorescent decays were recorded using a 5000U Single Photon Counting setup equipped with a cooled Hamamatsu R3809U-50 microchannel plate photomultiplier (IBH, UK). Laurdan was excited at 373 nm

with an IBH NanoLed 11 laser diode. The data were collected for a series of wavelengths ranging from 400 nm to 540 nm with a 10 nm step. Potentially present scattered light was eliminated by a cut-off emission filter > 399 nm. Each decay was fitted with a multi-exponential function using the iterative reconvolution procedure (IBH DAS6 software). Time-resolved emission spectra (TRES) were reconstructed from the recorded series of fluorescent decays and the corresponding steady-state emission spectrum.[42] To determine positions of maxima in TRES, $v(t)$, the TRES spectra were fitted by a log-normal function. The total spectral shift Δv was calculated as $\Delta v = [v(0) - v(\infty)]$. The so-called correlation function of solvent relaxation is expressed as $C(t) = [v(t) - v(\infty)]/[\Delta v]$ and allows for quantitative description of solvation dynamics occurring in the system. Finally, the mean solvent relaxation time equals $\tau_r = \int_0^\infty C(t)\mathrm{d}t$ per definition. TDFS experiments were performed at 283 K.

Conflicts of interest

There are no conflicts to declare.

Acknowledgements

Notes and references

1   R. Jahn, T. Lang and T. C. Südhof, *Cell*, 2003, **112**, 519–533.
2   S. Martens and H. T. McMahon, *Nat. Rev. Mol. Cell Biol.*, 2008, **9**, 543–56.
3   X. Chen, D. Araç, T.-M. Wang, C. J. Gilpin, J. Zimmerberg and J. Rizo, *Biophys. J.*, 2006, **90**, 2062–74.
4   H. Robson Marsden and A. Kros, *Angew. Chem. Int. Ed. Engl.*, 2010, **49**, 2988–3005.
5   T. C. Südhof and J. E. Rothman, *Science*, 2009, **323**, 474–7.
6   L. V Chernomordik, G. B. Melikyan and Y. A. Chizmadzhev, *Biochim. Biophys. Acta*, 1987, **906**, 309–52.
7   M. M. Kozlov and V. S. Markin, *Biofizika*, **28**, 242–7.
8   G. Stengel, R. Zahn and F. Höök, *J. Am. Chem. Soc.*, 2007, **129**, 9584–5.
9   A. Kashiwada, M. Tsuboi and K. Matsuda, *Chem. Commun. (Camb).*, 2009, 695–7.
10   M. Ma, A. Paredes and D. Bong, *J. Am. Chem. Soc.*, 2008, **130**, 14456–8.
11   Y. Gong, Y. Luo and D. Bong, *J. Am. Chem. Soc.*, 2006, **128**, 14430–1.
12   H. Robson Marsden, N. A. Elbers, P. H. H. Bomans, N. A. J. M. Sommerdijk and A. Kros, *Angew. Chem. Int. Ed. Engl.*, 2009, **48**, 2330–3.
13   F. Versluis, J. Voskuhl, B. van Kolck, H. Zope, M. Bremmer, T. Albregtse and A. Kros, *J. Am. Chem. Soc.*, 2013, **135**, 8057–8062.
14   H. R. Zope, F. Versluis, A. Ordas, J. Voskuhl, H. P. Spaink and A. Kros, *Angew. Chem. Int. Ed. Engl.*, 2013, **52**, 14247–51.
15   N. L. Mora, A. Bahreman, H. Valkenier, H. Li, T. H. Sharp, D. N. Sheppard, A. P. Davis and A. Kros, *Chem. Sci.*, 2016, **7**, 1768–1772.
16   M. Rabe, H. R. Zope and A. Kros, *Langmuir*, 2015, **31**, 9953–9964.
17   M. Rabe, C. Aisenbrey, K. Pluhackova, V. de Wert, A. L. Boyle, D. F. Bruggeman, S. A. Kirsch, R. A. Böckmann, A. Kros, J. Raap and B. Bechinger, *Biophys. J.*, 2016, **111**, 2162–2175.
18   H. Robson Marsden, A. V. Korobko, T. Zheng, J. Voskuhl and A. Kros, *Biomater. Sci.*, 2013, **1**, 1046.
19   M. Rabe, C. Schwieger, H. R. Zope, F. Versluis and A. Kros, *Langmuir*, 2014, **30**, 7724–7735.
20   J. Baumann and M. D. Fayer, *J. Chem. Phys.*, 1986, **85**, 4087.
21   G. Pähler, B. Lorenz and A. Janshoff, *Biochem. Biophys. Res. Commun.*, 2013, **430**, 938–43.
22   Y. A. Chen and R. H. Scheller, *Nat. Rev. Mol. Cell Biol.*, 2001, **2**, 98–106.
23   L. Shi, Q.-T. Shen, A. Kiel, J. Wang, H.-W. Wang, T. J. Melia, J. E. Rothman and F. Pincet, *Science (80-.).*, 2012, **335**, 1355–1359.
24   R. Mohrmann, H. de Wit, M. Verhage, E. Neher and J. B. Sorensen, *Science (80-.).*, 2010, **330**, 502–505.
25   R. Šachl, J. Bergstrand, J. Widengren and M. Hof, *J. Phys.D Appl. Phys.*, 2016, **49**, 114002 (11pp).

26   R. Šachl, I. Boldyrev and L. B.-Å. Johansson, *Phys. Chem. Chem. Phys.*, 2010, **12**, 6027–6034.

27   S. Y. Woo and H. Lee, *Sci. Rep.*, 2016, **6**, 1–13.

28   Š. Pokorná, A. Olżyńska, P. Jurkiewicz and M. Hof, Springer Berlin Heidelberg, 2012, pp. 141–159.

29   P. Jurkiewicz, J. Sýkora, A. Olzyńska, J. Humpolíčková and M. Hof, *J. Fluoresc.*, 2005, **15**, 883–894.

30   P. Jurkiewicz, L. Cwiklik, P. Jungwirth and M. Hof, *Biochimie*, 2012, **94**, 26–32.

31   P. Jurkiewicz, L. Cwiklik, A. Vojtíšková, P. Jungwirth and M. Hof, *Biochim. Biophys. Acta - Biomembr.*, 2012, **1818**, 609–616.

32   A. Melcrová, Š. Pokorná, S. Pullanchery, M. Kohagen, P. Jurkiewicz, M. Hof, P. Jungwirth, P. S. Cremer and L. Cwiklik, *Sci. Rep.*, 2016, **6**, 38035.

33   J. P. Segrest, H. De Loof, J. G. Dohlman, C. G. Brouillette and G. M. Anantharamaiah, *Proteins Struct. Funct. Genet.*, 1990, **8**, 103–117.

34   Vinod K. Mishra and M. N. Palgunachari, *Biochemistry*, 1996, **35**, 11210–11220.

35   M. Rabe, A. Boyle, H. R. Zope, F. Versluis and A. Kros, *Biopolymers*, 2015, **104**, 65–72.

36   T. Zheng, J. Voskuhl, F. Versluis, H. R. Zope, I. Tomatsu, H. R. Marsden, A. Kros, J. E. Rothman and X. Y. Zhu, *Chem. Commun.*, 2013, **49**, 3649.

37   I. Tomatsu, H. R. Marsden, M. Rabe, F. Versluis, T. Zheng, H. Zope and A. Kros, *J. Mater. Chem.*, 2011, **21**, 18927.

38   G. A. Daudey, H. R. Zope, J. Voskuhl, A. Kros and A. L. Boyle, *Langmuir*, 2017, **33**, 12443–12452.

39   P. K. J. Kinnunen, *Chem. Phys. Lipids*, 1992, **63**, 251–258.

40   J. M. Holopainen, J. Y. A. Lehtonen and P. K. J. Kinnunen, *Biophys. J.*, 1999, **76**, 2111–2120.

41   A. Benda, M. Beneš, V. Mareček, A. Lhotský, W. T. Hermens and M. Hof, *Langmuir*, 2003, **19**, 4120–4126.

42   M. L. G. Horng Ja Papazyan, a Maroncelli, M, *J. Phys. Chem.*, 1995, **99**, 17337.

Supporting Information

Distinct Roles of SNARE-mimicking Lipopeptides during Initial Steps of Membrane Fusion

Alena Koukalová, Šárka Pokorná, Aimee L. Boyle, Nestor Lopez Mora, Alexander Kros, Martin Hof and Radek Šachl*

Experimental section

Materials. 1,2-dioleoyl-*sn*-glycero-3-phosphocholine (DOPC), 1,2-dioleoyl-*sn*-glycero-3-phosphoethanolamine (DOPE), 1,2-dioleoyl-*sn*-glycero-3-phosphoethanolamine-N-(cap biotinyl) (sodium salt) (DOPE-Biotin) and cholesterol were purchased from Avanti Polar Lipids, Inc. (Alabaster, USA). Streptavidin was ordered from IBA GmbH (Göttingen, Germany). Fluorescent dyes Atto-488 maleimide, Atto-655 maleimide, DOPE-Atto-488 and DOPE-Atto-633 were obtained from ATTO-TEC (Siegen, Germany), whereas 1,1'-Dioctadecyl-3,3,3',3'-Tetramethylindodicarbocyanine-5,5'-Disulfonic Acid (DiD) was obtained from Life Technologies Corporation (Carlsbad, CA). Biotin-labeled bovine albumin (Biotin-BSA), salts (KCl, $Na_2HPO_4 . 7 H_2O$, $NaH_2PO_4 . H_2O$) and other chemicals (D-glucose, sucrose, EDTA) were purchased from Sigma Aldrich (St. Louis, USA). Organic solvents of spectroscopic grade were purchased from Merck (Darmstadt, Germany). All chemicals were used without further purification. Lipopeptides were prepared as described previously[1] and labeled by means of a modified maleimide – thiol reaction using maleimide Atto dyes. Lyophilized aliquots were kept in -80°C freezer. Before any measurement the lipopeptides or peptides were dissolved either in methanol or in phosphate buffer (25mM PBS, 100mM KCl, 1mM EDTA, pH 7.4), respectively.

Labelling of CP_nE_4/K_4 derivatives with Atto dyes. Purified lipopeptides were dissolved in HPLC-grade acetonitrile (MeCN) and 1.1 equivalents of the appropriate dye (Atto-655 maleimide or

Atto-488 maleimide) were dissolved in the same solvent. The two solutions were mixed and stirred in the dark for 1 hour before being diluted so the volume of MeCN was <20% of the total volume. Any unbound dye or unlabelled lipopeptide was subsequently separated from the labelled lipopeptide by HPLC purification using a C4 preparative column. A gradient of 25 – 95% MeCN in water over 30 minutes was employed. The fractions containing dye-labelled lipopeptides were pooled and the MeCN was removed by rotary evaporation before freeze-drying yielded the purified dye-labelled lipopeptides.

Labelling of E and K peptides with Atto dyes. The labelling of the non-lipidated peptides was performed by dissolving the peptides in PBS, pH 7.4 and adding this to 1.1 equivalents of the appropriate Atto dye in MeCN. The resulting solution was stirred in the dark for 1 hour before being diluted so the volume of both MeCN and PBS was <20% of the total volume. The labelled-peptide was separated from unbound dye and non-labelled peptide by HPLC using a C18 column and a gradient of 20-80% MeCN in water over 20 minutes. The fractions containing dye-labelled peptide were freeze-dried.

Preparation of giant unilamellar vesicles (GUVs). GUVs were prepared by electroformation described in detail in.[2] Briefly, appropriate volumes of lipids in $CHCl_3$ and lipopeptides dissolved in methanol:chloroform 1:1 (v/v) for diffusion studies or DiD dissolved in methanol for FRET measurements were mixed in glass tubes and spread on two hollowed titanium plates. All mixtures contained in addition 2 mol % of biotinylated DOPE. The remaining solvent was evaporated by mild heating of the plates, followed by putting the samples into vacuum for at least 1 hour. An electroformation chamber, consisting of the two hollowed plates, was filled with 255 mOsm sucrose solution and sealed with parafilm. An electroformation was conducted at

45 °C. An alternating electrical field of 10 Hz, 4V, was applied for the first 50 min, 2 Hz, 4 V for additional 20 min.

Determination of the distances of peptide segments of CP$_n$K-Atto-488/CP$_n$E-Atto-488 from the lipid-water interface by FRET.

The distances were determined by fitting time-resolved fluorescence (TRF) decays to a model that assumes homogeneous distribution of donors in two parallel planes and acceptors in two other parallel planes (**Figure S1** for an explanation).[3] The donors were represented by Atto-488 fluorophores attached to the C terminus of either CP$_n$E or CP$_n$K lipopeptides whereas the acceptors were represented by a lipid analogue DiD. The latter probe has a chromophore located at the lipid-water interface. In such case, FRET occurs between a plane of donors and two different planes of acceptors that are transversally separated from the former plane by $d_{l\text{-}m}$ or $d_{l\text{-}m}$ + d (Figure S1). Here, d is the thickness of the bilayer, which is given by the transversal distance between both acceptor planes, and $d_{l\text{-}m}$ the distance between the plane of donors (represented by Atto-488 attached to either CP$_n$E or CP$_n$K) and the lipid-water interface. The efficiency of FRET depends on the probability that a donor initially excited at the time $t = 0$ is still excited at the time $t = t$ later. This probability is called the survival probability $G(t)$ and for the case of energy transfer occurring between two parallel planes (a so-called *inter*-FRET) separated at a distance d and containing isotropically oriented probes equals

$$ln\, G_{\text{inter}}(t) = -\frac{C_2}{3}\left(\frac{d}{R_0}\right)^2 \left(\frac{2\mu}{3}\right)^{1/3} \int_0^{2/3\mu}(1 - e^{-s})s^{-4/3}ds, \tag{S1}$$

where $\mu = 3t\left(\frac{R_0}{d}\right)^6 \frac{1}{2\tau}$ and $s = 2\mu \cos^6\frac{\theta_r}{3}$.[3] θ_r stands for the angle between the bilayer normal and the vector connecting the locations of the donor and acceptor dipoles, τ for the average fluorescence lifetime of the donor in the absence of acceptors and C_2 for the reduced surface

concentration of the acceptors. C_2 determines the average number of acceptors found at maximum at the distance R_0 (a so-called Förster radius) from a donor. For a molar acceptor to lipid ratio (= $N_{acceptor}/N_{lipid}$) and a known value of the lipid headgroup area (= a_0), C_2 is given by $C_2 = \pi R_0^2 N_{acceptor}/(N_{lipid} a_0)$. The overall efficiency of FRET is determined by the joint probability $G^{tot}(t)$, which for the given spatial arrangement equals

$$G^{tot}(t) = G_{inter}(t, d_{l-m}) G_{inter}(t, d_{l-m} + d). \tag{S2}$$

This function steps in into the final expression that describes the fluorescence decay $F(t)$ of the donors in the presence of the acceptors

$$F(t) = G^{tot}(t) \sum_i \alpha_i \exp\left(-\frac{t}{\tau_i}\right). \tag{S3}$$

$F_D(t) = \sum_i \alpha_i \exp(-t/\tau_i)$ represents the decay of the donors in the absence of FRET. The distance of a peptide segment of CP$_n$K-Atto-488 or CP$_n$E-Atto-488 from the lipid water interface d_{l-m} was determined by fitting TRF decays to Equation S3.
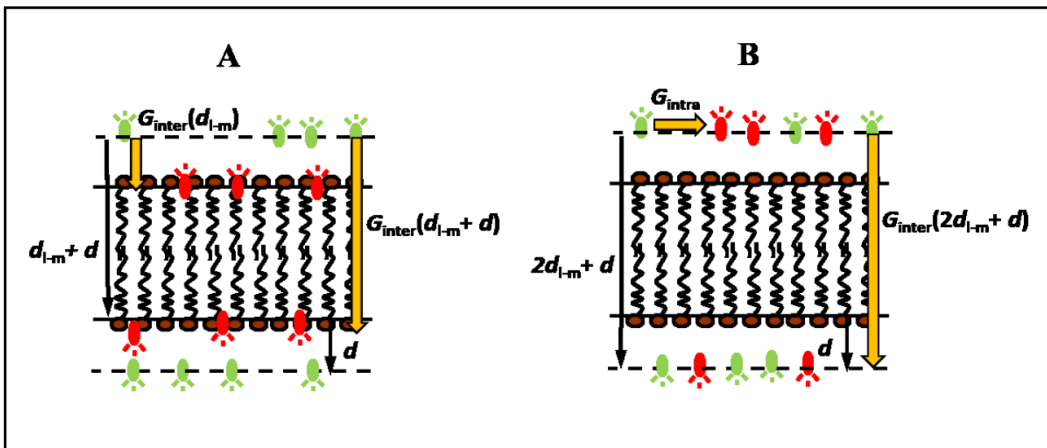
Figure S1. (A) When donors are localized in two parallel planes at the distance d_{l-m} from the lipid water-interface whereas acceptors are localized in two other planes mimicking the lipid-water interface FRET (characterized by the survival probabilities $G_{inter}(d_{l-m})$ and $G_{inter}(d_{l-m} + d)$)

occurs between one layer of donors and two other layers of acceptors; (B) On the other hand, when both donors and acceptors are localized in the same planes at the distance $d_{\text{l-m}}$ from the lipid water-interface FRET occurs both within the same leaflet (G_{intra}) as well as across the lipid bilayer ($G_{\text{inter}}(2d_{\text{lm}}+d)$). The thickness of the lipid bilayer is denoted by d in this cartoon.

The analysis of z-scan FCS (fluorescence correlation spectroscopy) and FCCS (fluorescence cross-correlation spectroscopy) data.

Z-scan FCS is a technique by which absolute diffusion coefficients D in a lipid bilayer are obtained. The method is based on measuring fluorescence autocorrelation functions (ACF) at well-defined positions along the z optical axis of a microscope. The acquired ACFs are fitted to a model that assumes Brownian diffusion of a dye in a plane and transition of the dye to the triplet state [4]

$$G(\tau) = 1 + \frac{1}{PN} \frac{1}{1+(\tau/\tau_{\text{D}})} \frac{1-T+T\,\exp(-\tau/\tau_{\text{T}})}{1-T} \tag{S4}$$

Here τ is a so-called lag-time, PN is the particle number denoting the number of fluorescent probes in the focal spot, τ_{D} the mean diffusion time, which equals the average time it takes to the probe to diffuse from the center of the spot to its boundary, T the fraction of the dye in the triplet state and τ_{T} the lifetime of the triplet state. Due to the Gaussian beam profile, τ_{2D} and PN values follow a parabolic dependence on Δz, which allows for determination of D according to [5]

$$\tau_{\text{2D}} = \frac{w_0^2}{4D}\left(1 + \frac{\lambda^2 \Delta z^2}{\pi^2 n^2 w_0^4}\right), \tag{S5}$$

where n is the refractive index, λ is the excitation wavelength and Δz the distance between the actual sample position and a reference position.

Similarly, FCCS is based on the analysis of cross-correlation functions (CCF), which can be obtained by correlating a signal from one detector (e.g. the green one, F_g) with the signal from a second detector (e.g. the red one, F_r) according to [6]

$$G_{gr}(\tau) = \frac{\langle F_g(t)F_r(t+\tau)\rangle}{\langle F_g(t)\rangle\langle F_r(t)\rangle} \, . \tag{S6}$$

The amplitude of a CCF is then given by

$$G_{gr}(0) = \frac{N_{gr}}{N_g N_r} \, , \tag{S7}$$

where $N_{g\text{-}r}$, N_g, N_r are the numbers of particles in the focal spot containing both green and red, only green or only red fluorophores, respectively. The maximum cross-correlation amplitude G_{gr}^{max} that can be obtained from an FCCS experiment is controlled by the total number of green/red- labelled fluorophores in the bilayer. For intance, if green-labeled A_g reacts with an excess of red-labelled B_g according to $A_g + B_r \Rightarrow A_gB_r + B_r$ the maximum cross-correlation amplitude equals

$$G_{gr}^{max}(0) = \frac{1}{G_{rr}(0)} \, , \tag{S8}$$

where $G_{rr}(0)$ is the auto-correlation amplitude obtained from the red channel. Correction of $G_{gr}^{max}(0)$ is necessary to account for imperfect overlap of the green and red excitation volumes. In our case, the overlap was estimated to 86%, $G_{gr}^{max,corr}(0) = 0.86G_{gr}^{max}(0)$. By normalizing $G_{gr}(0)$ with $G_{gr}^{max,corr}(0)$ according to $(G_{gr}^{norm}(0) = G_{gr}(0)/G_{gr}^{max,corr})$, a measure is obtained which reports on the extent by which A binds to B: if $G_{gr}^{norm}(0) = 1$ the entire population of A binds to B, if $G_{gr}^{norm}(0) = 0$ no binding occurs.

The brightness analysis

The brightness analysis allows for the determination of the number of emitting molecules in a moving object. It can thus be used to measure the size of an oligomer in terms of the number of fluorescently labelled molecules the cluster consist of:

$$oligomer\ size = \frac{\phi_{cluster}(z_0)}{\phi_{monomer}(z_0)}. \tag{S9}$$

Here, $\phi_{cluster}(z_0)$ is the brightness of a cluster and $\phi_{monomer}(z_0)$ is the brightness of a monomer at the centre of the lipid bilayer. The brightness values $\phi_i(z_0)$ are calculated from the average intensity $\langle I(t) \rangle$ and the known number of moving objects in the focal spot PN as

$$\phi_i(z_0) = \frac{\langle I(t) \rangle}{PN}. \tag{S10}$$

The center of the lipid bilayer can be found by the z-scan approach (see above).

Binding of E and K to DOPC/DOPE/Chol (50/25/25 mol%) bilayer: supporting experiments by z-scan FCS

Stronger binding of the peptide K_4 to the lipid bilayer was confirmed Z-scan FCS. In this approach, the mean diffusion time τ_D, i.e. the average time a fluorescent molecule spends in an illuminated focal spot, and the average number of molecules in the focal spot PN can be determined as a function of the distance from the bilayer center z. For molecules moving within the membrane, the dependence of both τ_D and PN on z should exhibit a parabolic shape as the central part of the focal spot moves from the bulk to the bilayer of a GUV, and further away into the vesicle interior. Such parabolic dependence was observed for a reference probe DOPE-Atto-488, which is a fluorescent lipid analogue moving freely in the bilayer, and for the peptide K_4-Atto-655, indicating efficient membrane binding (**Figure S2**). In the latter case, the shape of the parabola was asymmetric as a consequence of the considerable amount of K_4 that contributed to

the overall fluorescence from the bulk. On the other hand, the flat profiles of Figure S2 belonging to E_4 together with its very fast diffusion at the lipid bilayer point to no or very weak binding of E_4 to DOPE/DOPC/Chol (50/25/25 mol%) bilayer. Similar behavior was reported for shorter peptides E_3 and K_3 [7] as well as their analogs labelled by tryptophan.[8]
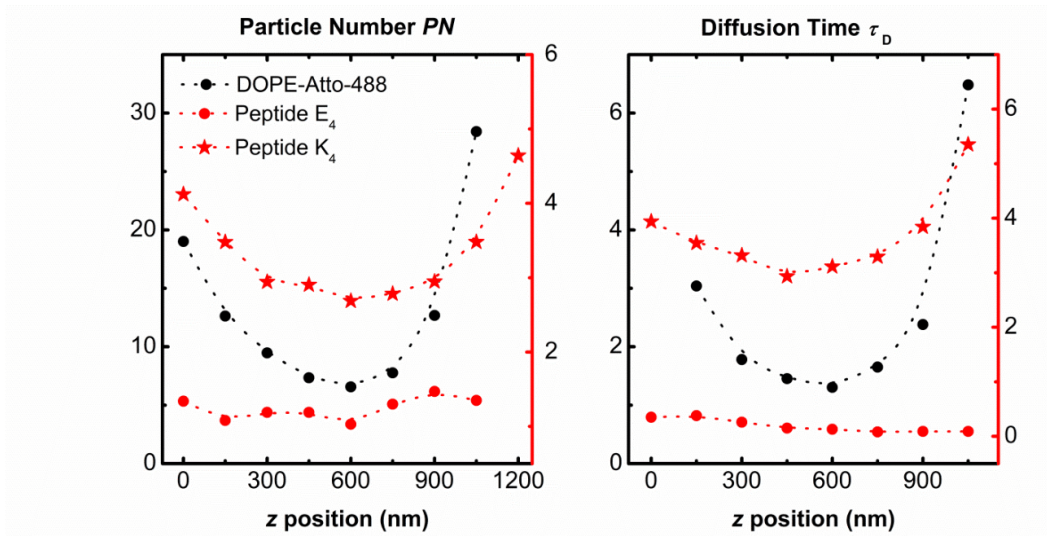

Figure S2. The particle number *PN* and the mean diffusion time τ_D as a function of the position *z* along the normal of the lipid bilayer. The dependencies shown are for peptide K_4 (red stars) and E_4 (red circles) and the reference lipid analog DOPE-Atto-488 (black circles). Dashed lines are displayed to guide the eye.

Homo-clustering of the lipopeptides as seen by FRET

FRET always leads to shortening of the average fluorescence lifetime from $\langle \tau_D \rangle$ to $\langle \tau \rangle$. Both $\langle \tau_D \rangle$ and $\langle \tau \rangle$ can be calculated from recorded time-resolved fluorescence decays by $\langle \tau \rangle = \frac{\int_0^\infty tF(t)dt}{\int_0^\infty F(t)dt}$. A frequently used parameter called the efficiency of FRET is determined by those values:[9]

$$E = 1 - \frac{\langle \tau \rangle}{\langle \tau_D \rangle}.$$ (S11)

To monitor clustering of the lipopeptides (LPs) by FRET one half of LP population was labelled by Atto-488 donors and the other half by Atto-655 acceptors. A fact was used that clustering brings individual lipopeptide molecules into close contact. Such behaviour results in enhanced E in comparison to the situation when LPs are homogeneously distributed in the bilayer. Therefore, a plot of E against the acceptor molar ratio $N_{\text{acceptor}}/N_{\text{lipid}}$ should yield a steeper dependence in comparison to the dependence that would be obtained for a homogeneous distribution of the probes. By knowing the distances of Atto-488 and Atto-655 chromophores from the lipid-water interface (see the manuscript for determination of these values) the latter dependence can be calculated (Equation S1-S3 and Equation S12 and S13) and compared with the experimental one. Because of structural similarities between the donors and acceptors it could be assumed that the donors and acceptors were found in the same plane. In such a case FRET takes place within the same plane (a so-called *intra*-FRET) and between two planes separated by a distance $d + 2d_{\text{l-m}}$ (see Figure S1 for explanation). Such considerations yield the joint probability

$$G^{\text{tot}}(t) = G_{\text{intra}}(t)G_{\text{inter}}(t, d + 2d_{\text{l-m}}), \tag{S12}$$

where G_{intra} denotes the survival probability accounting for *intra*-FRET [3]

$$ln\, G_{\text{intra}}(t) = -C_2 \Gamma\left(\frac{2}{3}\right)\left(\frac{t}{\tau}\right)^{1/3}. \tag{S13}$$

In Equation S13 Γ stands for the gamma function.

In contrast to the results for CP$_4$E$_4$-Atto-488/CP$_4$K$_4$-Atto-655 shown in the manuscript, the experimental dependencies of CP$_4$E$_4$-Atto-488/CP$_4$E$_4$-Atto-655 or CP$_4$K$_4$-Atto-488/CP$_4$K$_4$-Atto-655 shown here are even less steep than the theoretical ones (**Figure S3**). This happens 1) because the LPs do not homo-coil with each other and 2) because the theoretical dependencies were calculated for the case of donors and acceptors being localized exclusively in two identical parallel planes separated by the distance $d_{\text{l-l}}$ that corresponds to the transverse distance between

the planes ($d_{l\text{-}l} = d + 2d_{l\text{-}m}$, where d is the thickness of a lipid bilayer). However, we know from the analysis of FRET on GUVs (see the section above) that the peptide segments of LPs take up less defined positions along the normal of the lipid bilayer. This behavior separates the donors from the acceptors more than the theoretical dependence assumes. As a consequence of this, the density of the acceptors around each donor, which controls the efficiency of FRET, is lowered and yields a less steep dependence of the FRET efficiency E on ALR. The dependence was practically constant for CP_4E_4 and considerably steeper for CP_4K_4. Of note, the natural distribution of the peptide moieties in LPs along bilayer's normal leads in this case to more significant deviations from the theoretical dependence of E on ALR in contrast to the case where the donor plane is separated from the acceptor one. In the latter case, the effects cancel out, which actually explains the reason why the experimental dependence of E on ALR perfectly follows the theoretical trend of Figure 4 in the manuscript.
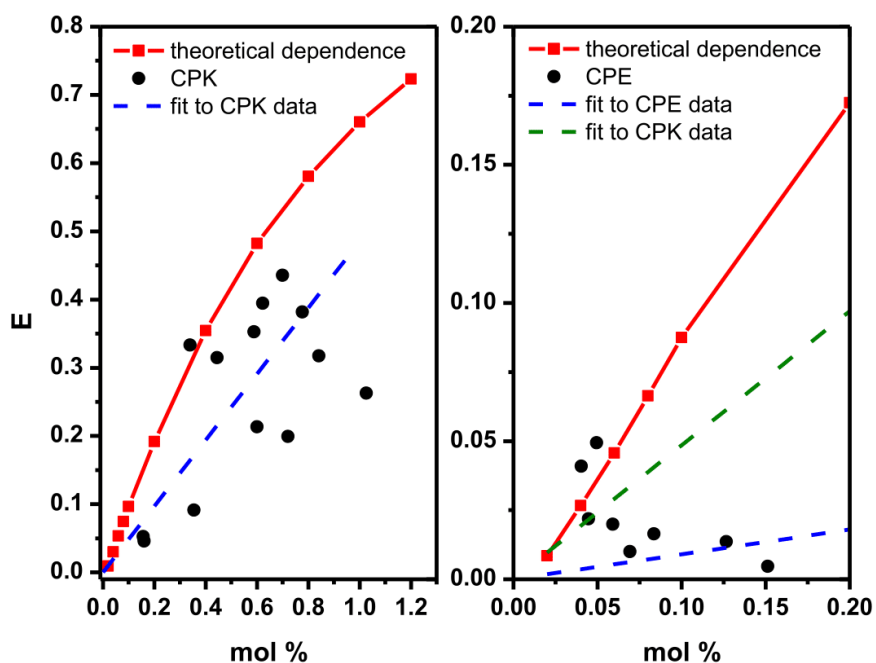
Figure S3. FRET efficiency E as a function of the acceptor to lipid ratio. The donor/acceptor

pair consisted of CP_4K_4-Atto-488/CP_4K_4-Atto-655 (left) or CP_4E_4-Atto-488/CP_4E_4-Atto-655

(right) fluorescently labelled lipopeptides. The experimental data are displayed as black points

and the fit to those points as a blue dashed line. A theoretical dependence is shown for reference

as well (red solid line). It was assumed in this dependence that the donors and acceptors are

homogeneously distributed in two parallel planes separated by the distance $d_{l\text{-}l}$, which

corresponds to the transverse distance of CP_4E_4/CP_4K_4 chromophores ($d_{l\text{-}l} = d + 2d_{l\text{-}m}$). For

better comparison, the fit to the data for CP_4K_4 is also shown in the right hand panel of this

figure (green dashed line). The donor to lipid ratio was 0.3 mol%.

Homo-clustering of the lipopeptides as seen by the brightness analysis and FCCS

Direct proof for homo-coiling would be a positive cross-correlation obtained from fluorescence cross-correlation spectroscopy (FCCS) experiments for one of the two following pairs reconstituted in the GUVs: CP_nE_4-Atto-488/CP_nE_4-Atto-655 or CP_nK_4-Atto-488/CP_nK_4-Atto-655. Co-diffusion of Atto-488 and Atto-655 labeled LPs would give rise to fluctuations in fluorescence intensity appearing in both detection channels, inducing a positive cross-correlation. The cross-correlation amplitude $G_{gr}(0)$ was, however, equal to zero for both CP_4E_4 and CP_4K_4 molecules (**Figure S4**).
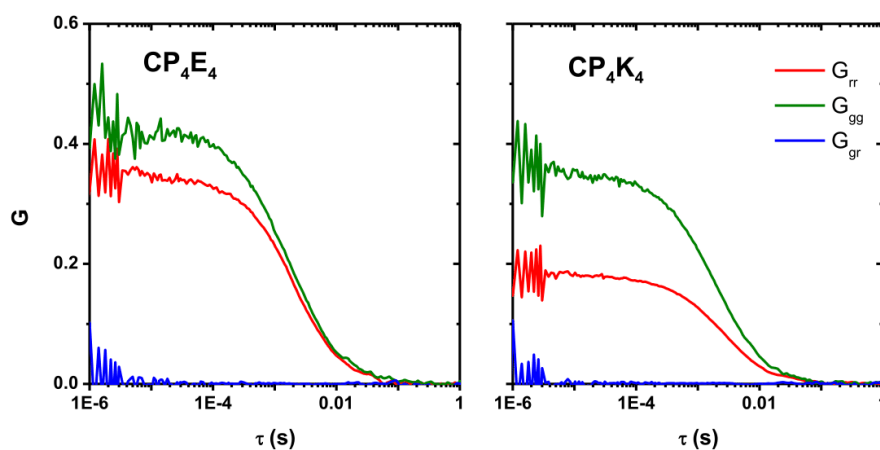
Figure S4. Demonstrative fluorescence auto- (G_{gg} and G_{rr}) and cross-correlation (G_{gr}) functions for CP_4E_4-Atto488/Atto-655 (left) and CP_4K_4-Atto-488/Atto-655 (right).

Brightness measurements which enable determination of the number of monomeric units in a cluster by comparison of the brightness of a monomer with that of a cluster supported the negative conclusion about homo-coiling (**Table S1**). The brightness of a $CP_{12}E_4$/$CP_{12}K_4$ monomer was, within an experimental error, the same as the brightness of a 'cluster' (= homo-coil).

Table S1. The brightness Φ of $CP_{12}E_4$-Atto-488/$CP_{12}K_4$-Atto-488 in DOPC/DOPE/Chol (50/25/25 mol%) bilayers at the LP to lipid ratio 1:20 000. The monomer brightness of $CP_{12}E_4$ or $CP_{12}K_4$ was determined by diluting Atto-488-labelled lipopeptides with an excess of unlabeled ones (1%).

		CP_4E_4	$CP_{12}E_4$	CP_4K_4	$CP_{12}K_4$
Φ	Monomer	-	1.79 ± 0.36	-	2.45 ± 0.36
	Potential cluster		1.91 ± 0.39		2.34 ± 0.27
$d_{l\text{-}m}$ (nm)		6.7 ± 0.6	6.0 ± 0.5	2.3 ± 0.2	2.2 ± 0.2

Distribution of the peptide segments of LPs along bilayer's normal

Broad distribution of the peptide segments of LPs along bilayer's normal follows from the difference in the time-resolved fluorescence (TRF) decays obtained from individual GUVs (see **Figure S5**). Fitting the average TRF decays yielded information about the average distances $d_{l\text{-}m}$ of the peptide segments from the lipid-water interface (**Table S1**).
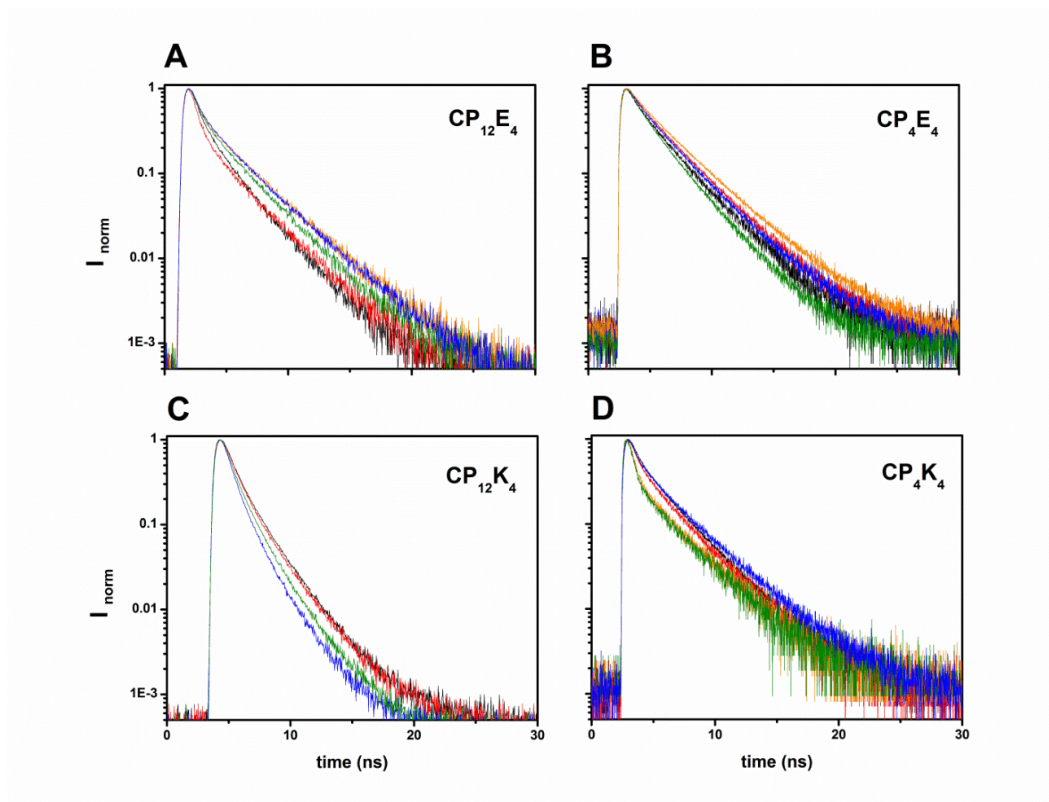
Figure S5. Time-resolved fluorescence decays of CP$_{12}$E$_4$-Atto-488 (A), CP$_4$E$_4$-Atto-488 (B), CP$_{12}$K$_4$-Atto-488 (C) or CP$_4$K$_4$-Atto-488 (D) in the presence of DiD acceptor obtained from individual GUVs. All samples showed variability of the decays obtained from individual GUVs.

References

1   F. Versluis, J. Voskuhl, B. Van Kolck, H. Zope, M. Bremmer, T. Albregtse and A. Kros, .

2   M. Lidman, Š. Pokorná, A. Dingeldein, T. Sparrman, M. Wallgren, R. Šachl, M. Hof and G. Gröbner, *Biochim. Biophys. Acta - Biomembr.*, 2016, **1858**, 1288–1297.

3   J. Baumann and M. D. Fayer, *J. Chem. Phys.*, 1986, **85**, 4087.

4   J. Widengren, Ü. Mets and R. Rigler, *J.Phys.Chem.*, 1995, **99**, 13368–13379.

5   A. Benda, M. Beneš, V. Mareček, A. Lhotský, W. T. Hermens and M. Hof, *Langmuir*,

2003, **19**, 4120–4126.

6   J. Ries, Z. Petrášek, A. J. García-Sáez and P. Schwille, *New J. Phys.*, , DOI:10.1088/1367-
        2630/12/11/113009.

7   G. A. Daudey, H. R. Zope, J. Voskuhl, A. Kros and A. L. Boyle, *Langmuir*, 2017, **33**,
        12443–12452.

8   M. Rabe, C. Aisenbrey, K. Pluhackova, V. de Wert, A. L. Boyle, D. F. Bruggeman, S. A.
        Kirsch, R. A. Böckmann, A. Kros, J. Raap and B. Bechinger, *Biophys. J.*, 2016, **111**,
        2162–2175.

9   B. Valeur, *Molecular Fluorescence Principles and Applications*, Wiley-VCH Verlag
        GmbH, New York, 2001.

Controlled liposomal membrane fusion triggered by fusogenic coiled-coil peptides assessed by simultaneous dual-color time-lapsed fluorescence microscopy

Controlled liposomal membrane fusion triggered by fusogenic coiled-coil peptides assessed by simultaneous dual-color time-lapsed fluorescence microscopy

Nestor Lopez Mora,[a†] Aimee L. Boyle,[a] Bart Jan van Kolck,[a] Anouk Rossen,[a] Šárka Pokorná,[b] Alena Koukalová,[b] Radek Šachl,[b] Martin Hof [b*] and Alexander Kros.[a*]

[a] Supramolecular and Biomaterials Chemistry, Leiden Institute of Chemistry, Leiden University, P.O. Box 9502, 2300 RA Leiden, The Netherlands.

[b] J. Heyrovský Institute of Physical Chemistry, Academy of Sciences of the Czech Republic, v.v.i., Dolejškova 2155/3, 182 23 Prague 8, Czech Republic.

Membrane fusion, lipopeptides, lipid & content mixing, dual color microscopy, FCS, lateral mobility.

ABSTRACT: We have employed a model system for membrane fusion, inspired by natural SNARE proteins, to facilitate fusion between Giant Unilamellar Vesicles (GUVs) and Large Unilamellar Vesicles (LUVs) under physiological conditions. In this system, SNARE proteins are replaced by two synthetic lipopeptide constructs comprising the coiled-coil heterodimer-forming peptides $K_4[(KIAALKE)_4]$ or $E_4[(EIAALEK)_4]$, a PEG spacer of variable length, and a cholesterol moiety to anchor the peptides into the liposome membrane. GUVs are functionalized with one of the lipopeptide constructs and the fusion process is followed by adding LUVs bearing the complementary lipopeptide. Dual-color time lapse fluorescence microscopy was used to visualize lipid and content mixing by monitoring fluorescence of GUVs. We observed the docking of LUVs onto the membrane of GUVs, a process which is not detectable in LUV-LUV studies, and the lipid mixing of the outer membranes. The lipid-mixing assay, together with fluorescence correlation spectroscopy (FCS), produced insights as to the K_4-membrane interaction which was further studied by varying the spacer length of the lipopeptide. Content-mixing assays showed a low efficiency of membrane fusion due to clustering of CP_nK_4-functionalized LUVs on the GUV target membranes. We showed that, through the use of the non-ionic surfactant Tween 20, content-mixing between GUVs and LUVs could be improved, meaning this system has the potential to be employed for drug delivery in biological systems.

INTRODUCTION

Numerous model systems for membrane fusion have been developed in recent years, which have employed a diverse range of molecules as fusogens. Examples of such fusogens include: hydrogen bonding motifs;[1] DNA;[2-7] PNA,[8,9] coiled-coil peptides,[10,11] and small molecule recognition motifs.[12-16] These systems exhibit varying efficiencies of fusion: some only facilitate hemifusion, or lipid-mixing; whereas others promote full fusion, resulting in content-mixing. For systems that demonstrate full fusion, not all are able to do so specifically, i.e. content-mixing is often accompanied by leakage.

We have previously developed a model system capable of specific, leakage-free, full fusion, which was inspired by SNARE-driven membrane fusion. This system comprises two coiled-coil-forming peptides named $K_4 [(KIAALKE)_4]$ and $E_4 [(EIAALEK)_4]$,[17] which serve as fusogenic recognition motifs. These are coupled to a cholesterol membrane anchor via a flexible polyethylene glycol (PEG) linker of variable length (Figure 1). The formation of a heterodimeric coiled-coil brings the two opposing membranes into close proximity, inducing efficient, leakage-free, membrane fusion.[18]

Numerous aspects of this system have been altered, including: the length and oligomer state of the peptides;[19,20] the PEG spacer length;[21] and the nature, and position of the lipid anchor,[22-24] and the effects of these variables on the fusion process has been investigated. Moreover, the system has been applied in the targeted delivery to the membrane of GUVs and cells.[25-28]

To date, Large Unilamellar Vesicles (LUVs), with sizes of approximately 100 nm, have been used to probe the various aspects of this model system, however the LUV–LUV interaction exhibits an inherent high degree of membrane curvature and tension, which may affect the energetics of the membrane fusion process. Moreover, the relative small size of LUVs does not allow for the visualization of the docking and fusion steps of the membrane fusion process, restricting studies to bulk measurements. By employing Giant Unilamellar Vesicles (GUVs) and mixing them with LUVs, fusion could be visualized in more detail, and would also be more relevant to natural fusion processes as the size of a typical GUV ranges from 1 – 20 µm, which is more representative of the size of a cell. There are a limited number of fusion studies which have been conducted

with GUVs and LUVs employing either natural SNARE proteins,[29,30] or amphipathic, monomeric peptides based on viral fusion protein sequences.[31,32] To the best of our knowledge, no designed, multi-component peptide system has been used to induce fusion of GUVs and LUVs.

Herein, we use time-lapse fluorescence microscopy to monitor membrane fusion of GUVs and LUVs under physiological ionic strength conditions, promoted by our synthetic coiled-coil peptide system. The peptide-functionalized GUVs (sizes 10–20 μm), act as a simple biophysical model of the plasma membrane of cells, and the fusion process is triggered upon the addition of LUVs bearing the complementary lipopeptide. We tested both the specific molecular recognition of the coiled-coil system by the mixing of membranes, via lipid-mixing assays, and the mixing of the inner aqueous contents through content-mixing assays by utilizing simultaneous dual-color fluorescence microscopy experiments (Figure 1).

EXPERIMENTAL SECTION

General. Details of all chemicals, synthesis of lipopeptides[21] and formation of GUVs,[33] can be found in the supporting information.

Labeling of GUVs with lipopeptides CP_nK_4 and CP_nE_4. GUVs were functionalized with 1 mol% CP_nK_4 or CP_nE_4 (n=4, 12). Stock solutions of CP_nK_4 or CP_nE_4 (15 μL, 50 μM in $CH_3OH:CHCl_3$ 1:1) were dried by evaporating the solvent under a gentle stream of air and subsequently placing in a vacuum oven overnight. The lipopeptide film was hydrated by adding 700 μL of PBS supplemented with $CaCl_2$ (1 mM), $MgCl_2$ (0.5 mM) and glucose (200 mM), referred to as supplemented PBS in this manuscript, vortexed and transferred to a microcentrifuge tube. 300 μL of a solution with free-floating GUVs was transferred into the microcentrifuge tube containing the lipopeptide solution. The mixture was incubated for 60 minutes before 300 μL of the GUV-lipopeptide mixture was transferred to a microscopy chamber for experiments.

Labeling of GUVs with lipopeptide CP_nK_4 and Tween 20. GUVs were functionalized with a mixture of 1 mol% CP_nK_4 and either 0.4 or 1 mol% (with respect to CP_nK_4) Tween-20. Stock solutions of CP_nK_4 (15 μL, 50 μM in $CH_3OH:CHCl_3$ 1:1) and Tween 20 (5.6 μL or 14 μL, 0.001 mM in CH_3OH) were mixed and dried by evaporating the solvent under a stream of air before being placed in a vacuum oven overnight. The CP_nK_4-Tween 20 film was hydrated by adding 700 μL of supplemented PBS, vortexed and transferred to a microcentrifuge tube. Subsequently 300 μL of a solution with free-floating GUVs was transferred into the microcentrifuge tube containing the CP_4K_4-Tween 20 mixture. The solution was incubated for 60 minutes before 300 μL was transferred to a microscopy chamber for experiments.

Formation of LUVs with lipopeptides CP_nK_4 or CP_nE_4 for lipid-mixing experiments. Peptide-functionalized LUVs were formed using 1 mol% CP_nK_4 or CP_nE_4 (n=4, 12). Lipid solutions (1 mL) with the lipid composition 50 mol% 1,2-dioleoyl-sn-glycero-3-phosphocholine (DOPC), 25 mol% 1,2-dioleoyl-sn-glycero-3-phosphoethanolamine (DOPE) and 25 mol% cholesterol (CH) (2:1:1 molar ratio, 1 mM), ATTO 633 DOPE (0.5 mol%) and lipopeptides CP_nK_4 or CP_nE_4 (50 μM in $CH_3OH:CHCl_3$ 1:1) were mixed and dried by evaporating the solvent and placing in a vacuum oven overnight. The dried lipid film was rehydrated by adding 1 mL of PBS supplemented with $CaCl_2$ (1 mM), $MgCl_2$ (0.5 mM) and sucrose (200 mM). The LUVs were subsequently formed by sonication at room temperature for 2-4 minutes to form LUVs with ~120 nm diameters, as determined by DLS (Zetasizer Nano-S, Malvern).

Formation of carboxyfluorescein-loaded LUVs with lipopeptides CP_nK_4 or CP_nE_4 for content mixing experiments. A lipid solution (1 mL) with the lipid composition DOPC:DOPE:CH (2:1:1 molar ratio, 1 mM) and 0.5 mol% ATTO 633 DOPE was prepared and subsequently dried under a gentle stream of air before placing in a vacuum oven overnight. The lipid film was hydrated by adding 1 mL of carboxyfluorescein (50 μM) in PBS supplemented with $CaCl_2$ (1 mM), $MgCl_2$ (0.5 mM) and sucrose (200 mM). The LUVs were formed by extrusion (0.4 μm polycarbonate membrane) in a mini extruder fitted with 250 μL syringes. Free carboxyfluorescein was separated from the liposome-encapsulated carboxyfluorescein by size exclusion using a Sephadex column (2.5 mL) with supplemented PBS as the eluent. Liposome formation was verified by DLS. Finally, these LUVs were functionalized with 1 mol% CP_nK_4 or CP_nE_4. A stock solution of CP_nK_4 or CP_nE_4 (200 μL, 50 μM in $CH_3OH:CHCl_3$ 1:1) was dried under a gentle stream of air and placed in a vacuum oven overnight. The lipopeptide film was hydrated by adding 200 μL of supplemented PBS and was subsequently mixed with the LUV solution (~2.5 mL) for 60 minutes before being used immediately for content mixing experiments with GUVs.

Lipid and content mixing assays LUVs-GUVs. The visualization of GUVs after lipopeptide labeling was achieved using a microscopy chamber which was pre-treated with an aqueous mixture of BSA (0.9 mg/mL) and biotin-BSA (0.1 mg/mL) for 30 minutes, followed by streptavidin for 30 minutes before rinsing with water. 100 μL of supplemented PBS and 200 μL of peptide-functionalized GUVs were transferred into the microscopy visualization chamber. The GUVs were left to sediment for 30 minutes before imaging. During imaging of the GUVs in a time lapse experiment, either 30 μL of peptide-functionalized LUVs, for a lipid-mixing experiment, or 60 μL of peptide-functionalized LUVs loaded with carboxyfluorescein for content-mixing experiments were added to the microscopy well and imaging was performed for 120 minutes after the arrival of LUVs into the microscopy chamber.

Imaging of GUVs during membrane fusion assays and data analysis. Imaging of GUVs was performed on a Leica TCS SPE confocal microscope system. Illumination was provided by a solid-state laser using a 488 nm laser (15% laser power) for irradiation of carboxyfluorescein and ATTO 488 DOPE, detection 500-550 nm, and a 635 nm laser (15% laser power) for irradiation of ATTO 633 DOPE, detection 650-700 nm. Analysis of the images was performed in ImageJ,[34] by measuring the average intensity of an area corresponding to one GUV for the series of time-lapsed microscopy image frames.

Z-scan Fluorescent Correlation Spectroscopy (z-scan FCS). FCS measurements were performed on an inverted home-built confocal microscope (IX71 Olympus, Hamburg, Germany). Excitation was achieved by two pulsed diode lasers at 470 nm (LDH-P-C-470) and 635 nm (LDH-D-C-635) produced by PicoQuant, Germany. The laser light (10 µW intensity in front of the objective) was pulsed alternately in order to avoid artefacts caused by signal bleed-through. The emitted light was detected by two single-photon avalanche diodes using 515/50 and 697/58 band pass filters (Chroma Rockingham, VT). Z-scan measurements were performed on top of a selected vesicle. The membrane was vertically scanned in 15 steps spaced 200 nm apart. A measurement at each point took 60 s. All data was analyzed using home-written scripts in Matlab (Mathworks, Natick, MA).

RESULTS AND DISCUSSION

GUVs with the lipid composition DOPC:DOPE:CH (2:1:1 molar ratio) were prepared by hydration of hybrid lipid/DexPEG hydrogel film substrates.[33] The lipid mixture was supplemented with ATTO 488 DOPE for fluorescence imaging during lipid-mixing experiments. The use of DexPEG substrates allows for the growth of GUVs under physiological conditions in good yields.[35] The lipid film was deposited on DexPEG substrates and hydrated at room temperature with phosphate buffer solution (PBS, pH=7.4), containing $CaCl_2$ (1 mM), $MgCl_2$ (0.5 mM) and sucrose (200 mM). After GUV formation, the vesicles were transferred to a solution containing supplemented PBS and 1 mol% of lipopeptide CP_nE_4 or CP_nK_4 (n=4, 12). The lipopeptides spontaneously insert into the GUV membrane via the cholesterol anchor (Figure 1), simulating the function of the transmembrane domain of SNARE proteins. Finally, peptide-functionalized GUVs were transferred to a microscopy chamber and were immobilized to the glass surface via streptavidin-biotin binding. The integrity of the GUVs was verified by fluorescence and bright field microscopy. In parallel, peptide-functionalized LUVs were prepared by sonication with the same lipid composition as used for GUVs, but doped with an ATTO 633 DOPE dye. The use of two different dyes for GUVs and LUVs avoids overlapping fluorescence signals in the lipid-mixing assays.

LUV-GUV lipid mixing was initiated by treating CP_4K_4-functionalized GUVs (~20 µm diameter) with 30 µL CP_4E_4-functionalized LUVs (1 mM, ~120 nm diameter) as represented in Figure 1. LUVs were added to a microscope chamber containing 300 µL of immobilized GUVs in supplemented PBS. Instead of performing fluorescence resonance energy transfer (FRET) assays with NBD-rhodamine pairs, a technique commonly employed in bulk liposomal measurements,[6,21,36,37] we took advantage of the
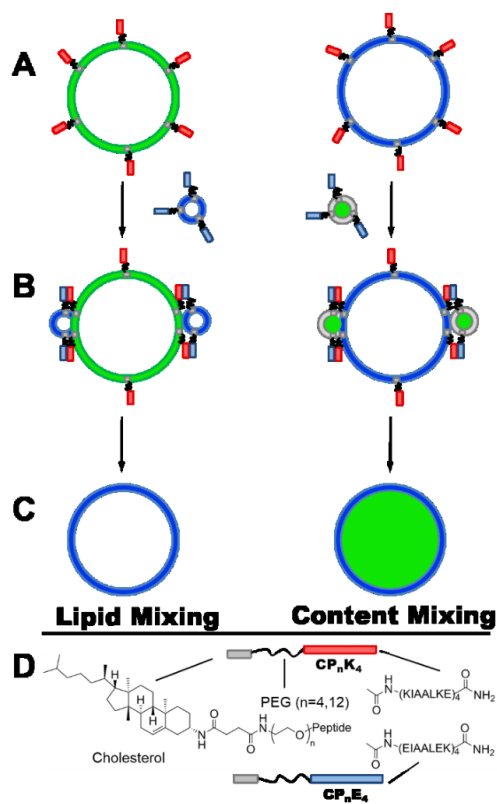
microscopic size of GUVs and visualized the lipid membrane of GUVs in a time-lapse dual-color imaging microscopy experiment, which in the best of our knowledge, represents the first example of lipid mixing between LUVs and GUVs in the presence of complementary synthetic fusogens.

Figure 1. Schematic representation of coiled-coil peptide-mediated membrane fusion between GUVs and LUVs. GUVs are functionalized with lipopeptide CP_nK_4 (red) and LUVs with CP_nE_4 (blue). Lipid-mixing is shown on the left and content-mixing on the right of the top panel. **A)** Spontaneous incorporation of the lipidated peptide into the lipid membrane via the cholesterol anchor results in the functionalization of GUVs with CP_nK_4. **B)** Addition of CP_nE_4-functionalized LUVs to CP_nK_4-functionalized GUVs leading to the formation of a coiled-coil complex which triggers fusion. **C)** Transfer of the fluorescent lipids and mixing of the inner aqueous contents of the GUV after fusion with LUVs represents lipid- and content-mixing. **D)** The structures of the CP_nK_4 and CP_nE_4 lipopeptides employed in this study.

Lipid mixing was detected simultaneously by dual-color fluorescence imaging of peptide-functionalized GUVs doped with ATTO 488 DOPE and peptide-functionalized LUVs labeled with ATTO 633 DOPE. The fluorescence signal from GUVs was monitored at 500-550 nm and from LUVs at 650-700 nm in a Leica TCS SPE confocal microscope every minute for one hour. LUVs and GUVs were observed to be in close proximity 15–20 minutes after LUV addition to the GUV solution, with LUV docking on GUV mem-

branes being detected after a further 5-15 minutes. Initially, LUV docking resulted in the appearance of 'spotty patches' and non-homogeneously distributed fluorescence on the edges of the GUVs.

After 30 minutes, the majority of the GUVs showed homogeneously distributed fluorescence over the entire GUV membrane, and this increased in intensity after 60 minutes (Figure 2A).
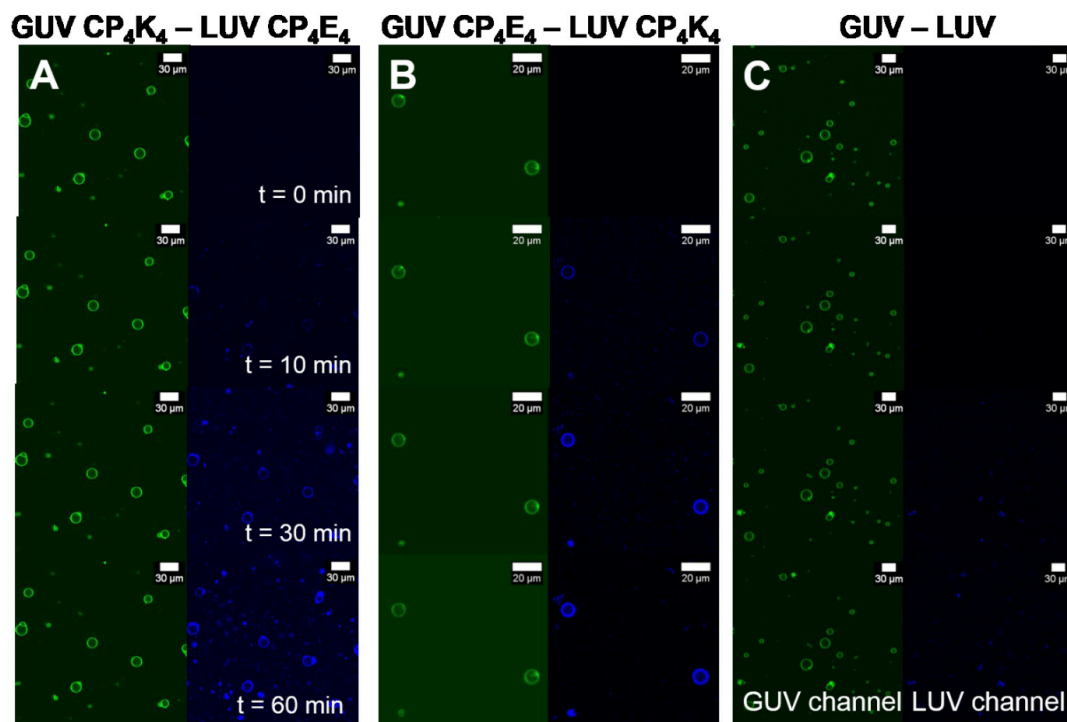

Figure 2. Time-lapse micrographs of the lipid-mixing assay between lipopeptide-functionalized GUVs and lipopeptide-functionalized LUVs before (time=0 minutes) and after (time=10, 30 and 60 minutes) appearance of LUVs in the confocal volume. The GUVs are excited at 488 nm and fluorescence emission is detected between 500-550 nm (green), while LUVs are excited at 633 nm and emission is detected between 650-700 nm (blue). **A**) Lipid-mixing assay between CP_4K_4-functionalized GUVs and CP_4E_4-functionalized LUVs, **B**) Lipid-mixing assay between CP_4E_4-functionalized GUVs and CP_4K_4-functionalized LUVs, **C**) Lipid-mixing assay between non-functionalized GUVs and non-functionalized LUVs. Imaging was performed every minute for one hour using a Leica TCS SPE microscope.

The presence of intact GUVs was verified by observing fluorescence in the green channel at the end of the assay. Interchanging the lipopeptides, i.e. functionalizing GUVs with CP_4E_4 and LUVs with CP_4K_4, also resulted in lipid mixing (Figure 2B). Switching the lipopeptides in this manner resulted in earlier docking and full lipid mixing after just 10 minutes. This result suggests that the interaction of CP_4K_4-functionalized LUVs with GUVs is stronger than with CP_4E_4-functionalized LUVs. Similar experimental conditions were used for a control experiment where non-functionalized GUVs and LUVs were mixed (Figure 2C). Some docking of LUVs was observed in the target membrane after one hour, likely promoted by the negative membrane curvature due to the presence of DOPE in both GUVs and LUVs.

As an additional control experiment, the lipopeptide was omitted from the target membrane of GUVs and the experiment was performed by mixing CP_4E_4 peptide-functionalized LUVs (Figure A1 in *SI*). Fluorescence imaging showed that CP_4E_4-functionalized

LUVs have minimal interaction with the non-functionalized GUV membrane, similar to the lipid-mixing assay in the absence of both lipopeptides. Moreover, we performed the converse lipid-mixing assay by mixing CP_4K_4-functionalized GUVs with non-functionalized LUVs (Figure A1 in *SI*). The fluorescence imaging showed that plain LUVs strongly interact with the CP_4K_4-functionalized GUVs, transferring the fluorescent lipid (ATTO 633 DOPE) to the membrane of GUVs after 30 minutes. The same peptide-membrane interaction is expected by switching peptide CP_4K_4 to LUVs and targeting to non-functionalized GUVs. Those control experiments reveal that peptide K_4 has a strong interaction with the membrane of both GUVs and LUVs. This interaction has been previously reported in lipid monolayer studies combined with surface sensitive infrared reflection absorption spectroscopy (IRRAS) and liposomal assays.[38,39]

In addition to lipid-mixing, this system was also evaluated for its ability to promote content mixing, which is the 'hallmark' of true fusion, between LUVs and GUVs (Figure 1, right). GUVs were prepared as described for lipid-mixing experiments, except that ATTO 633 DOPE was used in place of ATTO 488 DOPE. A solution of carboxyfluorescein at a self-quenching concentration (50 mM, pH 7) was encapsulated within LUVs by freeze-thawing, followed by extrusion, and the non-encapsulated carboxyfluorescein was removed by size exclusion chromatography. The resulting LUVs were subsequently incubated with the appropriate lipopeptide which spontaneously inserts into the lipid membrane. As the LUV solution was diluted by a factor of two after size exclusion, 60 µL of liposomes were added to the microscopy chamber in order to maintain a constant LUV concentration for both lipid- and content-mixing assays. GUVs were imaged for 60 minutes, taking an image every 60 seconds, by dual fluorescence imaging. The fluorescence signal was simultaneously monitored for GUVs (633 nm laser, filter detection 650-700 nm) and LUVs (488 nm laser, filter detection 500-550 nm). All the experiments were performed in duplicate. Detailed analysis for each experiment is presented in the supporting information (A2-A15). The size of individual GUVs was measured directly from the micrographs before and after the

membrane fusion assay, and no size difference in the diameter of GUVs was detected.

The content-mixing experiment between CP_4K_4-functionalized GUVs and CP_4E_4-functionalized LUVs is presented in Figure 3A. A considerable increase in background fluorescence was detected immediately after the addition of carboxyfluorescein-loaded LUVs. This is likely to be due to free carboxyfluorescein being released from the permeable membrane of LUVs, as a result of the high concentration of carboxyfluorescein. Docking of LUVs to the target membrane of GUVs could be observed after 10 minutes, despite the LUVs not being labeled with a fluorescent lipid. This suggests that, after the merging of LUVs with GUVs, a fraction of carboxyfluorescein from the highly-loaded LUVs is distributed along the lipid bilayer, depicting the boundaries of the GUVs, (Figure 3A, green channel t=10 min). This docking time correlates well with the lipid mixing results. Inner content mixing was observed after 30 minutes in the GUVs with small sizes (5-10 µm) and after 60 minutes in larger GUVs (>15 µm); however, inner content mixing was not observed in all the GUVs.
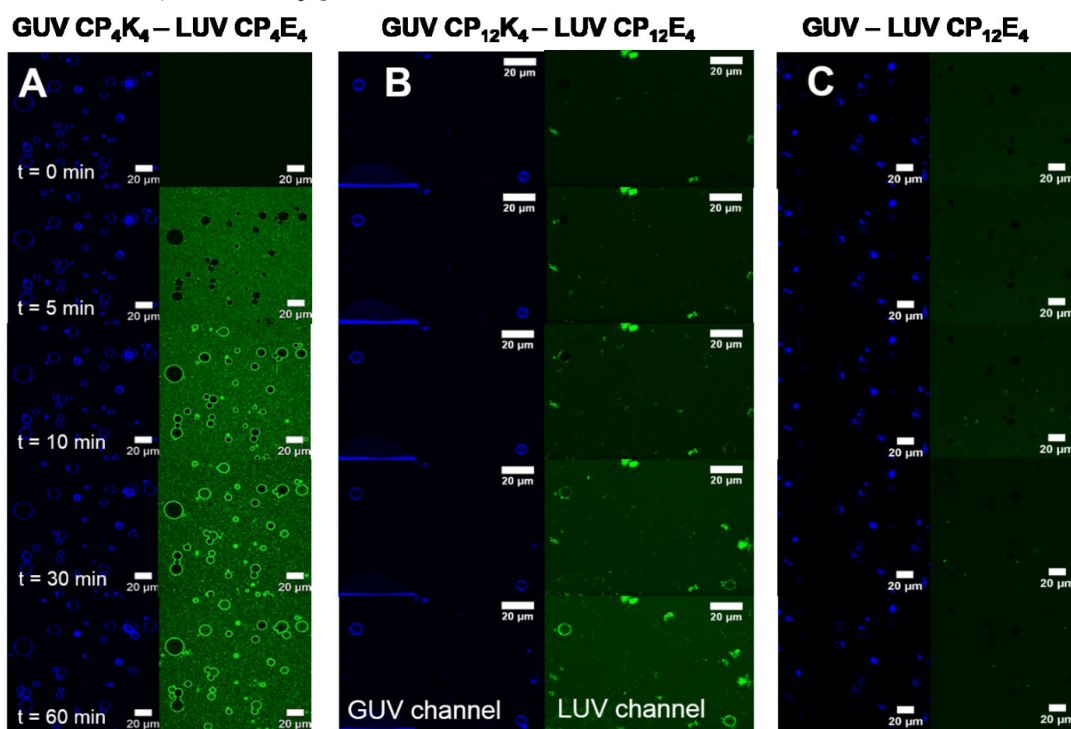

Figure 3. Time-lapse micrographs of the content-mixing assay between lipopeptide-functionalized GUVs and lipopeptide-functionalized LUVs before (time=0) and after (time=5, 10, 30 and 60 minutes) appearance of LUVs in the confocal volume. GUVs are excited at 633 nm and fluorescence emission is detected between 650-700 nm (blue), while LUVs are excited at 488 nm and the emission is detected between 500-550 nm (green). **A**) Content mixing assay between CP_4K_4-functionalized GUVs and CP_4E_4-functionalized LUVs, **B**) content-mixing assay between $CP_{12}K_4$-functionalized GUVs and $CP_{12}E_4$-functionalized LUVs, **C**) control content-mixing assay between non-functionalized GUVs and $CP_{12}E_4$-functionalized LUVs. Imaging was monitored every minute for one hour with a Leica TCS SPE microscope.

In an attempt to increase the quantity of GUVs undergoing content mixing, the length of the PEG spacer was changed from PEG_4 to PEG_{12}. The K_4 – membrane interaction is expected to decrease as a function of spacer length, positively impacting the membrane fusion efficiency as previously found for LUV-LUV fusion events.[21] Figure 3B shows the content mixing experiment between $CP_{12}K_4$-GUVs and $CP_{12}E_4$-functionalized LUVs loaded with carboxyfluorescein. Content mixing was observed in some vesicles with small sizes (5-10 μm) after 60 minutes imaging, but this content mixing was not detected for all imaged GUVs. The exclusion of lipopeptide K_4 from the membrane of GUVs in control experiments did not lead content-mixing, (Figure 3C), which indicates that the presence of CP_nK_4 is essential for full fusion to occur.

Analysis of individual GUVs after membrane fusion showed that GUVs that do not undergo content-mixing exhibit large amounts of clustering of LUVs in the target membrane. To probe this further, we performed an additional batch content-mixing experiment in a microcentrifuge tube using CP_4K_4-functionalized GUVs and CP_4E_4-functionalized LUVs in the presence and absence of the nonionic surfactant Tween 20. After 60 minutes, the GUVs were transferred from the tube to a microscope chamber containing fresh, supplemented PBS solution for dual fluorescence imaging. This transfer process helped with the removal of background fluorescence, which is not possible to avoid during the time lapse imaging. The micrograph for a single CP_4K_4-functionalized GUV after membrane fusion is presented in Figure 4A, no content mixing is observed, and for a single CP_4K_4-Tween 20 functionalized GUV in Figure 4B, where content mixing is observed. This result suggests that mixing CP_4K_4 and Tween 20 increases the fusion efficiency of the fusogenic system. We further studied this effect by preparing a CP_nK_4-Tween 20 (n=4, 12) mixture with two different Tween 20 concentrations (0.4 and 1 mol% respect to CP_nK_4) and incubated this mixture with GUVs. We then followed the same experimental procedure for the time-lapsed content-mixing assay as employed previously. A better performance with 1 mol%, in comparison to 0.4 mol%, Tween 20 observed (Figures A4-5 vs Figures A6-7 in *SI*), supporting our hypothesis that membrane fusion efficiency can be improved with the incorporation of Tween 20.

Time lapsed fluorescence microscopy images of selected CP_4K_4-Tween 20-labelled GUVs (GUV 9, Figure A7 in *SI*) and $CP_{12}K_4$-Tween 20-labelled GUVs (GUV 1, video in *SI*) undergoing content-mixing are presented in Figure 4C. No LUVs clustering was observed in these GUVs after 20 minutes, whereas in the absence of Tween 20 this clustering is detected after 10 minutes. The fluorescence intensity in the lumen of the GUVs increased after 25 minutes and plateaued after 60 minutes (Figure 4D). Most of the small GUVs exhibited content mixing after 60 minutes of imaging while larger vesicles gave less or no fluorescence, in agreement with the previous content-mixing experiments; however a higher number of GUVs did undergo content mixing upon the inclusion of Tween 20.
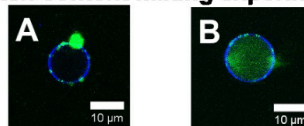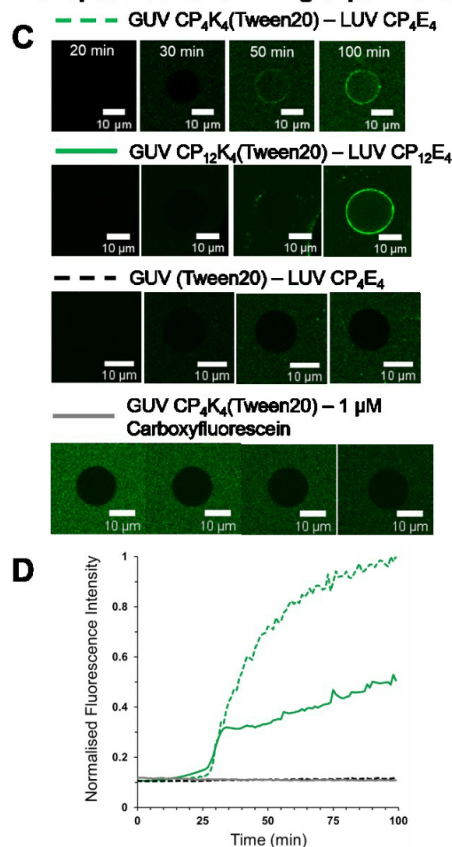

Figure 4. Batch and time-lapsed content-mixing experiments. **A**) Batch content-mixing assay after one hour of incubation of CP_4K_4-functionalized GUVs and CP_4E_4-functionalized LUVs. The micrograph is the overlay of fluorescence confocal microscopy images for 488 nm (green) and 633 nm (blue) channels that shows a single GUV in blue without content mixing and clustering of liposomes in green. **B**) Content-mixing assay after one hour of incubation of CP_4K_4-Tween 20 functionalized GUVs and CP_4E_4-functionalized LUVs. The micrograph shows a single GUV in blue with content mixing in green in the lumen of the GUV. Less clustering of LUVs is observed when Tween 20 is present. **C**) Time-lapsed fluorescence microscopy images of selected single GUVs undergoing content mixing with: GUV CP_4K_4-Tween 20 – LUV CP_4E_4, green dotted line; $CP_{12}K_4$-Tween 20 – LUV $CP_{12}E_4$, green solid line; GUV (Tween 20) – LUV CP_4E_4, black dotted line and GUV CP_4K_4-Tween 20 – 1 μM carboxyfluorescein, grey line. **D**) Nor-

malized fluorescence intensities over time in the lumen of single GUVs from **C**. Normalization profiles were calculated with the maximum fluorescence value obtained from the CP_4K_4-Tween 20– LUV CP_4E_4 assay.

We evaluated the effect of adding solely Tween 20 on the target membrane of GUVs by incubating plain GUVs with Tween 20 (1 mol%) and mixing with carboxyfluorescein-loaded CP_4E_4-functionalized LUVs (Figure 4C). After 60 minutes there was no carboxyfluorescein signal detected on the boundaries or in the interior of the GUVs, showing that the addition of Tween 20 alone does not promote content-mixing between GUVs and LUVs. Additionally, CP_4K_4-Tween 20 GUVs, were transferred to a microscope chamber and free carboxyfluorescein was added. The final concentration of carboxyfluorescein was adjusted to 1 μM, which gives similar background fluorescence to that detected in the membrane fusion experiments after the arrival of LUVs in the bottom of the chamber. Quantification of fluorescence inside individual GUVs showed that there was no carboxyfluorescein present in the interior of the GUVs 60 minutes after the experiment was started, (Figure 4C, lower panel) confirming that Tween 20 does not alter the membrane of GUVs, such that they become destabilized or leaky. In addition, several control experiments were performed to validate coiled-coil driven membrane fusion in the presence of Tween 20 (Figures A8-13 in *SI*). Removing CP_4K_4 from LUVs produced similar results to the experiment between non-functionalized GUVs and non-functionalized LUVs with minimal docking and no content transfer from LUVs to GUVs. Docking of non-functionalized LUVs on the target membrane of CP_4K_4-Tween 20 functionalized GUVs was visible in good agreement with the lipid-mixing experiment. However, visual content mixing was not obvious due to a high background fluorescence originating from the carboxyfluorescein loaded liposomes. Development of fluorescence over time showed a similar profile inside and outside GUVs (Figures A10-11 in *SI*).

We conclude from time-lapsed lipid- and content-mixing experiments that the strong interaction of CP_nK_4 with the lipid bilayer may cause destabilization of the GUV lipid membrane with the length of PEG spacer regulating this interaction. The incorporation of CP_nK_4 resulted in inhomogeneous fluorescence on the target membrane of individual GUVs due to LUVs clustering, which makes the evaluation of content-mixing efficiency challenging. However, our findings show that both CP_nE_4 and CP_nK_4 are necessary for efficient content-mixing and that the mixture of CP_nK_4-Tween 20 leads to an increase of content mixing events in single GUVs. Therefore, the effect of Tween 20 on the incorporation of CP_nK_4 and the effect of this mixture on the mobility of the membrane lipids was studied by z-scan fluorescence correlation spectroscopy (z-scan FCS).[40] Z-scan FCS experiments were performed with fluorescent lipopeptides CP_nK_4-Atto 488 and CP_nE_4-Atto 488 (n=4, 12). To facilitate this, a cysteine residue was introduced at the C-terminus of both peptides and the fluorescent dye ATTO 488 maleimide was coupled to this thiol-containing residue. The fluorescent lipopeptides to lipids ratio was set to 1:20,000, producing a final concentration of 0.005 mol% lipopeptide in the lipid

membrane of GUVs. The experimental concentration of 1 mol% lipopeptide, which is used in the lipid and content mixing assays was reached by mixing fluorescent lipopeptides with non-fluorescent lipopeptides at the ratio of 1:50,000. The lipid probe 1,1'-dioctadecyl-3,3,3',3'-tetramethylindo-dicarbocyanine perchlorate (DiD) was used as membrane tracer in a 1:100,000 dye:lipid ratio. The time-dependent intensity fluctuations were measured using z-scan FCS in order to calculate the autocorrelation function. This autocorrelation function was then fitted to a diffusion model which assumes free 2D diffusion, yielding lipopeptide and DiD diffusion coefficients (D), (Figure 4).
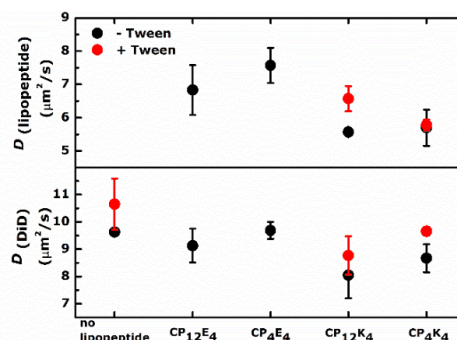

Figure 5. Diffusion coefficients (D) of CP_nE_4 and CP_nK_4 lipopeptides (black dots) and CP_nK_4-Tween 20 mixtures (red dots) in GUVs. Tween 20 concentration is 1 mol% of the particular lipopeptide amount. Every point plotted corresponds to the average of at least three different GUVs and the error bars correspond to the standard deviation.

The diffusion coefficients of the lipopeptides (D_{CPnE4} and D_{CPnK4}) (Figure 5, upper panel) were compared to those of DiD (Figure 5, lower panel), as DiD reflects the overall mobility of the lipid bilayer, which is sensitive to the presence of the lipopeptide incorporated. In general D measurements for all lipopeptide combinations were lower than the diffusion coefficient of only DiD (D_{DiD}). This indicates that the cholesterol anchors the lipopeptides strongly in GUV membrane, with the cholesterol being well incorporated.[41] The D_{DiD} values in the presence of CP_nE_4 are similar to the values of the D_{DiD} tracer in the absence of CP_nE_4, which indicates this lipopeptide has a similar mobility to the tracer with a weak mobility retardation with a longer PEG spacer. In contrast, a higher mobility restriction was found for D_{DiD} in the presence of CP_nK_4, with a 10% decrease of the diffusion coefficient for the shorter PEG_4 spacer and a 15% decrease with the longer PEG_{12} spacer in comparison with D_{DiD} in the absence of CP_nK_4. This result confirms the strong K_4–membrane interaction that was observed in the time lapsed lipid-mixing assay between CP_4K_4-functionalized GUVs and non-functionalized LUVs (Figure A1 in *SI*).

The addition of Tween 20 increases the D_{CPnK4} (n=4, 12) for the longer PEG_{12} spacer, while the shorter PEG_4 spacer remains the

7

same. This finding is in line with the decrease of the K_4 – membrane interaction as a function of spacer length previously found in the content mixing assay. Interestingly, the D_{DiD} increases in the presence of Tween 20 for all CP_nK_4 (n=4, 12) combinations. This increase in the D_{DiD} suggests the softening of the membrane lipids by Tween 20, which was corroborated in the absence of lipopeptides (Figure 5, red dots in the lower panel). Together, these data indicate that the incorporation of Tween 20 facilitates membrane fusion by softening the membrane lipids. Therefore the $CP_{12}K_4$-Tween 20 mixture could be an optimal candidate for improving membrane fusion efficiency, but surfactant-lipopeptide interactions should be considered more deeply in further studies.

CONCLUSIONS

In conclusion we successfully visualized coiled-coil driven membrane fusion between GUVs and LUVs under physiological conditions for the first time. The use of GUVs as a target membrane allowed the visualization of both liposome docking and membrane fusion by dual colour fluorescence microscopy. Time lapsed imaging provided additional insights as to the mechanism of the membrane fusion process and facilitated optimization of the fusion model. Clustering of CP_nK_4-functionalized LUVs was detected in the membrane of GUVs, decreasing the efficiency of coiled-coil formation and hence fusion. Incorporation of the surfactant Tween 20 together with CP_nK_4 produced softening of the target membrane, leading to an improvement in the efficiency of fusion. These results raise the hope that this coiled-coil-based membrane fusion system can be applied as a fast and efficient cellular drug delivery system in further studies.

ASSOCIATED CONTENT

Supporting Information. Chemicals, lipopeptides synthesis, fluorescent labelling of lipopeptides, GUVs formation method and full microscopy data sets of control experiments. A movie showing the content mixing experiment with the mixture $CP_{12}K_4$-Tween 20- $CP_{12}E_4$. This material is available free of charge via the Internet at http://pubs.acs.org.

AUTHOR INFORMATION

Corresponding Authors

* martin.hof@jh-inst.cas.cz; * a.kros@chem.leidenuniv.nl

Present Addresses

† Department of Chemistry, King's College London, Britannia House, 7 Trinity Street, London, SE1 1DB.

Notes

The authors declare no competing financial interest.

REFERENCES

(1)   Ma, M.; Paredes, A.; Bong, D. *J Am Chem Soc* **2008**, *130*, 14456.

(2)   Chan, Y. H. M.; van Lengerich, B.; Boxer, S. G. *Biointerphases* **2008**, *3*, FA17.

(3)   Jumeaux, C.; Wahlsten, O.; Block, S.; Kim, E.; Chandrawati, R.; Howes, P. D.; Hook, F.; Stevens, M. M. *Chembiochem* **2018**, *19*, 434.

(4)   Meng, Z. J.; Yang, J.; Liu, Q.; de Vries, J. W.; Gruszka, A.; Rodriguez-Pulido, A.; Crielaard, B. J.; Kros, A.; Herrmann, A. *Chemistry-a European Journal* **2017**, *23*, 9391.

(5)   Ries, O.; Loffler, P. M. G.; Rabe, A.; Malavan, J. J.; Vogel, S. *Organic & Biomolecular Chemistry* **2017**, *15*, 8936.

(6)   Stengel, G.; Zahn, R.; Hook, F. *Journal of the American Chemical Society* **2007**, *129*, 9584.

(7)   Chan, Y. H. M.; van Lengerich, B.; Boxer, S. G. *Proceedings of the National Academy of Sciences of the United States of America* **2009**, *106*, 979.

(8)   Lygina, A. S.; Meyenberg, K.; Jahn, R.; Diederichsen, U. *Angewandte Chemie-International Edition* **2011**, *50*, 8597.

(9)   Rabe, A.; Loffler, P. M. G.; Ries, O.; Vogel, S. *Chemical Communications* **2017**, *53*, 11921.

(10)   Kashiwada, A.; Tsuboi, M.; Takamura, N.; Brandenburg, E.; Matsuda, K.; Koksch, B. *Chemistry-a European Journal* **2011**, *17*, 6179.

(11)   Meyenberg, K.; Lygina, A. S.; van den Bogaart, G.; Jahn, R.; Diederichsen, U. *Chemical Communications* **2011**, *47*, 9405.

(12)   Gong, Y.; Luo, Y. M.; Bong, D. *Journal of the American Chemical Society* **2006**, *128*, 14430.

(13)   Kashiwada, A.; Tsuboi, M.; Matsuda, K. *Chemical Communications* **2009**, 695.

(14)   Kashiwada, A.; Yamane, I.; Tsuboi, M.; Ando, S.; Matsuda, K. *Langmuir* **2012**, *28*, 2299.

(15)   Whitehead, S. A.; McNitt, C. D.; Mattern-Schain, S. I.; Carr, A. J.; Alam, S.; Popik, V. V.; Best, M. D. *Bioconjugate Chemistry* **2017**, *28*, 923.

(16)   Valérie, M.-A.; Thaddée, G.-K.; Marie-Alice, G.-B.; Charlie, G.; M., S. J.; Jean-Claude, D.; Jean-Marie, L. *ChemPhysChem* **2001**, *2*, 367.

(17)   Litowski, J. R.; Hodges, R. S. *Journal of Peptide Research* **2001**, *58*, 477.

(18)   Marsden, H. R.; Elbers, N. A.; Bomans, P. H. H.; Sommerdijk, N.; Kros, A. *Angewandte Chemie-International Edition* **2009**, *48*, 2330.

(19)   Zheng, T. T.; Bulacu, M.; Daudey, G.; Versluis, F.; Voskuhl, J.; Martelli, G.; Raap, J.; Sevink, G. J. A.; Kros, A.; Boyle, A. L. *Rsc Advances* **2016**, *6*, 7990.

(20)   Zheng, T. T.; Voskuhl, J.; Versluis, F.; Zope, H. R.; Tomatsu, I.; Marsden, H. R.; Kros, A. *Chemical Communications* **2013**, *49*, 3649.

8

(21)   Daudey, G. A.; Zope, H. R.; Voskuhl, J.; Kros, A.; Boyle, A. L. *Langmuir* **2017**, *33*, 12443.

(22)   Crone, N. S. A.; Minnee, D.; Kros, A.; Boyle, A. L. *International Journal of Molecular Sciences* **2018**, *19*.

(23)   Versluis, F.; Dominguez, J.; Voskuhl, J.; Kros, A. *Faraday Discussions* **2013**, *166*, 349.

(24)   Versluis, F.; Voskuhl, J.; van Kolck, B.; Zope, H.; Bremmer, M.; Albregtse, T.; Kros, A. *Journal of the American Chemical Society* **2013**, *135*, 8057.

(25)   Mora, N. L.; Bahreman, A.; Valkenier, H.; Li, H. Y.; Sharp, T. H.; Sheppard, D. N.; Davis, A. P.; Kros, A. *Chemical Science* **2016**, *7*, 1768.

(26)   Yang, J.; Bahreman, A.; Daudey, G.; Bussmann, J.; Olsthoorn, R. C. L.; Kros, A. *ACS Central Science* **2016**, *2*, 621.

(27)   Yang, J.; Shimada, Y.; Olsthoorn, R. C. L.; Snaar-Jagalska, B. E.; Spaink, H. P.; Kros, A. *ACS Nano* **2016**, *10*, 7428.

(28)   Li, K.; C., A. S. H.; Sylvestre, B.; Alexander, K.; Frederick, C. *Angewandte Chemie International Edition* **2016**, *55*, 1396.

(29)   Tareste, D.; Shen, J.; Melia, T. J.; Rothman, J. E. *Proc Natl Acad Sci U S A* **2008**, *105*, 2380.

(30)   Witkowska, A.; Jahn, R. *Biophys J* **2017**, *113*, 1251.

(31)   Etzerodt, T. P.; Trier, S.; Henriksen, J. R.; Andresen, T. L. *Soft Matter* **2012**, *8*, 5933.

(32)   Kahya, N.; Pecheur, E. I.; de Boeij, W. P.; Wiersma, D. A.; Hoekstra, D. *Biophysical Journal* **2001**, *81*, 1464.

(33)   Mora, N. L.; Hansen, J. S.; Gao, Y.; Ronald, A. A.; Kieltyka, R.; Malmstadt, N.; Kros, A. *Chemical Communications* **2014**, *50*, 1953.

(34)   Schneider, C. A.; Rasband, W. S.; Eliceiri, K. W. *Nature Methods* **2012**, *9*, 671.

(35)   Mora, N. L.; Gao, Y.; Gutierrez, M. G.; Peruzzi, J.; Bakker, I.; Peters, R. J. R. W.; Siewert, B.; Bonnet, S.; Kieltyka, R. E.; van Hest, J. C. M.; Malmstadt, N.; Kros, A. *Soft Matter* **2017**, *13*, 5580.

(36)   Struck, D. K.; Hoekstra, D.; Pagano, R. E. *Biochemistry* **1981**, *20*, 4093.

(37)   Stryer, L.; Haugland, R. P. *Proceedings of the National Academy of Sciences* **1967**, *58*, 719.

(38)   Rabe, M.; Schwieger, C.; Zope, H. R.; Versluis, F.; Kros, A. *Langmuir* **2014**, *30*, 7724.

(39)   Rabe, M.; Aisenbrey, C.; Pluhackova, K.; de Wert, V.; Boyle, Aimee L.; Bruggeman, Didjay F.; Kirsch, Sonja A.; Böckmann, Rainer A.; Kros, A.; Raap, J.; Bechinger, B. *Biophysical Journal* **2016**, *111*, 2162.

(40)   Benda, A.; Benes, M.; Marecek, V.; Lhotsky, A.; Hermens, W. T.; Hof, M. *Langmuir* **2003**, *19*, 4120.

(41)   Kessel, A.; Ben-Tal, N.; May, S. *Biophysical Journal* **2001**, *81*, 643.

Controlled liposomal membrane fusion triggered by fusogenic coiled-coil peptides assessed by simultaneous dual-color time-lapsed fluorescence microscopy

Nestor Lopez Mora,[a] Aimee Boyle,[a] Bart Jan van Kolck,[a] Anouk Rossen,[a] Šárka Pokorná,[b] Alena Koukalová,[b] Radek Šachl,[b] Martin Hof[b] and Alexander Kros.[a*]*

[a] Supramolecular and Biomaterials Chemistry, Leiden Institute of Chemistry, Leiden University, P.O. Box 9502, 2300 RA Leiden, The Netherlands.

[b] J. Heyrovský Institute of Physical Chemistry, Academy of Sciences of the Czech Republic, v.v.i., Dolejškova 2155/3, 182 23 Prague 8, Czech Republic.

SUPPORTING INFORMATION

Contents: Page

1. **EXPERIMENTAL SECTION**

2. **DATASETS FOR TIME LAPSED LIPID, CONTENT MIXING AND
    CONTROL EXPERIMENTS BETWEEN GUVs AND LUVs.**

3. **REFERENCES**   S14

1. EXPERIMENTAL SECTION

Chemicals.

1,2-dioleoyl-sn-glycero-3-phosphocholine (DOPC), 1,2-dioleoyl-sn-glycero-3-phosphoethanolamine (DOPE), 1,2-dioleoyl-sn-glycero-3-phosphoethanolamine-N-(biotinyl) (sodium salt) (DOPE-Biotin), were purchased from Avanti Polar Lipids. Cholesterol (CH), Bovine Serum Albumin (BSA), biotin-labeled bovine albumin (Biotin-BSA), Streptavidin from Streptomyces avidinii, Polyethylene glycol sorbitan monolaurate (Tween 20), Calcium chloride anhydrous ($CaCl_2$), Magnesium chloride hexahydrate ($MgCl_2 \cdot 6\ H_2O$), 5(6)-carboxyfluorescein, Sodium Hydroxide (NaOH), sucrose and glucose were purchased from Sigma-Aldrich. 1,2-dioleoyl-sn-glycero-3-phosphoethanolamine-ATTO 488 (ATTO 488 DOPE), 1,2-dioleoyl-sn-glycero-3-phosphoethanolamine-ATTO 633 (ATTO 633 DOPE), ATTO 488 maleimide and ATTO 655 maleimide were purchased from ATTO-TEC GmbH. 1,1′-dioctadecyl-3,3,3′,3′-tetramethylindo-dicarbocyanine perchlorate (DiD) was supplied by Life Technologies Corporation (Carlsbad, CA). Fmoc-protected amino acids were purchased from Novabiochem and Biosolve. Sieber amide resin was purchased from Agilent Technology. Phosphate Buffered Saline (PBS, pH 7.4) was supplemented with $CaCl_2$ (1 mM) and $MgCl_2$ (0.5 mM) for all GUV studies. Lipid solutions of DOPC:DOPE:CH (50:25:25 molar ratio, 1 and 14 mM) were prepared in chloroform.

Synthesis of lipopeptides CP_4K_4 and CP_4E_4.

The spacer N_3-PEG$_4$-COOH, cholesteryl- 4-amino-4-oxobutanoic acid, and the lipopeptides CP_4K_4 and CP_4E_4 were synthesized and utilized following procedures previously reported.[1-3] The peptide segments E: NH_2-(EIAALEK)$_4$-CONH$_2$ and K: NH_2-(KIAALKE)$_4$-CONH$_2$ were synthesized using standard Fmoc chemistry on a peptide synthesizer (CEM-Liberty 1), then the spacer N_3-PEG$_4$-COOH was coupled to the N-terminus of the peptide segment. The azide terminal group on the spacer was reduced to an amine to obtain an N-terminal free amine for coupling to cholesteryl-4-amino-4-oxobutanoic acid using 5 eq. of DIPEA and 4 eq. of PyBOP in DMF over 72 h. Finally, the lipopeptides were purified by RP-HPLC with a Gemini C4 column to yield a pure product (Yield: 20-25%). The identity of the peptides and lipopeptides was determined by LC-MS.

Synthesis of lipopeptides $CP_{12}K_4$ and $CP_{12}E_4$.

The peptide segments E: NH_2-(EIAALEK)$_4$-GC-$CONH_2$ and K: NH_2-(KIAALKE)$_4$-GC-$CONH_2$ were synthesized using standard Fmoc chemistry on a peptide synthesizer (CEM-Liberty 1). After synthesis, the resin was washed with DMF and Fmoc-PEG$_{12}$-COOH (1.1 equivalents) was coupled to the N-terminus of the peptides using 3 equivalents of HCTU and 4 equivalents of DIPEA. The reaction was left to proceed overnight. The resin was then washed with DMF, before the PEG$_{12}$ molecule was Fmoc deprotected using a 20% piperidine in DMF solution. Deprotection was achieved by incubating the resin with the piperidine/DMF solution for 10 minutes. This process was repeated 3 times, after which the resin was washed with DMF. Cholesteryl hemisuccinate was coupled using the same methodology as for the PEG coupling, (3 equivalents of HCTU and 4 equivalents of DIPEA, overnight reaction). The resin was washed with DMF, followed by DCM, before the product was cleaved from the resin using a mixture of TFA:TIPS:EDT (95:2.5 :2.5). The cleavage solution was left for one hour before the peptide was precipitated in ice-cold diethyl ether. The peptide was collected by centrifugation before being dissolved in water and freeze dried. Finally, the lipopeptides were purified by RP-HPLC with a Gemini C4 column to yield a pure product (Yield: 20-25%). The identity of the peptides and lipopeptides was determined by LC-MS.

Fluorescent lipopeptides CP_nK_4 and CP_nE_4.

Lipopeptides were fluorescently labeled with ATTO 488 and ATTO 655 dyes via maleimide-thiol reaction. Cysteine N-terminated lipopeptides (1 mg) were dissolved in 1 mL DCM and 1.3 fold molar excess of ATTO maleimide dye solution (1 mg/mL) was added to the reaction vessel. The reaction mixture was stirred for 1 hour protected from the light. Then the solvent was evaporated in vacuum and the lipopeptides were purified by RP-HPLC with a Gemini C4 column. The identity of the fluorescently labeled lipopeptides was determined by MALDI-TOF Mass Spectrometry.

Formation of GUVs.

Giant Unilamellar Vesicles (GUVs) were grown on Dex-PEG hydrogel (1:1 molar ratio) coated microscope glass slide substrates as described previously.[4,5] Lipid solution (10 µL) with

the lipid composition DOPC/DOPE/CH (2/1/1 molar ratio, 14 mM), DOPE-Biotin (0.2 mol % respect to lipids) and ATTO 488 DOPE for lipid mixing experiments or ATTO 633 DOPE for content mixing experiments (0.1 mol % respect to lipids) was deposited on a hydrogel coated glass slide, then the lipid solution was dried by evaporating the chloroform under a gentle stream of air and subsequently it was placed in a vacuum oven overnight. A liquid chamber was made by placing a 15 mm (OD) glass O-Ring on top of the hydrogel and sealed with high vacuum silicon grease. The lipid film was hydrated by adding 400 µL of PBS supplemented with $CaCl_2$ (1 mM), $MgCl_2$ (0.5 mM) and sucrose (200 mM) into each chamber and the GUVs were formed overnight at room temperature.

Sample preparation for z-scan FCS

Giant unilamellar vesicles (GUVs) were prepared by electroformation[6,7] with the lipid composition DOPC/DOPE/Cholesterol (2/1/1). Additionally, the lipid mixture was supplemented with DiD in a lipid ratio 1/100 000 as membrane tracer and biotinylated DOPE (2 mol %) for immobilization of GUVs. The lipid mixture was spread on two hollow titanium electrode plates. Solvent evaporation was facilitated by mild heating of the plates and successive drying in vacuum for at least 1 hour. An electroformation chamber was made by putting together two plates, filled with 275mOsm sucrose solution and sealed with parafilm. Electroformation was performed following the successive voltage (V) sequence at 40 °C: 1) V (peak to peak) increased from 0.02 to 1.1 V at 10 Hz for 45 minutes, 2) V = 1.1 V at 10 Hz for 100 minutes and 3) V = 1.3 V at 4 Hz for 30 minutes. An observation chamber (Nunc® Lab-Tek® Chamber) was coated with biotin-BSA followed by streptavidin and filled with 360 µl of phosphate buffer (25mM PBS, 100mM KCl, 1mM EDTA, ~ 20 mM glucose, pH 7.4, 275 mOsm). 40 µl of GUV sucrose solution was incubated for 30 minutes with CP_nK_4 or CP_nE_4 lipopeptides and transferred to the observation chamber. For the experiments with Tween 20 the lipopeptides were mixed with 1 mol% Tween 20 (respect to the concentration of CP_nK_4). For FCS diffusion measurements lipopeptides fluorescently labelled with Atto-488 were used in 1/20 000 lipopeptide to lipid ratio. Higher concentrations of the lipopeptides were achieved mixing fluorescent labelled lipopeptides with unlabeled ones. GUVs were left for at least 20 minutes to settle down and immobilize via biotinylated DOPE-streptavidin-biotin-BSA linker to the glass on the bottom of the chamber. Measurements were carried out at room temperature.

2. DATASETS FOR TIME LAPSED LIPID, CONTENT MIXING AND CONTROL EXPERIMENTS BETWEEN GUVs AND LUVs.

Time lapsed lipid mixing control experiments between GUVs and liposomes.
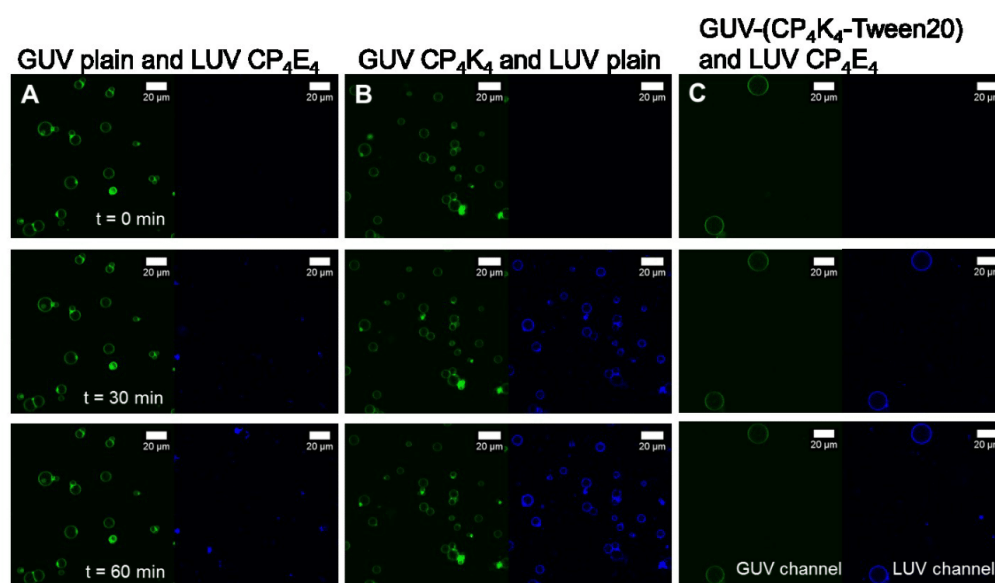

Figure A1. Time lapse micrographs of the lipid mixing control assay between GUVs and LUVs before (time=0) and after (time=30 and 60 minutes) appearance of LUVs in the confocal volume. The GUVs are excited at 488 nm and the emission of fluorescence is detected between 500-550 nm (green color), while LUVs are excited at 633 nm and the emission is detected between 650-700 nm (blue color). A) Lipid mixing assay between GUVs and CP_4E_4 labeled LUVs, B) Lipid mixing assay between CP_4K_4 labeled GUVs and non-labeled LUVs and C) Lipid mixing assay between CP_4K_4-Tween 20 labeled GUVs and CP_4E_4 labeled LUVs. Imaging was performed every minute during one hour in a Leica TCS SPE microscope.

Content mixing between CP₄K₄ labeled GUVs and CP₄E₄ labeled LUVs loaded with carboxyfluorescein.
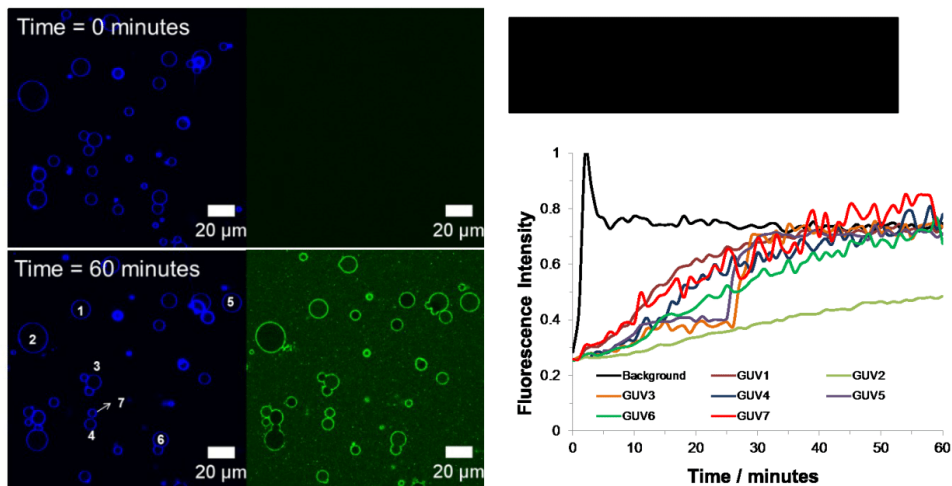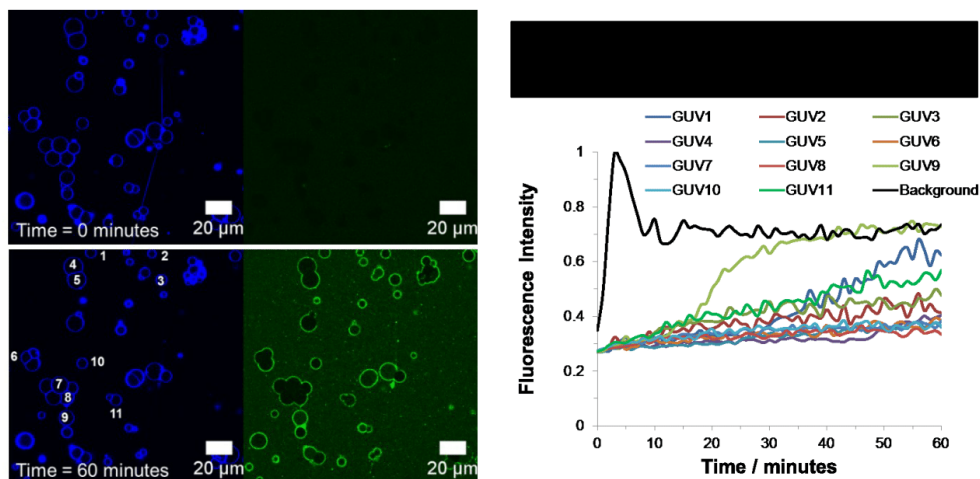

Figure A2. Fluorescence micrographs before (top) and after (bottom) addition of carboxyfluorescein loaded CP_4E_4 liposomes to CP_4K_4 GUVs. GUVs lipid membranes are supplemented with ATTO 633 DOPE (blue) and LUVs are loaded with carboxyfluorescein (green). In the right, normalized fluorescence intensity profiles over time for individual numbered GUVs and average background and in the upper panel the average diameter over time for GUVs.
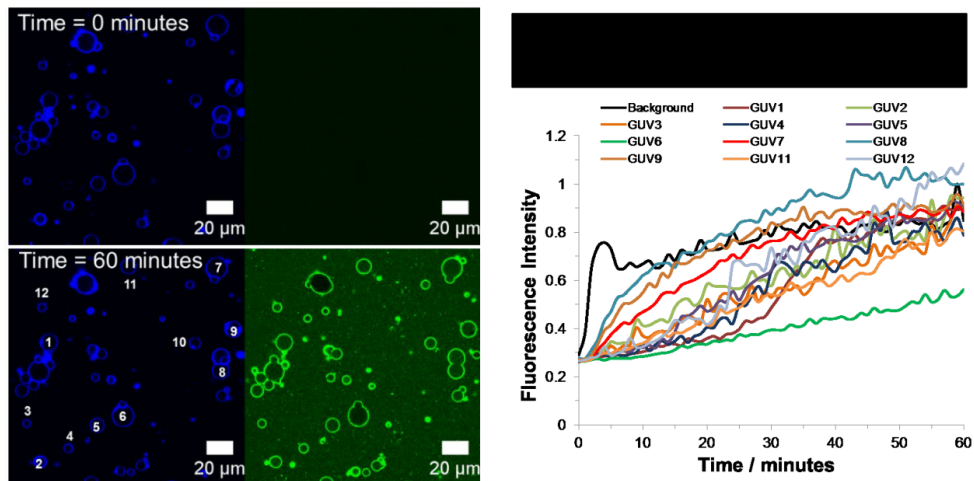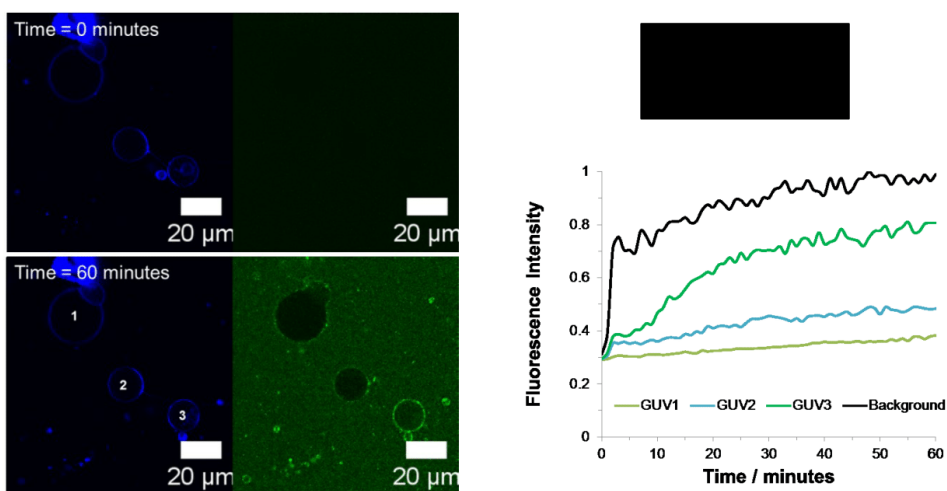

Figure A3. Fluorescence micrographs before (top) and after (bottom) addition of carboxyfluorescein loaded CP_4E_4 liposomes to CP_4K_4 GUVs. GUVs lipid membranes are supplemented with ATTO 633 DOPE (blue) and LUVs are loaded with carboxyfluorescein (green). In the right, normalized fluorescence intensity profiles over time for individual numbered GUVs and average background and in the upper panel the average diameter over time for GUVs.

Content mixing between 0.4 mol % Tween 20-CP$_4$K$_4$ labeled GUVs and CP$_4$E$_4$ labeled LUVs loaded with carboxyfluorescein.
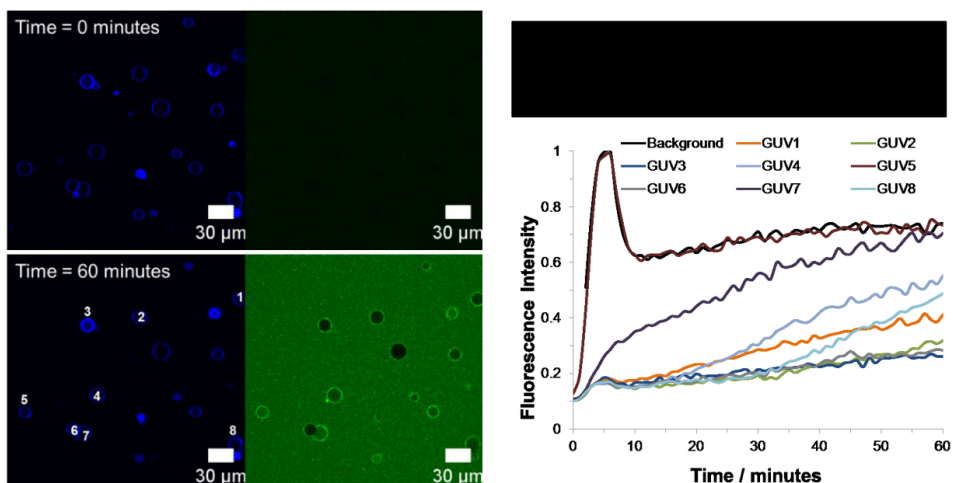

Figure A4. Fluorescence micrographs before (top) and after (bottom) addition of carboxyfluorescein loaded CP$_4$E$_4$ liposomes to CP$_4$K$_4$ GUVs. GUVs lipid membranes are supplemented with ATTO 633 DOPE (blue) and LUVs are loaded with carboxyfluorescein (green). In the right, normalized fluorescence intensity profiles over time for individual numbered GUVs and average background and in the upper panel the average diameter over time for GUVs.
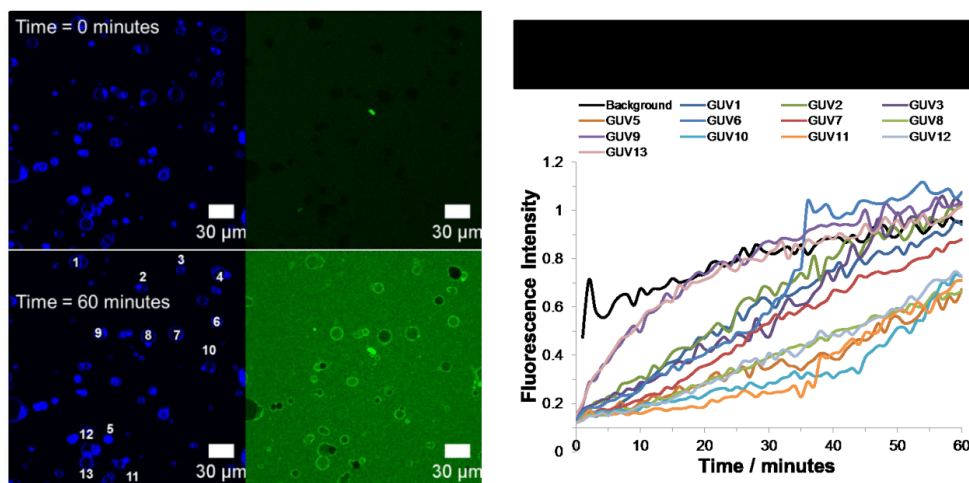

Figure A5. Fluorescence micrographs before (top) and after (bottom) addition of carboxyfluorescein loaded CP$_4$E$_4$ liposomes to CP$_4$K$_4$ GUVs. GUVs lipid membranes are supplemented with ATTO 633 DOPE (blue) and LUVs are loaded with carboxyfluorescein (green). In the right, normalized fluorescence intensity profiles over time for individual numbered GUVs and average background and in the upper panel the average diameter over time for GUVs.

Content mixing between 1 mol % Tween 20-CP$_4$K$_4$ labeled GUVs and CP$_4$E$_4$ labeled LUVs loaded with carboxyfluorescein.

Figure A6. Fluorescence micrographs before (top) and after (bottom) addition of carboxyfluorescein loaded CP$_4$E$_4$ liposomes to CP$_4$K$_4$ GUVs. GUVs lipid membranes are supplemented with ATTO 633 DOPE (blue) and LUVs are loaded with carboxyfluorescein (green). In the right, normalized fluorescence intensity profiles over time for individual numbered GUVs and average background and in the upper panel the average diameter over time for GUVs.

Figure A7. Fluorescence micrographs before (top) and after (bottom) addition of carboxyfluorescein loaded CP$_4$E$_4$ liposomes to CP$_4$K$_4$ GUVs. GUVs lipid membranes are supplemented with ATTO 633 DOPE (blue) and LUVs are loaded with carboxyfluorescein (green). In the right, normalized fluorescence intensity profiles over time for individual numbered GUVs and average background and in the upper panel the average diameter over time for GUVs.

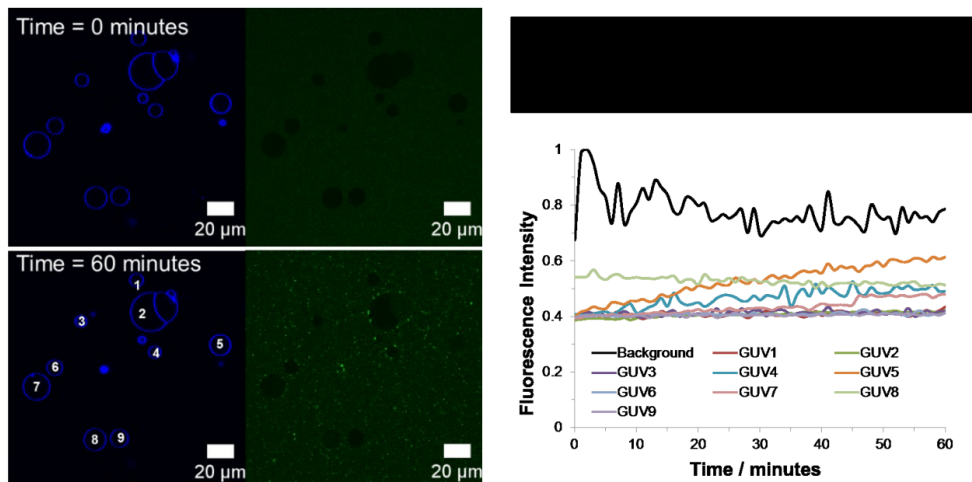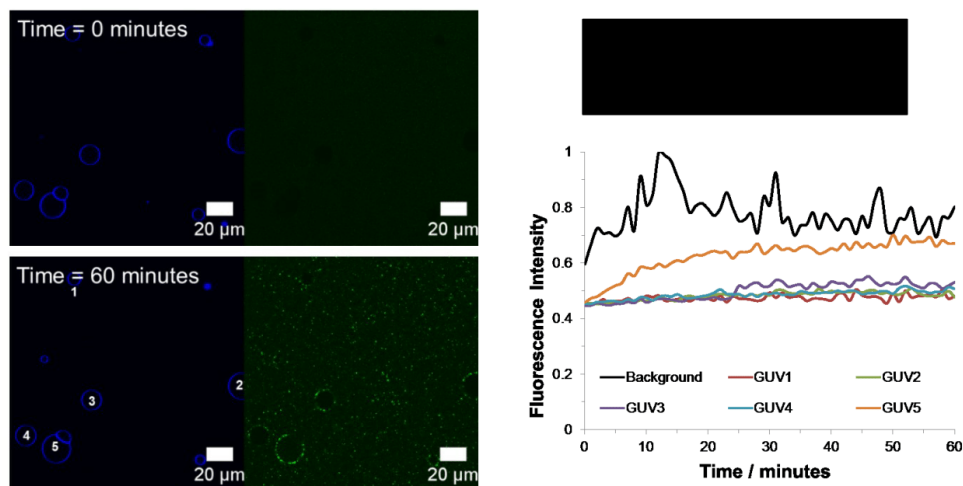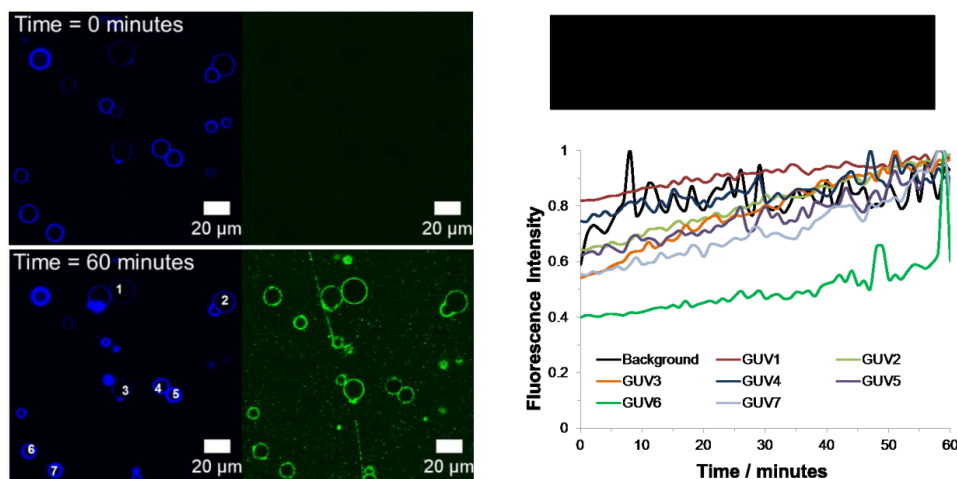*Control experiment between 1 mol % Tween GUVs and LUVs loaded with carboxyfluorescein.*

Figure A8. Fluorescence micrographs before (top) and after (bottom) addition of carboxyfluorescein loaded CP$_4$E$_4$ liposomes to CP$_4$K$_4$ GUVs. GUVs lipid membranes are supplemented with ATTO 633 DOPE (blue) and LUVs are loaded with carboxyfluorescein (green). In the right, normalized fluorescence intensity profiles over time for individual numbered GUVs and average background and in the upper panel the average diameter over time for GUVs.

Figure A9. Fluorescence micrographs before (top) and after (bottom) addition of carboxyfluorescein loaded CP$_4$E$_4$ liposomes to CP$_4$K$_4$ GUVs. GUVs lipid membranes are supplemented with ATTO 633 DOPE (blue) and LUVs are loaded with carboxyfluorescein (green). In the right, normalized fluorescence intensity profiles over time for individual numbered GUVs and average background and in the upper panel the average diameter over time for GUVs.
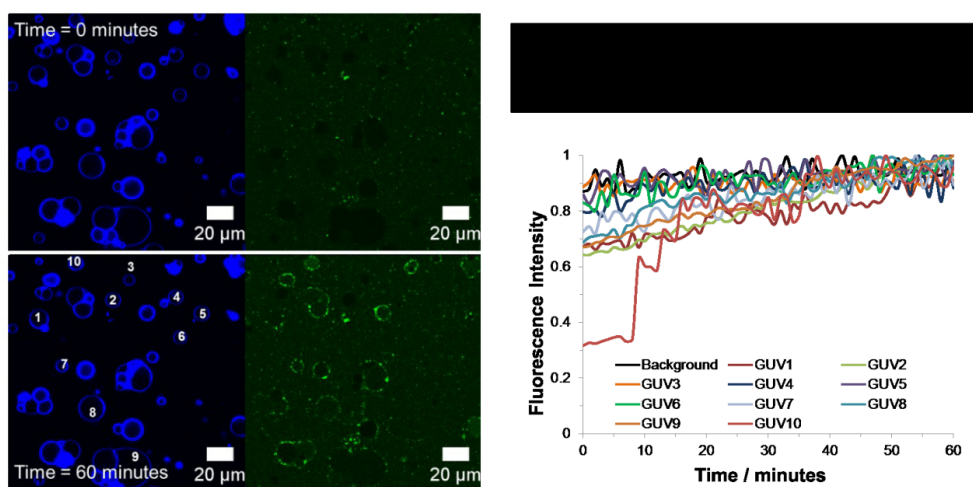
Control experiment between 1 mol % Tween-CP$_4$K$_4$ labeled GUVs and LUVs loaded with carboxyfluorescein.

Figure A10. Fluorescence micrographs before (top) and after (bottom) addition of carboxyfluorescein loaded CP$_4$E$_4$ liposomes to CP$_4$K$_4$ GUVs. GUVs lipid membranes are supplemented with ATTO 633 DOPE (blue) and LUVs are loaded with carboxyfluorescein (green). In the right, normalized fluorescence intensity profiles over time for individual numbered GUVs and average background and in the upper panel the average diameter over time for GUVs.

Figure A11. Fluorescence micrographs before (top) and after (bottom) addition of carboxyfluorescein loaded CP$_4$E$_4$ liposomes to CP$_4$K$_4$ GUVs. GUVs lipid membranes are supplemented with ATTO 633 DOPE (blue) and LUVs are loaded with carboxyfluorescein (green). In the right, normalized fluorescence intensity profiles over time for individual numbered GUVs and average background and in the upper panel the average diameter over time for GUVs.

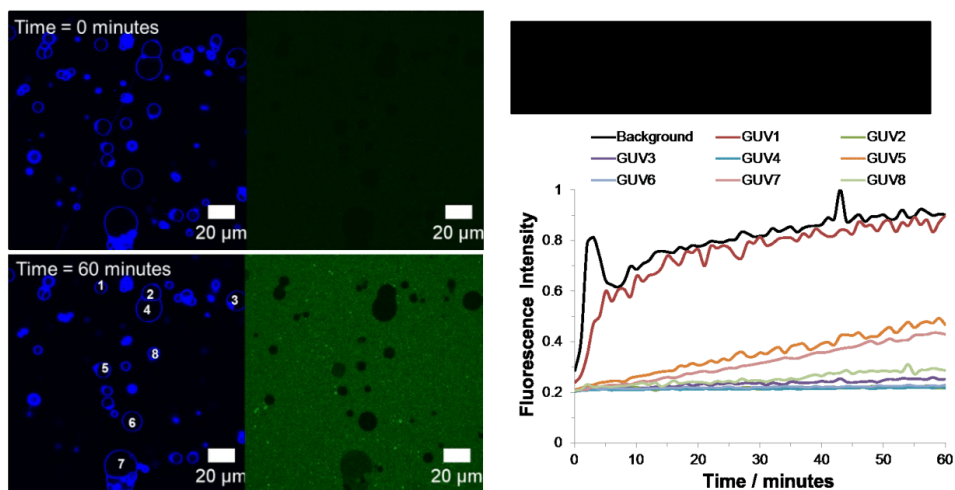*Control experiment between 1 mol % Tween GUVs and CP$_4$E$_4$ LUVs loaded with carboxyfluorescein.*

Figure A12. Fluorescence micrographs before (top) and after (bottom) addition of carboxyfluorescein loaded CP$_4$E$_4$ liposomes to CP$_4$K$_4$ GUVs. GUVs lipid membranes are supplemented with ATTO 633 DOPE (blue) and LUVs are loaded with carboxyfluorescein (green). In the right, normalized fluorescence intensity profiles over time for individual numbered GUVs and average background and in the upper panel the average diameter over time for GUVs.
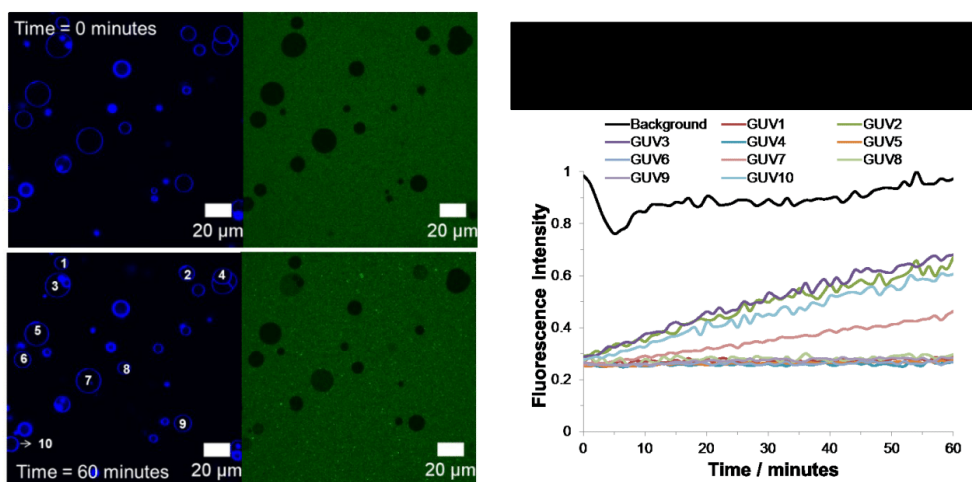

Figure A13. Fluorescence micrographs before (top) and after (bottom) addition of carboxyfluorescein loaded CP$_4$E$_4$ liposomes to CP$_4$K$_4$ GUVs. GUVs lipid membranes are supplemented with ATTO 633 DOPE (blue) and LUVs are loaded with carboxyfluorescein (green). In the right, normalized fluorescence intensity profiles over time for individual numbered GUVs and average background and in the upper panel the average diameter over time for GUVs.

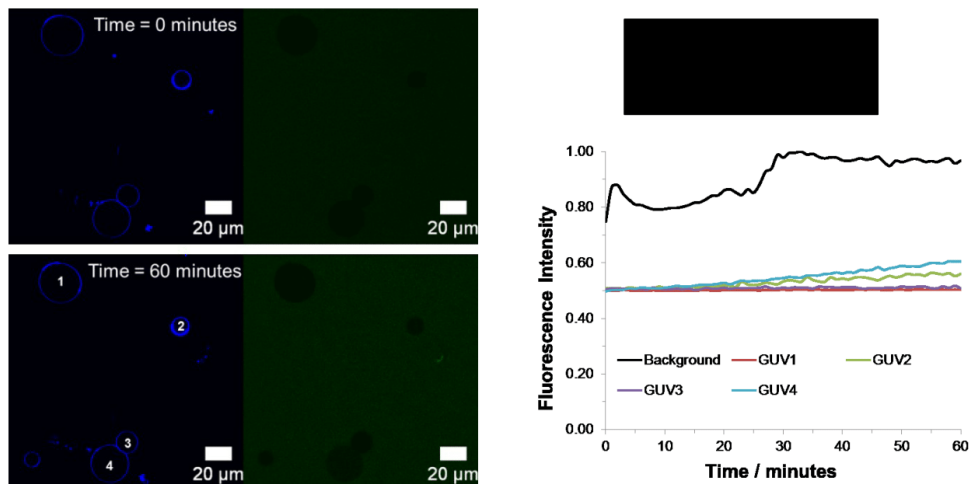*Leakage of 1 µM carboxyfluorescein into 1 mol % Tween-CP$_4$K$_4$ labeled GUVs.*

Figure A14. Fluorescence micrographs before (top) and after (bottom) addition of carboxyfluorescein loaded CP$_4$E$_4$ liposomes to CP$_4$K$_4$ GUVs. GUVs lipid membranes are supplemented with ATTO 633 DOPE (blue) and LUVs are loaded with carboxyfluorescein (green). In the right, normalized fluorescence intensity profiles over time for individual numbered GUVs and average background and in the upper panel the average diameter over time for GUVs.
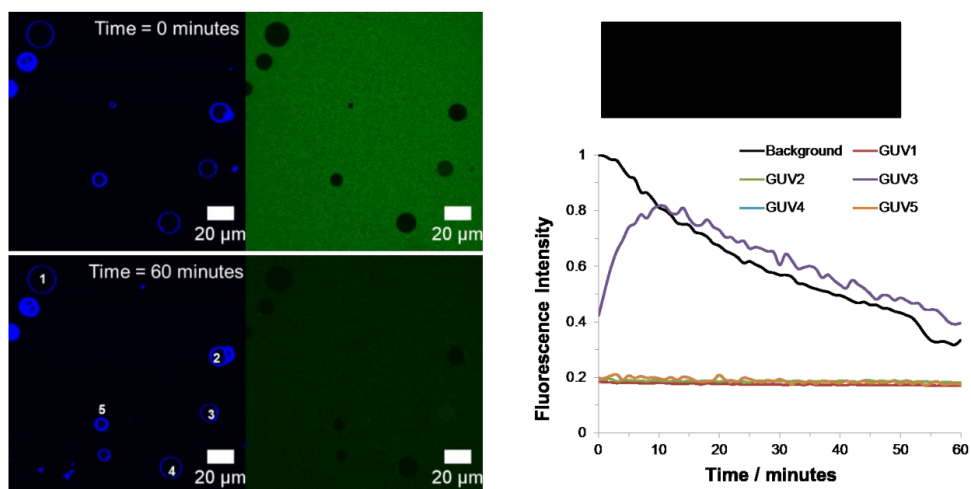

Figure A15. Fluorescence micrographs before (top) and after (bottom) addition of carboxyfluorescein loaded CP$_4$E$_4$ liposomes to CP$_4$K$_4$ GUVs. GUVs lipid membranes are supplemented with ATTO 633 DOPE (blue) and LUVs are loaded with carboxyfluorescein (green). In the right, normalized fluorescence intensity profiles over time for individual numbered GUVs and average background and in the upper panel the average diameter over time for GUVs.

3. REFERENCES

(1)   Voskuhl, J.; Wendeln, C.; Versluis, F.; Fritz, E. C.; Roling, O.; Zope, H.; Schulz, C.; Rinnen, S.; Arlinghaus, H. F.; Ravoo, B. J.; Kros, A. *Angew Chem Int Edit* **2012**, *51*, 12616.
(2)   Marsden, H. R.; Elbers, N. A.; Bomans, P. H. H.; Sommerdijk, N. A. J. M.; Kros, A. *Angew Chem Int Edit* **2009**, *48*, 2330.
(3)   Versluis, F.; Voskuhl, J.; van Kolck, B.; Zope, H.; Bremmer, M.; Albregtse, T.; Kros, A. *Journal of the American Chemical Society* **2013**, *135*, 8057.
(4)   Mora, N. L.; Hansen, J. S.; Gao, Y.; Ronald, A. A.; Kieltyka, R.; Malmstadt, N.; Kros, A. *Chem Commun* **2014**, *50*, 1953.
(5)   Mora, N. L.; Gao, Y.; Gutierrez, M. G.; Peruzzi, J.; Bakker, I.; Peters, R.; Siewert, B.; Bonnet, S.; Kieltyka, R. E.; van Hest, J. C. M.; Malmstadt, N.; Kros, A. *Soft Matter* **2017**, *13*, 5580.
(6)   Angelova, M. I.; Soleau, S.; Meleard, P.; Faucon, J. F.; Bothorel, P. *Prog Coll Pol Sci S* **1992**, *89*, 127.
(7)   Koukalova, A.; Pokorna, S.; Fiser, R.; Kopecky, V., Jr.; Humpolickova, J.; Cerny, J.; Hof, M. *Biochimica et biophysica acta* **2015**, *1848*, 444.